ABSTRACT

Title of Dissertation: PHOTOCHEMISTRY AND TRANSPORT OF TROPOSPHERIC OZONE AND ITS PRECURSORS IN URBAN AND REMOTE ENVIRONMENTS

Daniel Craig Anderson, Doctor of Philosophy, 2016

Dissertation Directed by: Professor Russell Dickerson and Professor Ross Salawitch
Department of Atmospheric and Oceanic Science

Tropospheric ozone (O_3) adversely affects human health, reduces crop yields, and contributes to climate forcing. To limit these effects, the processes controlling O_3 abundance as well as that of its precursor molecules must be fully characterized. Here, I examine three facets of O_3 production, both in heavily polluted and remote environments. First, using *in situ* observations from the DISCOVER-AQ field campaign in the Baltimore/Washington region, I evaluate the emissions of the O_3 precursors CO and NO_x ($NO_x = NO + NO_2$) in the National Emissions Inventory (NEI). I find that CO/NO_x emissions ratios derived from observations are 21% higher than those predicted by the NEI. Comparisons to output from the CMAQ model suggest that CO in the NEI is accurate within 15 ± 11%, while NO_x emissions are overestimated by 51-70%, likely due to errors in mobile sources. These results imply that ambient ozone concentrations will

respond more efficiently to NO_x controls than current models suggest. I then investigate the source of high O_3 and low H_2O structures in the Tropical Western Pacific (TWP). A combination of *in situ* observations, satellite data, and models show that the high O_3 results from photochemical production in biomass burning plumes from fires in tropical Southeast Asia and Central Africa; the low relative humidity results from large-scale descent in the tropics. Because these structures have frequently been attributed to mid-latitude pollution, biomass burning in the tropics likely contributes more to the radiative forcing of climate than previously believed. Finally, I evaluate the processes controlling formaldehyde (HCHO) in the TWP. Convective transport of near surface HCHO leads to a 33% increase in upper tropospheric HCHO mixing ratios; convection also likely increases upper tropospheric CH_3OOH to ~230 pptv, enough to maintain background HCHO at ~75 pptv. The long-range transport of polluted air, with NO four times the convectively controlled background, intensifies the conversion of HO_2 to OH, increasing OH by a factor of 1.4. Comparisons between the global chemistry model CAM-Chem and observations show that consistent underestimates of HCHO by CAM-Chem throughout the troposphere result from underestimates in both NO and acetaldehyde.

PHOTOCHEMISTRY AND TRANSPORT OF TROPOSPHERIC OZONE AND ITS PRECURSORS IN URBAN AND REMOTE ENVIRONMENTS

by

Daniel Craig Anderson

Dissertation submitted to the Faculty of the Graduate School of the
University of Maryland, College Park in partial fulfillment
of the requirements for the degree of
Doctor of Philosophy
2016

Advisory Committee:
Professor Russell R. Dickerson, Advisor
Professor Ross J. Salawitch, Advisor
Doctor Timothy Canty
Professor Sheryl Ehrman
Doctor Thomas Hanisco
Doctor Glenn Wolfe

Dedication

To my mother.

Acknowledgements

First, I would like to thank my advisors, Russ Dickerson and Ross Salawitch, for their patience, insight, and dedication to my academic and intellectual success. Thanks also to Tim Canty, Xinrong Ren, Jeff Stehr, Glenn Wolfe, Tom Hanisco, Julie Nicely, Dan Goldberg, and Tim Vinciguerra for their help throughout my time at the University of Maryland. Thanks also to my family, and especially to Jamie, who has endured, and will continue to endure, years of penury because of my life choices, but despite this fact, is always there for love and support.

Table of Contents

Table of Tables

Table of Figures

List of Acronyms

AEROCE	Atmosphere/Ocean Chemistry Experiment
AIRS	Atmospheric Infrared Sounder
AMAX-DOAS	Airborne Multi-Axis DOAS
ASHOE/MAESA	Airborne Southern Hemisphere Ozone Experiment/Measurement for Assessing the Effects of Stratospheric Aircraft
ATom	Atmospheric Tomography Mission
AWAS	Advanced Whole Air Sampler
BEIS	Biogenic Emission Inventory System
BWR	Baltimore Washington Region
CAA	Clean Air Act
CAM-Chem	Community Atmosphere Model with Chemistry
CAMx	Comprehensive Air Quality Model with Extensions
CAST	Coordinated Airborne Studies in the Tropics
CB05	Carbon Bond Mechanism, Version 5
CBIV	Carbon Bond Mechanism, Version 4
CEMS	Continuous Emissions Monitoring System
CEPEX	Central Equatorial Pacific Experiment
CESM	Community Earth System Model
CIMS	Chemical Ionization Mass Spectrometry
CMAQ	Community Multiscale Air Quality Model
CONTRAST	Convective Transport of Active Species in the Tropics
CTM	Chemical Transport Model
DC3	Deep Convective Clouds & Chemistry Experiment
DFGAS	Difference Frequency Generation Absorption Spectrometer
DISCOVER-AQ	Deriving Information on Surface conditions from Column and Vertically Resolved Observations Relevant to Air Quality
DOAS	Differential Optical Absorption Spectroscopy
dSCD	Differential Slant Column Density
DSMACC	Dynamically Simple Model of Atmospheric Chemical Complexity
EDT	Eastern Daylight Time
ENSO	El Niño/Southern Oscillation
EP	Eastern Pacific
EPA	Environmental Protection Agency
ER	Emissions Ratio
FAAM	Facility for Airborne Atmospheric Measurements
FINN	Fire Inventory for NCAR
FTIR	Fourier Transform Infrared Spectroscopy
GCMS	Gas Chromatography/Mass Spectrometry
GDAS	Global Data Assimilation System
GEOS5	Goddard Earth Observing System Model, Version 5
GHG	Greenhouse Gas
GV	Gulfstream V
HARP	HIAPER Airborne Radiation Package
HIPPO	HIAPER Pole-to-Pole Observations

HOLW	High Ozone/Low Water
HYSPLIT	Hybrid Single Particle Lagrangian Integrated Trajectory Model
INDOEX	INDian Ocean EXperiment
IPCC	Intergovernmental Panel on Climate Change
ISAF	*In situ* Airborne Formaldehyde
LIF	Laser Induced Fluorescence
LIS	Lightning Imaging Sensor
LOD	Limit of Detection
LWC	Liquid Water Content
MACR	Methacrolein
MBL	Marine Boundary Layer
MCE	Modified Combustion Efficiency
MCM	Master Chemical Mechanism
MECCA	Module Efficiently Calculating the Chemistry of the Atmosphere
MHP	Methyl hydroperoxide
mlUT	Mid-Latitude Upper Troposphere
MODIS	Moderate Resolution Imaging Spectroradiometer
MOPITT	Measurement of Pollution in the Troposphere
MOVES2010	Motor Vehicle Emissions Simulator
MOZAIC	Measurement of Ozone and Water Vapour on Airbus in-service Aircraft
MVK	Methyl-Vinyl Ketone
NAAQS	National Ambient Air Quality Standards
NAM	North American Model
NARR	North American Regional Reanalysis
NCAR	National Center for Atmospheric Research
NCEP FNL	National Center for Environmental Prediction Final Analysis
NEI	National Emissions Inventory
NH	Northern Hemisphere
OLR	Outgoing Longwave Radiation
OMI	Ozone Monitoring Instrument
PAN	Peroxyacetyl Nitrate
PBL	Planetary Boundary Layer
PEM-Tropics	Pacific Exploratory Mission in the Tropics
PILS	Particle into Liquid Separator
POLMIP	POLARCAT Model Intercomparison Project
PV	Potential Vorticity
PVU	Potential Vorticity Unit
RAMMPP	Regional Atmospheric Measurement Modeling and Prediction Program
RCP	Representative Concentration Pathway
RF	Research Flight
RH	Relative Humidity
RMSE	Root Mean Square Error
SAGEIII	Stratospheric Aerosol and Gas Experiment III
SCR	Selective Catalytic Reduction

$SEAC^4RS$	Studies of Emissions, Atmospheric Composition, Clouds and Climate Coupling by Regional Surveys
SH	Southern Hemisphere
SHADOZ	Southern Hemisphere Additional Ozonesondes
SIP	State Implementation Plan
SMOKE	Sparse Matrix Operator Kernel Emissions
SNCR	Selective Non-Catalytic Reduction
SZA	Solar Zenith Angle
TD-LIF	Thermal Decomposition Laser Induced Fluorescence
TES	Technology Experiment Satellite
TOGA	Trace Organic Gas Analyzer
TOGA-COARE	The Tropical Ocean Global Atmosphere Coupled Ocean Atmosphere Response Experiment
TRACE-A	Transport and Atmospheric Chemistry in the Atlantic
TRACE-P	Transport and Chemical Evolution over the Pacific
TRMM	Tropical Rainfall Measuring Mission
TTL	Tropical Tropopause Layer
TUV	Tropospheric Ultraviolet and Visible Radiation Model
TWP	Tropical Western Pacific
US	United States
UTC	Coordinated Universal Time
UWCM	University of Washington Chemical Model
VOC	Volatile Organic Compound
WINTER	Wintertime Investigation of Transport, Emission, and Reactivity
WRF	Weather Research and Forecasting Model
WS-CRDS	Wavelength Scanned Cavity Ringdown Spectroscopy
ΣAN	Sum of alkyl and organic nitrates
ΣPAN	Sum of PAN and PAN-like compounds

Chapter 1 Introduction

Tropospheric ozone (O_3) is a secondary atmospheric pollutant produced *in situ* through photochemical reactions and transported from the stratosphere, where naturally occurring O_3 shields the earth's surface from harmful ultraviolet radiation. In a pristine environment, tropospheric O_3 functions primarily as a hydroxyl (OH) precursor, an oxidant that readily removes volatile organic compounds (VOCs), methane, CO, and other species from the atmosphere. Ozone is also a greenhouse gas (GHG), absorbing outgoing longwave radiation and warming the troposphere. At mixing ratios only slightly higher than the natural background surface O_3 can adversely affect human health and damage plant life. Because of these harmful effects on health and agriculture as well as the climatic influence of tropospheric O_3, the processes controlling O_3 production and transport in both urban and remote regions need to be characterized fully. In this dissertation, I investigate three aspects of O_3 production and transport:

- Accuracy of the emissions of the O_3 precursors CO and NO_x ($NO_x = NO + NO_2$) in the urban, mid-Atlantic United States (US) as estimated in the EPA's 2011 National Emissions Inventory (NEI);
- The origin of high O_3/low H_2O (HOLW) structures, ubiquitous in the Tropical Western Pacific (TWP) during winter 2014;
- Dynamical and chemical processes controlling formaldehyde (HCHO), an O_3 precursor, in the TWP.

In the remainder of this chapter, I discuss the importance of tropospheric O_3 as well as the current state of the science concerning the chemical and dynamical processes

controlling the atmospheric abundances of O_3, NO_x, CO, and HCHO. I then describe more thoroughly the questions addressed in this dissertation.

1.1 Importance of Tropospheric Ozone

In the absence of anthropogenic pollution, O_3 acts primarily as an oxidant and as a precursor to other reactive molecules. Ozone readily reacts with alkenes, for example, in an ozonolysis reaction, to produce oxidized VOCs. At wavelengths less than 318 nm, tropospheric O_3 photolyzes to produce $O(^1D)$, which quickly reacts with H_2O to form OH (Reactions (1.1) – (1.2)) or is quenched to $O(^3P)$ to reform O_3. OH is the dominant atmospheric sink for CH_4, CO, and most VOCs, all of which eventually oxidize to CO_2.

Through its relationship with OH, O_3 also indirectly affects the concentration of other important trace gases, altering both stratospheric and tropospheric composition. The hydroxyl radical removes some brominated species, such as CH_2Br_2, as well as many short-lived chlorinated halocarbons from the atmosphere. In the TWP, the region of dominant troposphere-to-stratosphere transport [*Holton et al.*, 1995; *Stohl et al.*, 2003], it has been suggested that low OH concentrations, which can result from low O_3 and/or NO concentrations, allow for transport of these brominated compounds to the stratosphere, where they can react to destroy stratospheric O_3 [*Gao et al.*, 2014; *Rex et al.*, 2014].

$$O_3 + h\nu \rightarrow O_2 + O(^1D) \quad \lambda < 318 \text{ nm} \qquad (1.1)$$
$$O(^1D) + H_2O \rightarrow 2OH \qquad (1.2)$$

Tropospheric O_3 is also a greenhouse gas with an average global radiative forcing of ~0.4 W/m^2, approximately equal to that of CH_4 [*IPCC*, 2013]. Unlike the longer-lived GHGs, O_3 is not well-mixed in the atmosphere, and local radiative forcing can be substantially higher than the global average [*Hansen et al.*, 1997]. Regionally, O_3 in the tropics has a larger impact on global surface air temperature than that in the mid-latitudes

[*Fishman et al.*, 1979; *Shindell and Faluvegi*, 2009; *Stevenson et al.*, 2013]. Likewise, the efficacy of O_3 radiative forcing varies with altitude, with perturbations in upper tropospheric O_3 having a stronger effect on surface temperatures than at lower altitudes [*Forster and Shine*, 1997]. O_3 chemistry can also indirectly affect the global radiative budget. Changes in atmospheric O_3 and consequently OH can alter the lifetime of methane, a potent GHG with a global warming potential approximately 25 times that of CO_2 over 100 years [*IPCC*, 2013].

Surface O_3 adversely impacts both human health and the economy. Long-term exposure to O_3 can limit lung and cardiac function, exacerbate chronic respiratory illnesses, and precipitate early mortality [*Bell et al.*, 2006; *Park et al.*, 2005]. Mixing ratios as low as 20 ppbv contribute to this increased mortality, with risk growing exponentially as O_3 mixing ratios increase [*Bell et al.*, 2006]. Analyzing pollutant exposure and mortality rates in a cohort of Americans from 1977 to 2000, *Jerrett et al.* [2009] found a 3-4% increase in the risk of death from respiratory causes for every 10 ppbv increase in exposure to O_3. On the global scale, exposure to surface O_3 presently results in between 140,000 and 900,000 premature respiratory-related deaths annually, with the highest mortality rates in Eastern Asia, India, and North America [*Silva et al.*, 2013]. By 2050, annual global health care costs related to O_3 exposure could reach $580 billion [*Selin et al.*, 2009].

Exposure to O_3 has similar deleterious economic effects on the agricultural industry. At mixing ratios above 40 ppbv [*Fuhrer et al.*, 1997], O_3 reduces photosynthetic function through multiple pathways in most staple crops [*Fiscus et al.*, 2005]. Ozone damages dicots (*e.g.* cotton, peanuts, and soybeans) more than monocots

(*e.g.* sorghum, corn, and wheat), with yields of the former presently being reduced by approximately 7-16% globally due to O_3 exposure [*Heagle*, 1989; *Van Dingenen et al.*, 2009]. In combination with high temperatures and dry conditions, O_3 is even more damaging to both soybeans and corn [*McGrath et al.*, 2015]. Estimates of global crop yield loss for corn, soybeans, wheat, and rice from O_3 damage range between $11-26 billion for the year 2000 [*Avnery et al.*, 2011; *Van Dingenen et al.*, 2009].

Rapid industrialization since the late 19th century has greatly increased ambient O_3 mixing ratios, particularly in the extra-tropical Northern Hemisphere [*Lamarque et al.*, 2005; *Staehelin et al.*, 1994]. The combination of health, economic, and climate effects have led many mid-latitude countries to reduce O_3 precursor emissions, in an attempt to reverse this trend. Due to regulation from laws such as the Clean Air Act (CAA), growth in ambient O_3 mixing ratios has stopped or reversed in many areas in the eastern US, Europe, and Japan [*Cooper et al.*, 2012; *Oltmans et al.*, 2006]. Certain urban centers, such as the Baltimore/Washington Region (BWR), still frequently experience high O_3, particularly in summer; these values often exceed the National Ambient Air Quality Standard (NAAQS) of 70 ppbv set by the US Environmental Protection Agency (EPA) [*He et al.*, 2014]. In developing countries, such as China, rapid growth in emissions of O_3 precursors are offsetting the gains seen in the industrialized world, as ground-based observations show significant increases in O_3 in the late 20th/early 21st century [*Verstraeten et al.*, 2015; *Wang et al.*, 2001; *Wang et al.*, 2009]. Because O_3 has a lifetime on the order of weeks [*Stevenson et al.*, 2006], transport of O_3 from eastern Asia leads to increases in free troposphere O_3 over the Pacific, Hawaii, and the western US [*Cooper et al.*, 2010; *Lin et al.*, 2014].

1.2 Processes Controlling Tropospheric Ozone

Processes controlling production of tropospheric O_3 vary markedly between polluted environments, where large concentrations of NO_x promote formation of O_3, and the remote, marine atmosphere, where abundant water and insolation promote destruction of O_3. On a global scale, exchange between the stratosphere and troposphere is important in setting the natural background; at the local scale, stratospheric intrusions can be important for temporary O_3 maxima several times larger than background.

1.2.1 Photochemical Ozone Production in a Polluted Environment

In the eastern US, background surface O_3 at rural sites is on the order of 45 ppbv, during the summer and spring [*Cooper et al.*, 2012]. A mixture of meteorology – high temperatures combined with stagnant air associated with the Bermuda High – and chemistry [*Fiore et al.*, 2003; *Logan*, 1989; *Shen et al.*, 2015; *Zhu and Liang*, 2013] can significantly increase summer O_3 mixing ratios to values well above the 70 ppbv EPA O_3 standard [*He et al.*, 2014]. Reaction schemes A and B below show general O_3 production mechanisms in a polluted environment where R represents any VOC, M represents N_2 or O_2, and an asterisk denotes a molecule in an excited state.

Reaction Scheme A

$$R + OH \rightarrow R'CH_3 + H_2O \quad (1.3)$$

$$R'CH_3 + O_2 + M \rightarrow R'CH_3O_2 + M^* \quad (1.4)$$

$$R'CH_3O_2 + NO \rightarrow R'CH_3O + NO_2 \quad (1.5)$$

$$R'CH_3O + O_2 \rightarrow R'CH_2O + HO_2 \quad (1.6)$$

$$HO_2 + NO \rightarrow NO_2 + OH \quad (1.7)$$

$$2 * (NO_2 + h\nu \rightarrow (O^3P) + NO) \quad \lambda < 415 \text{ nm} \quad (1.8)$$

$$2 * ((O^3P) + O_2 + M \rightarrow O_3 + M^*) \quad (1.9)$$

$$\textbf{Net: } R + 4O_2 \rightarrow H_2O + R'CH_2O + 2O_3 \quad (1.10)$$

Reactions (1.5) and (1.7) drive O_3 production through the creation of NO_2 by the reaction of NO with either HO_2 or $R'O_2$. CO can also lead to O_3 formation, via Reaction Scheme B, although in most polluted environments, Reaction Scheme A dominates.

Reaction Scheme B

$$CO + OH \rightarrow CO_2 + H \quad (1.11)$$
$$H + O_2 + M \rightarrow M^* + HO_2 \quad (1.12)$$
$$HO_2 + NO \rightarrow NO_2 + OH \quad (1.13)$$
$$NO_2 + h\nu \rightarrow O(^3P) + NO \quad (1.14)$$
$$O(^3P) + O_2 + M \rightarrow O_3 + M^* \quad (1.15)$$
$$\textbf{Net: } CO + 2O_2 \rightarrow CO_2 + O_3 \quad (1.16)$$

At low NO_x mixing ratios, the RO_x abundance ($RO_x = HO_2 + OH + RO_2 + RO$) is controlled by reactions (1.17) – (1.19), in which the individual RO_x species react with one another to form water and peroxides [*Thornton et al.*, 2002]. In this so-called NO_x-limited regime, reductions in NO_x lead to reductions in O_3 production. In the eastern US, with the exception of a small portion of New York City, the atmosphere presently appears to be in this NO_x-limited regime [*Duncan et al.*, 2010]. At high NO_x mixing ratios, RO_x molecules react with the NO_x species (Reactions (1.20) – (1.21)) in the so-called VOC-limited regime, titrating out NO_x to produce HNO_3 and alkyl nitrates. Here, reductions in ambient NO_x mixing ratios can lead to increases in O_3 production. The exact transition between the NO_x- and VOC-limited regimes is therefore dependent on both the NO_x and VOC mixing ratios. Knowledge of the O_3 production regime for a given location has practical, air quality policy implications, as the efficacy of policy actions (*i.e.* reducing emissions of NO_x, VOCs, or both) depends on the limiting reagent.

$$HO_2 + OH \rightarrow H_2O + O_2 \quad (1.17)$$
$$HO_2 + HO_2 + M \rightarrow M^* + H_2O_2 + O_2 \quad (1.18)$$
$$HO_2 + RO_2 \rightarrow ROOH + O_2 \quad (1.19)$$
$$OH + NO_2 + M \rightarrow HNO_3 + M^* \quad (1.20)$$
$$NO + RO_2 + M \rightarrow RONO_2 + M^* \quad (1.21)$$

1.2.2 Ozone Production in Tropical Biomass Burning Plumes

Photochemical O_3 production is not limited to the urban environment. Fossil fuel emissions in the tropics are significantly lower than in the Northern mid-latitudes [*Granier et al.*, 2011]. Nevertheless, O_3 in the tropical troposphere can exceed 70 ppbv

and has a distinct structure, with total tropospheric column O_3 peaking over the Atlantic and minimizing over the Pacific [*Fishman et al.*, 1991; *Sauvage et al.*, 2006]. This elevated O_3 is most likely due to photochemical production within biomass burning plumes from fires in Africa and South America, with additional *in situ* production aided by NO_x in the upper troposphere provided by lightning [*Fishman et al.*, 1991; *Sauvage et al.*, 2006; *Thompson et al.*, 1996]. *Poppe et al.* [1998] estimated global O_3 production from biomass burning emissions at between 96 and 160 Tg per year, slightly lower than the 170 Tg per year found by *Jaffe and Wigder* [2012]. Precursor emissions and the resultant O_3 formation vary significantly by year and are strongly dependent on the phase of the El Niño/Southern Oscillation (ENSO) [*Chandra et al.*, 2009]. In biomass burning regions, *in situ* observations show that this O_3 production can account for 29-55% of tropospheric column O_3 [*Thompson et al.*, 1996], while chemistry transport models (CTMs) show that, globally, biomass burning increases tropospheric O_3 levels by only 4-5%, primarily in the tropics [*Ziemke et al.*, 2009].

Ozone production in biomass burning plumes is dependent on multiple variables, including fuel type, fire temperature and age, as well as plume dilution and transport [*Jaffe and Wigder*, 2012]. While most fires detrain in the planetary boundary layer (PBL) or the lower free troposphere [*Labonne et al.*, 2007], deep convection can loft emissions from these fires into the mid and upper troposphere [*Pickering et al.*, 1996], where O_3 lifetimes are significantly larger than in the PBL. If O_3 precursors are kept near the surface, in an area of subsidence, for example, biomass burning has little influence on total column O_3 [*Chatfield and Delany*, 1990]. In freshly lofted plumes, however, O_3 production ranges from approximately 2 ppbv/day to over 7 ppbv/day, with higher

production over tropical forests due to large isoprene concentrations [*Kita et al.*, 2002; *Pickering et al.*, 1992]. Production in urban plumes is significantly higher, with median values between 3 and 11 ppbv/hour for various American urban centers [*Kleinman*, 2002].

The relative abundance of nitrogen-containing compounds also substantially affects O_3 production. In some fresh, undiluted plumes from tropical fires, NO_x mixing ratios place O_3 production in the VOC limited regime, resulting in comparatively low O_3 production rates [*Poppe et al.*, 1998]. Dilution with ambient air lowers the NO_x mixing ratio and results in increases in O_3 mixing ratios of up to 70% over undiluted plumes [*Chatfield and Delany*, 1990; *Poppe et al.*, 1998]. The reservoir species peroxyacetyl nitrate (PAN) and NO_x, the predominant forms of reactive nitrogen in fresh plumes, are converted to HNO_3 as the plumes age, reducing the available reactive nitrogen necessary for O_3 production [*Mauzerall et al.*, 1998]. In boreal fires, where emitted NO_x is quickly converted to PAN, biomass burning plumes can be depleted in O_3, in comparison to background air [*Alvarado et al.*, 2010; *Paris et al.*, 2009]. As plumes age, PAN is converted back to NO_x, and O_3 production can increase in the plume far downwind of the emission source [*Parrington et al.*, 2013].

1.2.3 Ozone in the Remote Marine Atmosphere

The pristine environment over the remotest parts of the world's oceans is characterized by low CO and NO_x mixing ratios and surface O_3 on the order of 20 ppbv or lower [*Dickerson et al.*, 1999; *Hernández et al.*, 2001; *McFarland et al.*, 1979; *Read et al.*, 2008; *Rex et al.*, 2014; *Rhoads et al.*, 1997]. In the absence of anthropogenic pollution, Reaction Scheme C dominates, where Reaction (1.23) is the rate-limiting step

in converting O_3 to OH. Large near-surface H_2O concentrations in the remote marine atmosphere make Reaction (1.23) the dominant loss mechanism in the lower troposphere. In the upper troposphere, where H_2O concentrations are orders of magnitude lower, this reaction is negligible, resulting in net O_3 production in the tropics [*Collins et al.*, 2000]. Reaction Scheme C alone, however, cannot reproduce observed surface O_3. Reactions with Br or I radicals, denoted as X in Reaction Scheme D, are also necessary [*Dickerson et al.*, 1999; *Read et al.*, 2008]. Deposition to the sea surface, with wind-dependent deposition velocities of between 0.01 and 0.08 cm/s [*Chang et al.*, 2004], can remove significant O_3, up to one third the amount removed by photochemical loss [*Heikes et al.*, 1996].

Reaction Scheme C

$$O_3 + h\nu \rightarrow O_2 + O(^1D) \quad (1.22)$$
$$O(^1D) + H_2O \rightarrow 2OH \quad (1.23)$$
$$OH + O_3 \rightarrow HO_2 + O_2 \quad (1.24)$$
$$HO_2 + O_3 \rightarrow 2O_2 + OH \quad (1.25)$$

In a polluted environment, deposition and lack of NO_2 photolysis cause a nocturnal O_3 minimum; in the remote marine boundary layer (MBL), surface O_3 minimizes during the day as photolysis destroys O_3 and produces more OH radicals via Reactions (1.22) – (1.23). At night, downward transport from the free troposphere replenishes the depleted surface O_3.

Reaction Scheme D

$$X + O_3 \rightarrow XO + O_2 \quad (1.26)$$
$$XO + XO \rightarrow 2X + O_2 \quad (1.27)$$
$$XO + IO \rightarrow X + OIO \quad (1.28)$$
$$XO + HO_2 \rightarrow HOX + O_2 \quad (1.29)$$
$$HOX + h\nu \rightarrow OH + X \quad (1.30)$$
$$XO + NO \rightarrow NO_2 + X \quad (1.31)$$

In highly convective regions, like the TWP warm pool, convection lofts surface air throughout the tropospheric column, creating an O_3 profile that is nearly constant with

altitude [*Kley et al.*, 1997; *Rex et al.*, 2014; *Thompson et al.*, 2012]. Mid-tropospheric filaments with O_3 much larger than the marine background are frequently observed [*Newell et al.*, 1999; *Stoller et al.*, 1999]. These filaments are suggestive of long-range pollutant transport. Observations and analysis from the Atmosphere/Ocean Chemistry Experiment (AEROCE) suggest that stratosphere/troposphere exchange associated with frontal systems as well as continental boundary layer air, lofted by convection, can explain high O_3 observed off the coast of Bermuda (32° N, 64°-68° W) [*Dickerson et al.*, 1995; *Prados et al.*, 1999]. Studies conducted in the TWP cite stratospheric intrusions [*Newell et al.*, 1999; *Stoller et al.*, 1999], transport from the mid-latitudes [*Hayashi et al.*, 2008; *Kley et al.*, 1997], and photochemical production within biomass burning plumes [*Blake et al.*, 1999; *Folkins et al.*, 1997; *Kondo et al.*, 2004; *Singh et al.*, 2000] as possible filament sources. I discuss the validity of these competing ideas in Chapter 4.

Based on the reactions in the preceding sections, net photochemical O_3 production in the free troposphere in regions with low NO_x concentrations, ignoring halogen radicals, can be estimated by Equation (1.1), where brackets indicate concentrations, k is the reaction constant, and term (2) represents the sum of O_3 production from all organic peroxide compounds.

$$\underset{(1)}{\frac{d[O_3]}{dt}} = \underset{(1)}{k_5[NO][HO_2]} + \underset{(2)}{\sum k_i[RO_2]_i[NO]} - \underset{(3)}{k_{21}[O\ ^1D][H_2O]} - \underset{(4)}{k_{22}[OH][O_3]} - \underset{(5)}{k_{23}[HO_2][O_3]} \qquad \text{Equation (1.1)}$$

Globally, the production terms (terms 1 & 2) are slightly larger than the loss terms (terms 3 – 5) in Equation (1.1). *Fusco and Logan* [2003] report a global photochemical production of 4870 Tg/yr and loss of 4390 Tg/yr. Comparing 26 global CTMs, *Stevenson et al.* [2006] estimate production and loss terms of 5110 ± 606 and 4668 ± 727 Tg/yr, respectively. Deposition to the surface, on the order of 1000 Tg/yr, is also a substantial

O_3 loss mechanism [*Collins et al.*, 2000; *Stevenson et al.*, 2006], closing the O_3 budget and maintaining the balance between production and loss.

1.2.4 Stratosphere/Troposphere Exchange

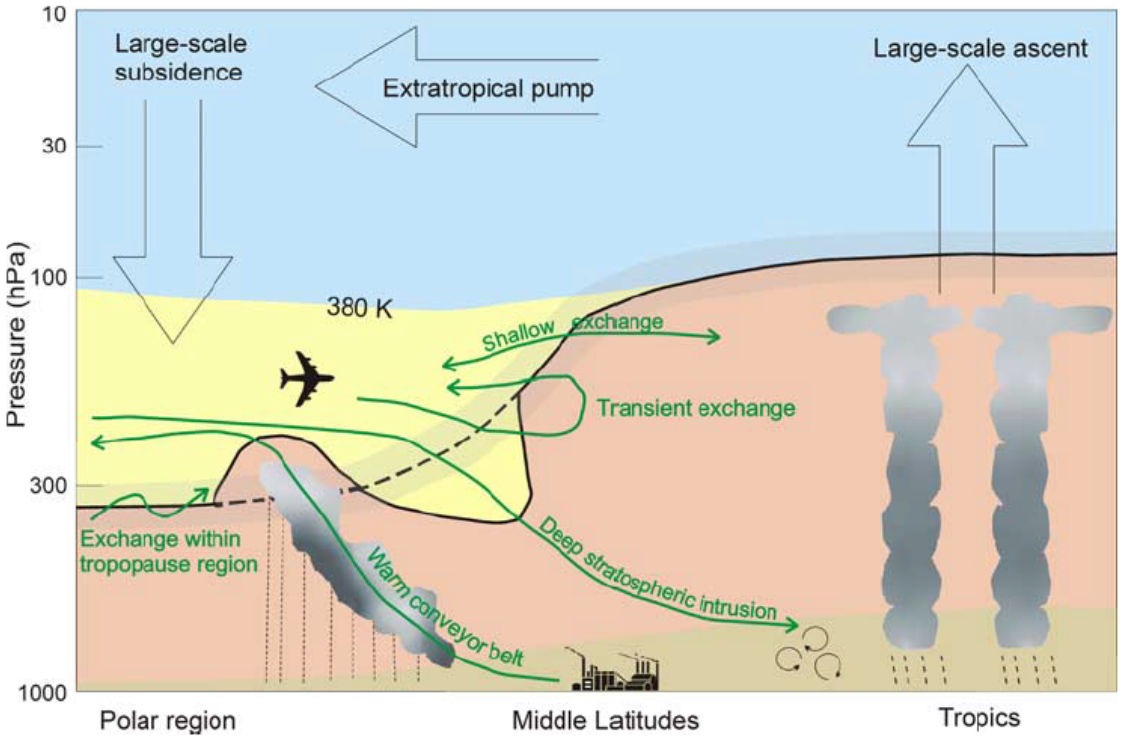

Figure 1.1: Schematic of stratosphere/troposphere exchange. Taken from *Stohl et al.* [2003].

Differences in dynamical stability between the stratosphere and troposphere prevent easy transport between the two regions. The troposphere is heated from below by conduction and longwave radiation emitted at the earth's surface, resulting in a positive lapse rate (*i.e.* temperature decreases with altitude). The stratosphere, on the other hand, is heated from above by O_2 and O_3 photolysis, resulting in a negative lapse rate and high potential vorticity (PV), both of which act as a dynamical barrier to mixing with the troposphere. The two layers are separated by the tropopause, a region with a small lapse rate and typically defined by PV = 2 PVU (1 PVU = 10^{-6} Ks^2/kg) [*Holton et al.*, 1995]. Tropopause heights vary with latitude, with heights in the polar regions

significantly lower than in the tropics [*Stohl et al.*, 2003]. Thus, isentropic surfaces in the mid-latitude stratosphere can be in the tropical upper troposphere, providing a pathway for adiabatic transport from the stratosphere to the troposphere.

Annual stratosphere to troposphere O_3 transport is on the order of 500-600 Tg/yr, equivalent to ~10% of the *in situ* photochemical production in the troposphere [*Collins et al.*, 2000; *Fusco and Logan*, 2003; *Lelieveld and Dentener*, 2000; *Stevenson et al.*, 2006]. The relative importance of stratosphere-to-troposphere O_3 transport differs by latitude, altitude, and season. *Fusco and Logan* [2003] found that, in the GEOS-CHEM model, removing stratospheric flux reduced tropospheric ozone mixing ratios near the mid-latitude tropopause by 20-50 ppbv, about 30% lower than the summer time mean and 50% lower than the winter mean. At the surface, stratospheric influence is far weaker, accounting for only 4-6 ppbv of wintertime and ~1 ppbv of summertime O_3. Using a separate CTM, *Lelieveld and Dentener* [2000] found a stronger stratospheric influence in both summer (5-10%) and winter (30-50%) for O_3 at 700 hPa.

The predominant transport pathways for stratosphere/troposphere exchange are shown in Figure 1.1. Transport to the stratosphere occurs primarily in the tropics, resulting from injection due to overshooting tops in deep convective systems, connecting the ascent in the tropospheric Hadley circulation to the Brewer Dobson circulation in the stratosphere [*Stohl et al.*, 2003]. Transport from the stratosphere to the troposphere generally occurs in the mid-latitudes by a number of mechanisms, generally associated with baroclinic instability. Such mechanisms include Rossby wave breaking [*Holton et al.*, 1995], tropopause folding [*Danielsen*, 1968], and transport in mesoscale convective complexes [*Pan et al.*, 2014].

In the Northern Hemisphere, stratosphere to troposphere exchange maximizes in the winter and early spring, when strong latitudinal temperature gradients increase baroclinic instability. Stratospheric intrusions originate primarily in the storm track regions over the Atlantic and Pacific Oceans between 40° and 65°N. When stratospheric air intrudes to pressures greater than 700 hPa, so-called deep exchange events, the ultimate destination peaks at 30° south of the origin, allowing for transport to the tropics [*Sprenger*, 2003]. Stratosphere to troposphere transport can also be aided by westerly ducts, regions of upper level westerlies in climatological easterly zones. Large amplitude Rossby waves can break in these westerlies, promoting mixing within the equatorial regions [*Waugh et al.*, 1994]. *Waugh and Polvani* [2000] found that transport through this mechanism maximizes in the boreal winter over the Pacific (100° – 180° W) and Atlantic Oceans (0° – 50° W).

1.3 Ozone Precursors

As described in the previous section, NO_x is instrumental in O_3 production through the reaction of NO with both HO_2 and RO_2 as well as the photolysis of NO_2, which liberates $O(^3P)$ radicals. Through its reaction with OH, CO produces HO_2, also necessary for O_3 production. Both species are the product of fossil fuel and biomass combustion. Formaldehyde is also a significant HO_2 source.

1.3.1 Emissions and Chemistry of NO_x

Annual global NO_x emissions are on the order of 35 TgN/year [*Martin et al.*, 2003]. Fossil fuel combustion, the largest contributor (~20 TgN/year), accounts for over 50% of these emissions, followed by biomass burning, lightning, and soil (~5 TgN/year each) [*Holland et al.*, 1999; *Jaegle et al.*, 2005; *Martin et al.*, 2003; *Schumann and*

Huntrieser, 2007]. There is, however, significant uncertainty in the source strength of the latter three contributors, particularly soil NO_x [*Davidson and Kingerlee*, 1997; *Martin et al.*, 2003]. Atmospheric NO_x concentrations vary by orders of magnitude between urban and remote areas, ranging from 1 to 20 ppbv and 0.01 to 0.1 ppbv, respectively [*Seinfeld and Pandis*, 2006].

1.3.1.1 NO_x Emissions

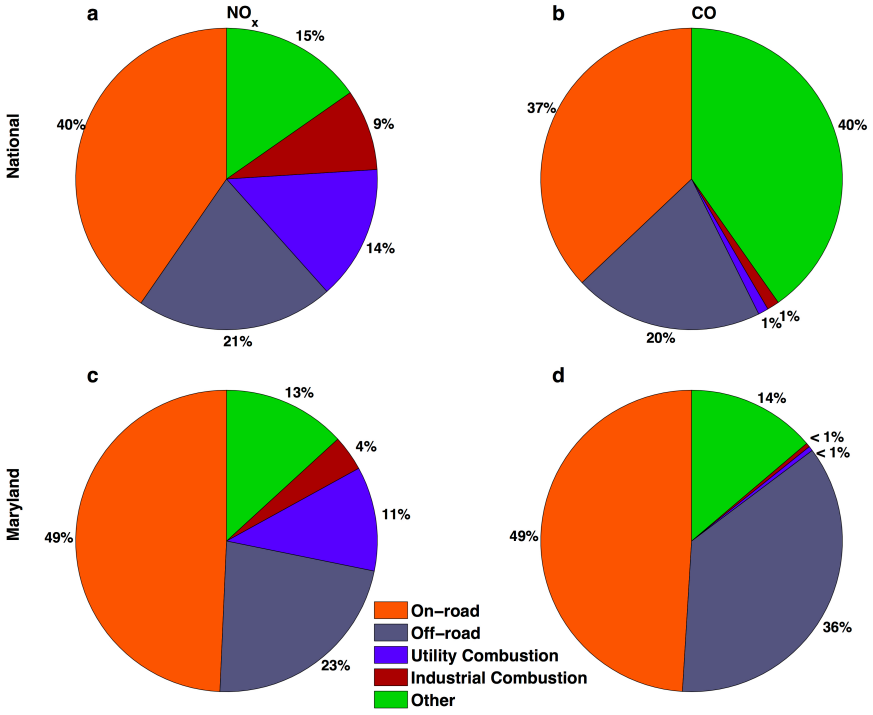

Figure 1.2: National (**a** & **b**) and Maryland (**c** & **d**) emissions of NO_x (**a** & **c**) and CO (**b** & **d**) by sector according to the 2011 NEI. Total emissions for the US (Maryland) are 1.3×10^{10} (1.5×10^{8}) kg and 6.7×10^{10} (6.8×10^{8}) kg for NO_x and CO, respectively.

Fossil fuel combustion dominates anthropogenic NO_x emissions in the US. Figure 1.2 shows American and Maryland NO_x emissions by sector as estimated in the 2011 NEI, Version 2. Mobile emissions, including both on- and off-road sources, are dominant, accounting for 61 and 72% nationally and in Maryland, respectively. Point source emissions, which include fossil fuel combustion in both power plants and the

industrial sector, are the other major contributors, producing another 23% of national NO_x emissions.

Recent regulations promulgated under the CAA have led to significant decreases in both on-road and power plant emissions. In the US, on-road NO_x emissions decreased by ~65% between 1990 and 2010 [*McDonald et al.*, 2012], primarily because of the incorporation of 3-way catalytic converters into gasoline vehicles [*Skalska et al.*, 2010]. Catalytic converters aid in changing NO_x, CO, and hydrocarbons into the unreactive species N_2 and CO_2. NO_x emissions reductions from diesel engines have been less dramatic, however, and as a result, diesel vehicles now account for approximately three quarters of American mobile NO_x [*Ban-Weiss et al.*, 2008; *Dallmann and Harley*, 2010]. The influence of diesel NO_x emissions is even more apparent in the United Kingdom, where diesel vehicles comprise a larger fraction of the on-road fleet than in the US. There, the trend in decreasing ambient NO_x concentrations has plateaued in recent years, primarily because of the relatively poor NO_x emissions controls for diesel engines as compared to gasoline vehicles [*Carslaw et al.*, 2011].

Implementation of NO_x control strategies has also led to significantly reduced power plant NO_x emissions, primarily through selective catalytic reduction (SCR) and selective non-catalytic reduction (SNCR) schemes [*Skalska et al.*, 2010]. SCR and SNCR convert NO to N_2 via reactions with NH_3 or urea (NH_2CONH_2). This reduction is evident in both *in situ* observations in smoke stacks from the Continuous Emission Monitoring System (CEMS), which show reductions of 45% from 1990 to 2004 in emitted NO_x [*US EPA*, 2005], and remotely by satellite observations [*Kim et al.*, 2006]. Also contributing to these reductions is the recent switch from coal to natural gas as the

combustion source in power plants, as hydraulic fracturing techniques have reduced the cost of natural gas extraction. *de Gouw et al.* [2014] found that switching to natural gas reduced power plant NO_x emissions by 40% from 1997 to 2012 over what power plants would have emitted if they continued to use coal. These reductions do not take into account, however, the increased NO_x emissions associated with hydraulic fracturing [*Roy et al.*, 2014].

While NO_x emissions in the mid-latitudes are dominated by fossil fuel combustion, biomass burning is the major NO_x contributor in the tropics. Emissions of nitrogen-containing compounds from biomass burning vary with fire temperature, season, and fuel type, and unlike fossil fuel combustion, emitted NO_x depends on the nitrogen content of the fuel source [*Jaffe and Wigder*, 2012; *Lacaux et al.*, 1996]. Also unlike fossil fuel combustion, biomass burning emits a wide range of nitrogen-containing compounds, including NO_x (primarily in the form of NO), NH_3, cyanides (HCN and CH_3CN), N_2, N_2O, and various other trace species [*Akagi et al.*, 2011; *Andreae and Merlet*, 2001; *Goode et al.*, 1999; *Lobert et al.*, 1990]. Estimates of the fraction of total nitrogen-containing compounds emitted as NO_x range from 12% [*Goode et al.*, 1999; *Lobert et al.*, 1990] to 21% [*Hurst et al.*, 1994]. Ammonia emissions estimates are similar to that of NO_x, while N_2 can comprise between 30 and 40% of total nitrogen-containing compounds [*Kuhlbusch et al.*, 1991]. The cyanides comprise a much smaller fraction, generally less than 1% [*Hurst et al.*, 1994] of total nitrogen, but serve as excellent tracers of biomass burning, since fires are the dominant global emissions source of both HCN and CH_3CN [*de Gouw et al.*, 2003; *Holzinger et al.*, 1999; *Lobert et al.*, 1990].

The relative emissions of the individual species vary with the fire stage. Briefly, after ignition, fires undergo pyrolysis, in which a suite of VOCs is released in the form of a flammable white smoke [*Andreae and Merlet*, 2001]. Once temperatures increase to about 800 K, these VOCs and other species ignite, beginning the flaming stage. In this phase, oxidized products such as NO_x, N_2, and N_2O dominate [*Goode et al.*, 1999]. Once the combustible species are exhausted, temperatures decrease and smoldering begins, where reduced products – NH_3 and cyanides – are more favorably generated [*Yokelson et al.*, 1997]. The fire stage can be described by the modified combustion efficiency (MCE), shown in Equation (1.2), where CO and CO_2 are mixing ratios. The MCE ranges between 0.8 (smoldering phase) and 1 (flaming phase) for wildfires [*Yokelson et al.*, 1997].

$$MCE = \frac{[CO_2]}{[CO_2] + [CO]} \qquad \text{Equation (1.2)}$$

Fuel type, in addition to fire stage, also significantly influences biomass burning emissions of NO_x and other nitrogen-containing compounds. Emissions factors of NO_x, HCN, and CH_3CN by fuel type from two studies (*Andreae and Merlet* [2001] and *Akagi et al.* [2011]) are shown in Table 1.1. The large uncertainty in *Andreae and Merlet* [2001] for most fuel types as well as the differences between the two studies demonstrates the large variability in biomass burning emissions, even for the same fuel type. *Andreae and Merlet* [2001] found emissions of 1.6, 3.0, and 3.9 g NO_x/kg fuel for tropical forests, extratropical forests, and savanna emissions respectively, while *Akagi et al.* [2011] lists emissions from the same sources as 2.55, 1.12, and 3.9 g NO_x/kg fuel. Emissions from boreal forests are more than a factor of two lower than the tropical forests and savanna (Table 1.1), primarily because of the dominance of smoldering

combustion in the extratropics [*Akagi et al.*, 2011; *Jaffe and Wigder*, 2012]. Low NO_x emissions in boreal forest fires suggests that O_3 production in their plumes would be minimal and several studies suggest that O_3 is actually depleted downwind of these fires [*Alvarado et al.*, 2010; *Paris et al.*, 2009].

Table 1.1: Emissions factors for selected species in g per kg fuel for different biomass burning fuel sources. For each fuel type, emissions from *Andreae and Merlet* [2001] are shown on the left and from *Akagi et al.* [2011] on the right. Only *Akagi et al.* [2011] estimated emissions from boreal forests.

	Tropical Forests		**Savanna**		**Extratropical Forests**		**Boreal Forests**
NO_x	1.6 ± 0.7	2.55 ± 1.40	3.9 ± 2.4	3.9 ± 0.80	3.0 ± 1.4	1.12 ± 0.69	0.90 ± 0.69
HCN	0.15	0.42 ± 0.26	0.025-0.031	0.41 ± 0.15	0.15	1.41 ± 0.60	0.73 ± 0.19
CH_3CN	0.18	0.41 ± 0.10	0.11	0.11 ± 0.058	0.19	0.61	0.61
CO	104 ± 20	93 ± 27	65 ± 20	63 ± 17	107 ± 37	122 ± 44	127 ± 45
C_2H_2	0.21 – 0.59	0.44 ± 0.35	0.29 ± 0.27	0.24 ± 0.10	0.27 ± 0.09	0.19 ± 0.09	0.18 ± 0.10
C_6H_6	0.39-0.41	0.39 ± 0.16	0.23 ± 0.11	0.20 ± 0.084	0.49 ± 0.08	1.11	1.11

1.3.1.2 NO_x Chemistry

$$N_2 + O \leftrightarrow N + NO \quad (1.32)$$
$$O_2 + N \leftrightarrow NO + O \quad (1.33)$$
$$\textbf{Net}: N_2 + O_2 \rightarrow 2NO \quad (1.34)$$

NO_x, generally emitted as NO, forms at high temperatures by the Zeldovich Mechanism (Reactions (1.32)-(1.34)) and by nitrification and denitrification in soils [*Parton et al.*, 2001]. NO_2 forms by the reaction of NO with O_3 (Reaction (1.35)), HO_2 (Reaction (1.13)), or RO_2 (Reaction (1.5)). In sunlight, NO_2 rapidly photolyzes to produce NO and $O(^3P)$ (Reaction (1.8)). NO_2 can also react with OH to produce HNO_3 (Reaction (1.20)) or with O_3 to form NO_3 (Reaction (1.36)). Daytime NO_3 concentrations are negligible due to rapid photolysis. Nighttime NO_3 concentrations, however, can be significant, reaching 100 pptv or higher [*Seinfeld and Pandis*, 2006]. NO_3 reacts with NO_2, forming N_2O_5, which, depending on temperature, can dissociate back to the reactants (Reaction (1.37)). Reaction (1.37) favors N_2O_5 production at low temperatures and high NO_2 concentrations. Assuming a rate constant of $1.36 \times 10^{15}\exp(-11300/T)$, the

lifetime of N_2O_5 with respect to its thermal dissociation increases from 17 seconds to 8 hours from 300 to 250 K [*Ide et al.*, 2008]. Heterogeneous reactions with water can then convert the N_2O_5 to HNO_3 (Reaction (1.38)) [*Wayne et al.*, 1991]. In some locations, this heterogeneous chemistry can produce approximately 1/3 of observed HNO_3, making conversion of N_2O_5 to HNO_3 a significant NO_x sink [*Alexander et al.*, 2009; *Brown et al.*, 2004]. The lifetime of NO_x and HNO_3 ranges from several hours to a day in the PBL of the eastern US, while the NO_x lifetime in the free troposphere is on the order of 5-10 days [*Jaegle et al.*, 1998b; *Liang et al.*, 1998].

$$NO + O_3 \rightarrow NO_2 + O_2 \quad (1.35)$$
$$NO_2 + O_3 \rightarrow NO_3 + O_2 \quad (1.36)$$
$$NO_3 + NO_2 + M \leftrightarrow N_2O_5 + M^* \quad (1.37)$$
$$N_2O_5 + H_2O_{(aq)} \rightarrow 2HNO_3 \quad (1.38)$$

NO_x species can also react to form longer-lived compounds, such as PAN and alkyl/organic nitrates, both of which can dissociate to reform NO_x. The longer lifetimes of PAN and organic nitrates, as compared to NO_x, allows for long-range transport of nitrogen-containing compounds between emission and the site of O_3 formation, making these reactions important for air quality regulation [*Beaver et al.*, 2012; *Derwent and Jenkin*, 1991; *Moxim et al.*, 1996]. Because of the interconversion of these species and their importance to atmospheric chemistry, NO_x, PAN, alkyl nitrates, NO_3, N_2O_5, and HNO_3 are known collectively as NO_y.

PAN and PAN-like compounds have the general structure, $RC(O)OONO_2$, where R is any organic group, the simplest of which is CH_3. PAN is formed by oxidation of acetaldehyde by OH and subsequent reactions with O_2 and NO_2 (Reactions (1.39)-(1.41)) [*Finlayson-Pitts and Pitts*, 1999]. Like N_2O_5, at high temperatures, PAN can thermally dissociate to its precursor molecules. Cold environments, however, strongly favor PAN

formation, making PAN a large NO_x reservoir at low temperatures. For example, assuming a rate constant of $4.0 \times 10^{16}\exp(-13600/T)$, the lifetime of PAN with respect to its thermal dissociation increases from 20 minutes to 122 days from 300 to 250 K [*Orlando et al.*, 1992]. If then transported back to a warm environment, PAN will dissociate, liberating its nitrogen and organic components, which can further react to produce O_3 [*Moxim et al.*, 1996].

$$CH_3CHO + OH \rightarrow CH_3CO + H_2O \quad (1.39)$$
$$CH_3CO + O_2 + M \rightarrow CH_3C(O)O_2 + M^* \quad (1.40)$$
$$CH_3C(O)O_2 + NO_2 + M \leftrightarrow CH_3C(O)OONO_2 + M^* \quad (1.41)$$

Like PAN, alkyl nitrates are a NO_x reservoir. These compounds form when an alkylperoxy radical (RO_2) reacts with NO_2 to form $RONO_2$ [*Atkinson et al.*, 1982; *Carter and Atkinson*, 1989]. Other organic radicals, particularly those formed by isoprene oxidation, can also react with NO_2 to form nitrate compounds [*Paulot et al.*, 2009]. Organic nitrate molecules are destroyed by either photolysis or OH oxidation, converting the nitrogen back to NO_x and freeing the organic component, as with PAN. The lifetimes of the individual nitrate species vary significantly, from hours to days, strongly affecting their ability to transport nitrogen long distances [*Clemitshaw et al.*, 1997; *Perring et al.*, 2009]. In the eastern United States, isoprene nitrate chemistry dominates, consuming 15-19% of emitted NO_x and exporting approximately 10% of that NO_x far from the emission site [*Horowitz et al.*, 2007]. In some instances, transported isoprene nitrates dominate over those produced locally [*Beaver et al.*, 2012]. Likewise, transport of alkyl [*Atlas*, 1988] and isoprene [*Paulot et al.*, 2012] nitrates can bring NO_x to remote locations

NO_y species are primarily removed from the atmosphere by dry and wet deposition in the form of HNO_3 [*Hanson and Lindberg*, 1991]. While there is still much uncertainty on deposition velocities of individual NO_y species, which vary strongly with

foliage type and meteorology, estimated values for HNO_3, NO_2, and NO range up to 2.6, 0.20, and 0.04 cm/s respectively, making NO and NO_2 deposition negligible compared to that of HNO_3 [*Clarke et al.*, 1997; *Hanson and Lindberg*, 1991; *Meyers et al.*, 1991]. In arid regions, dry deposition can dominate; in the eastern US, dry deposition of HNO_3 is estimated to account for 30-50% of total deposition of NO_y species [*Bytnerowicz and Fenn*, 1996; *Meyers et al.*, 1991].

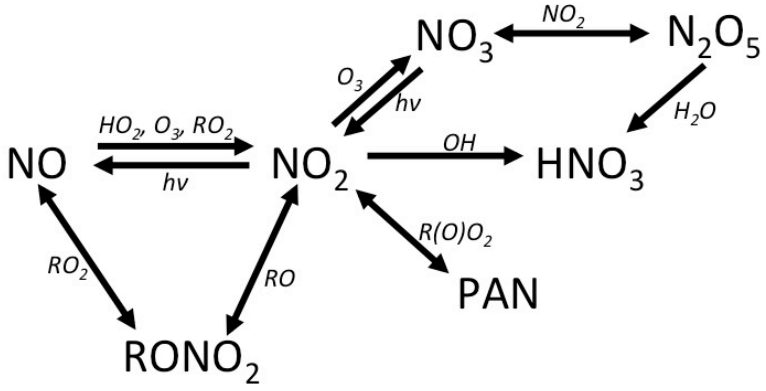

Figure 1.3: Summary of NO_y Chemistry

HNO_3 is highly soluble in water and is easily scavenged by clouds and precipitation, which can lead to significant wet deposition of nitrogen species in the mid-Atlantic US [*Holland et al.*, 2005]. HNO_3 can also react with NH_3 to form ammonium nitrate aerosol (Reaction (1.42)), which, like gaseous HNO_3, can either be scavenged by precipitation or dry deposit at the surface [*Seinfeld and Pandis*, 2006]. NO_y chemistry is summarized in Figure 1.3.

$$HNO_{3(g)} + NH_{3(g)} \rightarrow (NH_4NO_3)_{aq} \quad (1.42)$$

1.3.2 Emissions and Chemistry of CO

Atmospheric CO is produced as a byproduct of incomplete combustion and the oxidation of VOCs. Total CO emissions, both primary and secondary, are on the order of 2500 Tg/year [*Duncan et al.*, 2007; *Holloway et al.*, 2000; *Hooghiemstra et al.*, 2012].

Fossil fuel combustion and biomass burning emit ~700 and 400 – 500 Tg CO/year respectively [*Granier et al.*, 2011; *Hooghiemstra et al.*, 2012]. Secondary CO production through methane and VOC oxidation generates approximately 680 and 760 Tg/year, respectively [*Holloway et al.*, 2000]. In environments with large isoprene emissions, such as the Southeastern US, *in situ* CO production roughly equals that directly emitted by fossil fuel combustion [*Hudman et al.*, 2008]. Estimates of CO emissions vary significantly between bottom-up and top-down inventories, particularly for biomass burning and VOC oxidation [*Arellano et al.*, 2004; *Kopacz et al.*, 2010]. For example, estimating primary emissions from inverse modeling of satellite observed CO, *Kopacz et al.* [2010] estimated global, primary CO emissions to be 57% higher than those from bottom-up inventories. In regions dominated by CO emissions from biomass burning, their *a posteriori* inventory was 53%, 77%, and 86% higher in South America, Southeast Asia, and Southern Africa, respectively.

As with NO_x emissions, fossil fuel combustion dominates anthropogenic CO emissions in the mid-latitudes. Unlike NO_x, however, power plant emissions comprise less than 1% of CO emissions, both nationally and in Maryland (Figure 1.2). Mobile emissions, both on- and off-road account for ~85% of CO emissions in Maryland and 57% nationally. Despite the dominance of mobile emissions, three-way catalytic converters have drastically reduced American CO emission from gasoline vehicles, leading to a threefold decrease in ambient CO mixing ratios from 1975 to 2000 [*Hallock-Waters et al.*, 1999; *Parrish*, 2006]. In some developing countries, particularly those in Southeast Asia, mobile CO emissions are dominated by two-stroke engines, which tend to emit high CO and low NO_x [*Dickerson et al.*, 2002].

In the Southern Hemisphere and tropics, CO emissions are dominated by biomass burning [*Hooghiemstra et al.*, 2012; *J W Kaiser et al.*, 2012; *Wiedinmyer et al.*, 2011]. Globally, interannual variability in CO emissions is almost exclusively dependent on changes in biomass burning [*Voulgarakis et al.*, 2015]. As with NO_x, CO emissions from fires are highly dependent on fuel type and fire stage. Smoldering fires tend to emit more CO than fires in the flaming stage due to increased incomplete combustion associated with lower fire temperatures [*Jaffe and Wigder*, 2012]. Table 1.1 lists CO emissions factors for four different fuel types. Per kilogram of combusted fuel, boreal forests emit the most CO, consistent with the fact that boreal fires mostly undergo smoldering combustion, followed by extratropical forests, tropical forests, and savanna fires, which have an emission factor about half that of boreal forests. Despite the difference in emission factors, tropical forests and savannas are still the dominant global source of biomass burning CO because of the high frequency of fires in the tropics and the comparatively lower number of fires in the boreal region [*Wiedinmyer et al.*, 2011]. In winter and early spring, CO emissions from biomass burning are dominated by fires in the NH African tropics and mainland Southeast Asia [*Voulgarakis et al.*, 2015; *Wiedinmyer et al.*, 2011].

The dominant CO sink is its reaction with OH to form CO_2 (Reaction (1.11)). Through this conversion to CO_2, CO indirectly affects the earth's radiative budget and the atmosphere's oxidative capacity, although this effect is small in comparison to the radiative forcing of climate from the direct emission of CO_2 [*IPCC*, 2013; *Logan et al.*, 1981]. CO removal by dry deposition is negligible, making its lifetime of one to two months entirely dependent on the reaction with OH [*Kopacz et al.*, 2010].

1.3.3 Emissions and Chemistry of Formaldehyde

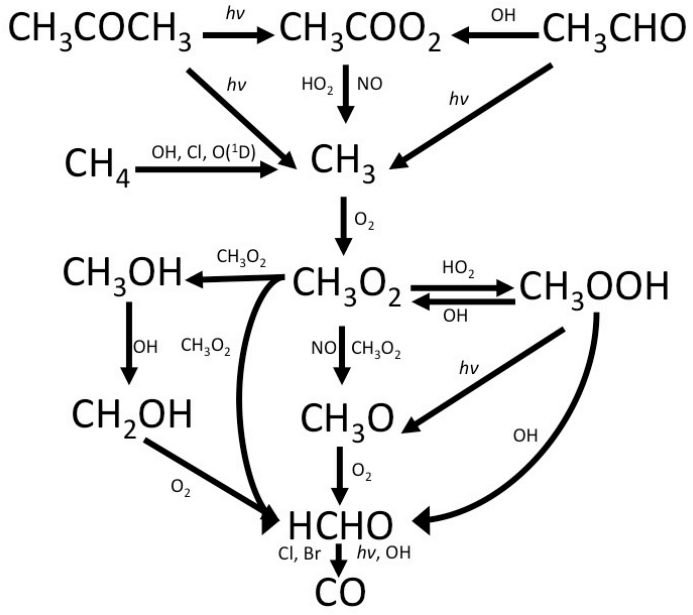

Figure 1.4: Summary of the major pathways for formaldehyde production in the absence of isoprene. After *Stickler et al.* [2006].

The atmospheric HCHO budget is dominated by *in situ* production, with methane oxidation estimated to provide ~967 Tg yr^{-1} of HCHO and oxidation of other hydrocarbons contributing an additional 250 Tg yr^{-1} [*Fortems-Cheiney et al.*, 2012]. There are minor primary emissions, on the order of 10 Tg yr^{-1} or less, from biomass burning [*Akagi et al.*, 2011; *Andreae and Merlet*, 2001], industry [*Friedfeld et al.*, 2002; *Garcia et al.*, 2006; *Parrish et al.*, 2012], agriculture [*J Kaiser et al.*, 2015], automobiles [*Grosjean et al.*, 2001; *Lipari and Swarin*, 1982], shipping [*Marbach et al.*, 2009], and vegetation [*DiGangi et al.*, 2011]. The short atmospheric lifetime of HCHO prevents long-range transport of these primary emissions to remote regions [*Vigouroux et al.*, 2009]. Oceanic emission has also been suggested as a primary HCHO source in the remote marine environment [*Zhou and Mopper*, 1997]. While isoprene and other VOCs are significant HCHO precursors in areas with large biogenic or anthropogenic emissions [*Millet et al.*, 2006; *Palmer et al.*, 2003], in the remote marine environment, atmospheric

HCHO is primarily produced by methane oxidation [*Ayers et al.*, 1997]. In addition, there are non-negligible contributions from acetone [*Jaegle et al.*, 2000], methanol [*Jaegle et al.*, 2000], and acetaldehyde [*Singh et al.*, 2004]. This *in situ* production in remote regions typically results in HCHO mixing ratios from 200 to 400 pptv near the surface and significantly lower values, frequently below 100 pptv, in the upper troposphere [*Ayers et al.*, 1997; *Fried et al.*, 2011; *Fried et al.*, 2003; *Frost et al.*, 2002; *Heikes et al.*, 2001; *Jones et al.*, 2009; *Still et al.*, 2006].

Formaldehyde production from methane is generally initiated by reaction with OH, $O(^1D)$, or Cl, producing the peroxymethyl radical (CH_3O_2) ((1.43)–(1.45)). Globally, oxidation by the chlorine radical occurs primarily in the PBL where heterogeneous production of Cl is high [*Vigouroux et al.*, 2009]. In the tropical, upper troposphere, however, low OH concentrations, driven by cold temperatures and the resultant low H_2O concentrations, increase the importance of reaction (1.44), which can account for 10 to 30% of total methane oxidation in this region [*Lary*, 2005]. The peroxymethyl radical reacts to produce CH_3O (1.47), methyl hydroperoxide (CH_3OOH) (1.48), solely HCHO (1.49), or HCHO and methanol (CH_3OH) (1.50). Methyl hydroperoxide can either react with OH (1.51) to form HCHO directly or photolyze (1.52) to produce CH_3O, which reacts quickly with O_2 to form HCHO (1.53).

As with methane, OH oxidizes methanol to produce CH_2OH (1.54), which quickly reacts with O_2 to form HCHO. Both acetone and acetaldehyde can either photolyze or react with OH ((1.55) – (1.57)). Only the dominant reaction pathways are highlighted here. Acetone photolysis, followed immediately by reaction with O_2, produces CH_3O_2 and $CH_3C(O)O_2$. Similarly, acetaldehyde photolysis produces a

combination of CH_3O_2, CO, and HO_2, while OH oxidation of acetaldehyde produces $CH_3C(O)O_2$. $CH_3C(O)O_2$ can react with either HO_2 (1.58) or NO (1.59) to produce CH_3O_2.

$$CH_4 + OH \rightarrow CH_3 + H_2O \quad (1.43)$$
$$CH_4 + Cl \rightarrow CH_3 + HCl \quad (1.44)$$
$$CH_4 + O(^1D) \rightarrow CH_3 + HCl \quad (1.45)$$
$$CH_3 + O_2 + M \rightarrow CH_3O_2 + M^* \quad (1.46)$$
$$CH_3O_2 + NO \rightarrow CH_3O + NO_2 \quad (1.47)$$
$$CH_3O_2 + HO_2 \rightarrow CH_3OOH + O_2 \quad (1.48)$$
$$CH_3O_2 + HO_2 \rightarrow HCHO + H_2O + O_2 \quad (1.49)$$
$$CH_3O_2 + CH_3O_2 \rightarrow HCHO + CH_3OH + O_2 \quad (1.50)$$
$$CH_3OOH + OH \rightarrow HCHO + OH + H_2O \quad (1.51)$$
$$CH_3OOH + h\nu \rightarrow CH_3O + OH \quad (1.52)$$
$$CH_3O + O_2 \rightarrow HCHO + HO_2 \quad (1.53)$$
$$CH_3OH + OH \rightarrow H_2O + HCHO + HO_2 \quad (1.54)$$
$$CH_3CHO + h\upsilon \rightarrow CH_3 + CO + HO_2 \quad (1.55)$$
$$CH_3CHO + OH \rightarrow CH_3COO_2 + H_2O \quad (1.56)$$
$$CH_3COCH_3 + h\upsilon \rightarrow CH_3COO_2 + CH_3 \quad (1.57)$$
$$CH_3C(O)O_2 + HO_2 \rightarrow CH_3 + OH \quad (1.58)$$
$$CH_3C(O)O_2 + NO \rightarrow CH_3 + NO_2 \quad (1.59)$$

Chemical sinks of HCHO include two photolytic pathways as well as reactions with OH, NO_3, Cl, and Br. Oxidation of HCHO by OH (1.60) has no net effect on total HO_x, as OH is converted to HO_2 in the presence of NO_x. At low NO_x concentrations, however, HCHO oxidation acts as an effective OH sink, as the conversion of HO_2 to OH is inhibited [*Gao et al.*, 2014]. Photolysis is a significant source of HO_2 as well as H_2 ((1.61)-(1.62)). *Toyota et al.* [2004] found that, for a representative mid-latitude MBL with BrO mixing ratios on the order of 2 pptv, the bromine pathway accounted for 1% or less of HCHO destruction. Similar results were found over the Indian Ocean MBL for the INDian Ocean EXperiment (INDOEX) campaign in which the modeled daily maximum of BrO was ~0.1 pptv [*Wagner et al.*, 2002]. Inorganic bromine in both these studies was derived from aerosol observations, not from measurements of BrO. NO_3 is

only abundant at night and is a negligible daytime HCHO sink. Other removal mechanisms include dry and wet deposition [*Economou and Mihalopoulos*, 2002; *Thompson*, 1980; *Tost et al.*, 2007] and processing in clouds [*Amato et al.*, 2007; *Barth et al.*, 2003; *Tost et al.*, 2007]. Formaldehyde chemistry is summarized in Figure 1.4.

$$OH + HCHO \rightarrow CO + H_2O + HO_2 \quad (1.60)$$
$$HCHO + h\upsilon \rightarrow CO + H_2 \quad (1.61)$$
$$HCHO + h\upsilon \rightarrow CO + 2HO_2 \quad (1.62)$$
$$HCHO + Br \rightarrow HBr + CO + HO_2 \quad (1.63)$$
$$HCHO + Cl \rightarrow HCl + CO + HO_2 \quad (1.64)$$
$$NO_3 + HCHO \rightarrow HNO_3 + CO + HO_2 \quad (1.65)$$

1.4 Study Goals

In this work, I investigate three distinct areas that affect photochemical O_3 production and transport. In Chapter 2, I focus on the chemistry and emissions of O_3 precursors in the BWR, an urban area in the US mid-Atlantic. I use data obtained during summer 2011 in the Deriving Information on Surface conditions from Column and Vertically Resolved Observations Relevant to Air Quality (DISCOVER-AQ) field campaign, as well as output from the Community Multiscale Air Quality (CMAQ) model to investigate NO_x and CO emissions. The main goals of that chapter are:

1. Determination of the CO to NO_x emissions ratio in the BWR using regression analysis and estimation of any underlying uncertainties;
2. Evaluation of the accuracy of CO and NO_x emissions in the 2011 NEI using the observed emissions ratios and output from CMAQ, and if disagreement between observations and the NEI does exist, determination of the reasons for that disagreement;
3. Comparison of observed CO, total NO_y, and the NO_y constituents to CMAQ output to evaluate the model chemistry.

In Chapter 3, I describe the CONvective TRansport of Active Species in the Tropics (CONTRAST) and Coordinated Airborne Studies in the Tropics (CAST) campaigns, both conducted in winter 2014 in the TWP. Data from these campaigns are used to investigate the origin of HOLW structures that were frequently observed during the campaigns in Chapter 4. A combination of *in situ* and remotely sensed observations, as well as Eulerian and Lagrangian models are used to determine:

1. The relative contributions of stratospheric, mid-latitude, and tropical air to the observed O_3 in the HOLW structures;
2. The impact of biomass burning, fossil fuel combustion, and stratospheric intrusions on O_3 in the TWP;
3. Whether the dry air observed in the HOLW structures originates from large-scale descent in the tropics, horizontal advection from the mid-latitudes, or from some other source.

In Chapter 5, I determine the chemical and dynamical processes controlling the atmospheric concentration and distribution of HCHO observed during CONTRAST and discuss the impacts of these processes on upper tropospheric HO_x. Here, I investigate, among other things:

1. The impacts of convection on upper tropospheric HCHO composition and the effects of this convection on HO_x production from HCHO;
2. The dominant sources and sinks of HCHO in the TWP;
3. The representation of HCHO and its precursors in the Community Atmosphere Model version 4.0 with chemistry (CAM-Chem).

Finally, in Chapter 6, I summarize the results found in this work, their potential impacts, and provide suggestions for future research.

Chapter 2 Evaluation of CO and NO_x Emissions and Chemistry over the Eastern United States

The majority of this chapter appeared previously as *Anderson et al.* [2014]. Where appropriate, data and citations have been updated with information released after publication. Content has also been reorganized for clarity.

2.1 Background

Both NO_x and CO adversely affect human health and are O_3 precursors, a secondary air pollutant that can cause respiratory ailments in vulnerable populations [*Bell et al.*, 2006; *US EPA*, 2008; 2010]. Enactment of the CAA has significantly reduced CO and NO_x concentrations in the US. Maximum ambient CO concentrations in urban areas decreased by a factor of three between 1977 and 2000 while NO_x concentrations have decreased by a factor of two over the same period, putting both species well below the NAAQS set by the EPA [*He et al.*, 2013; *Parrish*, 2006]. Ozone concentrations have decreased comparatively little, with multiple sites across the country exceeding NAAQS limits [*Cooper et al.*, 2012; *Fiore et al.*, 1998]. This is particularly true in the BWR which has significant surface O_3 throughout, especially over the Chesapeake Bay [*Goldberg et al.*, 2014].

The reduction in ambient CO and NO_x concentrations is reflected in estimates of changes in emissions [*Bishop et al.*, 2012]. National, on-road NO_x emissions decreased by ~65% between 1990 and 2010 [*McDonald et al.*, 2012]. Different regulatory strategies for diesel and light duty vehicles have increased the ratio of diesel to light duty NO_x emissions by a factor of two between 1997 and 2006, with diesel emissions now accounting for ~75% of mobile NO_x emissions (both on- and off-road) [*Ban-Weiss et al.*,

2008; *Dallmann and Harley*, 2010]. For light duty vehicles, emissions from about 1% of the fleet are responsible for almost 33% of CO and 16% of NO_x emissions [*Bishop et al.*, 2012]. These significant changes in emissions and sources must be accurately reflected in inventories, such as the NEI, to allow for proper estimation of NO_x and CO concentrations used in air quality models and for the development of policies to reduce ambient O_3.

The EPA produces the NEI every three years, estimating annual, county-level emissions of criteria air pollutants from On-Road, Off-Road, Point, and Area sources. States can use these emissions to develop State Implementation Plans (SIPs) as part of their obligation to reduce ambient pollution under the CAA. The 2011 NEI version 2 estimates nationwide emissions of 7.4×10^7 (2.4×10^{12}) and 1.45×10^7 (2.9×10^{11}) short tons (moles) of CO and NO_x respectively, assuming NO_x is emitted as NO_2. According to the NEI, nationally, mobile sources (both on- and off-road) account for 57% of CO and 62% of NO_x emissions; electricity generation accounts for 1% of CO and 14% of NO_x. The relative importance of mobile CO and NO_x emissions is even larger in Maryland, accounting for 85% and 72% of total emissions respectively.

Multiple attempts to evaluate the NEI's accuracy over different spatial scales have provided conflicting results for CO and NO_x. In a tunnel study in Van Nuys California, *Fujita et al.* [2012] found that the Motor Vehicle Emissions Simulator (MOVES2010) model overestimates NO_x and CO on-road emissions factors by 38-50% and 12-41% respectively. *Brioude et al.* [2013], using an inverse modeling approach in the Los Angeles (LA) basin, determined that NEI estimates of emissions were high for both species, CO by 37-43% and NO_x by 27-32%. Also in LA, *Pollack et al.* [2013] found

that the observed NO_x/CO ratio was approximately half the value estimated by the California Air Resources Board emissions inventory, often regarded as more accurate than the NEI. On the national scale, *Parrish* [2006] concluded that the NEI overestimated CO emissions by ~100%, while NO_x emissions were accurate. Comparing measured NO_y values from Houston to output from the CMAQ model, *Yu et al.* [2012] found that modeled values of NO_y (approximately the sum of NO, NO_2, alkyl nitrates, PANs, and HNO_3) are a factor of two too high and conclude that NEI NO_x emissions must likewise be too high. *Rappenglueck et al.* [2013], using roadside monitoring of on-road emissions, found a CO/NO_x emissions ratio of 6 mol/mol in Houston and that both MOBILE6 and MOVES overestimate this ratio by 92% and 24%, respectively. *Doraiswamy et al.* [2009] also claim that NEI NO_x emissions are overestimated, after finding that NO_x mixing ratios calculated in CMAQ using the Carbon Bond IV (CB4) chemical mechanism were too high by a factor of 1.7 when compared to observations.

In the BWR, *Castellanos et al.* [2011] found, from comparing observations in the Regional Atmospheric Measurement Modeling and Prediction Program (RAMMPP) campaign to CMAQ model output, that NEI CO emissions were correct or slightly underestimated while NO_x emissions from mobile sources were likely overestimated. *Lu et al.* [2015] applied an exponentially modified Gaussian method to Ozone Monitoring Instrument (OMI) data combined with reanalysis winds to conclude that NEI NO_x emissions in the BWR were overestimated by 62% in 2011. There is little agreement among these studies on the NEI's accuracy, for either CO or NO_x, showing both under- and overestimation for both species.

Here, I use extensive *in situ* observations from the DISCOVER-AQ field campaign in the BWR to evaluate NO_x and CO emissions in the NEI. I calculate emissions ratios of CO/NO_x using a novel method from these observations. The CMAQ model is then used to model CO, NO_y, and the NO_y constituents during July 2011. Output from the model is then compared to the *in situ* observations, and in the case of CO, remotely sensed observations, to evaluate both CMAQ and the NEI.

2.2 Methodology

2.2.1 DISCOVER-AQ

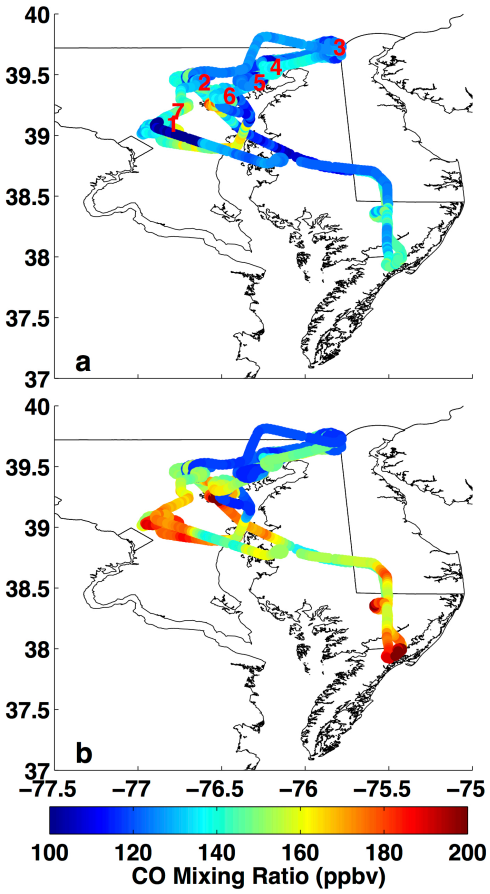

Figure 2.1: CO along the flight track (1 July 2011). (**a**) Observed (**b**) Modeled. Spiral and transect locations are marked in (**a**). 1. Beltsville 2. Padonia 3. Fairhill 4. Aldino 5. Edgewood 6. Essex 7. I-95

Part 1 of DISCOVER-AQ was conducted in the BWR during July 2011. One of the mission's primary goals was to increase understanding of severe O_3 episodes in the

US Mid-Atlantic region. The NASA P3-B measured trace gas composition – including CO, NO, NO_2, O_3, HNO_3, the sum of PAN and PAN-like compounds (ΣPAN), the sum of alkyl nitrates (ΣAN), and total NO_y – aerosol properties, and meteorological variables. Vertical profiles for all species were obtained over six locations – Beltsville, Padonia, Fairhill, Aldino, Edgewood, and Essex – in the BWR from approximately 0.3 to 5 km above ground level. Locations coincided with ground monitors of surface pollution and provided a range of urbanization and pollution. Flights were conducted over 14 days with the flight path shown in Figure 2.1, allowing for approximately three spirals at each site per day, for a total of 242. 43 horizontal transects were flown at approximately constant altitude over a segment of the I-95 interstate between Beltsville and Baltimore. All flights were during daylight hours and on days without rain. Flight days were selected to provide a mixture of lightly and heavily polluted air masses.

CO was measured using the NASA DACOM diode laser spectrometer [*Sachse et al.*, 1987]. Measurement uncertainty is 2%. CO and all other trace gases in this study were sampled at 1 Hz, unless otherwise noted and then averaged over 15s to reduce noise and uncertainty. Total NO_y, NO, NO_2, and O_3 were measured with a 4-channel chemiluminescence instrument with an uncertainty of 20% [*Ridley and Grahek*, 1990]. A thermal decomposition laser induced fluorescence instrument (TD-LIF) measured NO_y constituents, including ΣPAN, HNO_3, and ΣAN [*Farmer et al.*, 2006]. Individual species were measured at 1 Hz, but instrumental design precluded simultaneous measurement of species. Directly measured NO_y and NO_y calculated from the summing of constituents agree within 15% over the entire campaign.

Other measured trace gases include formaldehyde and isoprene. Formaldehyde was measured by difference frequency generation absorption spectroscopy (DFGAS), with a detection limit of 94 pptv and a 1σ uncertainty of ~4% [*Lancaster et al.*, 2000]. Isoprene was measured with Proton Transfer Reaction Mass Spectrometry (P3B) and a Perkin-Elmer Gas Chromatograph – Flame Ionization Detector automated VOC analyzer (surface observations at Essex) [*Lindinger et al.*, 1998].

Water-soluble aerosol mass concentration was measured with a Brechtel Manufacturing Inc. Particle Into Liquid Separator (PILS) with a 5-minute sampling frequency. Ion concentrations – including NO_3^-, NO_2^-, SO_4^{2-}, NH_4^+, and various metallic ions – were measured with ion chromatography [*Mulik et al.*, 1976]. Organic carbon was measured with a Siever Total Organic Carbon Analyzer and converted to organic matter concentration by multiplying organic carbon by a factor of 1.8 [*Turpin and Lim*, 2001]. Black carbon mass concentrations were measured with a Droplet Measurement Technologies single particle soot photometer with a 20% uncertainty. See *Crumeyrolle et al.* [2013] for more information on aerosol measurements.

2.2.2 Model setup

CMAQ model version 5.0 was run, driven offline by meteorological fields from the Weather and Research Forecasting (WRF) model 3.3, to simulate concentrations of CO and NO_y over the experimental domain for July 2011 and to provide a basis of comparison between the NEI and observed emissions ratios. A complete model setup can be found in *Loughner et al.* [2014].

WRF was run at resolutions of 36 × 36, 12 × 12, 4 × 4, and 1.33 × 1.33 km in the horizontal with 34 vertical levels, ranging from 1000 to 100 hPa. The atmosphere's

lowest 2 km contains 16 layers to capture variations in the PBL accurately. The North American Regional Reanalysis (NARR) was used for initial and boundary conditions.

Anthropogenic emissions input into CMAQ were from the 2005 NEI projected to 2011, including emissions changes due to growth and emissions controls to be implemented by 2012 [*US EPA*, 2011]. The CO/NO_x emissions ratio over the state of Maryland between the recently released 2011 NEI and the projection in this study agree within 20%, with values of 7.5 and 9 moles/moles respectively, indicating that this analysis is realistic and can provide insight into the 2011 NEI. Mobile emissions of CO and NO_x from on-road vehicles were calculated with the Motor Vehicle Emissions Simulator 2010 (MOVES2010) [*US EPA*, 2012]. National default vehicle age distributions were used. This does not capture any change in vehicle fleet precipitated by the 2008 economic recession, which could make the actual vehicle fleet older than that used here. The distribution of vehicle miles travelled between light- and heavy- duty vehicles were pre-processed from state level defaults to the county level. Likewise, default driving cycle settings were used.

Area emissions were horizontally distributed using EPA spatial surrogates, while hourly values of point and area emissions were determined using EPA temporal surrogates. Point sources were vertically distributed based on the meteorology, stack height, and the temperature and velocity of the emissions exiting the stack. The Sparse Matrix Operator Kernel Emissions (SMOKE) modeling system was used to create inputs for the CMAQ model runs [*Houyoux and Vukovich*, 1999]. Biogenic emissions were calculated on-line during CMAQ model runs by the Biogenic Emission Inventory System

(BEIS). Lightning NO_x was placed at the location of flashes using lightning flash data from the National Lightning Detection Network [*Allen et al.*, 2012].

2.2.3 Calculation of Emissions Ratios

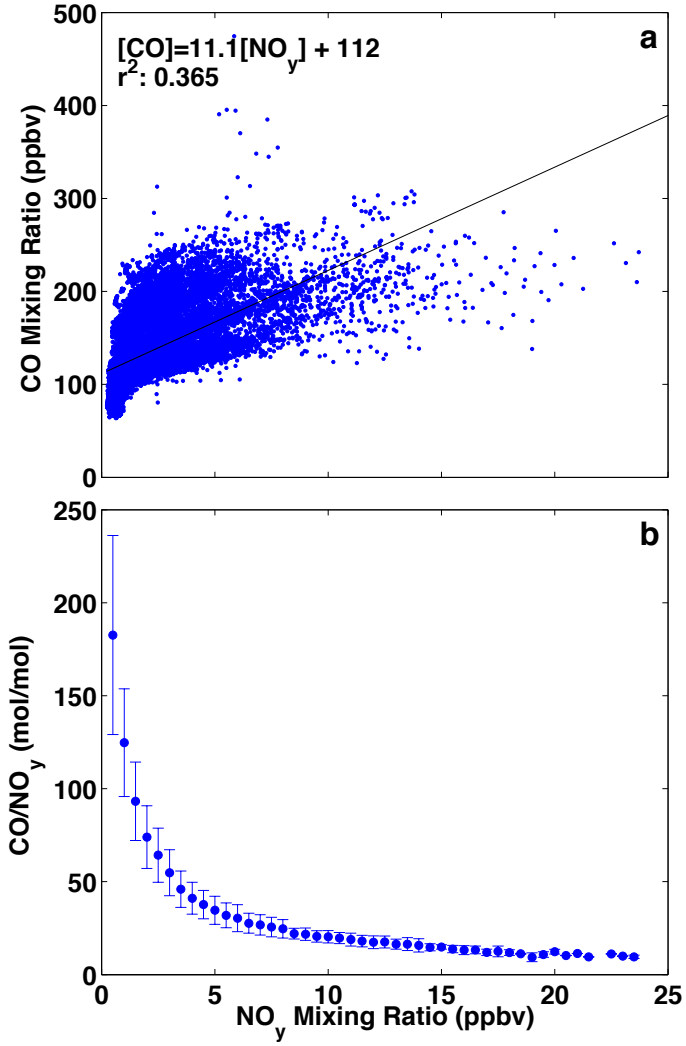

Figure 2.2: (**a**) Regression of all measured CO and NO_y mixing ratios for the entire campaign. Black line is the line of best fit. (**b**) Data from (**a**) plotted as the ratio of CO/NO_y vs NO_y mixing ratio. Data are separated into 0.5 ppbv bins. Mean values are shown with error bars of $\pm 1\sigma$.

To calculate the emissions ratio of CO to NO_x from the *in situ* observations, CO and NO_y concentrations from the PBL for each spiral/transect were regressed against one another using an orthogonal linear regression, assuming uncertainties in both constituents [*Crutzen et al.*, 1979]. Because of diurnal variation in PBL depth and a lack of a clearly

defined mixed layer in many spirals, a PBL depth of 1.5 and 0.7 km was assumed for all spirals after and before noon local time, respectively. The resulting slope yields the change in CO with respect to NOy. Assuming no *in situ* production or loss of either compound, this slope is the emissions ratio (ER) of CO to NO_x, or ER = $\mathbf{\Delta}(CO)/\mathbf{\Delta}(NO_y)$, where deltas represent the increase over background concentrations. NO_y was used to estimate NO_x emissions because air parcels were not measured at the emission location. Substantial conversion of NO_x to NO_y occurs between emission and observation, while the comparatively long NO_y lifetime reduces the likelihood of NO_y species loss. The implications of lifetime and the assumption of no *in situ* production or loss are discussed in Section 2.3.2.

2.3 Results

2.3.1 Measured Emissions Ratios

A regression of all measured CO against NO_y (Figure 2.2a) shows low linear correlation ($r^2 = 0.36$). This likely results from the spatiotemporal variability in sampled NO_x emissions. Parcels sampled later in the day or away from major sources are more likely to have NO_x converted to NO_y followed by deposition. Figure 2.2b demonstrates this aging effect clearly. At low NO_y concentrations, CO/NO_y is high and almost exponentially increasing, indicating significant NO_y loss. The majority of measurements lie in this regime. As the NO_y concentration increases, however, CO/NO_y decreases and asymptotically approaches a CO/NO_y ratio of 10.5. Analysis of individual spirals and transects provides a more accurate estimate of this ratio.

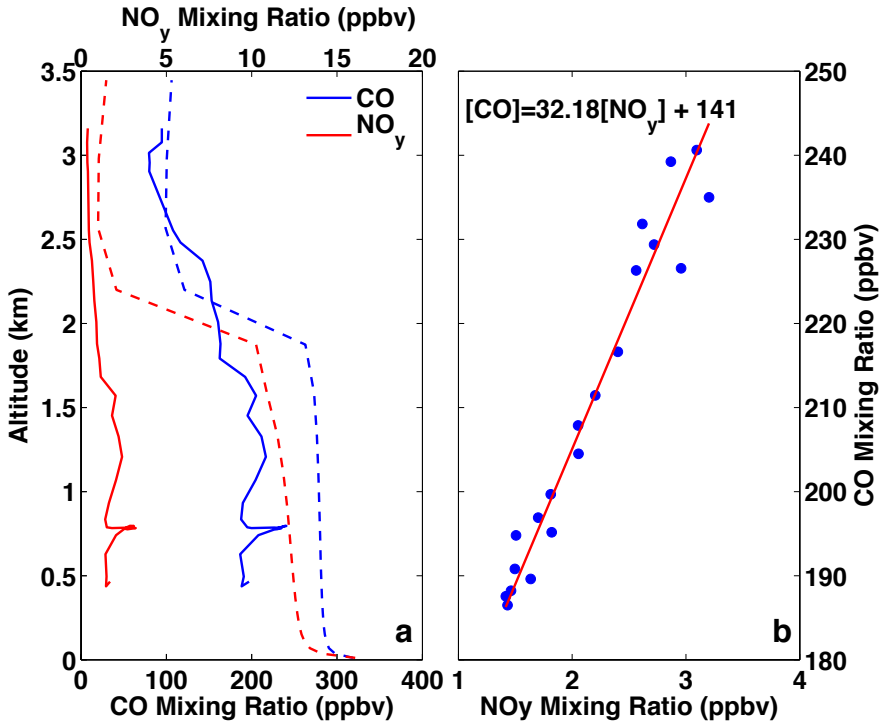

Figure 2.3: (**a**) Sample vertical profiles of CO and NO_y over Padonia, MD (11 July 2011, 16:30 -16:50 EDT). Solid lines are observations; dashed lines are from the 1.33 km resolution CMAQ run. (**b**) Regression of CO and NO_y in the PBL (0-1.5 km) for the profile shown in panel (**a**).

Vertical CO and NO_y profiles for a sample spiral over Padonia, MD on 11 July 2011 between 16:30 and 16:50 Eastern Daylight Time (EDT) are shown in Figure 2.3a. The two profiles show excellent correlation below 1.5 km, the assumed PBL height. Sharp changes in one species, indicative of different air parcels, are closely mirrored in the other, providing the degrees of freedom necessary for a regression analysis. The two species, plotted against one another in Figure 2.3b, show a highly linear relationship for concentrations in the PBL. A linear relationship with a statistical significance of $p < 0.05$ is found for 175 of the 287 spirals and transects, with a geometric average of 11.2 ± 1.19 mol CO/mol NO_x. Total uncertainty is the mean of the fit uncertainty of each regression added in quadrature with the mean of the standard errors for each site. Geometric means reflect the dominant mode of the emissions ratio distribution, which is more lognormal than Gaussian.

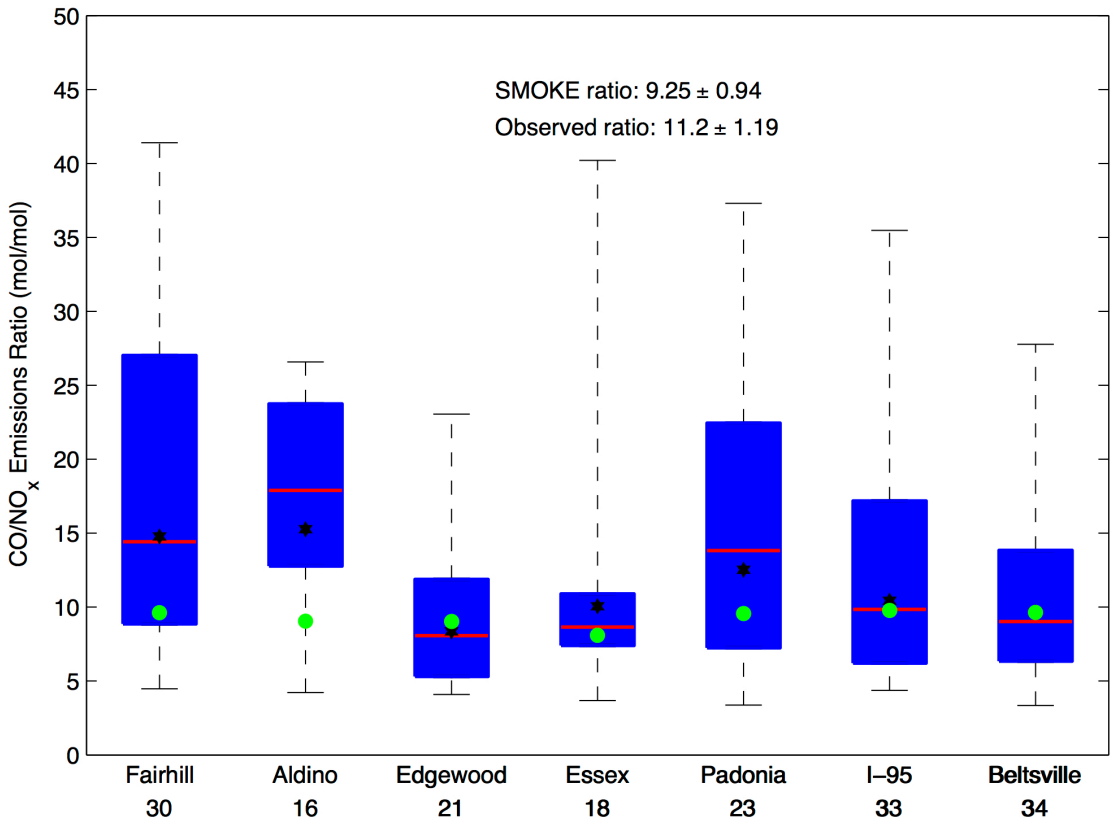

Figure 2.4: Distribution of observed CO/NO_x emissions ratios for each spiral/transect location. Red line is the median, star is the average, box edges are the 25th and 75th percentiles, and whiskers are the 5 and 95th percentiles. All other box-and-whisker plots have the same configuration. Circles show the average emissions ratio from SMOKE along 24- hour back trajectories. Numbers under the location names are the number of profiles/transects observed with correlations having a $p < 0.05$.

Figure 2.4 shows the distribution, by location, of observed ratios for all spirals and transects with $p < 0.05$. Ratios varied significantly among the sites, with values at Edgewood, 8.36 ± 0.95, almost a factor of 2 lower than those at Aldino, 15.3 ± 1.6, the site with the highest mean ratio. Edgewood's proximity to the Chesapeake Bay allows for greater influence from marine emissions, which tend to emit high NO_x and low CO [*Williams et al.*, 2009]. The bay breeze, a feature common to Edgewood in this study, could contribute to the low observed CO/NO_x ratios, as the meteorology could allow for the accumulation or removal of pollutants, altering the observed emissions ratio.

Figure 2.4 also shows the average CO/NO_x emissions ratio from SMOKE by location. Values were calculated along 24-hour back trajectories for all measured spirals with observed correlation between CO and NO_y. The NEI agrees within 10% with CO/NO_y observations at Edgewood, Beltsville, and I-95, while it underestimates the ratio at the other sites by up to a factor of 1.7. Evaluation of the CO/NO_x emissions ratios by linear regression of the vertical CMAQ concentration profiles is not possible. Profiles of CO and NO_y at multiple CMAQ resolutions are essentially constant with height in the PBL (see Figure 2.3), resulting in only one degree of freedom and no statistically significant results.

Table 2.1: Observed CO/NO_x ratios by location and time. Morning and afternoon are defined as before and after 12 EDT, respectively.

Location	Latitude (°N)	Longitude (°W)	Overall	Morning	Afternoon
Fairhill	39.726	75.835	14.8 ± 1.43	8.14 ± 1.27	19.9 ± 1.44
Aldino	39.567	76.212	15.3 ± 1.60	12.2 ± 2.59	16.4 ± 2.63
Edgewood	39.442	76.315	8.36 ± 1.00	6.71 ± 1.01	9.57 ± 1.11
Essex	39.333	76.494	10.1 ± 1.54	7.12 ± 1.30	11.5 ± 1.52
Padonia	39.436	76.635	12.5 ± 1.64	8.37 ± 1.86	15.5 ± 1.94
I-95	39.202	76.796	10.4 ± 0.95	7.98 ± 0.77	13.8 ± 0.99
Beltsville	39.055	76.832	9.67 ± 1.08	7.54 ± 1.02	11.3 ± 1.03
Overall	N/A	N/A	11.2 ± 1.19	7.93 ± 1.07	13.8 ± 1.07

Each site exhibited significant variation in measured CO/NO_y ratios, spanning an order of magnitude at some locations. Figure 2.5 shows substantial diurnal variation, with the lowest average CO/NO_x ratios in the morning and a general increasing tendency as the day progresses. Morning, times before noon EDT, CO/NO_x ratios average 7.93 ± 1.07 while afternoon values are about 13.8 ± 1.07, a 74% increase. This pattern holds true at each location, as shown in Table 2.1, with Edgewood significantly lower in the morning than the other sites. Afternoon values are most likely a better indicator of the actual CO/NO_x emissions ratio because the PBL is more thoroughly mixed during this time. *In situ* CO production from biogenic VOC oxidation also contributes to this

phenomenon. Isoprene emissions peak in the early afternoon with increasing temperatures and can lead to substantial CO production [*Hudman et al.*, 2008]. Further discussion of CO production from biogenic emissions is included in the next section.

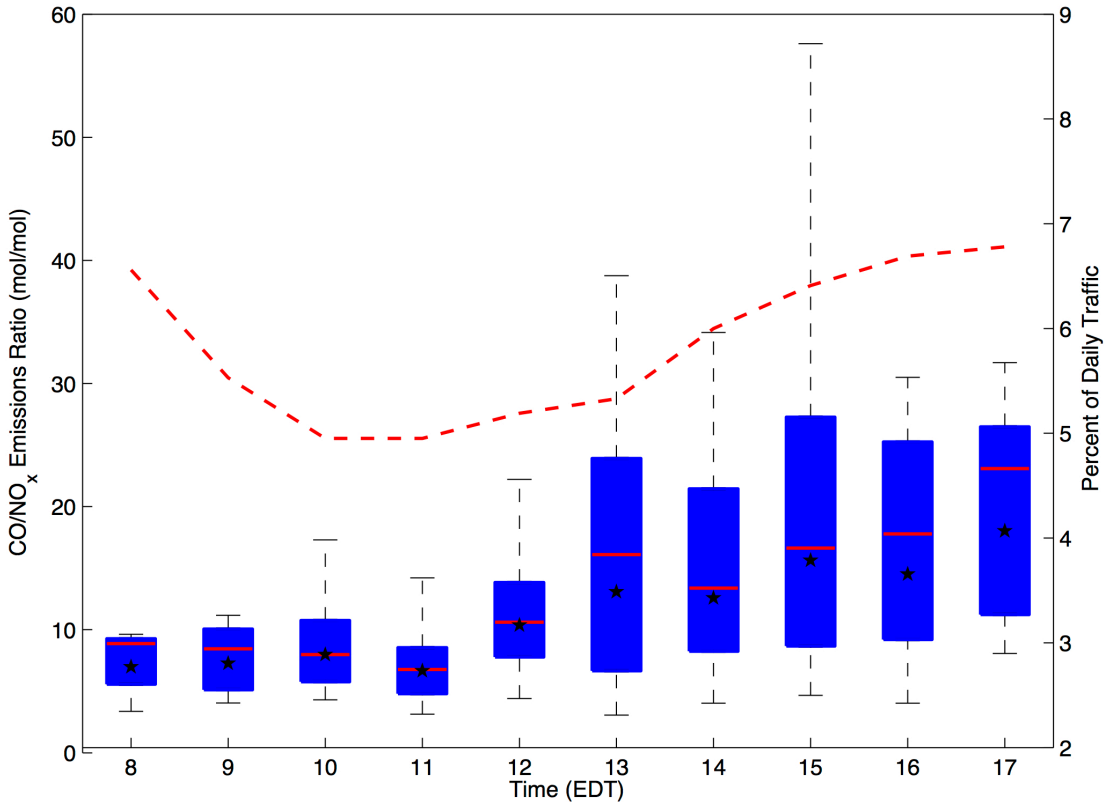

Figure 2.5: The distribution of emissions ratios by time of day. Black stars are the average value for each hour. Fraction of Maryland on-highway traffic, by hour, is shown with the dotted red line.

Figure 2.4 also shows good agreement between CO/NO_x emissions ratios in the NEI and on I-95. I-95 has a different mixture of vehicle types than the other locations, which are dominated heavily by local traffic. While an hourly breakdown of heavy- versus light-duty vehicles is not available for the portion of I-95 observed in this study, daily averages show that heavy-duty vehicles comprise approximately 10% of the traffic on I-95, although in some locations it is as high as 30%, compared to only 5% in city centers [*Maryland Department of the Environment*]. These measurements most likely underestimate the total fraction of heavy-duty vehicles on I-95, however, as most traffic

counters are located at interstate on- and off-ramps and therefore will not include all trucks on the interstate itself. The value presented here should be viewed as a lower bound. Because diesel engines tend to emit more NO_x and less CO than light duty vehicles, a larger fraction of diesel engines on I-95 as compared to the other locations in this study could explain the agreement.

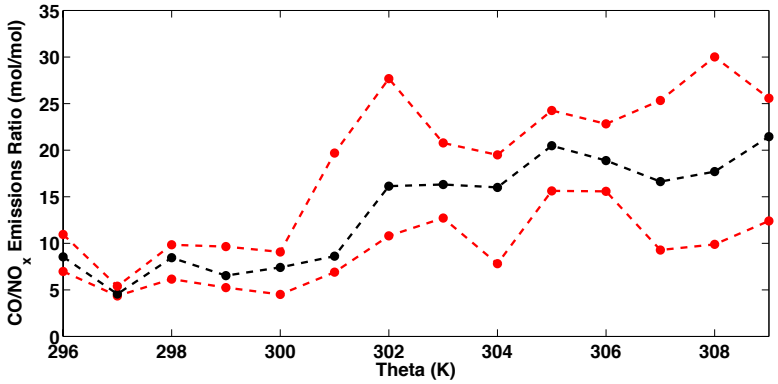

Figure 2.6: Temperature dependence of the observed CO/NO_x emissions ratio. Data are separated into 1 K potential temperature bins. 25th (red), 50th (black), and 75th (red) percentiles are shown for each potential temperature bin.

The dependence of the CO/NO_x emissions ratio with potential temperature is shown in Figure 2.6. Potential temperature (θ), instead of air temperature, is used because emissions ratios were derived over the depth of the PBL, and, assuming a well-mixed boundary layer, θ is approximately constant with altitude. The median emissions ratio is essentially constant at ~8 mol/mol for θ less than 302 K. At and above this θ, the emissions ratio increases dramatically, by a factor of two, to ~16 mol/mol. This step change suggests a physical mechanism in the emissions of either NO_x, CO, or both above this threshold temperature. This idea is discussed more fully in section 2.4.

2.3.2 Uncertainties in the Observed Emissions Ratio

2.3.2.1 CO Uncertainties

With a lifetime of ~1 month, CO losses should not have any measurable effect on the observed CO/NO_x ratio [*Seinfeld and Pandis*, 2006]. Isoprene, the dominant VOC in the BWR, oxidizes to produce CO, however [*Morales*, 1998]. Figure 2.7a shows the isoprene profile over Essex for July 2011 as measured from the P3B and at the surface. Isoprene mixing ratio decreases quickly with height, dropping by greater than a factor of four from the surface to 1 km, showing the reactivity of isoprene.

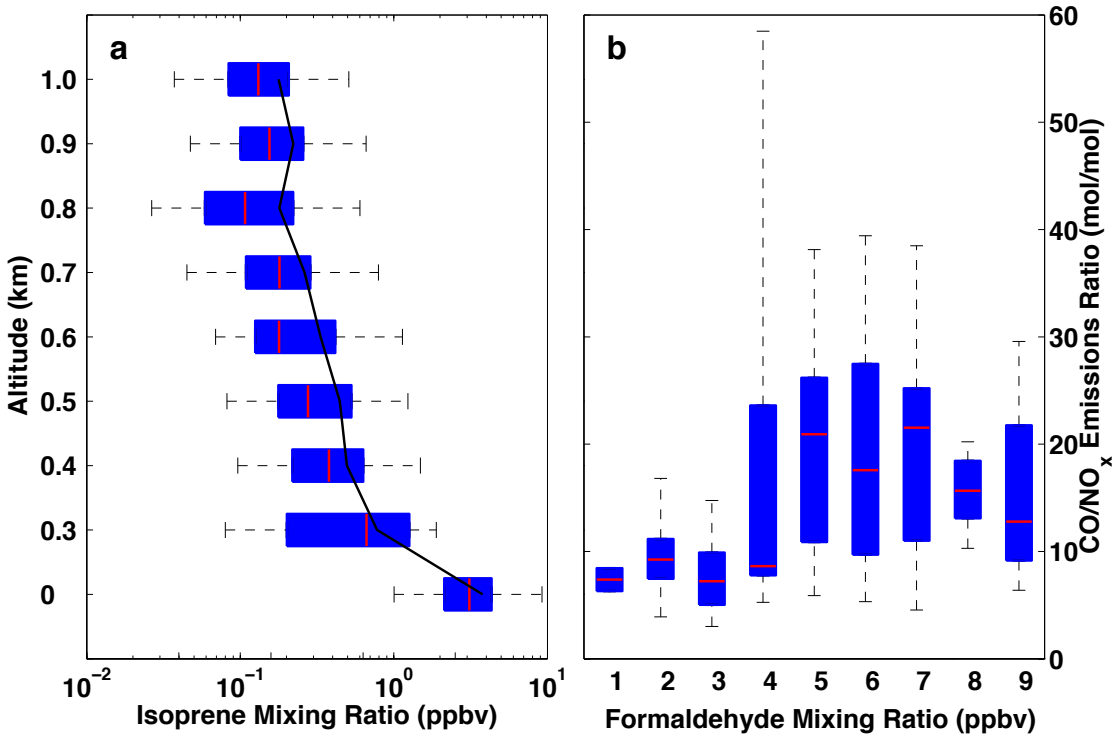

Figure 2.7: (**a**) Vertical isoprene profile over Essex, MD. Surface measurements are from MDE ground monitors. All other measurements were taken aboard the P3B. (**b**) Comparison of CO/NO_x emissions ratio to formaldehyde mixing ratio.

The relationship between formaldehyde and the CO/NO_x ratio also demonstrates the effect of VOC chemistry on CO. Isoprene and other VOCs strongly promote formaldehyde formation at low altitudes in the BWR. High formaldehyde mixing ratios

indicate a highly oxidative environment in which *in situ* CO formation is more likely. This effect is shown in Figure 2.7b. While CO/NO_x ratios vary widely at all formaldehyde mixing ratios, median CO/NO_x ratios clearly increase with increasing formaldehyde concentrations, demonstrating the observable effect of VOCs on CO concentrations.

To calculate an upper bound on CO production from isoprene, it was assumed that CO was produced directly from isoprene, neglecting intermediate reactions found in nature and in the Carbon Bond mechanism version 5 (CB05), the chemical mechanism in CMAQ. Hydroxyl concentration was taken from the 12km CMAQ run, with daytime average hydroxyl concentration remaining approximately constant with height, about 7×10^6 molecules/cm^3, to about 1 km. Using a reaction constant of $k = 3.10 \times 10^{-11} \exp(-350/T)$ [*S P Sander et al.*, 2011b], the production of CO at each model level was calculated, and then integrated to approximately 1 km. Measured CO concentrations were also integrated to 1 km, subtracting out the background concentration of 100 ppbv, calculated as the average CO mixing ratio for the entire campaign above 2 km.

At the surface, isoprene-produced CO can account for as much as 45% of total CO, but because of the quick e-folding lifetime, this percentage quickly becomes negligible with increasing height, dropping to less than 1% by 0.5 km. For the total PBL column, ~6% of CO could be attributed to production from isoprene degradation.

2.3.2.2 NO_y Uncertainties

In contrast, substantial new NO_y compounds are not produced naturally, except by lightning. Because observations were made in the PBL on days without deep convection, contributions from lighting NO_x are minimized. NO_y, which is removed by wet and dry

deposition as well as by conversion to aerosols, has an atmospheric lifetime substantially shorter than that of CO.

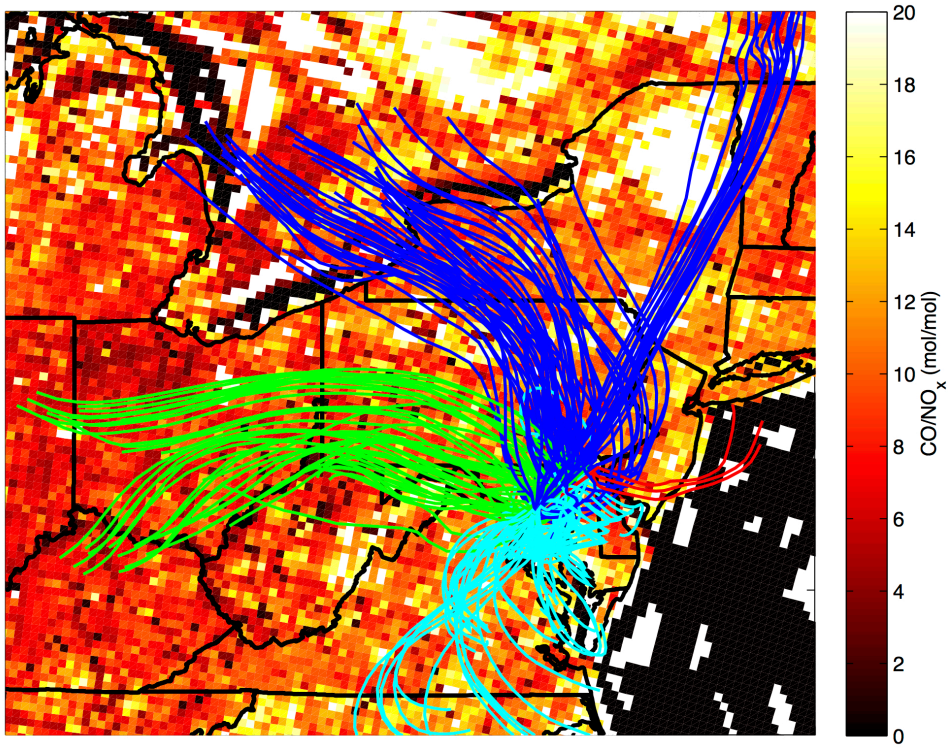

Figure 2.8: 24-hour back trajectories calculated with the HYSPLIT model for all measured profiles with a significant correlation between CO and NO_y. Back trajectories are superimposed over the average emissions ratio output by SMOKE and color-coded by source region. Observed CO/NO_x emissions ratios for each region are 11.5 ± 0.21 for Upstate New York (blue), 15.4 ± 0.33 for the Ohio River Valley (green), 15.9 ± 0.27 for Virginia/North Carolina (cyan), and 13.4 ± 0.67 for Long Island (red).

Although observations were made on days without precipitation, air parcels could have been exposed to precipitation within the previous 24 hours, allowing for the possibility of wet deposition, especially of highly soluble HNO_3. 24-hour back trajectories (Figure 2.8) were calculated using NOAA's HYbrid Single Particle Lagrangian Integrated Trajectory (HYSPLIT) model, driven by the North American Model (NAM) 12 km reanalysis [*Draxler and Hess*, 1997; *Stein et al.*, 2015]. Precipitation rates along those trajectories were also output. Trajectories were produced at three vertical levels to ensure that there was no significant backing or veering of winds with height. While there was never precipitation on the day of measurement, several air

parcels experienced rain the previous afternoon. Separating the two groups yields CO/NO_x ratios of 8.86 ± 1.03 for those that were exposed to rain and 12.0 ± 1.26 for those that were not. Had wet deposition occurred recently enough to affect the measured emissions ratios, those air parcels that had been exposed to precipitation would have a higher ratio than those that had not. The opposite is seen here, indicating that removal of HNO_3 by precipitation does not affect the results. The difference between the precipitation and no precipitation groupings results from the large fraction of measurements in the precipitation group being made in the morning (approximately 2/3), emphasizing that the difference is from the temporal variation and not removal by wet deposition.

Determination of sampled air age provides even better evidence of local emissions' dominance. Air parcel age was estimated directly using two methods, chemical kinetics and average wind speed. For the former, it is assumed that conversion of NO_2 to HNO_3 occurs in a single step via reaction with the OH radical and that there is no significant loss of NO_2 to other pathways [*Bertram et al.*, 2007]. With this assumption, the age of a plume can be estimated by Equation (2.1), in which the inverse of τ is equal to k_1 (the reaction constant for the OH + NO_2 reaction) multiplied by the average OH concentration in the PBL for each spiral taken from CMAQ.

$$\frac{[NO_2(t)]}{[NO_2(t)] + [HNO_3(t)]} = e^{-\frac{t}{\tau}} \qquad \text{Equation (2.1)}$$

k_1 was determined according to the method described by *S P Sander et al.* [2011b]. NO_2 and HNO_3 observations from the P3B were also averaged over the PBL for each spiral. The average, calculated air parcel age was 3.2 ± 1.2 hours. This agrees with estimates determined from mean synoptic winds and distance from major urban centers.

Dry deposition removes little NO_y within the first hours after emission. Deposition velocities were calculated from CMAQ generated deposition fluxes and modeled HNO_3 concentrations at 1 km. The average HNO_3 deposition velocity for each location is 1.95 cm/s, assuming a PBL height of 1.5 km. This value is in line with previous estimates [*Meyers et al.*, 1991]. It was assumed that the deposition velocities of other NO_y species were negligible. The e-folding lifetime of HNO_3 with respect to dry deposition is therefore on the order of 22 hours. Since the average air parcel age is approximately 3 hours, assuming first order rate loss due to dry deposition, only 15% of the HNO_3 could have been lost. Assuming average PBL concentrations of HNO_3 and NO_y, 1.45 and 3.54 ppbv respectively, this translates to a loss of only 6% of the nitrogen species.

The lack of wet deposition suggests that the observed emissions were local. Consistent with this theory is the lack of variation in emissions ratios based on source region. Air masses arrive in the BWR region primarily from three distinct areas, Upstate New York, the Ohio River Valley, and Virginia/North Carolina (Figure 2.8), with only a few air masses originating from the Long Island region. The observed emissions ratios from these regions are 8.65 ± 1.05, 12.4 ± 1.36, 13.6 ± 1.24, and 15.3 ± 3.44 mol CO/mol NO_y respectively. Uncertainties are standard error. The northerly air masses are lower than the other regions by about 30%, but the values are not substantially different, given the wide spread of values for each location. Because emissions sources in these regions vary significantly, emissions ratios measured during DISCOVER-AQ should show distinct ratios for air parcels arriving from these different regions if pollutant concentrations at the surface were dominated by long-range transport. While the mean

emissions ratio from Upstate New York is lower than the others, the emissions ratios from the other directions overlap within the measurement uncertainty, suggesting that the measured emissions are local.

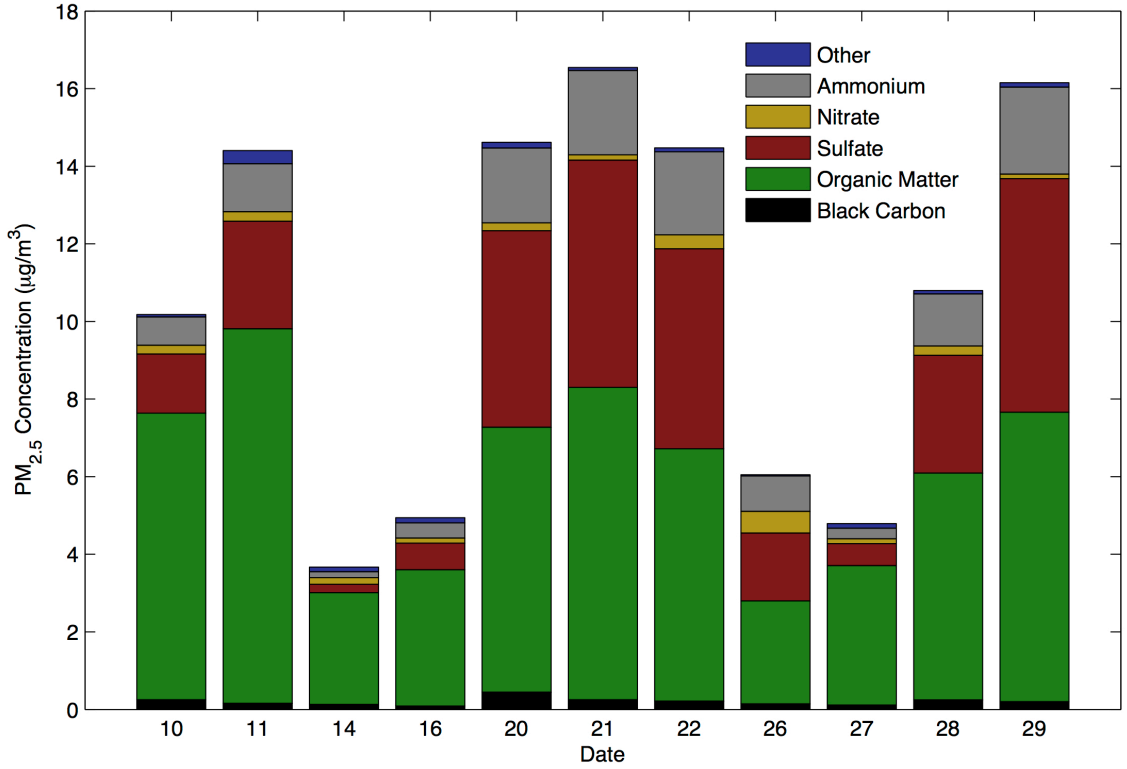

Figure 2.9: Daily average aerosol concentration and composition as measured by the PILS onboard the P3B. The "other" category includes nitrite, chloride, sodium, potassium, magnesium, and calcium.

Processing of NO_y compounds by clouds could lead to the conversion of nitrogen into aerosol particles. Aerosol composition, including that of nitrates and nitrites, was also measured during DISCOVER-AQ and is shown as daily averages in Figure 2.9. Organic matter and sulfates dominate aerosol composition, with nitrates and nitrites making up 2.8 ± 2.4% and 0.064 ± 0.035% (1σ) of total aerosol mass, or 0.23 ± 0.13 µg/m^3 and 0.0062 ± 0.0029 µg /m^3. There is only minor net conversion of NO_y to aerosolized form. The time resolution of the aerosol data and data gaps in nitrate and nitrite loading preclude a spiral-by-spiral determination of the fraction of nitrogen in the

aerosol phase. Using the average daily NO_y concentrations in the PBL, 3.54 ppbv or 8.7 $\mu g/m^3$ at 950 hPa and 293 K, this nitrogen aerosol loading is 4 ± 2% of the total nitrogen (NO_y + aerosol nitrite and nitrate). This loss of nitrogen is on the order of the instrument uncertainty for NO_y measurements. In addition, the NO_y inlet was not filtered for aerosols, although inlet design does inhibit the measurement of aerosols larger than approximately 1 μm in diameter, so the estimate of nitrogen aerosol loading should be viewed as an upper bound.

Loss of gaseous HNO_3 to the aqueous phase in cloud water is another source of uncertainty, although like dry deposition, this would only have a small effect on the observed CO/NO_y ratio. Liquid water content (LWC) from WRF was averaged for each grid cell for all daytime hours during July 2011. Hourly values were not used because of the low accuracy of the WRF cloud output. For each model level, the amount of HNO_3 in clouds was determined using the Henry's Law constant for HNO_3, the modeled HNO_3 concentration and averaged LWC, and then integrated to 3 km. Column NO_y was also calculated. The percent nitrogen in clouds along the 24 hour back trajectories was determined, and the average value for each spiral location is less than 1%, with the 95^{th} percentile at all sites staying well below 1.5%, indicating that there is no significant loss of nitrogen to clouds. This is further confirmed by the low nitrogen concentration in aerosol form described above. In total, about 7% of NO_y is removed from the atmosphere between emission and measurement, indicating that CO/NO_x emissions ratios can be determined from NO_y observations.

From the comparison between the observations and the modeled emissions, it is apparent that the NEI has the incorrect CO/NO_x emissions ratio. To determine whether

the NEI emissions of CO, NO_x, or both are overestimated, observed concentrations of CO and NO_y were compared with CMAQ model output.

2.3.3 Evaluation of CO Emissions

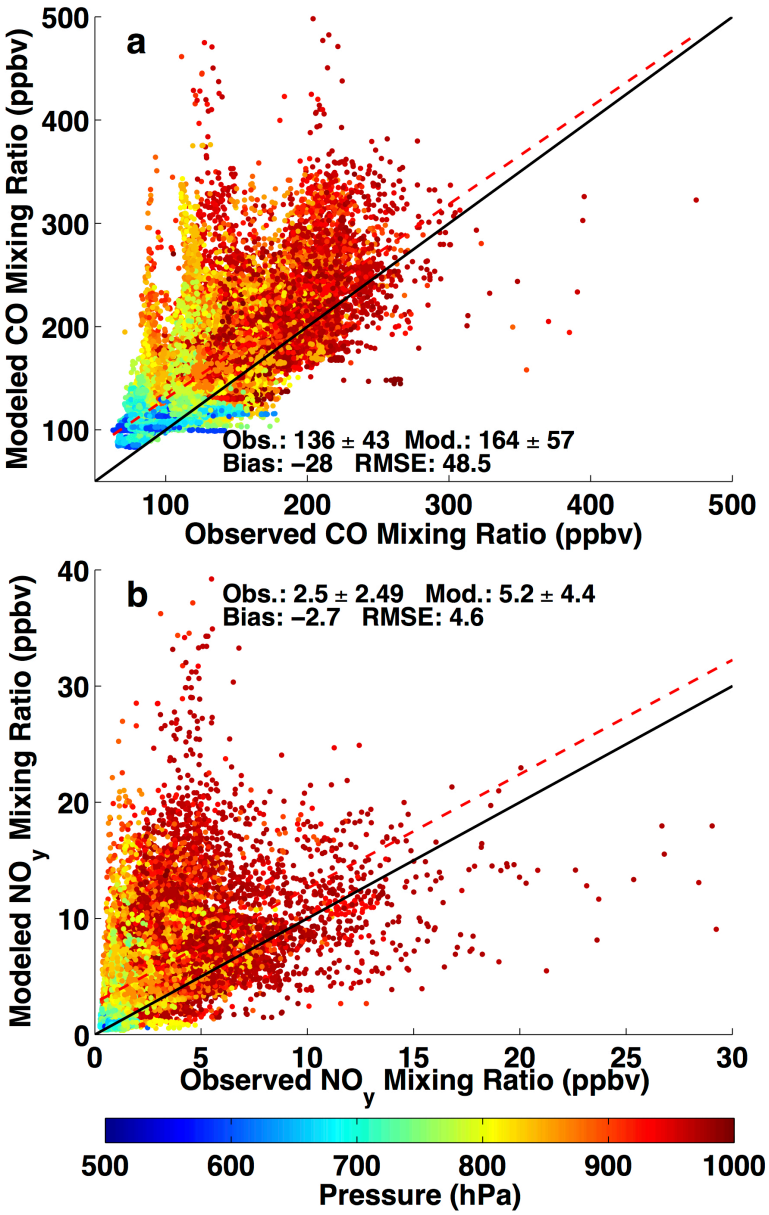

Figure 2.10: (**a**) Regression of measured and modeled CO for all flight days during DISCOVER-AQ. Values after means are 1σ. (**b**) Same as (**a**) but for NO_y. Solid line is the 1:1 line; dashed line, the line of best fit. The observed mean and standard deviation (Obs.), modeled mean and standard deviation (Mod.), mean bias (observations – model), and RMSE are shown for both.

To determine the accuracy of CO emissions in the NEI, *in situ* CO observations were compared with the 1.33 km resolution CMAQ output. Figure 2.1a shows observed

CO mixing ratios for a representative flight day. Mixing ratios were relatively constant throughout the region, remaining between about 100 and 170 ppbv. CMAQ output (Figure 2.1b) has a similar spatial distribution with an overall high bias of 15 ppbv, indicating excellent agreement between model and observations.

All campaign observations are plotted against the CMAQ model output in Figure 2.10a. As in Figure 2.1, the model has a slight high bias, as most values rest above the 1:1 line. The mean observed CO concentration, for the entire campaign, was 136 ± 43 ppbv (1σ), with the model showing a high a bias of 28 ppbv and a root mean square error (RMSE) of 48 ppbv. The relatively low bias suggests that mean CO emissions for the BWR are reasonable albeit a bit too high. The bias varied between +3% and +72% for the different flight days likely due to errors in boundary conditions and uncertainties in isoprene chemistry and emissions in CMAQ. The high bias was also consistent for all pressure levels, indicating that the model is, over this time period, capturing vertical mixing and not holding CO too close to the surface.

To evaluate both the CMAQ CO output and the NEI CO emissions, I used the Measurement of Pollution in The Troposphere (MOPITT) V5J product, which includes both the thermal and near infrared channels for improved sensitivity to near-surface CO, as compared to the thermal infrared only MOPITT product (Figure 2.11a) [*Deeter et al.*, 2012; *Worden et al.*, 2010]. The MOPITT V5 products and validation results are described in *Deeter et al.* [2013]. CMAQ CO mixing ratios were averaged over the month of July 2011 in each grid cell, regridded to correspond with the MOPITT grid (1° × 1°), and values between 800 and 900 hPa were averaged to calculate a layer value, comparable to that of MOPITT. The model was then sampled using the MOPITT

averaging kernel and *a priori* data. Results are shown in Figure 2.11b. Comparison between MOPITT observations and CMAQ output, are highly correlated ($r^2 = 0.73$). The average CO mixing ratio over the CMAQ domain was 123 ppbv, 4 ppbv lower than MOPITT, with an overall RMSE of 15.9 ppbv, showing excellent agreement between the model and satellite observations. CO mixing ratios over the urban portion of the BWR are slightly lower in CMAQ than in MOPITT, while CO is about 15% higher in CMAQ over the Delmarva Peninsula and Chesapeake Bay. These comparisons between CMAQ and MOPITT agree excellently with the *in situ* observations from the P3B.

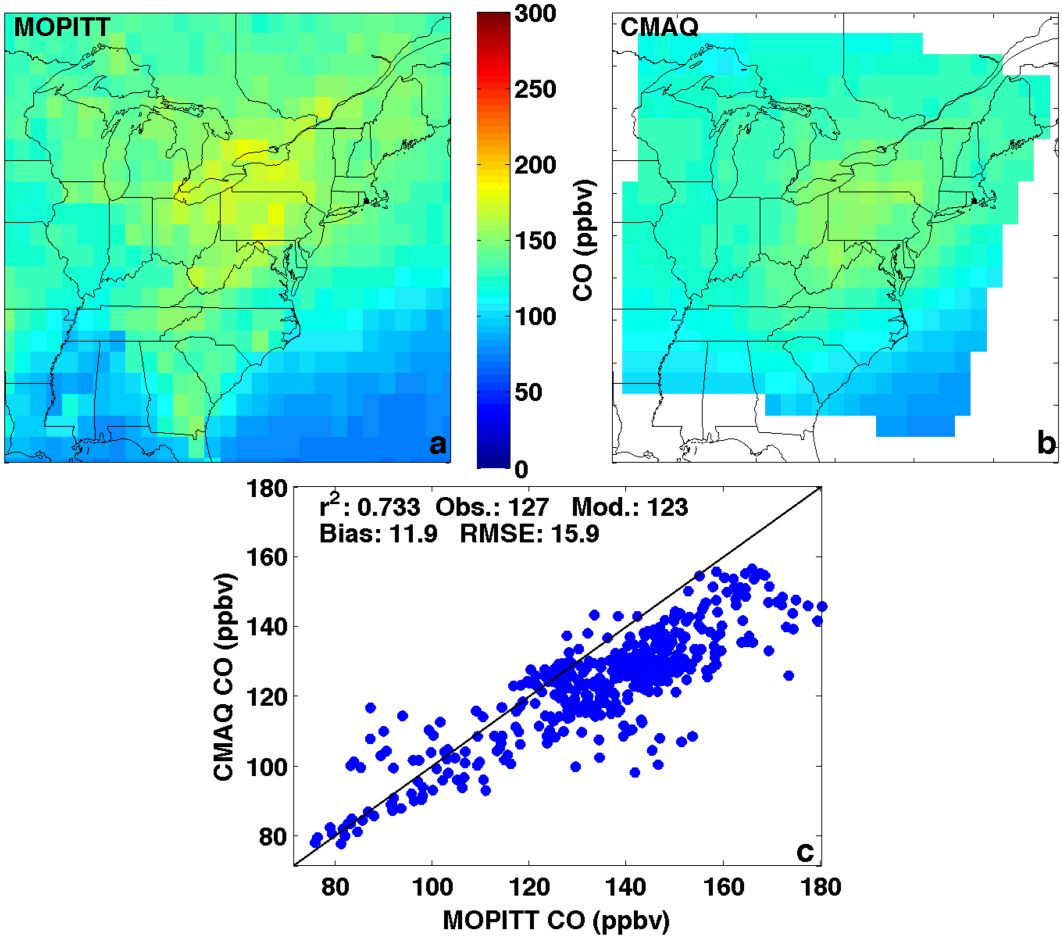

Figure 2.11: (**a**) MOPITT monthly averaged CO concentration at the 900 hPa level for July 2011 (**b**) CMAQ monthly averaged CO concentration at the 900 hPa level with the MOPITT averaging kernel. (**c**) Regression of measured and modeled CO over the CMAQ modeling domain. The mean of MOPITT CO over the model domain (Obs.), the mean CMAQ CO (Mod.), mean bias (MOPITT – CMAQ), and RMSE are also shown.

Comparison of *in situ* and remote observations with CMAQ output indicates that the NEI is overestimating anthropogenic CO emissions. Combining the 21% high bias of the model with the estimate of the *in situ* CO production by isoprene, the NEI overpredicts CO concentrations by approximately 15%. This overprediction and the difference between observed and modeled CO/NO_x emissions ratios indicate that the NEI must significantly overestimate NO_x emissions.

2.3.4 Evaluation of NO_x Emissions

Comparison of measured and modeled NO_y mixing ratios (Figure 2.10b) shows consistent and significant overestimation of NO_y by CMAQ as well as weak correlation ($r^2 = 0.29$). The observed mean NO_y mixing ratio for the campaign was 2.49 ± 2.42 ppbv (1σ), a factor of two lower than the model (5.2 ± 4.39 ppbv). Table 2.2 shows the agreement for individual NO_y constituents. NO, NO_2, and HNO_3 all agree with observations within 25%, although there is a consistent high bias and low correlation. ΣPAN and ΣAN are overestimated by a factor of 2.3 and 3.0 respectively. The discrepancy between the measured and modeled NO_y species in addition to the incorrect emissions ratios in SMOKE indicate errors in both the model's NO_y chemistry and the NEI's NO_x emissions.

Table 2.2: Comparison between measured and modeled NOy and its constituents for 3 model runs: a base case, a Chemistry run (factor of 10 reduction in ΣAN lifetime), and a Chemistry + Emissions run (ΣAN lifetime and 50% mobile NOx emissions reductions). Data are for the entire campaign. A positive bias indicates the model is higher than observations.

		Base (ppbv)		Chemistry (ppbv)		Chem + Emissions (ppbv)	
Species	Obs. Mean	Model Mean	Model Bias	Model Mean	Model Bias	Model Mean	Model Bias
NO_y	2.5	5.2	2.7	4.5	2.1	3.7	1.2
HNO_3	1.07	1.3	0.26	1.5	0.39	1.1	0.03
NO	0.17	0.20	0.022	0.19	0.017	0.14	-0.03
NO_2	0.78	0.85	0.068	0.87	0.093	0.64	-0.14
ΣPAN	0.61	1.4	0.81	1.6	0.97	1.4	0.77
ΣAN	0.32	0.96	0.65	0.48	0.16	0.44	0.12

Model runs altering the chemistry and emissions confirm this statement. In addition to the previously discussed CMAQ run, two additional runs were conducted: one in which the alkyl nitrate reaction constant was increased by a factor of 10, bringing the lifetime in better agreement with observations in areas with high isoprene concentrations [*Horowitz et al.*, 2007], and one combining this altered alkyl nitrate chemistry with a factor of two reduction in all mobile NO_x emissions. A comparison of the NO_y constituents from these runs is shown in Table 2.2. These model runs are meant to be illustrative of the relative impacts of chemistry and emissions and are not an attempt to model air quality precisely. Altering reaction kinetics brings modeled and measured ΣAN into better agreement (last row, Table 2.2) but has little effect on the overall NO_y concentration, reducing the amount by only a fraction of a ppbv [*Canty et al.*, 2015] . When the 50% reduction in mobile NO_x emissions is included, however, the modeled NO_y concentrations drop significantly, reducing the overall disagreement between measurement and model to 1.2. Measured and modeled NO, NO_2, and HNO_3 all agree within 20%, though NO and NO_2 concentrations are both underestimated and there is still poor correlation for all three species ($r^2 < 0.3$). Modeled ΣPAN is still a factor of 2.3 too high while ΣAN now agrees within 40%. Significant alterations to the model chemistry are still required.

Point source NO_x emissions (*e.g.* power plants and boilers) from SMOKE and from the Continuous Emissions Measurement System (CEMS) for the state of Maryland were compared for July 2011 to evaluate the accuracy of SMOKE's point source emissions, since the model was run before daily data were available. SMOKE emissions were approximately constant, while the monitored emissions showed significant temporal

variability, varying by almost a factor of 5 (Figure 2.12a). Although daily agreement between the model and CEMS is poor, the measured and modeled values agree within 1% on a monthly average. Modeled point source NO_x emissions cannot be responsible for the significant NO_y overestimation.

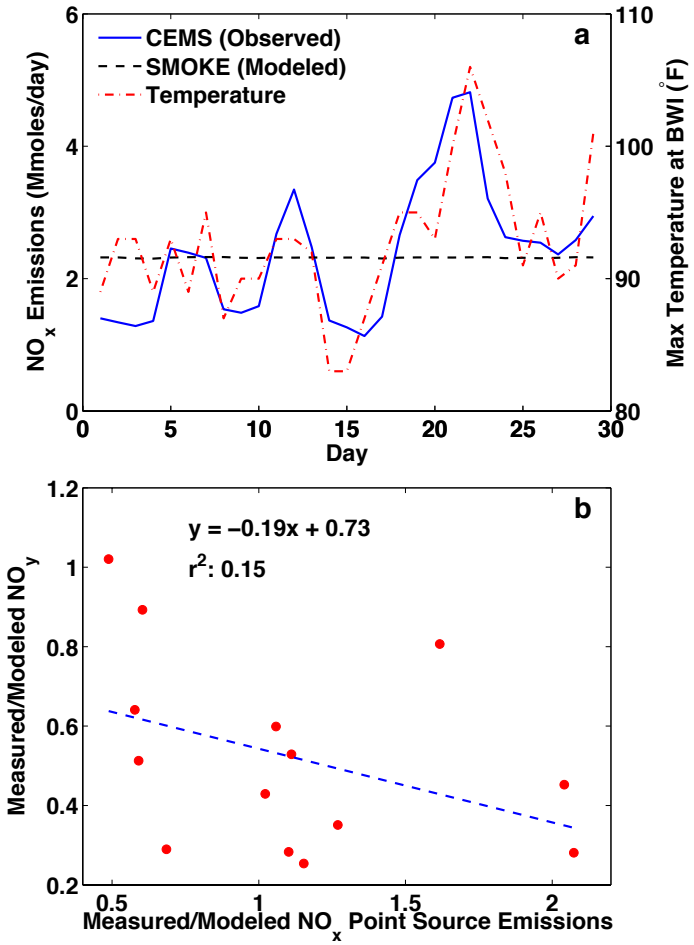

Figure 2.12: (**a**) Comparison of point source emissions from SMOKE and from observations (CEMS). The maximum daily temperature at Baltimore Washington International Airport is provided for reference. (**b**) Ratio of the average observed and modeled NO_y concentrations versus the ratio of measured point source NO_x emissions to modeled emissions.

This is further confirmed by Figure 2.12b, which shows the ratio of CEMS to SMOKE NO_x emissions plotted against the ratio of observed to modeled NO_y mixing ratios. If daily discrepancies between measured and modeled point source emissions caused the modeled NO_y overestimation, days with CEMS measurements greater than

SMOKE emissions (CEMS/SMOKE > 1) would have a ratio of Measured/Modeled NO_y greater than 1. Figure 2.12b shows no trend between the two ratios. Because the NEI estimates that 73% of Maryland's NO_x emissions stem from mobile sources and the point source emissions used in the CMAQ model runs are, on average, correct, emissions from the mobile sector are the most likely source of the overestimate of NO_x emissions.

2.4 Discussion

CO/NO_x emissions ratios in the BWR were found to be 11.2 ± 1.2, a factor of 1.21 higher than the NEI. Comparison between *in situ* observations, MOPITT, and CMAQ show that observed CO emissions are ~21 ± 11% higher than modeled emissions, with 4-7% of CO concentration stemming from isoprene oxidation. The NEI overestimates CO emissions by 15 ± 11% (1σ).

Figure 2.13 shows the ratio of the observed CO/NO_x emissions ratio to that predicted by the NEI for each location corrected for *in situ* CO production and errors in the NEI's CO emissions (squares). Values greater than 1 indicate a higher ratio than that predicted by the NEI. Because the data are corrected for CO, the resulting values are also the ratio of observed to NEI predicted NO_x emissions, showing explicitly the NEI's overestimation of NO_x emissions across the experimental domain. Combining these data with the uncertainties in dry deposition and aerosolization of NO_y species yields an overestimation of NO_x emissions by the NEI of 44 ± 26% (1σ). Using a linear, least squares method with CO as the independent variable, instead of the orthogonal regression previously discussed, yields an overestimate in NO_x emissions of 75 ± 24%. Because uncertainty in the CO measurement is an order of magnitude lower than for NO_y, this regression method is equally valid, implying that the true NEI NO_x emissions

overestimate is likely in the region of overlap between the two, or 51-70%. Figure 2.13 also shows the same analysis but using the NEI 2011, version 2 (triangles). CO/NO_x emissions ratios were calculated in the same manner as that used for the projection in this study. The ratio of observed to NEI CO/NO_x emissions ratios is even larger for the NEI 2011, which incorporates the updated on-road emissions model, MOVES2014. CO emissions for the 2011 NEI have not been evaluated using CMAQ, so there has not been a correction for any error in CO emissions estimates. While I cannot quantitatively estimate the error in NO_x emissions without an additional CMAQ run, it is likely that NO_x emissions are overestimated by an even greater factor in the updated inventory than in the projection used here.

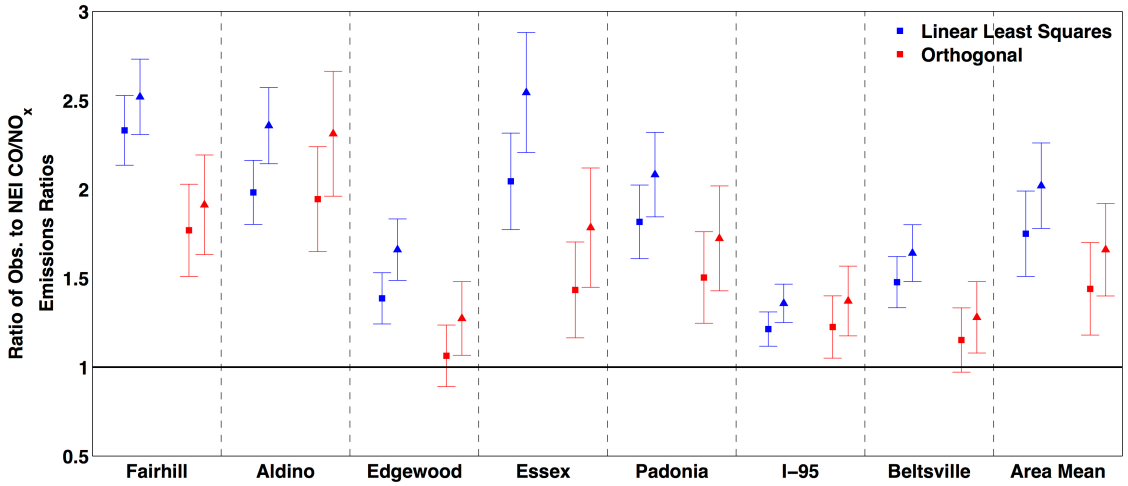

Figure 2.13: Ratio of observed CO/NO_x emissions ratios to those predicted by the NEI by location. Values are corrected for CO uncertainties. Blue are derived using the linear least squares method, and red are derived with an orthogonal linear regression. Uncertainties are the 1σ uncertainties in the NEI values and observations added in quadrature. The squares show the results for the emissions inventory used in this study (NEI2005 projected to 2011), while the triangles show the same results but using the NEI2011 version 2.

This evaluation of CO in the NEI is consistent with the results of Castellanos *et al* (2011), who found that CO emissions in the inventory were within the combined uncertainty of the observations. The NO_x emissions overestimate of 62% predicted by *Lu et al.* [2015] falls within the middle of my estimate. Discrepancies between this work

and that of Brioude (2013), who found overestimates of CO emissions by approximately 40%, are most likely because of differences in the composition of the mobile fleet in the two regions (the Los Angeles basin and the BWR). The lower end of this study's estimate of inaccuracies in NO_x emissions agrees with Brioude. Observed emissions ratios from this study lie slightly above those found by Fujita *et al.* (2012) in the Van Nuys Tunnel as well. Fujita, like Brioude, measured a different vehicle fleet in addition to measuring only on-road sources, whereas this study evaluated all emissions sources. This study also confirms the overestimation of NO_y by a factor of two in CMAQ found by Yu *et al* (2012) for their Houston study.

Comparison of modeled and measured point source NO_x emissions show excellent agreement, implying that the most likely source of error in the NEI NO_x emissions is mobile sources, which make up approximately 50-75% of NO_x emissions in the BWR depending on the time of day. Assumptions in MOVES2010 may be responsible for this NO_x emissions overestimate. Further exploration into the model mechanics is needed for definitive determination of the overestimate source(s). The model's treatment of emissions from aging vehicles is one likely contributor; the NEI overestimate of NO_x emissions could indicate that engines produce less NOx and catalytic converters degrade more slowly than assumed by MOVES2010. MOVES2010 likely fails to capture the dependence of NO_x emissions on vehicle age accurately. Similarly, *Bishop et al.* [2012] show that 1% of the vehicle fleet could emit as much as 15% of total NO_x emissions, indicating that misrepresentation of the attributes of these outliers in emissions inventories could have significant effects on the estimated emissions. Additionally, the strong temperature dependence of the observed CO/NO_x

emissions ratio suggests that MOVES2010 and likely MOVES2014 do not take into account any temperature dependence of NO_x conversion in catalytic converters. The observed dependence is consistent with cars running an enriched fuel mixture at hot ambient temperatures, which would increase CO and decrease NO_x production. Further investigation of this mechanism is needed, however, to determine whether this is the cause of the discrepancy between observations and the NEI.

Incorrect emissions apportionment to the diesel portions of the on- and off-road fleets would lead to significant errors in the ratio of CO to NO_x emissions. Incorrect emission factors are also another possible source of error. *Lindhjem et al.* [2012] found that the use of MOVES2010 emissions factors increased NO_x emissions by 50% in comparison to those found in the previous EPA model, MOBILE6. While further studies with the recently released 2011 NEI are needed, its CO/NO_x ratio for Maryland is even lower than the values used in this study.

If mobile emissions are indeed overestimated by 51-70%, then the relative importance of NO_x emissions from other sectors, particularly point and area sources, increases dramatically. It will then be even more pressing to ensure the development of effective policies to reduce NO_x emissions from these other sources to decrease ambient NO_y concentrations, reduce O_3 production, and improve air quality. Because models indicate that, for the majority of the O_3 non-attainment area, areas of NO_x inhibiting O_3 formation are very small and Maryland is in the NO_x limited regime for O_3 production [*Chameides et al.*, 1992], significant reductions in NO_x emissions should result in significant and observable reductions in O_3 mixing ratios and a dramatic improvement in

air quality. Reductions in NO_x may be more effective than predicted by CMAQ, but policy measures aiming to reduce NO_x emissions must be directed at the correct sectors.

Chapter 3 The CONvective TRansport of Active Species in the Tropics (CONTRAST) and Coordinated Airborne Studies in the Tropics (CAST) Campaigns

In this chapter, I describe the CONTRAST and CAST campaigns analyzed in Chapters 4 and 5. In addition, I include a discussion of the models and satellite output common to both studies.

3.1 Field campaigns

3.1.1 CONTRAST

The CONTRAST campaign [*Pan et al.*, 2016] consisted of 16 research flights conducted using the National Center for Atmospheric Research (NCAR) Gulfstream V (GV) aircraft during January and February 2014. Objectives of the campaign included determining the budget and speciation of very short-lived halogen compounds in the TWP and investigating the transportation pathways of these and other chemicals from the MBL to the tropical tropopause layer in a strongly convective environment. Research flights (RF) were either based out of Guam (13.5°N, 144.8°E) or conducted in transit between Broomfield, CO (39.95°N, 105.1°W), the home-base of the GV, and Guam. Flights from Guam spanned latitudes from the northern coast of Australia to Japan and altitudes from approximately 0.5 to 15.5 km. Transit flights (RF01, RF02, RF16) as well as portions of flights that sampled mid-latitude air have been excluded from this analysis, unless otherwise indicated. Tracks of the CONTRAST flights considered here are shown in Figure 3.1; these flights include all that sampled exclusively in the tropics. 63 vertical profiles were conducted during these flights, offering unprecedented sampling in the

middle and upper troposphere of the TWP. RF15 sampled the lower, mid-latitude stratosphere near Japan, as evidenced by O_3 mixing ratios that approached 1 ppmv. The mixing ratio of stratospheric species quoted here are taken from this flight segment, where stratospheric air is defined as having $O_3 > 200$ ppbv.

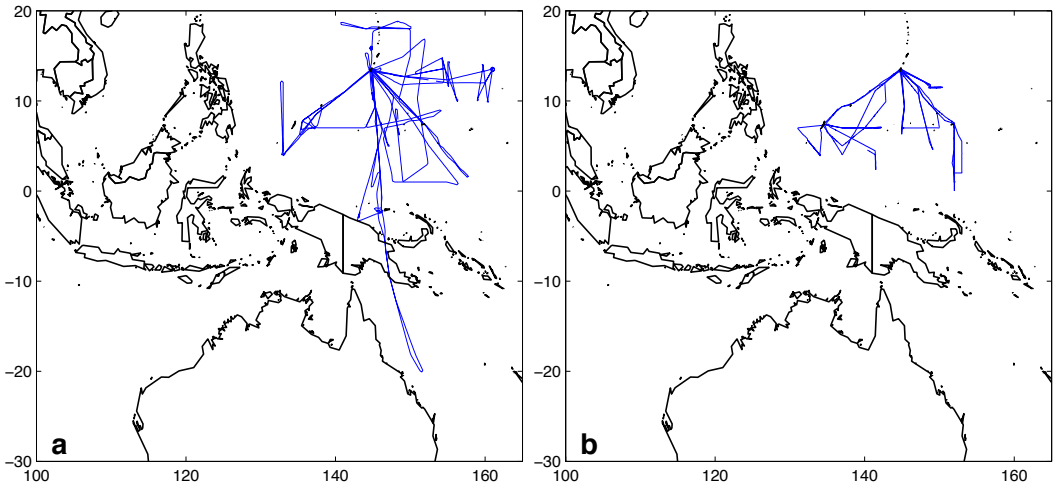

Figure 3.1: Tracks for (**a**) CONTRAST and (**b**) CAST flights analyzed in this study.

The NCAR GV aircraft was outfitted to measure various trace gases, meteorological parameters, and radiative flux. O_3, NO, and NO_2 were measured by chemiluminescence at 1 Hz [*Ridley and Grahek*, 1990]. The 2σ precisions of O_3, NO, and NO_2 at 1Hz sampling frequency, in the troposphere, are below 1 ppbv, 20 pptv, and 40 pptv, respectively. Precision and bias uncertainties were calculated for each measurement and added in quadrature to calculate a total 2σ uncertainty with mean values of 1.2 ppbv and 4.5 pptv for O_3 and NO, respectively, averaged over 35 sec. O_3 has been corrected for quenching due to ambient H_2O [*Boylan et al.*, 2014]. CO was also measured at 1 Hz, with an Aero-Laser 5002 vacuum ultraviolet fluorescence instrument [*Gerbig et al.*, 1999] with a 2σ uncertainty of 3 ppbv ± 3%. Methane was measured by wavelength-scanned cavity ringdown spectroscopy (WS-CRDS) using a Picarro G1301-c analyzer [*Crosson*, 2008]. Measurement uncertainty is 3 ppbv (2σ) for a 0.2 sec

averaging time. Water vapor was measured by an open-path, laser hygrometer at 2 wavelengths (1853.37 and 1854.03 nm), allowing for the sampling of H_2O mixing ratios spanning 5 orders of magnitude [*Zondlo et al.*, 2010]. Data were reported at 1 Hz with a 2σ precision of < 3%. Relative humidity was calculated from observed H_2O and temperature. Reported RH is with respect to water for temperatures above 0°C and with respect to ice for temperatures below 0°C.

Table 3.1: Detection limit and uncertainty of observations from the TOGA instrument used in this study. Uncertainties are in percent and pptv, shown in parenthesis. The uncertainty for a given observation is the higher of the two values.

Species	LOD (pptv)	Uncertainty (% or pptv)	Species	LOD (pptv)	Uncertainty (% or pptv)
Acetaldehyde	5	20 (10)	**Isoprene**	1	15 (2)
Acetone	20	20 (40)	**Methacrolein**	1	20 (2)
Acetonitrile	1	40 (2)	**Methanol**	20	30 (40)
Acrolein	1	30 (2)	**MVK**	1	20 (2)
Benzene	1	15 (2)	**i-Pentane**	0.5	15 (1)
Butanal	1	30 (2)	**n-Pentane**	0.5	15 (1)
i-Butane	0.5	15 (1)	**Propanal**	5	20 (10)
n-Butane	0.5	15 (1)	**Propane**	10	30 (20)
Formaldehyde	20	100 (80)	**Tetrachloroethylene**	0.3	15 (0.6)
Hydrogen Cyanide	10	50 (20)			

The trace organic gas analyzer (TOGA) measured a suite of trace gases via gas chromatography/quadrupole mass spectrometry (GCMS) with a sampling time of 35 sec and 2 min between sampling periods [*Apel*, 2003]. Measured species relevant to this study are acetone (CH_3COCH_3), acetaldehyde (CH_3CHO), hydrogen cyanide (HCN), acetonitrile (CH_3CN), tetrachloroethylene (C_2Cl_4), propanal (C_2H_5CHO), butanal (C_3H_8CHO), benzene (C_6H_6), methanol (CH_3OH), acrolein (CH_2CHCHO), propane (C_3H_8), n-butane (C_4H_{10}), i-butane ($CH_3CH_2(CH_3)CH_3$), n-pentane (C_5H_{12}), i-pentane ($CH_3CH_2(CH_3)CH_2CH_3$), isoprene (C_5H_8), and the isoprene decomposition products methyl vinyl ketone (MVK) and methacrolein (MACR). Measurement uncertainties and Limits of Detection (LODs) for these species are listed in Table 3.1. The LOD increases linearly above 12 km to 1.5 times its value at 15 km.

The Advanced Whole Air Sampler (AWAS) also measured a suite of trace gases, including ethyne (C_2H_2), ethane (C_2H_6), n-butane, i-butane, n-pentane, i-pentane, and benzene. AWAS acquires up to 60 samples of ambient air per flight in electropolished stainless steel canisters. Sampling time is pressure dependent. Canisters were analyzed post-flight using GCMS. All CONTRAST data used in this study have been averaged over the TOGA observation time, unless otherwise indicated. The sampling resolution for vertical flight segments for data averaged over the TOGA sampling period is approximately 210 m.

Photolysis frequencies were calculated from up and downwelling, spectrally resolved actinic flux density by the HIAPER Airborne Radiation Package (HARP). The system uses independent, 2 pi steradian optical collectors connected via ultraviolet enhanced fiber optics to charge-coupled device detectors. Spectra were collected every 6 sec at ~0.8 nm resolution between 280 and 600 nm with a full-width at half maximum of 1.7 and 2.4 nm in the ultraviolet and visible, respectively. Total photolysis frequencies were calculated from the actinic flux as well as laboratory determinations of molecular cross sections and quantum yields [*Shetter and Muller*, 1999]. Estimated total, 1σ uncertainties in photolysis frequencies relevant to this study are ±25%, ±12%, and ±20% for j_{O1D}, j_{NO2}, and j_{HCHO}.

Bromine monoxide (BrO) was measured remotely with Differential Optical Absorption Spectroscopy (DOAS) and *in situ* via chemical ionization mass spectrometry (CIMS). The Airborne Multi-Axis (AMAX) DOAS instrument measured scattered sunlight at various elevation angles, including zenith and nadir, allowing for the calculation of a BrO differential slant column density (dSCD) [*Baidar et al.*, 2013].

These dSCDs were then converted to a mixing ratio along the flight track using radiative transfer calculations, accounting for measurement geometry, atmospheric scattering, and inversion techniques. The BrO detection limit for a 60 sec sampling time is ~0.3 pptv. BrO was also measured by CIMS [*Chen et al.*, 2016; *Liao et al.*, 2012]. Here, BrO was reacted with the iodine ion and then detected with a quadrupole mass filter. HOBr and Br_2 were also detected using the same technique, but only the sum of the two is reported because of possible conversion of HOBr to Br_2 in the sample chamber. Calibrations were performed online using Cl_2 as a calibration gas, and detection limits for BrO and HOBr+Br_2 were 0.6 to 1.6 pptv and 1.3 to 3.5 pptv, respectively.

3.1.1.1 Formaldehyde Observations in CONTRAST

Formaldehyde was measured by the *In Situ* Airborne Formaldehyde (ISAF) instrument. A complete instrument description can be found in *Cazorla et al.* [2015], and only a brief summary is given here. ISAF relies on the laser induced fluorescence (LIF) technique. A pulsed UV fiber laser is tuned to a HCHO rovibronic absorption line at 353.163 nm. A fraction of the excited HCHO molecules relax to the ground state by fluorescence, and the resultant photons are counted by a photomultiplier tube. Non-resonant background signal is measured at a nearby wavelength (353.168 nm) with no HCHO absorption. The difference between the photon count at these two wavelengths is proportional to the mixing ratio of HCHO.

The instrument is calibrated through standard dilution of a ~500 ppbv primary HCHO standard (Scott Specialty Gas) to zero air. The calibration factor is dependent on cell pressure, which affects the number density, absorption line broadening, and quenching of the sample. Data are sampled by ISAF at 10 Hz and reported at 1 Hz. At 1

Hz, the detection limit is 36 pptv, and the instrument precision is better than 20% above 100 pptv. For the upper tropospheric background observed in CONTRAST (between 50 and 75 pptv), instrument precision is closer to 30%, as uncertainty at these mixing ratios is dictated by variations in the background signal..

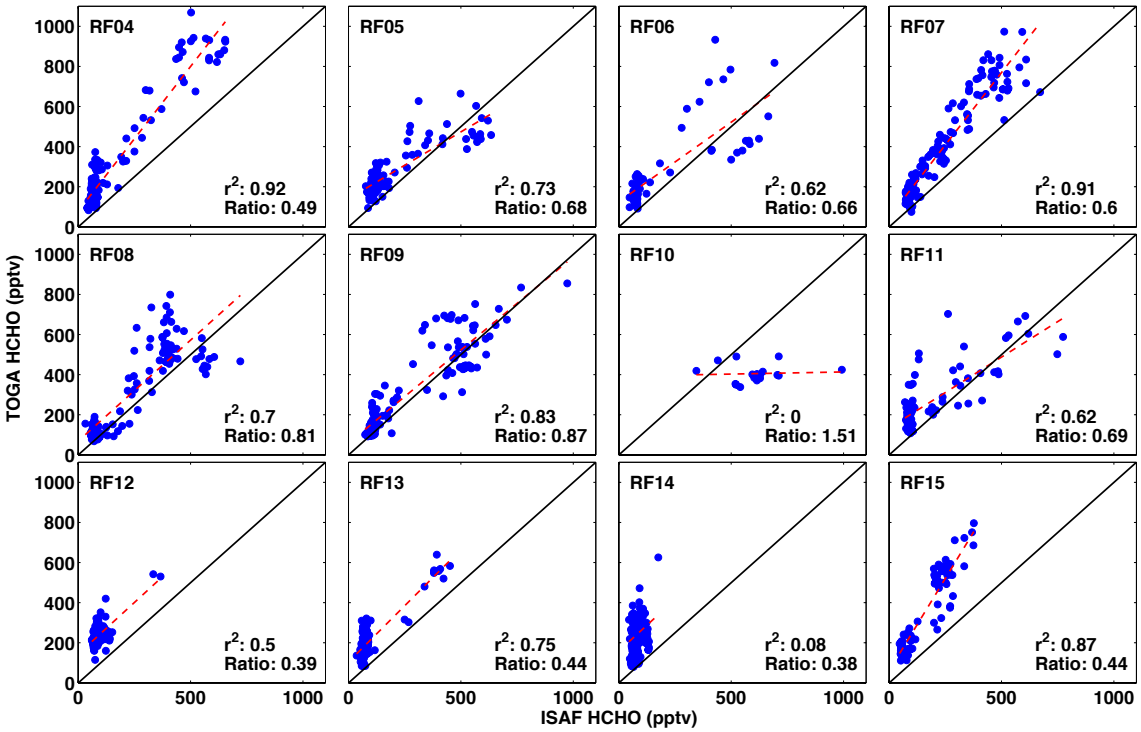

Figure 3.2: Regression of HCHO measured by ISAF against that measured by TOGA for each flight analyzed in this study. ISAF data are averaged over the TOGA observation time. Points below the TOGA limit of detection have been removed. The solid, black line is the 1:1 line, and the red, dashed line is the line of best fit found using a linear, least squares regression. The r^2 and mean ratio of ISAF HCHO to TOGA HCHO is also shown for each flight.

Additional HCHO observations were made by the TOGA instrument, with an LOD of 20 pptv and a measurement uncertainty of 100% or 80 pptv, whichever is higher. A regression of ISAF and TOGA HCHO is shown in Figure 3.2 for each flight analyzed here. In general, there is moderate linearity between the two instruments, with r^2 values greater than 0.5 for ten of the twelve flights. For these ten flights, observations from ISAF were consistently lower than TOGA, with the mean ratio of ISAF to TOGA HCHO varying between 0.39 and 0.87. It is beyond the scope of this work to determine the

source of the discrepancy between the two instruments. Unless otherwise specified, all measurements cited here are from ISAF, which has been deployed on multiple field campaigns and been rigorously compared to observations from a DFGAS instrument [*Arkinson et al.*, in preparation; *Cazorla et al.*, 2015] during the Deep Convective Clouds and Chemistry (DC3) experiment [*Barth et al.*, 2015].

3.1.2 CAST

The CAST campaign [*Harris et al.*, 2016] was conducted simultaneously with CONTRAST. Whereas observations during CONTRAST were concentrated in the mid- to upper troposphere, the goal of CAST was to observe O_3, CO, NO, very short-lived organic halogen species, and radicals in the MBL and lower troposphere. Together, the two campaigns provide coverage of the TWP from just above the ocean surface to the base of the tropical tropopause layer. CAST flights were based out of Guam, Chuuk (7.4°N, 151.8°E), and Palau (7.5°N, 134.5°E) and covered altitudes from near the surface (30 m above mean sea level) to 8 km. The research portion of this campaign consisted of 23 flights during January and February 2014; 17 of these flights provided observations between 300 and 700 hPa and are analyzed here. CONTRAST and CAST flights were jointly coordinated at a shared operations center in Guam.

CAST was conducted using the Facility for Airborne Atmospheric Measurements (FAAM) BAE-146a aircraft. NO was measured with an Air Quality Design, 2-channel chemiluminescence instrument through reaction with O_3 with a 2σ uncertainty of 15%. O_3 was measured at 0.1 Hz with a Thermo Environmental 49c O_3 analyzer by UV absorption with a 2σ uncertainty of ~0.8 ppbv. CO was measured with an Aero-Laser 5002 instrument at 1 Hz with a 2σ uncertainty of ~1.4 ppbv. Water vapor mixing ratios

were calculated from the observed dew point, measured with a General Eastern Dew point Hygrometer. HCN, BrO, Br_2, HOBr, and HCl were measured by Chemical Ionization Mass Spectrometry (CIMS) [*Le Breton et al.*, 2013].

3.1.3 Comparison of CAST and CONTRAST Data

No wingtip-to-wingtip comparisons of observations for the CAST and CONTRAST campaign instruments were acquired, due to air traffic concerns in the remote TWP. To compare HCN observations, data from TOGA and the CIMS instrument were selected for background conditions (Relative Humidity (RH) > 70% and O_3 < 25 ppbv) and sorted into 0.5 km bins. The mean ±1σ values of HCN for both campaigns strongly overlap, with CAST HCN slightly lower. The mean ratio of CAST to CONTRAST HCN for all altitude bins was 0.90 ± 0.21. A similar process was used to compare O_3 observations, selecting for measurements with RH > 70%. The mean CAST to CONTRAST ratio of O_3 values was 0.98 ± 0.26. Since flights were conducted in different air masses and often on different days, this agreement indicates the measurements of O_3 and HCN obtained during CAST and CONTRAST are directly comparable.

3.2 Back Trajectories

Ten day kinematic back trajectories along the flight track were calculated using the NOAA HYSPLIT model [*Stein et al.*, 2015]. Relative humidity, temperature, and pressure were output along the trajectory, and H_2O mixing ratios were calculated using the Clausius-Clapeyron relation. Relative humidity, as output by HYSPLIT, is with respect to ice for temperatures below −20°C and a linear blend of RH with respect to ice and water for temperatures between 0° and −20°C. HYSPLIT RH was post-processed to

convert all points with temperatures between 0°C and −20°C to RH with respect to ice, to render HYSPLIT RH directly comparable to *in situ* RH.

The trajectories allowed for vertical displacement, using estimates of the vertical wind from assimilated meteorological fields. Trajectories from CONTRAST were computed along the flight track at 2 min intervals for pressures between 300 and 700 hPa, corresponding with the time between TOGA observations. CAST data were averaged over 35 s (TOGA integration time) and trajectories were calculated at 2 min intervals (TOGA sampling interval) along the flight track, to make the analysis of CAST data using trajectories analogous to the CONTRAST analysis. Global Data Assimilation System (GDAS) meteorological fields at 1°×1° resolution drove the HYSPLIT model. Potential vorticity (PV), at 6-hour resolution from the National Center for Environmental Prediction (NCEP) final (FNL) analysis, was interpolated to the back trajectory through a bilinear interpolation in the horizontal and a linear interpolation in the vertical and time coordinates.

Trajectories were stopped at the time and place where precipitating convection was encountered. In the TWP, convection promotes mixing with MBL air, altering air parcel composition. Precipitation rates from the Tropical Rainfall Measuring Mission (TRMM) satellite were combined with cloud top heights calculated from geostationary satellite infrared measurements to estimate where convective precipitation occurs. This technique provides coverage of the entire tropics. The convective precipitation product is available at 0.25°×0.25° (latitude, longitude) resolution with a time step of 3 hours and was obtained from Lenny Pfister at NASA Ames. Intersection of a trajectory with precipitating convection was defined as a point on the trajectory being within 25 km of

convection in the horizontal and being at or below the cloud top height. A 25 km radius is used to account for uncertainty in the back trajectory calculation; results shown below are insensitive to reasonable variations of the size of this radius.

3.3 CAM-Chem

The Community Atmosphere Model version 4.0 (CAM4) is the atmospheric component of the global chemistry-climate model Community Earth System Model (CESM) [*Lamarque et al.*, 2012]. When run with active chemistry, it is known as CAM-Chem. Here, the model was run offline, with meteorological fields specified by the NASA Goddard Earth Observing System, Version 5 (GEOS5) model, with a horizontal resolution of 0.94° latitude × 1.25° longitude and 56 vertical levels. The model chemistry scheme includes a detailed representation of tropospheric and stratospheric chemistry (~180 species; ~500 chemical reactions), including very short-lived halogens. *Fernandez et al.* [2014] provide details on surface emissions, wet and dry deposition, heterogeneous reactions, and photochemical processes of halogens used within CAM-Chem.

Anthropogenic emissions of O_3 and aerosol precursors are from the Representative Concentration Pathway (RCP) 6.0 scenario for 2014 [*Meinshausen et al.*, 2011; *van Vuuren et al.*, 2011]. Biomass burning emissions are from the Fire INventory for NCAR (FINN) [*Wiedinmyer et al.*, 2011], which combines observations of biomass burning and vegetation/land cover type from the MODerate resolution Imaging Spectrometer (MODIS) and emissions factors from multiple datasets to produce a gridded global product with a 1 km × 1 km resolution. To determine the relative contributions of biomass burning from individual regions, CO emitted from fires in

Africa as well as CO emitted from fires in Southeast Asia were treated as separate variables, referred to here as tagged CO.

Chapter 4 Determination of the Origin of High O_3/ Low H_2O Structures in the Tropical Western Pacific

This chapter was published as *Anderson et al.* [2016] and has been reorganized for clarity.

4.1 Background

Tropospheric O_3 is an important greenhouse gas. Ozone has exerted an increase in the global radiative forcing of climate of ~0.4 Wm^{-2} between 1750 and 2011, almost equal to that of CH_4 over the same time period [*IPCC*, 2013]. The largest contribution to the climatic influence of O_3 is due to enhancements over background in the tropical upper troposphere [*Shindell and Faluvegi*, 2009; *Stevenson et al.*, 2013]. Elevated surface O_3 adversely affects human health and agriculture [*Avnery et al.*, 2011; *Bell et al.*, 2006]. Legislation enacted to protect public health has significantly reduced emissions of O_3 precursors from automobiles, factories, and power plants throughout the industrialized world, particularly in the Northern Hemisphere (NH) mid-latitudes [*Parrish*, 2006; *Vestreng et al.*, 2009]. Surface O_3 levels in the industrialized extra-tropics have plateaued or fallen dramatically in response to these actions [*Cooper et al.*, 2012; *Oltmans et al.*, 2006]. It is unclear whether the measures taken to reduce surface O_3 in the extra-tropics will reduce the climatic impact of O_3, since its largest radiative influence is in the tropics.

4.1.1 Proposed extratropical tropospheric origin of HOLW structures

In the MBL of the TWP, O_3 is removed by photochemical reactions involving halogen radicals of marine biogenic origin, resulting in O_3 abundances of ~20 ppbv or lower [*Dickerson et al.*, 1999; *Read et al.*, 2008]. Local convection can transmit this low

O_3 air throughout the tropospheric column [*Kley et al.*, 1997], resulting at times in O_3 profiles that have mixing ratios of ~20 ppbv over an extended altitude range [*Oltmans et al.*, 2001; *Rex et al.*, 2014]. Air masses with elevated O_3 are frequently accompanied by water vapor mixing ratios depressed with respect to the local background, particularly in the mid-troposphere [*Pan et al.*, 2015]. These HOLW structures inhibit mixing and convection [*Mapes and Zuidema*, 1995], alter the local radiative heating profile [*Parsons et al.*, 2000], and affect the atmosphere's oxidative capacity [*Rex et al.*, 2014].

Large increases in O_3 relative to these low background values have frequently been observed in the TWP mid-troposphere [*Blake et al.*, 1999; *Folkins et al.*, 1997; *Hayashi et al.*, 2008; *Kley et al.*, 1997; *Kondo et al.*, 2004; *Newell et al.*, 1999; *Oltmans et al.*, 2001; *Ridder et al.*, 2012; *Singh et al.*, 2000; *Stoller et al.*, 1999]. Many of these studies note that water vapor tends to be depressed, with respect to the local background, for these high O_3 air parcels [*Blake et al.*, 1999; *Folkins et al.*, 1997; *Hayashi et al.*, 2008; *Kley et al.*, 1997; *Newell et al.*, 1999; *Oltmans et al.*, 2001; *Singh et al.*, 2000; *Stoller et al.*, 1999], often attributing the HOLW structures to sources outside the tropical troposphere. *Stoller et al.* [1999] conclude that stratospheric air is the dominant source of HOLW air parcels observed over the TWP during multiple aircraft campaigns conducted in September – October 1991, February – March 1994, and September – October 1996. This conclusion was mainly based on the co-location of high PV with a few HOLW structures. These early campaigns lacked the instrumentation to measure the suite of chemical compounds sampled during modern campaigns, particularly the biomass burning tracer HCN. *Newell et al.* [1999] reach a similar conclusion, analyzing the same data as Stoller *et al.* in addition to observations from the Measurement of Ozone and

Water Vapour on Airbus in-service Aircraft (MOZAIC) campaign from between 1994 and 1997. They note elevated CO and CH_4 in some of their observed HOLW structures, citing entrainment of biomass burning emissions into stratospheric air. Using back trajectory analysis in addition to sonde measurements of O_3 and H_2O from 6 years of Southern Hemisphere Additional Ozonesondes (SHADOZ) data at three sites across the Pacific, *Hayashi et al.* [2008] argue that transport from the mid-latitude upper troposphere (mlUT) is the dominant source of high mid-tropospheric O_3 in the TWP, with biomass burning only a minor contributor in some months. *Kley et al.* [1997] likewise hypothesize a mlUT origin for HOLW features near 700 hPa measured by ozonesondes in the equatorial western Pacific during the Central Equatorial Pacific Experiment (CEPEX) and The Tropical Ocean Global Atmosphere Coupled Ocean Atmosphere Response Experiment (TOGA-COARE) campaigns conducted in the Fall of 1992. Finally, *Ridder et al.* [2012] attribute enhancements in O_3 and CO observed remotely in the NH TWP during October – November 2009 to fossil fuel combustion in Asia, Europe, and North America (*i.e.* the mid-latitudes) and in the Southern Hemisphere (SH) to a combination of fossil fuel combustion and biomass burning.

Numerous other studies claim that low H_2O in the TWP mid-troposphere, defined here as 300 to 700 hPa, is dominated by the transport of dry air from the mid-latitudes. *Yoneyama and Parsons* [1999] conclude horizontal advection from the mid-latitudes, likely through Rossby wave breaking, creates the observed distribution of dry air during the TOGA-COARE experiment. Combining satellite data and trajectory simulations, *Waugh* [2005] finds that high PV intrusions in the subtropics lead to low RH in the intrusion itself and high RH ahead of the intrusion, consistent with transport from the

lower stratosphere and the deep tropical troposphere, respectively. *Cau et al.* [2007] conclude that a dominant dry air source in the TWP is dehydration of air parcels via poleward movement of upper tropical tropospheric air into the jet followed by slow descent driven by radiative cooling. This study relied on 24-day back trajectories and did not account for the presence of convective precipitation, which is known to greatly alter air mass composition. *Galewsky et al.* [2005] conclude, using a modeled tracer method and NCEP reanalysis data, that mid-latitude eddies and isentropic transport are the dominant source of low H_2O in the subtropics in December-February 2001/02. This analysis focused on the zonal mean distribution of H_2O. The subtropical location of their water minimum is coincident with earth's major deserts, which means this region is decoupled from convective precipitation that rehydrates other regions of the tropics. Conversely, *Dessler and Minschwaner* [2007] concluded that deep convective outflow associated with the Hadley circulation is the largest source of low H_2O in the tropical eastern Pacific. This analysis, which focuses on the deep tropics (20° N – 20° S) of the western Pacific, similarly suggests low water is controlled by outflow of the Hadley circulation.

4.1.2 Proposed biomass burning origin of HOLW structures

Other studies cite the importance of biomass burning in controlling tropical O_3, particularly over the Atlantic Ocean and in the SH, but fail to account for the origin of low H_2O in HOLW air parcels. *Jacob et al.* [1996] find that tropical processes alone, including *in situ* photochemical production from biomass burning emissions and lightning NO_x ($NO_x = NO + NO_2$), can reproduce observed tropical O_3 distributions using measurements over the South Atlantic during the Transport and Atmospheric Chemistry

in the Atlantic (TRACE-A) campaign in September – October 1992. Other studies have attributed high O_3 observed in the TWP to photochemical production in biomass burning plumes. *Oltmans et al.* [2001] investigated the O_3 climatology over 3 locations (Fiji, Samoa, and Tahiti) in the TWP from the SHADOZ network. Elevated, mid-tropospheric O_3 was found at these sites, particularly in September and October. Back trajectory analysis connected some of these O_3 enhancements in Fiji and Samoa to biomass burning in Indonesia, and it was noted that air parcels descended approximately 3 km in transit. In the Pacific Exploratory Mission in the Tropics (PEM-Tropics) A campaign conducted in the Eastern and Central Pacific of the SH in August – September 1996, both *Blake et al.* [1999] and *Singh et al.* [2000] attribute elevated O_3 in HOLW parcels to photochemical production from biomass burning in Africa and South America based on elevated mixing ratios of biomass burning tracers (C_2H_2, NO_x, CO, CH_3Cl, PAN, and C_2H_6) in the structures. Similar to Oltmans *et al.*, Blake *et al.* and Singh *et al.* posit large-scale subsidence as a possible cause of the low H_2O but offer no quantitative support for this supposition. *Folkins et al.* [1997] observed HOLW air over Fiji (18° S) at ~120 hPa during the Airborne Southern Hemisphere Ozone Experiment/Measurement for Assessing the Effects of Stratospheric Aircraft (ASHOE/MAESA) campaign in October 1994. These air parcels were enhanced in reactive nitrogen compounds and had high N_2O mixing ratios, indicative of a tropospheric origin. They attributed the low H_2O to transport from the mlUT using 10-day isentropic trajectories but did not provide any quantitative analysis of the effect of thermodynamics or descent on observed H_2O. Finally, *Kondo et al.* [2004] attribute increases in O_3 of 26 ppbv over a 31 ppbv background in the western Pacific to biomass burning during the Transport and Chemical

Evolution over the Pacific (TRACE-P) campaign (February – April 2001). These studies either ignore the low H_2O [*Kondo et al.*, 2004], offer limited explanation [*Blake et al.*, 1999; *Oltmans et al.*, 2001; *Singh et al.*, 2000], attribute low H_2O to extra-tropical transport [*Folkins et al.*, 1997], or do not describe H_2O [*Jacob et al.*, 1996].

The source of high O_3 as well as the dynamical processes controlling the low H_2O in HOLW structures prevalent in the TWP is clearly unresolved. Previous studies have lacked the chemical sophistication as well as the large sampling frequency described here to determine the source of these structures unequivocally. Here, I analyze aircraft and ozonesonde observations, model output, and satellite data to understand the origin of the HOLW air parcels observed in the TWP during winter 2014. The CONTRAST and CAST aircraft campaigns based in Guam (13.5°N, 144.8°E) provide a comprehensive suite of chemical measurements. I examine the 11 CONTRAST and 17 CAST flights that provided unprecedented sampling of the TWP mid-troposphere during January and February 2014 (Fig. 3). These *in situ* observations are supplemented by satellite measurements of water vapor and outgoing longwave radiation (OLR) from the Level 3, Version 6 daily Atmospheric Infrared Sounder (AIRS) product as well as fire counts from the Version 1, Collection 5 monthly MODIS product. Ten day, kinematic back trajectories were initialized along the CAST and CONTRAST flight tracks using the HYSPLIT model, driven by GDAS meteorology, to connect observed air parcels to their source regions. The CAM-Chem chemical transport model was run with tagged biomass burning tracers to further elucidate ozone sources and was evaluated with ozonesonde observations in Nairobi, Kenya and Hanoi, Vietnam from the SHADOZ network. Models, satellite data, and aircraft observations are used to show that anthropogenic fires

in tropical Africa and Southeast Asia are the dominant source of the high O_3 and that the low H_2O results from large-scale descent within the tropical troposphere, after detrainment of biomass burning plumes.

4.2 Methodology

4.2.1 Sondes

Profiles of ozone were measured with electrochemical concentration cell ozonesondes from the SHADOZ campaign [*Thompson et al.*, 2012]. Data used here are from observations over Hanoi, Vietnam and Nairobi, Kenya and were downloaded from the SHADOZ archive (http://croc.gsfc.nasa.gov/shadoz). Nairobi data were acquired over 5 days in January and February 2014 using a 0.5% half buffer KI solution with launch times near 8 UTC. Hanoi data were taken over 4 days in January and February 2014, using a 0.5% unbuffered KI solution and launch times near 6 UTC.

4.2.2 Satellite Data

Fire count data are from the MODIS instrument onboard the Terra satellite, with a local overpass time of approximately 10:30 [*Giglio et al.*, 2006]. The version 1 monthly product from collection 5, available at a 1°×1° (latitude, longitude) spatial resolution, is used. MODIS data were downloaded from ftp://neespi.gsfc.nasa.gov. The Level 3, Version 6 daily AIRS product for OLR and water vapor, at 1°×1° horizontal resolution, is also used [*Susskind et al.*, 2012; *Tian et al.*, 2013]. AIRS is onboard the Aqua satellite with a local overpass time of approximately 13:30. AIRS data were downloaded from ftp://acdisc.sci.gsfc.nasa.gov/ftp/data/s4pa/Aqua_AIRS_Level3. Water vapor data cited here are pressure layer averages.

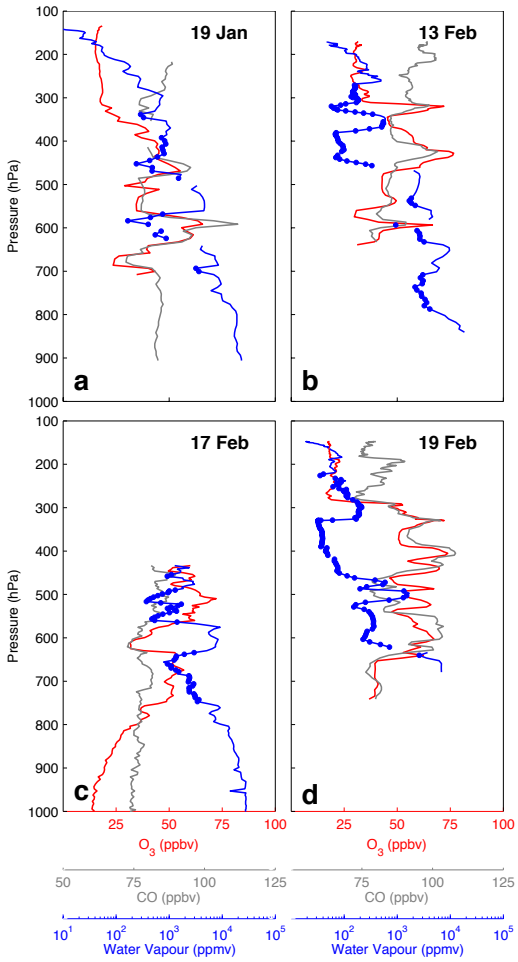

Figure 4.1: Sample profiles of 10 sec averaged O_3 (red), CO (grey), and H_2O (blue) from four flights during CONTRAST (panels **a**, **b**, and **d**) and CAST (panel **c**). Blue circles indicate measurements of H_2O mixing ratios for which RH < 20%. Relative humidity is with respect to water and with respect to ice for temperatures above and below 273 K, respectively. Vertical profiles have a characteristic horizontal length of approximately 300 km.

4.2.3 Box Model

Net photochemical production of O_3 was calculated using Equation (4.1) [*Jacob et al.*, 1996] for various CONTRAST profiles, where brackets indicate concentration and k_i represents the reaction constant for a given reaction:

$$\frac{d[O_3]}{dt} = k_1[NO][HO_2] + k_2[NO][CH_3O_2] - k_3[O_3][OH] - k_4[O_3][HO_2] - k_5[H_2O][O^1D] \quad \text{Equation (4.1)}$$

CH_3O_2 comprised greater than 95% of RO_2 for the majority of modeled points, so O_3 production from other RO_2 species has been ignored. HO_2, CH_3O_2, and $O(^1D)$ were

not measured; to determine net production of O_3, these species were calculated using the Dynamically Simple Model of Atmospheric Chemical Complexity (DSMACC) box model [*Emmerson and Evans*, 2009]. Model runs were only conducted for CONTRAST flights because of lack of necessary volatile organic compound data for CAST. The model uses a subset of the Master Chemical Mechanism (MCM) [*Jenkin et al.*, 2003; *Saunders et al.*, 2003] v3.3 [*Jenkin et al.*, 2015] and was initialized with observations of NO_2, MVK, MACR, acetone, isoprene, methanol, and acetaldehyde. The box model was constrained by GV observations of meteorological parameters, $j(NO_2)$, $j(O^1D)$, O_3, CO, NO, HCHO, H_2O, C_3H_8 and CH_4. The abundance of NO and j-values was allowed to vary with time of day. Photolysis frequencies for all reactions were calculated with the Tropospheric Ultraviolet and Visible radiation model version 4.2 (TUV) [*Madronich*, 1992] and then scaled using observations of $j(O^1D)$ and $j(NO_2)$. Data were averaged over 10 sec. Data from the TOGA instrument were linearly interpolated in time to create a 10 sec dataset. All output has been integrated over the diel cycle to produce 24 hour mean photochemical production of O_3, because of the diurnal variation of radical species. Model results were compared to output from another box model, the University of Washington Chemical Model (UWCM) [*Wolfe and Thornton*, 2011], which was constrained and initialized with the same set of input parameters. Between 300 and 700 hPa, the mean ratio of net O_3 production found using DSMACC and UWCM was 1.01.

4.3 Results

4.3.1 Origin of the High Ozone

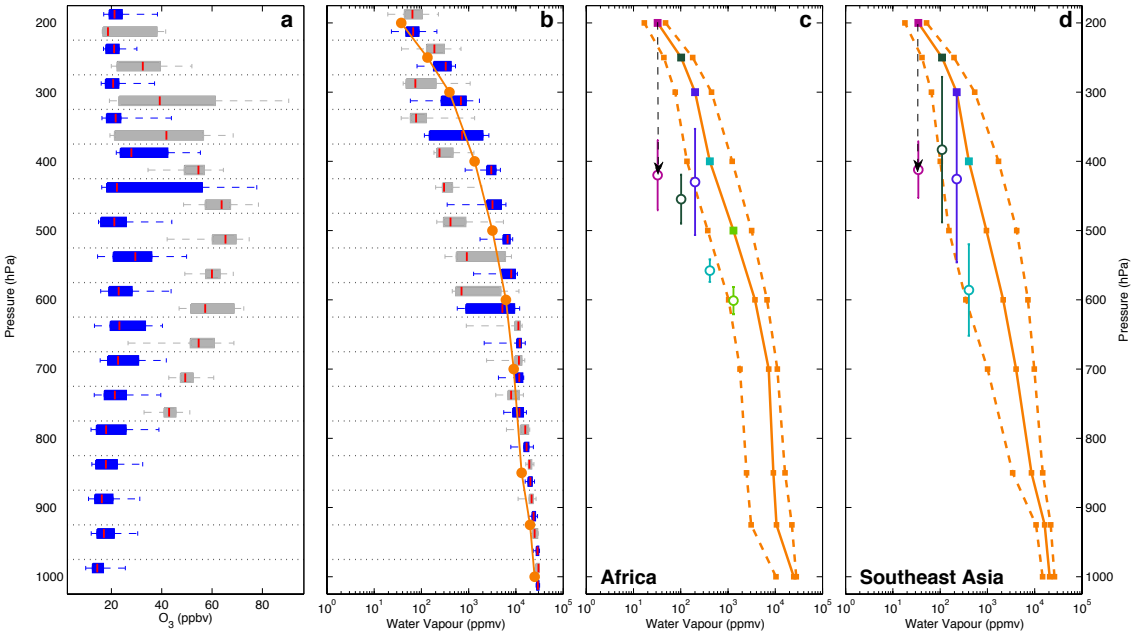

Figure 4.2: (**a**) Profiles of in situ O_3 during CAST and CONTRAST for two modes of RH (blue, RH > 20%; grey, RH < 20%). Box and whisker plots show 5th, 25th, 50th, 75th, and 95th percentiles for 50 hPa pressure bins. Each bin is delimited by a dotted line, and the two modes (grey and blue boxes) for a given pressure bin are offset for clarity. Between 400 and 700 hPa, the average (minimum) number of observations per blue and grey box is 650 (414) and 330 (43), respectively. Observations between 300 and 400 hPa were more limited with a minimum of 20 and a maximum of 56 observations. (**b**) Distribution of H_2O for two modes of HCN (grey, HCN > 150 pptv; blue, HCN < 150 pptv). Median AIRS H_2O over the ascending branch of the Hadley Cell (orange). Between 300 and 700 hPa, the average (minimum) number of observations per blue and grey box is 129 (28) and 111 (19), respectively. (**c**) Median (solid), 5th and 95th percentiles (dashed) of AIRS H_2O over the African biomass burning region (orange). Open circles represent the mean endpoint of descent ±1σ of trajectories starting over the African biomass burning region and arriving over the TWP, for various initial pressures (closed squares). (**d**) Same as (**c**) but for trajectories starting over Southeast Asia.

Representative O_3, CO, and H_2O profiles from the CAST and CONTRAST campaigns are shown in Figure 4.1. Unless otherwise specified, all references to H_2O in this chapter refer to water vapor. Mixing ratios of O_3 and H_2O in these profiles exhibit strong anti-correlation; *i.e.* elevated O_3 is closely associated with low RH. These HOLW structures were a pervasive feature seen throughout both campaigns. Here I define a HOLW structure as an air parcel satisfying the simultaneous criteria of O_3 > 40 ppbv and

RH < 20%, where RH in this study is with respect to water for T > 273 K and to ice for T < 273 K. Relying solely on composition to define HOLW structures allows for the inclusion of both sharply-defined, thin features (*e.g.* Figure 4.1a) as well as those that occupy a large fraction of the tropospheric column (*e.g.* Figure 4.1d). HOLW features were primarily located between 300 and 700 hPa and observed during 45 of 104 independent profiles (*i.e.* air parcels were not intentionally resampled). For air parcels with RH > 20%, median O_3 was nearly constant with altitude at ~20 ppbv (Figure 4.2a). For air with RH < 20%, median O_3 peaked at 60 ppbv near 450 hPa, three times greater than background, and decreased to about 40 ppbv at 750 and 300 hPa.

Kinematic trajectories connect nearly all of these HOLW structures to tropical regions with active biomass burning. Figures 4a & 3.4b show 10-day back trajectories found using the HYSPLIT model [*Stein et al.*, 2015]. Trajectories are colored by observed aircraft O_3 (invariant along each trajectory) and RH along the trajectory as output by HYSPLIT. Each trajectory stops at the estimate of the point of last precipitating convection, derived from a combination of cloud top height and precipitation data from geostationary satellites and the TRMM satellite. I stop the trajectories at the point of last precipitating convection because convection lofts MBL air into the upper troposphere, where it detrains throughout the column, creating a nearly uniform O_3 profile and a water vapor profile controlled by the local saturation vapor pressure [*Pan et al.*, 2015]. This convection effectively resets air parcel composition, removing any influence from outside the TWP. Further, global transport models are unable to reproduce the small-scale wind fields associated with deep convection, creating large uncertainty for back trajectories beyond this point. Air parcels originating from the

clean SH and Eastern Pacific (EP) had unimodal O_3 and RH distributions, with medians of 22 ppbv and 63%, respectively. Trajectories originating west of the study region, primarily over Africa and Southeast Asia, exhibit a bimodal distribution. Assuming a mixture of two Gaussian distributions, the two modes are described by one with peak O_3 and RH of 21 ppbv and 60% and another with peaks of 55 ppbv and 4.5%. The low O_3 trajectories are indicative of air parcels under local influence (*i.e.* convectively controlled in the TWP). The high O_3 trajectories originated over regions of active biomass burning in the tropics and reached the TWP along the upper branch of the Walker Circulation (Figure 4.3a).

4.3.1.1 Regression Analysis

Simultaneous elevation of CO and O_3 in the HOLW structures, in addition to regression analysis, suggests a tropospheric origin. Local maxima in O_3 and CO profiles closely track one another (Figure 4.1), with r^2 values between these two species ranging from 0.46 to 0.72 (Figure 4.4) for the profiles shown in Figure 4.1. A campaign-wide regression of CO and O_3 for air parcels that trace back to continental regions yields r^2 = 0.61. Photochemical enhancement ratios of O_3 with respect to CO ($\Delta O_3/\Delta CO$) for the profiles shown in Figure 4.1 range between 0.97 and 2.85 mol/mol. *Mauzerall et al.* [1998] found that fresh biomass burning plumes had enhancement ratios of ~0.15 mol/mol while plumes older than 6 days had values on the order of 0.75 mol/mol. These

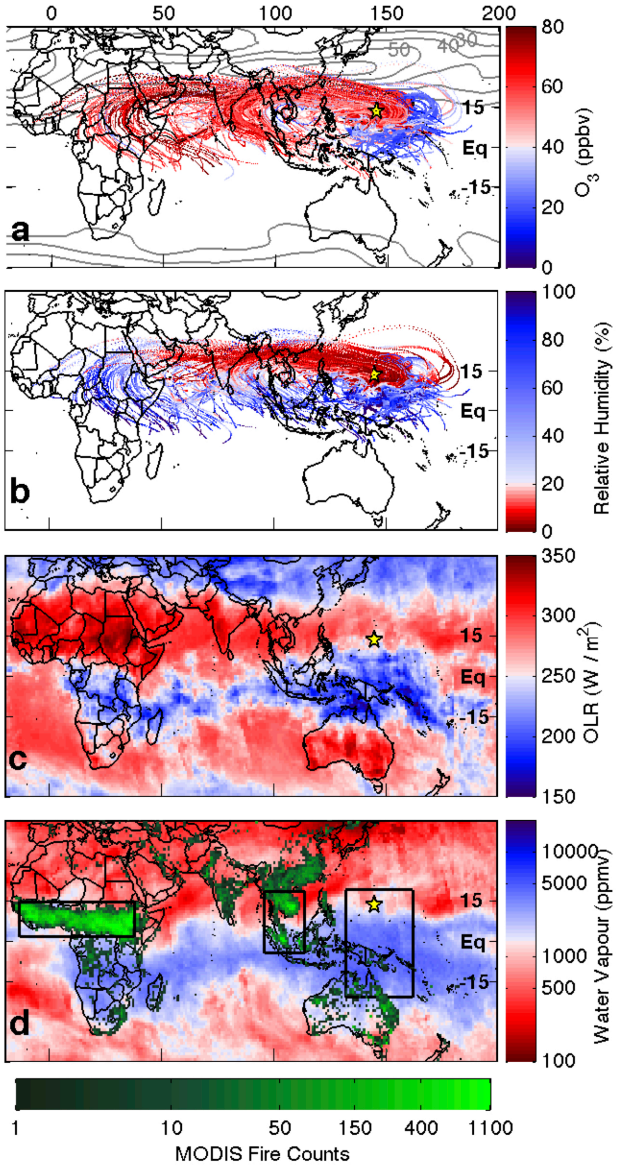

Figure 4.3: (**a**) 10-day, HYSPLIT back trajectories for CONTRAST RF03-05 and RF07-14 and all CAST flights for observed pressures between 300 and 700 hPa. Trajectories are stopped when encountering convective precipitation and coloured by observed O_3. For clarity, only every third is shown. Contours are zonal winds at 200 hPa averaged over January and February 2014 in 10 m/s intervals. The yellow star shows Guam. (**b**) Same as (**a**) but colored by HYSPLIT RH along the trajectory (see methods). (**c**) AIRS daytime OLR averaged over CONTRAST and CAST flight days. (**d**) Same as (**c**) but for AIRS H_2O at 500 hPa. MODIS fire counts are the total for January and February 2014. Black rectangles represent the African and Southeast Asian tropical biomass burning regions (determined subjectively by the high fire counts) and the CONTRAST/CAST study region.

results are consistent with *Parrington et al.* [2013] who found mean enhancement ratios of 0.81 mol/mol with a maximum ratio of 2.55 for boreal biomass burning plumes older than 5 days. Both comparisons suggest the air parcels analyzed here are significantly

aged and the enhancement ratios lie at the upper end of previous observations. This agrees with the back trajectories and photochemical aging analysis, discussed below, both of which yield air parcel ages of ~10 days. NO is also elevated in these air parcels (Figure 4.5), though the correlation with O_3 is not as prominent as for other species. This is likely due to the conversion of NO to other nitrogen-containing species, such as alkyl nitrates, PAN, and HNO_3, none of which were measured during CONTRAST.

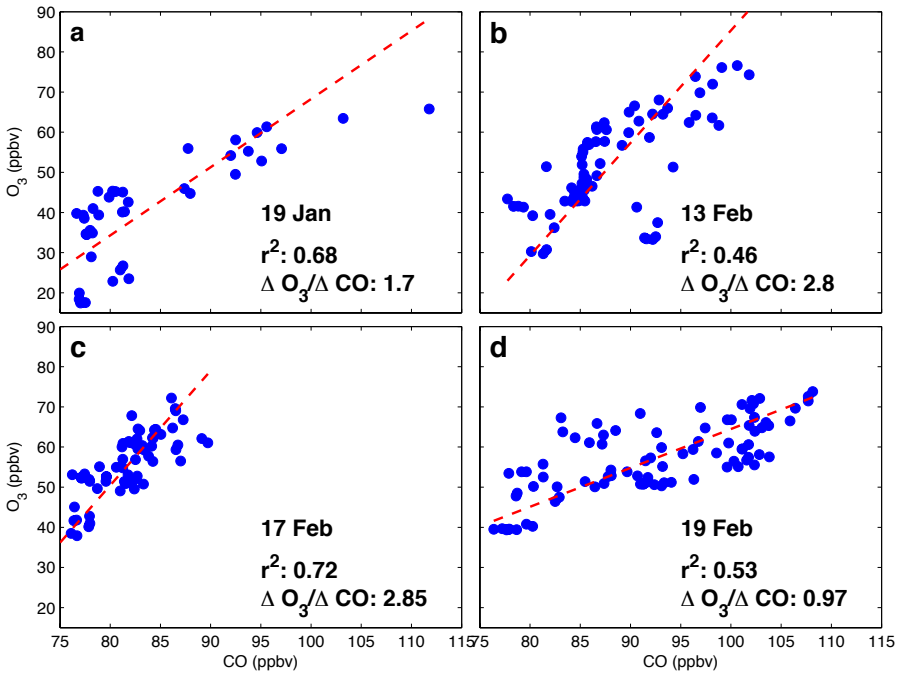

Figure 4.4: Regression of CO against O_3 for the data shown in Figure 4.1, for pressures between 300 and 700 hPa. The $\Delta O_3/\Delta CO$ ratio for all profiles suggests significantly aged air, consistent with the back trajectory and photochemical aging analyses. The dashed red line is the best fit via orthogonal linear regression. Flight dates, slope, and r^2 values are shown for all panels

Regression of CO against O_3 for all observations (Figure 4.6) reveals four distinct air mass types observed during the CAST and CONTRAST campaigns: stratospheric, marine, and two distinct polluted regimes, one with elevated CO, NO, and O_3 and the other with only elevated CO. Known stratospheric air was encountered on two flights into the sub-tropics and is characterized by high NO and a strong anti-correlation

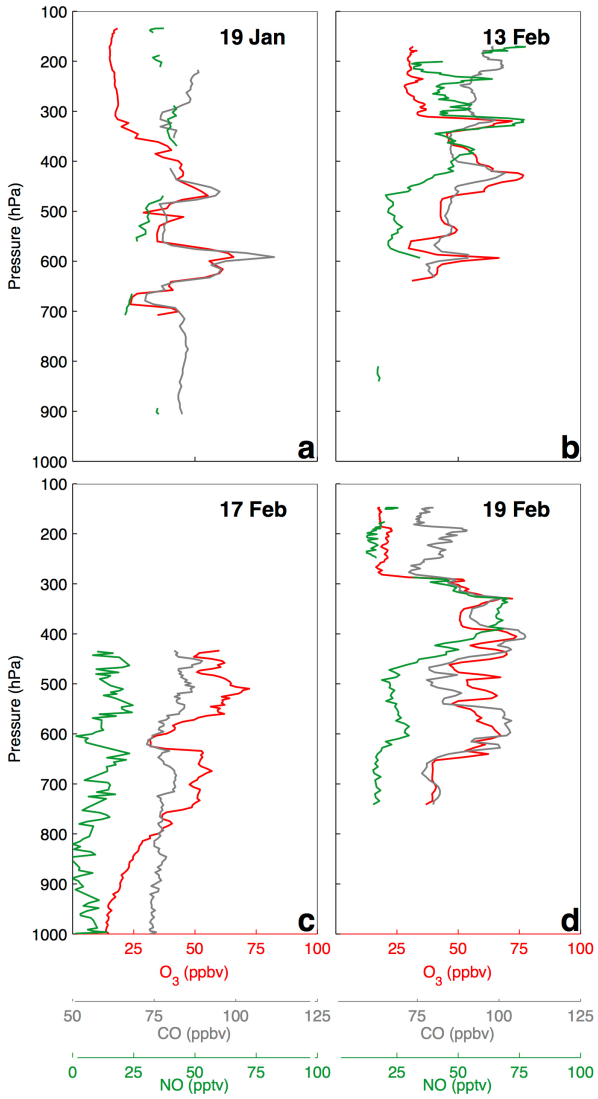

Figure 4.5: Sample profiles from CONTRAST (panels **a**, **b**, and **d**) and CAST (panel **c**) from the four flights shown in Figure 4.1. O_3 (red), CO (grey), and NO (green) are shown. All data are 10 sec averages.

between CO and O_3. Data collected during these two flights are excluded from the majority of the HOLW analysis, since my focus is on the tropical troposphere, but are used below to argue against a stratospheric origin of these structures. Parcels with marine characteristics (low CO, NO, and O_3) all originated from the SH or EP (Figure 4.7). Back trajectory analysis of the two polluted regimes connects the high CO, NO, and O_3 parcels to biomass burning regions in central Africa or Southeast Asia. The high CO/low NO/low O_3 parcels have various geographic origins in Southeast Asia, which

could be reflective of emissions of high CO and low NO_x from two-stroke engines, dominant in this region of the world.

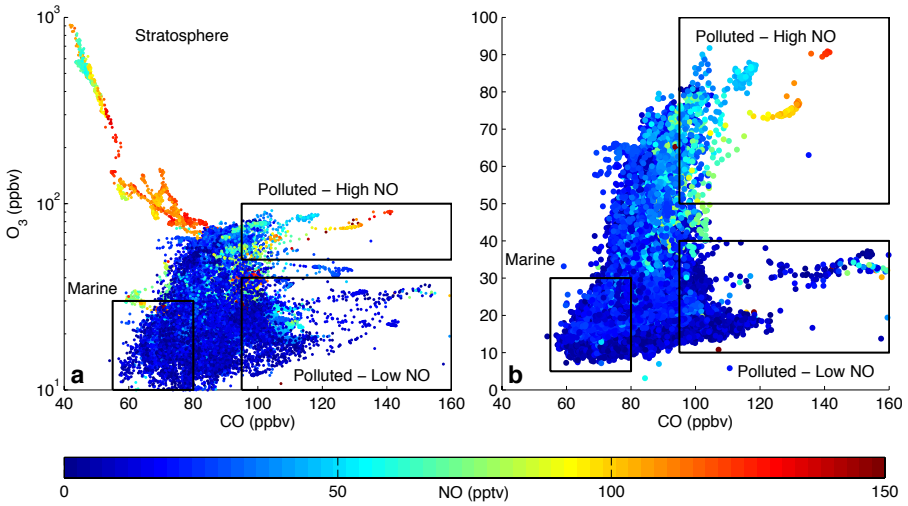

Figure 4.6: 10 sec averaged O_3 regressed against CO observations, colored by NO. (**a**) Data from all CONTRAST and CAST flights. (**b**) Data analyzed in the trajectory analysis. CONTRAST data are for RF03-05 and RF07-14, and CAST data are for the 17 flights that provided observations between 300 and 700 hPa.

Analysis of other chemical tracers suggest that the observed O_3 in the HOLW structures is likely produced photochemically in biomass burning plumes. Both HCN and CH_3CN are emitted almost exclusively by biomass burning [*Holzinger et al.*, 1999]. Elevated mixing ratios of either species in an air parcel therefore suggests a biomass burning origin. Figure 4.8 shows the profiles of these two species as well as O_3 and the industrial tracer tetrachloroethylene (C_2Cl_4) for the same flights as Figure 4.1. Panels (b) – (d) show very tight correlations of O_3 with HCN and CH_3CN, while, in panel (a), HCN and CH_3CN are elevated between 400 and 700 hPa. Over the entire campaign, air parcels with back trajectories that trace back to Africa and Southeast Asia have a high correlation between O_3 and HCN ($r^2 = 0.80$), demonstrating significant biomass burning influence. The enhancement ratio of CH_3CN to CO (4.02 pptv/ppbv) for the HOLW structures is consistent with CH_3CN emissions from tropical forest burning (Figure 4.9) [*Akagi et al.*,

2011] and is significantly higher than the enhancement ratio for CH_3CN emissions from fossil fuel combustion (<0.1 pptv/ppbv) [*de Gouw et al.*, 2003]. The biomass burning tracers benzene (C_6H_6) and ethyne (C_2H_2) also show strong correlation with CO ($r^2 > 0.6$) as seen in Figure 4.10, further confirming the origin of these air parcels.

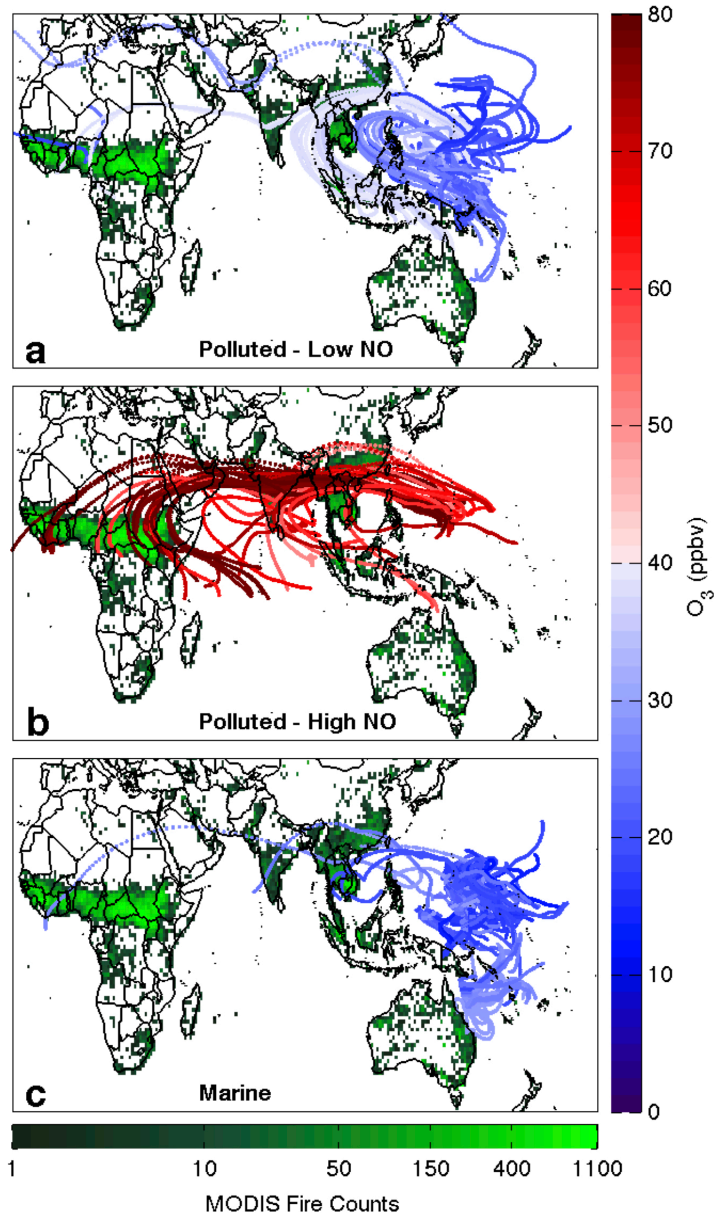

Figure 4.7: Same back trajectories as in Figure 4.3 but separated by the CO regimes illustrated in Figure 4.6. The sum of January and February 2014 MODIS fire counts is shown in green.

4.3.1.2 Photochemical Aging Analysis

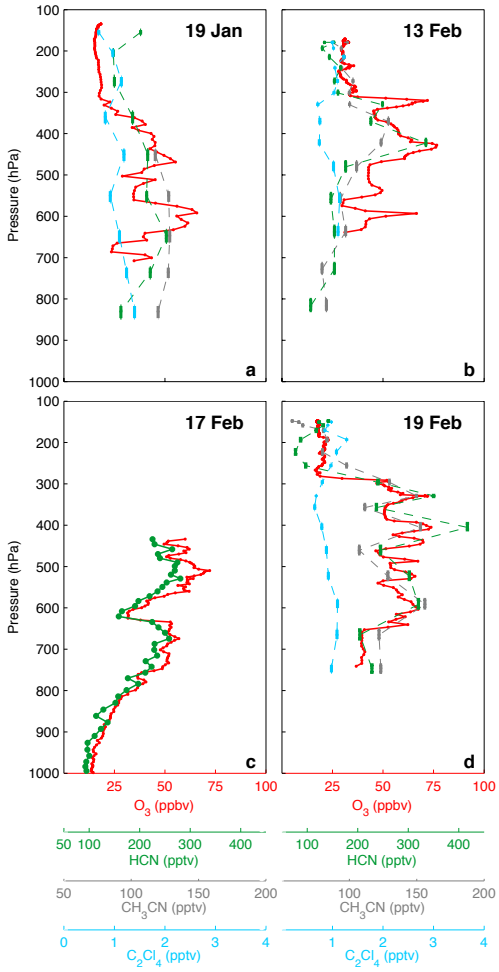

Figure 4.8: Sample profiles from CONTRAST (panels **a**, **b**, and **d**) and CAST (panel **c**) from the four flights shown in Figure 4.1. O_3 (red), CH_3CN (grey), HCN (green), and C_2Cl_4 (light blue) are shown. O_3 data are 10 sec averages. CH_3CN and C_2Cl_4 were not measured during CAST. CONTRAST HCN, CH_3CN, and C_2Cl_4 were sampled for 35 sec at 2 min intervals. Vertical bars show the pressure range traversed during sampling.

Photochemical aging is consistent with the back trajectory analysis. Both C_6H_6 and C_2H_2 have lifetimes much shorter than that of CO [*Mauzerall et al.*, 1998]. Based on modeled OH from CONTRAST, C_6H_6, C_2H_2, and CO in the TWP have lifetimes of approximately 6, 12, and 35 days, respectively. All species are primarily removed by reaction with OH (Reactions (4.1)-(4.5)), so the change in CO with respect to either C_6H_6 or C_2H_2 relative to the initial emissions ratio allows determination of a photochemical age

[*Parrish et al.*, 2007]. Rate constants for reactions (4.3) - (4.4) were taken from IUPAC [*Atkinson et al.*, 2006] and from NASA JPL 2011 [*S P Sander et al.*, 2011b] for reactions (4.1), (4.2), and (4.5).

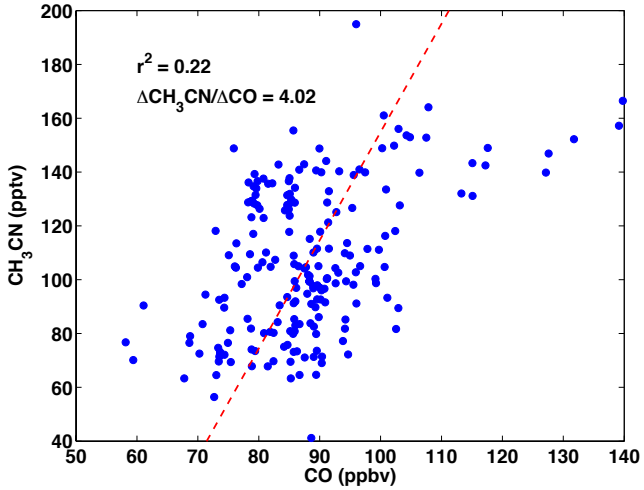

Figure 4.9: Regression of CO against CH_3CN for all observations where O_3 > 40 ppbv and RH < 20%. The dashed red line is the best fit via orthogonal linear regression. The $\Delta CH_3CN/\Delta CO$ enhancement ratio and r^2 values are also shown. The $\Delta CH_3CN/\Delta CO$ ratio is consistent with emissions from burning of a tropical forest.

$$OH + CO \rightarrow CO_2 + H \quad (4.1)$$
$$OH + CO \rightarrow HOCO \quad (4.2)$$
$$OH + C_6H_6 \rightarrow H_2O + C_6H_5 \quad (4.3)$$
$$OH + C_6H_6 \rightarrow HOC_6H_6 \quad (4.4)$$
$$OH + C_2H_2 \rightarrow HOCHCH \quad (4.5)$$

All reactions have first order kinetics, so the ratio of the CO concentration at time t, [CO(t)], to that of benzene, [C_6H_6(t)], is described by Equation (4.2) [*Parrish et al.*, 2007], where k_{CO} is the sum of the rate constants for reactions (4.1) and (4.2), k_{C6H6} is the sum of the rate constants for reactions (4.3) and (4.4), ER(t) is the enhancement ratio of CO to C_6H_6 at time t, and ER_0 is the ratio of [CO] to [C_6H_6] at the time of emission. The expression for C_2H_2 is analogous. If all the other variables are known, the expression can be solved for t, the photochemical age.

$$ER(t) = \frac{[CO(t)]}{[C_6H_6(t)]} = ER_0 e^{-[OH]t(k_{CO} - k_{C_6H_6})} \quad \text{Equation (4.2)}$$

The enhancement ratios of CO to C_6H_6 and CO to C_2H_2 over the entire campaign were determined by using an orthogonal linear regression for parcels where $O_3 > 40$ ppbv and RH < 20% (Figure 4.10). The slope of these lines is the enhancement ratio. This was done over a campaign-wide basis and not for each profile because of the limited sampling frequency of C_6H_6 and C_2H_2. Separate regressions were done for the TOGA and AWAS C_6H_6 measurements. Values of r^2 for all regressions were greater than 0.61. The value of ER_0 for the two relations was assumed to be 724 mol CO/mol C_6H_6 and 241 mol CO/mol C_2H_2, which are characteristic of a tropical forest [*Andreae and Merlet*, 2001]. The photochemical age varied by less than 0.5 days when emissions ratios for other vegetation types were considered. Constant values of temperature (247 K), pressure (350 hPa), and [OH] (1.7×10^6 cm^{-3}) were assumed when calculating the photochemical age. Temperature and pressure values were the average along the back trajectory for the HOLW filaments, and 1.7×10^6 cm^{-3} is the 24-hour mean OH concentration for parcels between 300 and 700 hPa from the box model runs. Equation (4.2) also assumes that any mixing with ambient air dilutes both species equally.

The photochemical age for C_6H_6 with respect to CO as determined by the TOGA and AWAS measurements were 13 and 8 days, respectively. The photochemical age for C_2H_2 was 11 days. These photochemical ages are broadly consistent with the elapsed period of time between detrainment of biomass burning plumes over Africa and Southeast Asia and transit to the TWP indicated by the back trajectory analysis (5 ± 4 and 7 ± 2 for Southeast Asia and Africa, respectively). The difference between the age indicated by back trajectory analysis and that of photochemical aging is likely due to dilution of biomass burning plumes with ambient air. Dilution would tend to artificially

inflate the photochemical age since only CO is present in appreciable amounts in the background TWP. These relatively short values for photochemical age show the composition of air in the HOLW structures is of recent origin, rather than reflective of a hemispheric background.

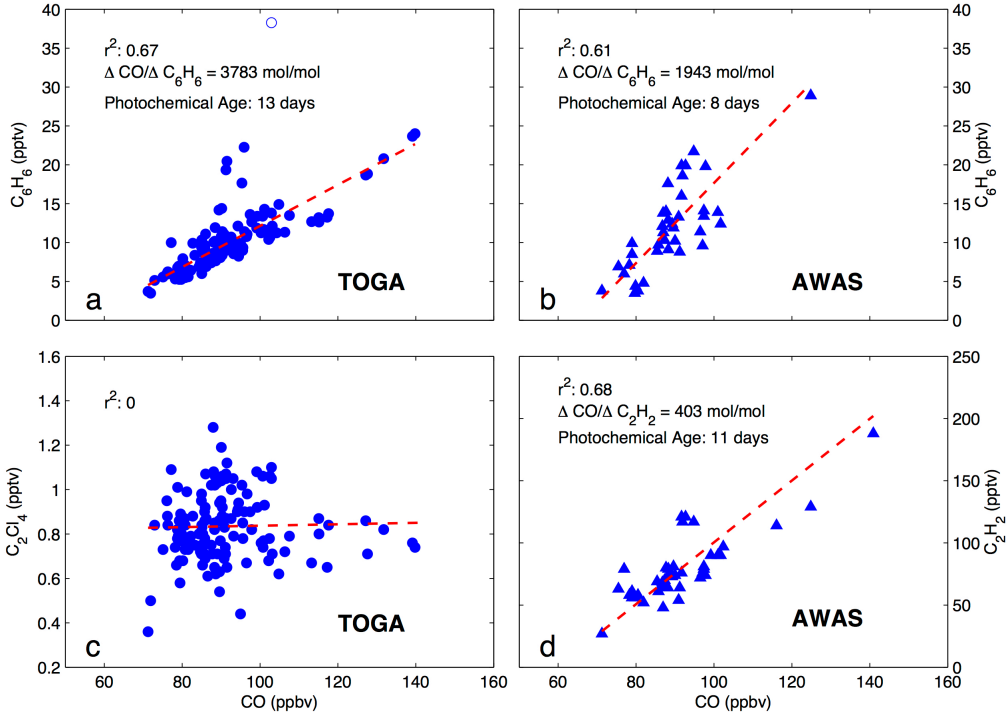

Figure 4.10: Regression of CO against: Total Organic Gas Analyzer (TOGA) C_6H_6 (**a**); Advanced Whole Air Sampler (AWAS) C_6H_6 (**b**); TOGA C_2Cl_4 (**c**); and AWAS C_2H_2 (**d**). Data are only for the HOLW structures (O_3 > 40 ppbv and RH < 20%). The dashed red line is the best fit via orthogonal linear regression. A single data outlier (open circle, panel **a**) has been excluded from the analysis. Values of r^2 are shown for all panels; enhancement ratios and photochemical ages are shown for panels (**a**), (**b**) and (**d**).

4.3.2 Evaluation of CAM-Chem and Photochemical Box Model Output

Tagged tracers for biomass burning CO in the CAM-Chem model [*Lamarque et al.*, 2012], run using assimilated meteorology, support this interpretation. A strong African biomass burning influence is frequently seen in the upper troposphere over much of the TWP and extending as far east as Hawaii, at times accounting for 17% of total CO (Figure 4.11). Deep convection can loft emissions from fires into the upper troposphere, where strong westerlies transport pollutants long distances [*Pickering et al.*, 1996].

Southeast Asian emissions are prominent throughout the tropospheric column (Figure 4.11).

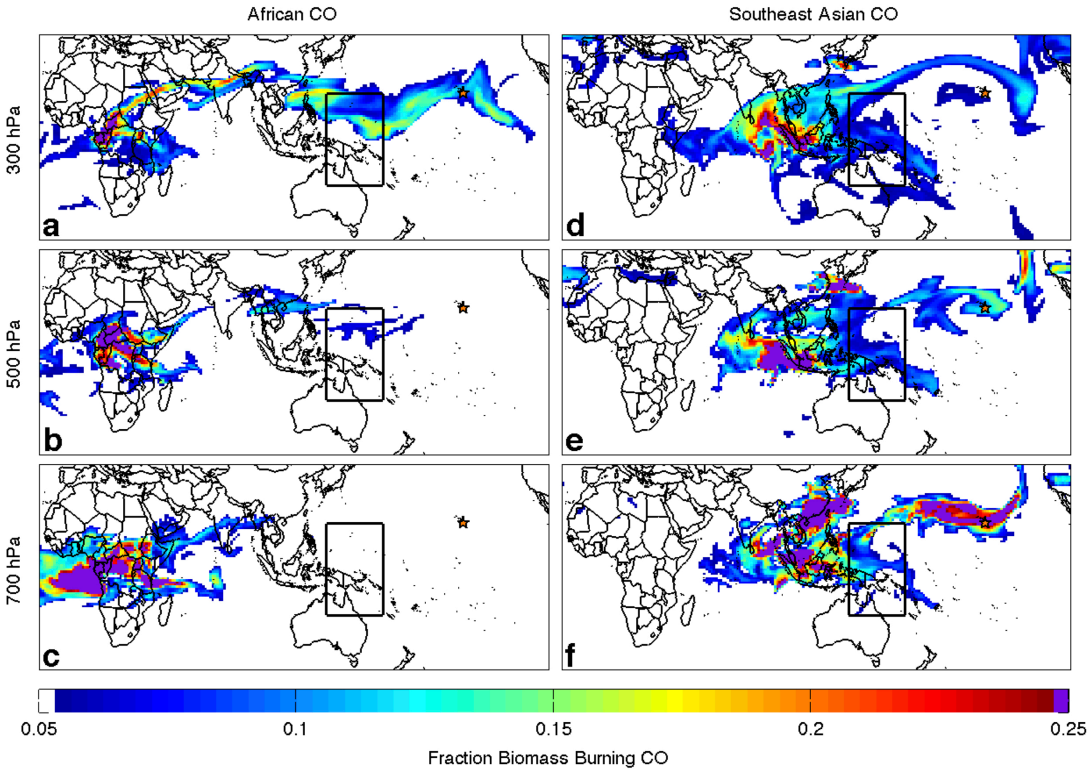

Figure 4.11: Fraction of CO produced from biomass burning on 11 Feb 2014 from Africa (**a-c**) and 25 Feb 2014 from Southeast Asia (**d-f**) at 300 (**a** & **d**), 500 (**b** & **e**), and 700 (**c** & **f**) hPa found using tagged CO in CAM-Chem. The CAST/CONTRAST study region is shown by the rectangle, and Hawaii is shown by the orange star to provide perspective in interpretation of the model results.

Analysis of ozonesonde observations, CAM-Chem O_3, and photochemical box model output quantitatively show the high O_3 likely originates within the tropical troposphere. Regions of tropical biomass burning have elevated O_3 as compared to the rest of the tropics, with an O_3 maximum over Africa and the Atlantic basin and a minimum over the TWP [*Fishman et al.*, 1991; *Sauvage et al.*, 2006; *Thompson et al.*, 1996]. Median O_3 in Central Africa and Southeast Asia from CAM-Chem was ~50 ppbv (Figure 4.12(a)) and ~40 ppbv (Figure 4.13a), respectively, a factor of 2 greater than background O_3 in the TWP. I compare the CAM-Chem output to ozonesonde [*Thompson*

et al., 2012] measurements over Nairobi (Figure 4.12b) and Hanoi (Figure 4.13b), both strongly influenced by biomass burning, to evaluate CAM-Chem model performance. Mean O_3 from the ozonesondes generally lie within 1σ of the mean CAM-Chem value, suggesting the model accurately captures the mean O_3 profile in these locations. Means, instead of medians, are compared because only four or five ozonesonde profiles for each site are available for the study period. Transport of O_3 from these biomass burning regions cannot explain all of the observed O_3 in the HOLW structures, however, as values frequently peaked at ~75 ppbv, implying there must be photochemical production as the air parcels travel from the biomass burning region.

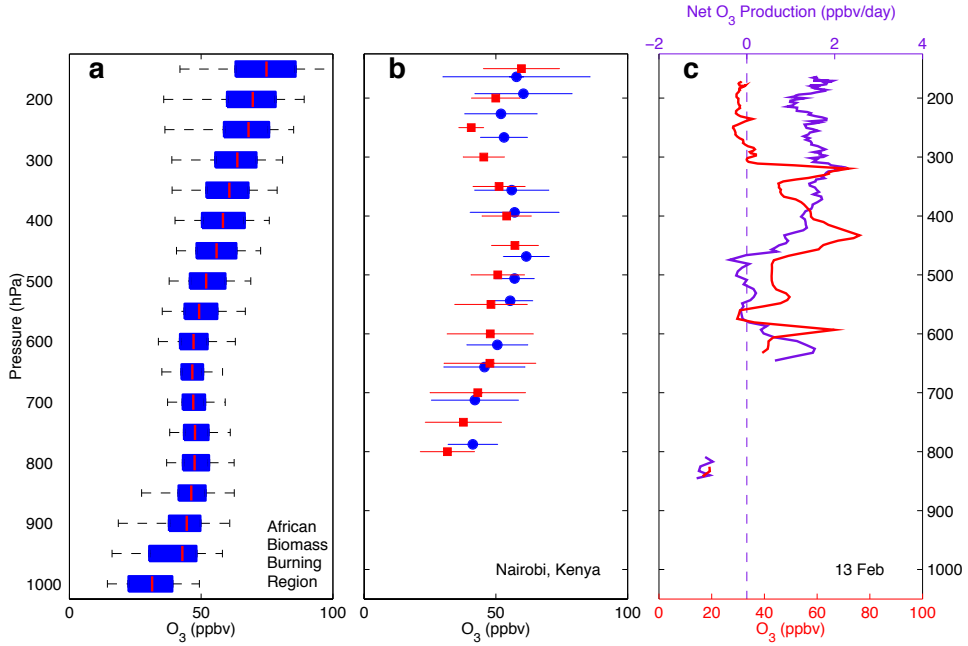

Figure 4.12: (**a**) Vertical distribution of CAM-Chem O_3 in the African biomass burning region (i.e. black box Figure 4.3); 5th, 25th, median, 75th, and 95th percentiles are shown. (**b**) Mean ±1σ of SHADOZ ozonesonde observations over Nairobi, Kenya for January and February 2014 (red). Mean ±1σ CAM-Chem O_3 modeled over Nairobi sampled on the same days as the ozonesondes (blue). (**c**) O_3 profile from Figure 1 (red) and net O_3 production in the profile (purple, top axis), calculated using the DSMACC photochemical box model (see methods).

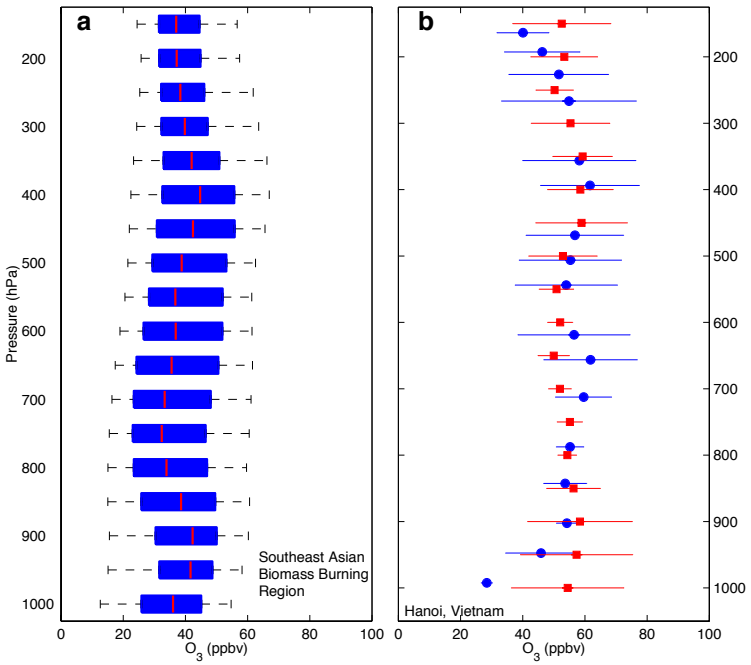

Figure 4.13: Same as Figure 4.12 (**a**) and (**b**) except for the Southeast Asian biomass burning region (a) and ozonesonde observations over Hanoi, Vietnam (**b**).

To estimate the net O_3 production in the HOLW structures, a box model constrained by CONTRAST observations (see methods) was run for the profiles shown in Figure 4.1. Net O_3 production in the HOLW structures was on the order of ~2 ppbv/day (Figure 4.12c & Figure 4.14). The value calculated here is a lower bound to net O_3 production in the plume. It is likely that photochemical production along the flight track is significantly lower than in fresh biomass burning plumes, which would be enriched in both NO_x and VOCs as compared to the more aged air observed in CONTRAST. Production of NO_x by lightning, a significant contributor to upper-tropospheric NO_x [*Staudt et al.*, 2002], would likely further enrich fresh plumes that were lofted into the upper troposphere through deep convection. These fresh plumes can have O_3 production rates of 7 ppbv/day or higher [*Thompson et al.*, 1996]. As the air ages, however, the abundance of HNO_3 in the plume will increase [*Mauzerall et al.*, 1998], making NO_x unavailable for O_3 production. VOCs will also be oxidized to less reactive species by

OH, and dilution with background air will tend to counteract photochemical production of O_3. Nevertheless, a net O_3 production rate of ~2 ppbv/day over 5-10 days, combined with initial O_3 of 40-50 ppbv in the outflow of biomass burning, is consistent with the observed O_3 in the HOLW structures.

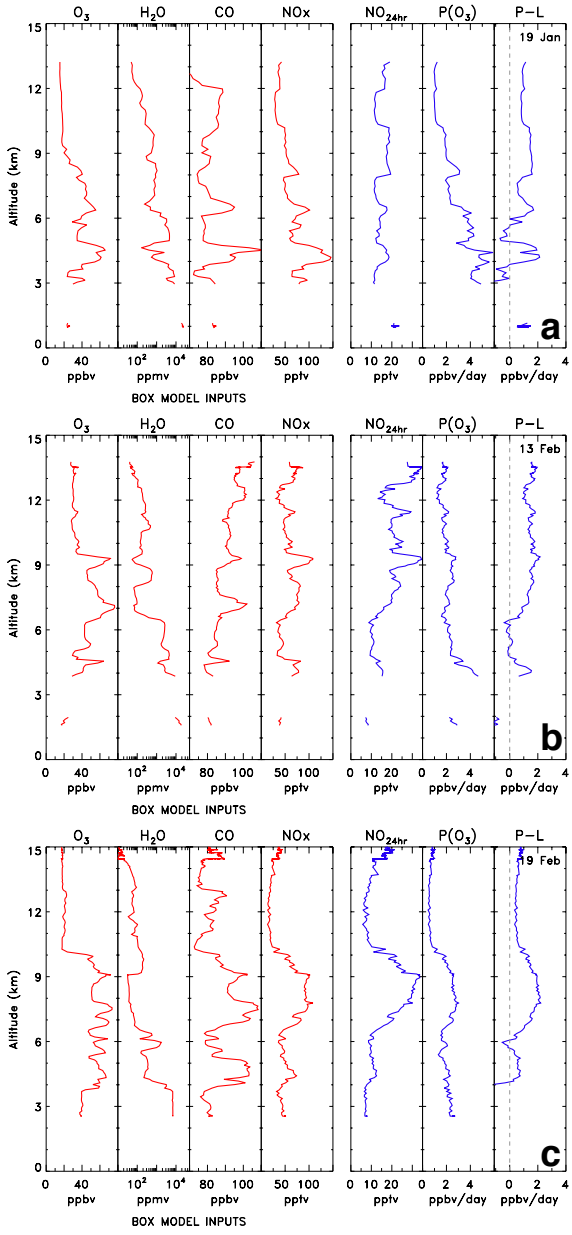

Figure 4.14: Vertical profiles of observed O_3, H_2O, CO, and NO_x (red) from the CONTRAST flights in Figure 4.1 used as input for the DSMACC photochemical box model. Model outputs (blue) are 24-hour averaged NO, gross O_3 production ($P(O_3)=k_1[NO][HO_2]+k_2[NO][CH_3O_2]$), and net O_3 production ($P(O_3)^{Net}=P(O_3)-k_3[O_3][OH]-k_4[O_3][HO_2]-k_5[O^1D][H_2O]$). Panels show data from (**a**) 19 Jan 2014 (**b**) 13 Feb 2014 (**c**) 19 Feb 2014.

4.3.3 Low Water Vapor Origin

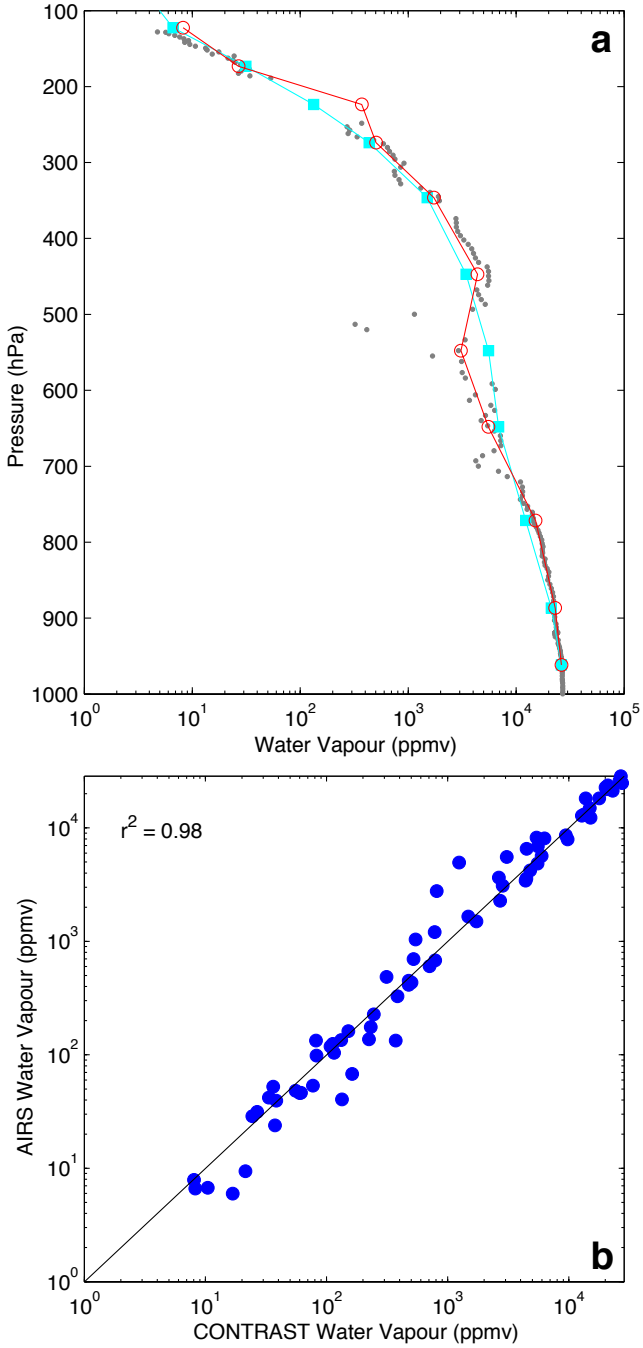

Figure 4.15: (**a**) Vertical profile of H_2O mixing ratio from CONTRAST RF11 conducted at 7.1°N and 143°E on 13 Feb 2014. Grey dots are *in situ* observations, red, open circles are *in situ* observations averaged over the AIRS layers, and cyan, closed squares are AIRS observations. AIRS data have been bilinearly interpolated to the profile coordinates. (**b**) *In situ* H_2O from one profile from every CONTRAST flight, averaged to the AIRS layers, regressed against AIRS H_2O interpolated to the respective profile location.

I now turn to the origin of low H_2O. As with O_3, H_2O observed during CAST and CONTRAST has two distinct modes, suggesting that H_2O in the TWP is controlled both locally and by large-scale processes from outside the study region. For air parcels with HCN < 150 pptv, the H_2O profile follows the saturation vapor pressure (Figure 4.2b, blue boxes), suggesting that the H_2O mixing ratio is controlled by local thermodynamics associated with deep convection. CONTRAST flights designed to measure fresh convective outflow were the only tropical flights where HOLW structures were not observed [*Pan et al.*, 2015]. Parcels with HCN > 150 pptv had H_2O mixing ratios an order of magnitude lower than the local saturation vapor pressure. This is consistent with transport of dry air from outside of the TWP. Potential mechanisms to produce the dry air include horizontal advection from the mid-latitudes as well as large-scale descent in the tropics. The association of low H_2O with high HCN indicates these air parcels originate from biomass burning regions.

AIRS measurements [*Gettelman et al.*, 2004] and trajectory analysis strongly support the supposition that the observed departures from background H_2O result from large-scale descent in the tropics. The ascending and descending branches of the Hadley Cell, as determined by AIRS OLR, are shown in Figure 4.3c as regions with OLR < 250 W/m^2 (blue) and OLR > 250 W/m^2 (red), respectively [*Johanson and Fu*, 2009]. AIRS H_2O averaged over the ascending branch agrees well with *in situ* H_2O in the low HCN air parcels (Figure 4.2b). Regression of *in situ* H_2O observations from CONTRAST to co-located AIRS retrievals of H_2O (Figure 4.15) shows these data sets are in excellent agreement ($r^2 = 0.98$), allowing for direct comparison of the satellite retrieved H_2O to the *in situ* observations. These profiles are characteristic of deep convection, leading to RH >

70%. Back trajectories show the RH < 20% air parcels frequently originate in the ascending branch of the Hadley Cell, flow anti-cyclonically towards the descending branch, and then reach the TWP along the prevailing westerlies (Figure 4.3). Air parcels originating over Africa descend 202 ± 64 hPa, on average, leading to significant decline in RH during transit to the TWP (Figure 4.3b). Figure 4.2c shows the AIRS H_2O profile over Africa (orange lines and squares). The final H_2O profile over the TWP after subsidence (circles), assuming conservation of the H_2O mixing ratio in transit, quantitatively agrees with *in situ* H_2O for the enhanced HCN mode (grey symbols, Figure 4.2b). Similar agreement is found for AIRS H_2O profiles over Southeast Asia (Figure 4.2d). This analysis demonstrates large-scale descent of tropical biomass burning plumes, on their transit to the TWP, can produce the dry element of the HOLW structures.

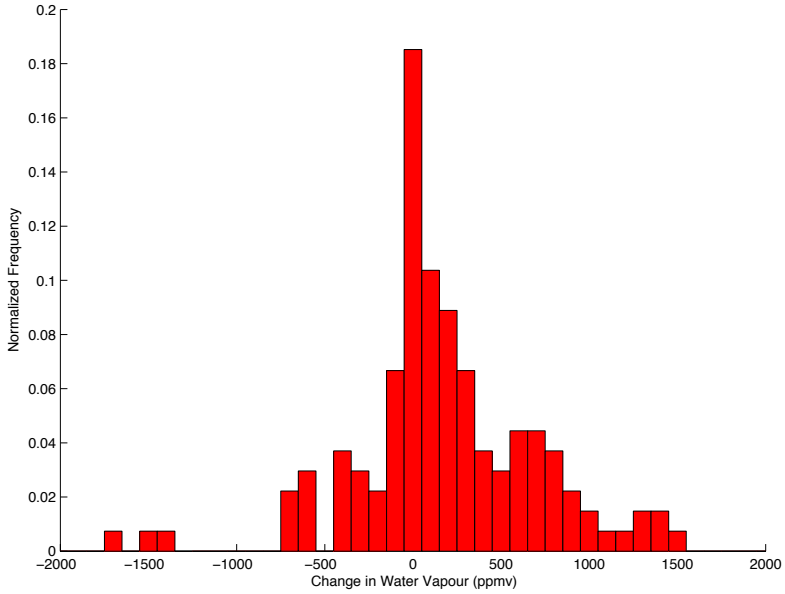

Figure 4.16: Normalized distribution of the change in water vapor mixing ratio along the back trajectories for the HOLW structures. The change in water vapor is defined as the difference between the H_2O mixing ratios at the trajectory starting point (*i.e.* the trajectory initialization point along the flight track) and the trajectory end point (*i.e.* 10 days prior to observation or the point of last precipitating convection). Water vapor was calculated from the RH output by the HYSPLIT model, which is based on GDAS meteorology (see methods). Positive values indicate the water vapor mixing ratio has increased during transit to the TWP.

Drying of the air parcels by mixing with mid-latitude air or transport to higher latitudes is not supported by the back trajectory analysis. To determine whether air parcels were moistened or dried during transit, the difference between the H_2O mixing ratios at the trajectory end point (*i.e.* 10 days before observation or the point of last precipitating convection) and the trajectory starting point (*i.e.* the trajectory initialization point along the flight track) was calculated for all HOLW structures. Water vapor mixing ratios were calculated from the RH and temperature output by the HYSPLIT model along each trajectory. Figure 4.16 shows a histogram of these changes in H_2O. For the majority of air parcels (> 80%), the H_2O mixing ratio either increased or did not change in transit to the TWP. This moistening indicates that the majority of the HOLW structures encountered by the CAST and CONTRAST aircraft did not require additional condensation after detrainment to account for the low RH. In fact, these air parcels moistened (experienced a modest increase in H_2O mixing ratio) in transit, likely due to mixing with background air. The low RH is due to large-scale descent in the tropics and does not require condensation in the mlUT.

4.3.4 Potential Origins Outside the Tropical Troposphere

Mixing with mlUT air is inconsistent with the air mass history and observed composition of the HOLW structures. Parcel trajectories with high O_3 began in the tropics and remained south of the jet core (Figure 4.3a), indicating minimal contact with mid-latitude air. None of the back trajectories connect the HOLW air parcels to the mid-latitudes. This is consistent with the chemical composition of the filaments. Tetrachloroethylene, a tracer of industrial pollution, has an atmospheric lifetime on the order of 4 months and is primarily emitted in the NH mid-latitudes, creating a strong

latitudinal gradient. Air masses in the tropics influenced by mid-latitude emissions from China frequently have C_2Cl_4 mixing ratios greater than 2 pptv versus a tropical background of 1 pptv or less [*Ashfold et al.*, 2015]. Tetrachloroethylene mixing ratios in the HOLW structures are a factor of 1.7 times smaller than that observed in the mid-latitude free troposphere during CONTRAST (0.89 and 1.52 pptv, respectively), suggesting little influence from the mid-latitudes. This is further confirmed by the lack of correlation between C_2Cl_4 and either high O_3 (Figure 4.8) or CO (Figure 4.10c).

Stratospheric origin is also inconsistent with the observed composition of the HOLW structures. Elevated O_3 in the remote TWP can have plausible sources from the polluted troposphere or the O_3 rich stratosphere, resulting in enhancements of a similar magnitude. Mixing line analysis using measurements of at least two other tracers with distinctly different abundances in the troposphere and stratosphere can be used to assess the relative contribution of each potential source [*Pan et al.*, 2007]. Here I use CO and H_2O as tracers of the polluted troposphere and the stratosphere, respectively. The fraction of stratospheric air, f_{STRAT} was calculated from Equation (4.3), where H_2O_{OBS} is the observed H_2O mixing ratio, H_2O_{STRAT} is the stratospheric H_2O mixing ratio, and H_2O_{TROP} is the altitude dependent background tropospheric H_2O mixing ratio.

A constant stratospheric H_2O mixing ratio of 3 ppmv was assumed based on the mean observed H_2O (3.1 ± 0.1 ppmv) from RF15, which probed the lower stratosphere. Background tropospheric H_2O was calculated by filtering 10 sec averaged data for air parcels with RH > 70% and O_3 < 20 ppbv, leading to a profile similar to that shown by the blue bars in Figure 4.2b. These data were then averaged into 1 km altitude bins.

An inferred stratospheric CO mixing ratio, denoted $CO_{STRAT\ INFERRED}$ was calculated based on f_{STRAT} found using Equation (4.3). The relation for $CO_{STRAT\ INFERRED}$ is shown in Equation (4.4), where variables have analogous definitions to those in Equation (4.3). A value for CO_{TROP} of 85 ppbv was used, based on the median mixing ratio of CO for air parcels with RH > 70%. Since CO_{TROP} showed little variation with altitude, a constant value was used.

$$H_2O_{OBS} = f_{STRAT}H_2O_{STRAT} + (1 - f_{STRAT})H_2O_{TROP} \quad \text{Equation (4.3)}$$

$$CO_{STRAT\ INFERRED} = \frac{CO_{Obs} - (1 - f_{STRAT})CO_{TROP}}{f_{STRAT}} \quad \text{Equation (4.4)}$$

The mixing line analysis shows that to reproduce the observed H_2O profile, mixing of stratospheric and background air would require more than 90% stratospheric air for the majority of observed parcels (Figure 4.17b) and, in turn, a stratospheric CO mixing ratio of > 75 ppbv for the vast majority of the air parcels (red bars, Figure 4.17c). Observed stratospheric CO was 47.6 ± 6 ppbv (2σ) (grey bar, Figure 4.17c). Only ~1% of parcels had an inferred stratospheric CO within the observed range of stratospheric CO, demonstrating a negligible role for stratospheric influence on the HOLW structures using mixing line analysis. Stratospheric influence was also estimated by interpolating PV to the calculated back trajectories. Only 4% of observed air parcels encountered stratospheric air, defined as intersecting a PV surface > 2 Potential Vorticity Units (PVU) [*Holton et al.*, 1995] along the trajectory (Figure 4.17a). Relaxing the tropopause definition to 1.5 PVU does not significantly alter this percentage. The combination of low PV air along the trajectories and the mixing line analysis indicates negligible

stratospheric influence on the composition of the TWP mid-troposphere during CAST and CONTRAST.

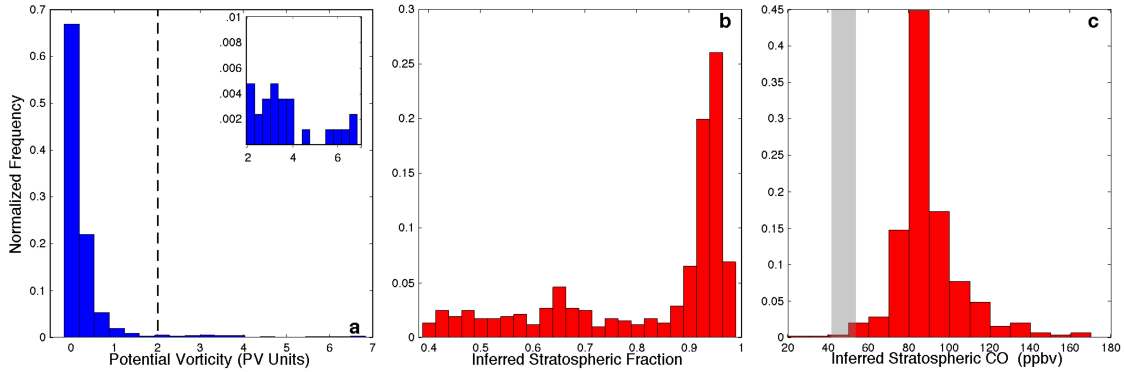

Figure 4.17: (**a**) Distribution of the maximum absolute value of potential vorticity along the back trajectories for all air parcels observed between 300 and 700 hPa that have travelled over the southeast Asian and/or African biomass burning regions. (**b**) Distribution of the inferred stratospheric fraction of air (f_{STRAT}) needed to explain the low H_2O in the HOLW filaments, if the depression in H_2O were solely due to stratospheric intrusion. (**c**) Distribution of inferred stratospheric mixing ratio of CO ($CO_{STRAT\ INFERRED}$) assuming the fraction of stratospheric air shown in (**b**). Grey area represents the mean ±2σ of CO observed in the stratosphere during CONTRAST RF15 (O_3 > 200 ppbv). This mixing line analysis suggests negligible stratospheric influence on the composition of the TWP mid-troposphere during CAST and CONTRAST.

Frequent deep convection in the EP likely prevents stratospheric air from reaching the study region. The westerly duct near 180-200° E, a region of preferential transport from the mlUT to the tropics, could potentially supply stratospheric HOLW air to the study area [*Waugh and Polvani*, 2000]. However, trajectories originating from the SH and EP encountered precipitating convection ~2.2 days prior to observation, *i.e.* these trajectories do not extend back to the westerly duct. Convection promotes mixing with MBL air, removing any extra-tropical signature, as evidenced by the low O_3 mixing ratios for air originating from the EP as discussed above.

4.4 Discussion

I have shown that the high O_3 in the HOLW structures sampled in the TWP during winter 2014 is quantitatively consistent with a tropical, biomass burning source and that the low H_2O mixing ratio is consistent with large-scale descent in the tropics. In

a sense, low RH acts as a tropospheric age of air indicator in the tropics. Photochemical O_3 production driven by emissions from biomass burning regions, in combination with large-scale descent of tropical, tropospheric air parcels that do not experience active precipitation, leads to a strong anti-correlation of H_2O and O_3. Prior analyses of HOLW structures, which suggested an extra-tropical tropospheric origin [*Hayashi et al.*, 2008; *Kley et al.*, 1997; *Newell et al.*, 1999; *Ridder et al.*, 2012; *Stoller et al.*, 1999], lacked the chemical sophistication of CAST and CONTRAST, relying primarily on ozonesondes or a limited number of chemical tracers in their analyses. Dynamical features suggested as possible mechanisms to bring dry air into the tropics – intrusions of high PV [*Waugh*, 2005], Rossby wave breaking [*Yoneyama and Parsons*, 1999], and drying through mixing with the sub-tropical jet [*Cau et al.*, 2007; *Galewsky et al.*, 2005] – are inconsistent with the results presented here. These prior studies tend to focus on the subtropics rather than the tropics, use trajectories calculated without consideration of convective precipitation and at times in isentropic coordinates, or provide an interpretation for H_2O that is qualitative rather than quantitative. Aircraft and satellite data indicate that large-scale descent in the tropics associated with the Hadley circulation exerts primary control on the H_2O composition of the TWP troposphere for air parcels that have not experienced recent convection.

The attribution of the high O_3 in these HOLW structures suggests a potentially larger role for biomass burning in the radiative forcing of climate in the remote TWP than is commonly appreciated. Tropical tropospheric O_3 is a greenhouse gas, exerting a strong radiative forcing on global climate [*Shindell and Faluvegi*, 2009; *Stevenson et al.*, 2013]. However, present efforts to limit emissions of O_3 precursors are primarily focused on

industrial activities and fossil fuel combustion that occur outside the tropics [*Granier et al.*, 2011]. If the high O_3 in these filaments is primarily of tropical origin, then present legislation to limit the emission of O_3 precursors in the extra-tropics may have little, if any, positive impact for the radiative forcing of climate due to tropospheric O_3. While it is beyond the scope of this work to estimate the radiative effects of these HOLW structures, biomass burning [*Giglio et al.*, 2006] and HOLW [*Newell et al.*, 1999] structures are pervasive features of the tropics throughout the year, implying that these structures could have a substantial impact on both global and regional radiative forcing of climate.

Chapter 5 Distribution, Production, and Loss of Formaldehyde in the TWP

5.1 Introduction

Formaldehyde (HCHO) is a pervasive trace gas that provides insight into the dynamical and chemical processes controlling atmospheric composition. Following its photolysis and subsequent photochemistry, HCHO is an important source of the hydroperoxyl radical (HO_2) in both urban [*Volkamer et al.*, 2010] and remote [*Mahajan et al.*, 2010; *Whalley et al.*, 2010] regions. In the upper troposphere, HCHO is a dominant OH precursor [*Jaegle et al.*, 1998a], affecting the atmosphere's oxidative capacity. Knowledge of the distribution of HCHO thus aids in constraining production of HO_x ($HO_x = OH + HO_2$) in chemical models. Because of its relatively short atmospheric lifetime, on the order of 2-3 hours in the tropics, and its vertical concentration profile with surface values almost an order of magnitude larger than those in the upper troposphere, HCHO is also a suitable tracer for recent convection [*Borbon et al.*, 2012; *Fried et al.*, 2008]. To understand the atmospheric HO_x budget, particularly in the TWP where an OH minimum has been hypothesized [*Rex et al.*, 2014], the chemistry and dynamical processes controlling HCHO composition must be thoroughly characterized. A discussion of the chemistry controlling atmospheric HCHO is found in Section 1.3.3.

Formaldehyde observations are limited in the TWP. Satellite retrievals of HCHO in this region, though covering the width of the Pacific basin, are often hampered by small signals and can only provide total column content [*Li et al.*, 2015]. Other remotely sensed observations can provide higher accuracy but are limited spatially and temporally. *Peters et al.* [2012], using a DOAS technique, found total column HCHO to be between 2

and 4×10^{15} molecules cm^{-2} in the western Pacific during Oct. 2009 as part of the TransBrom cruise. These observations provided a diurnal profile of the HCHO column content but were limited to the narrow path of the ship-track and provide no information about variations of HCHO concentration with altitude. *In situ* observations can provide altitudinal profiles but still are limited by the low ambient HCHO concentrations. *Heikes et al.* [2001] measured HCHO with an enzyme-derivatization fluorescence technique with a LOD of 50 pptv during the PEM-Tropics B campaign, conducted in the central Pacific during Mar. to Apr. 1999 at altitudes between the surface and ~12 km. More than 25% of observations were below the LOD, with median values at 8 km on the order of 100 pptv. *Fried et al.* [2003] measured HCHO with TDLAS, with an LOD primarily between 50 and 80 pptv, in the western Pacific as part of the TRACE-P campaign (Feb. to Apr. 2001). Between 8 and 12 km, the aircraft ceiling, median HCHO values were 51 pptv in the western Pacific, but these observations were designed to measure outflow from Asia, not the remote tropics. These HCHO measurements suffered from LODs in the range of typical upper tropospheric HCHO mixing ratios and did not sample the tropical tropopause layer (TTL), the region between approximately 14 and 18.5 km that acts as a transition zone between the tropical troposphere and stratosphere and is the site of significant outflow from deep convection [*Fueglistaler et al.*, 2009].

Understanding the distribution of HCHO and its sources in the tropical upper troposphere and TTL is critical in understanding the HO_x budget, particularly in the absence of OH and HO_2 observations. *Prather and Jacob* [1997] found that convective injection of CH_3OOH, a HCHO precursor, and possibly H_2O_2 drive HO_x concentrations in the tropical upper troposphere and that HO_x production from HCHO is negligible.

They did not, however, have direct observations of HCHO to constrain their model. *Jaegle et al.* [1997], in addition, found that acetone photolysis is also a large HO_x source. Nicely *et al.* [2016] showed that underestimates of HCHO in the CAM-Chem model in the TWP led to underestimates in upper tropospheric OH on the order of ~5%. They also showed that the CTMs in the POLARCAT Model Intercomparison Project (POLMIP) [*Emmons et al.*, 2015] all significantly underestimate observed NO mixing ratios in the TWP, suggesting that the HO_x partitioning in these global models is likely incorrect. Further evaluation of chemicals and processes governing the HO_x budget in the TWP upper troposphere is needed.

Agreement between observations of HCHO and model output varies dramatically among studies that focused on the remote, marine environment. The chemistry and emissions of HCHO and its precursors is still not completely understood. *Fried et al.* [2011] showed that observations of HCHO over the eastern Pacific Ocean from the INTEX-B campaign (Apr. to May 2006) could be reproduced by a photochemical box model from the surface to ~11 km and that methane oxidation was the dominant precursor. In the GABRIEL campaign, conducted off the coast of Guyana and over the Atlantic Ocean during Oct. 2005, *Stickler et al.* [2007] found that Lagrangian and photochemical box modeling overestimated HCHO by a significant amount. They concluded that, to match observations, there must be either significant entrainment of low HCHO air from the free troposphere or higher deposition to the ocean surface than considered in the model. *Jones et al.* [2009] determined that methane chemistry alone is insufficient to produce HCHO comparable to surface observations in a remote New Zealand site as inferred from a high-resolution Fourier Transform Infrared Spectrometer

(FTIR). *Vigouroux et al.* [2009] compared column HCHO measured by FTIR and DOAS instruments at Reunion, a remote island in the Indian Ocean, to output from the IMAGES model, a global CTM, finding that the model underestimated column HCHO by between 15 and 29%. Finally, *Zeng et al.* [2015] showed that four global chemistry models underestimated column HCHO by approximately 50% in the Southern Hemisphere, as compared to FTIR observations , suggesting these models lack a significant HCHO source.

Here, I use *in situ* observations of HCHO collected during the CONTRAST campaign to characterize, for the first time, the HCHO distribution in the TWP from the surface to approximately 15 km, the level of deep convective outflow. Back trajectories and satellite observations are used in conjunction with these observations to determine the relative contributions of HCHO and other species to HO_x production in the tropical upper troposphere. I then use observations of a suite of VOCs and other species from both the CONTRAST and CAST campaigns and a photochemical box model to evaluate our current understanding of HCHO chemistry. These observations are also compared to output from the CAM-Chem CTM to assess the representation of HCHO in a global chemistry model.

5.2 Methodology

For a discussion of the CONTRAST and CAST campaigns, including a description of the HCHO observations used here, see Chapter 3.

5.2.1 Formaldehyde Column Content

Total tropospheric column HCHO was calculated for each profile with observations throughout the troposphere. Tropopause height was defined as the pressure

above which PV remained at an absolute value greater than 2 PVU [*Holton et al.*, 1995]. Surface pressure and PV, available at 6-hour resolution from the NCEP FNL analysis, were bilinearly interpolated in space and linearly interpolated in time to the profile latitude, longitude, and mean sampling time. Formaldehyde measurements, averaged over 10 sec, were binned into 40 pressure bins ranging from the tropopause to the surface. Data between the tropopause and the lowest observed pressure were extrapolated using an exponential fit of observed HCHO at the 5 lowest available pressures. A similar extrapolation was used from the highest observed pressure to the surface. For missing data within the observed pressure range, if data observations were made within 1° of latitude and longitude on that day and in that pressure bin, data were filled in with the mean of those data. Otherwise, data were linearly interpolated. Only profiles where less than 25% of the pressure-binned values were interpolated or extrapolated are included in the analysis.

Values for column HCHO were then calculated from Equation (5.1) [*Salawitch et al.*, 2002]:

$$HCHO\ column\ =\ 2.1335\times10^{16}\int_{p_{TROP}}^{p_s} HCHO\,dp \qquad \text{Equation (5.1)}$$

$$constant = \frac{10^{3}\times10^{-6}\times R}{k\times g} \qquad \text{Equation (5.2)}$$

where HCHO is in ppmv, p_s is the surface pressure, and p_{TROP} is the pressure at the tropopause, both in hPa. The constant before the integral is calculated from Equation (5.2), where R is the gas constant for dry air, k is Boltzmann's constant, and g is the acceleration due to gravity, all in CGS units.

5.2.2 Box Model Setup

Formaldehyde mixing ratios were calculated using the University of Washington Chemical Model (UWCM) version 3 box model [*Wolfe and Thornton*, 2011]. The model was run with a subset of the MCM [*Jenkin et al.*, 2003; *Saunders et al.*, 2003] version 3.3.1 [*Jenkin et al.*, 2015]. Inorganic bromine and chlorine chemistry from the Module Efficiently Calculating the Chemistry of the Atmosphere (MECCA) v 3.0 [*R Sander et al.*, 2011a] as well as the reaction of methane with O^1D [*Atkinson et al.*, 2006] were also included. Observational constraints were averaged over the TOGA sampling interval, and only intervals with simultaneous observations of CO, O_3, CH_4, relative humidity, and HCHO were used. The modeled intervals were further restricted to aircraft sampling between 20°S and 20°N at a solar zenith angle (SZA) less than 60°. Missing data for other species were linearly interpolated in time. The model was constrained with observations from CONTRAST of temperature, pressure, relative humidity, O_3, NO, CO, CH_4, CH_3OH, acetone, acetaldehyde, propanal, butanal, acrolein, isoprene, methanol, propane, ethyne, and benzene. The model was also initialized with observed MVK and MACR and was constrained to estimates of BrO, HOBr, Cl, Br_2, Br, and ethene as described below. The model was run forward in time, with all constrained concentrations and meteorology held constant but photolysis frequencies varying with time of day. The diurnal cycle was repeated for 4 days for each set of observations, which was found sufficient to bring HCHO into steady state. Observations by the TOGA instrument below the detection limit are estimated at 30% of the LOD.

Observations of NO_2, particularly in the upper troposphere, were likely biased high by interference with organic nitrates (see, for example, *Nault et al.* [2015]).

Therefore, I constrain the model to match observed NO and calculate NO_2. I initialized the model with estimated NO_2 found assuming instantaneous steady state with NO using Equation (5.3), where k_{NO+O3} is the reaction constant for the reaction of NO with O_3 [*S P Sander et al.*, 2011b], j_{NO2} is the observed photolysis frequency, and brackets indicate concentration. A regression of observed NO_2, for modeled points not affected by nitrate interference, and estimated NO_2 using the pseudo steady state approach is shown in Figure 5.1. While the correlation between the two values is low ($r^2 = 0.19$), the mean of the absolute value of the difference between the two NO_2 mixing ratios is 13.3 pptv, near the 1σ uncertainty of the NO_2 measurement (~12 pptv), suggesting that the estimate is realistic. Modeled values of NO_2, HCHO, OH, and HO_2 are insensitive to how NO_2 was initialized, varying by less than 0.1% when initializing with twice the NO_2 values estimated found using Equation (5.3).

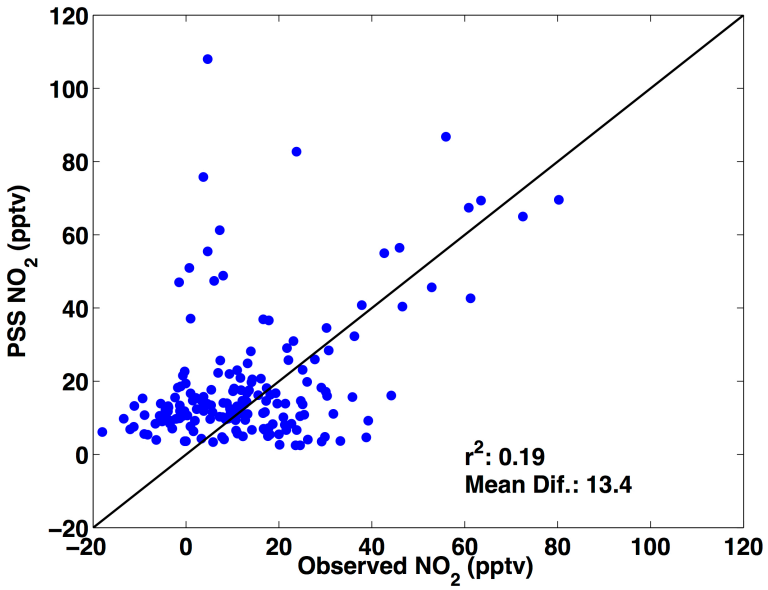

Figure 5.1: Regression of observed NO_2 and NO_2 calculated using the pseudo steady state approximation represented by Equation (5.3). Observed NO_2 values are only those without interference from nitrate species. The black line is the 1:1 line. The r^2 and the mean of the absolute difference between the observed and pseudo steady state NO_2 is also shown.

Ethyne, which was only measured by the AWAS instrument and at a sampling frequency less than that of the TOGA species, was linearly interpolated to the TOGA observation time. For times before and after AWAS observations began as well as for flights without AWAS observations, ethyne mixing ratios were estimated from the median, campaign-wide profile. Ethene mixing ratios were not measured during CONTRAST and are taken from the CAM-Chem model, described in section 3.3.

$$[NO_2] = \frac{k_{NO+O3}[O_3][NO]}{j_{NO_2}} \qquad \text{Equation (5.3)}$$

Photolysis rates are allowed to vary with the diel cycle, and as such, parameterizations are used to calculate the photolysis frequency at SZAs other than that at the observed time. To calculate the photolysis frequency for a given reaction, I use reaction dependent parameterizations provided by the MCM, described by Equation (5.4). Here, χ is SZA and l, m, and n are reaction-specific coefficients. For photolysis reactions including halogen species not included in the MCM, parameterizations, using the MCM formulation, were determined from observed photolysis frequencies. The observed HARP photolysis rates for a given halogen species from all flights in the tropics were binned according to SZA. Median values for each bin were then fit to Equation (5.4) as described in *Jenkin et al.* [1997]. All modeled photolysis rates are then multiplied by a scaling factor determined by calculating the ratio of the HARP and modeled photolysis frequencies at the time of observation. Photolysis rates provided by the HARP instrument include H_2O_2, NO_2, O_3, HONO, HNO_3, HCHO, acetaldehyde, propanal, acetone, glyoxal, MVK, MACR, methyl nitrate, ethyl nitrate, CH_3OOH, BrCl, ClO, $BrNO_3$, Br_2, Cl_2, BrO, $ClNO_3$, and HOBr. Photolysis rates not provided by the

HARP instrument were scaled to observed j_{O1D}. Scaling these values to j_{NO2} alters the mean modeled HCHO by less than 0.1 pptv.

$$J = l(cos\chi)^m \exp(-n * sec\chi) \quad \text{Equation (5.4)}$$

5.2.2.1 Inorganic Bromine

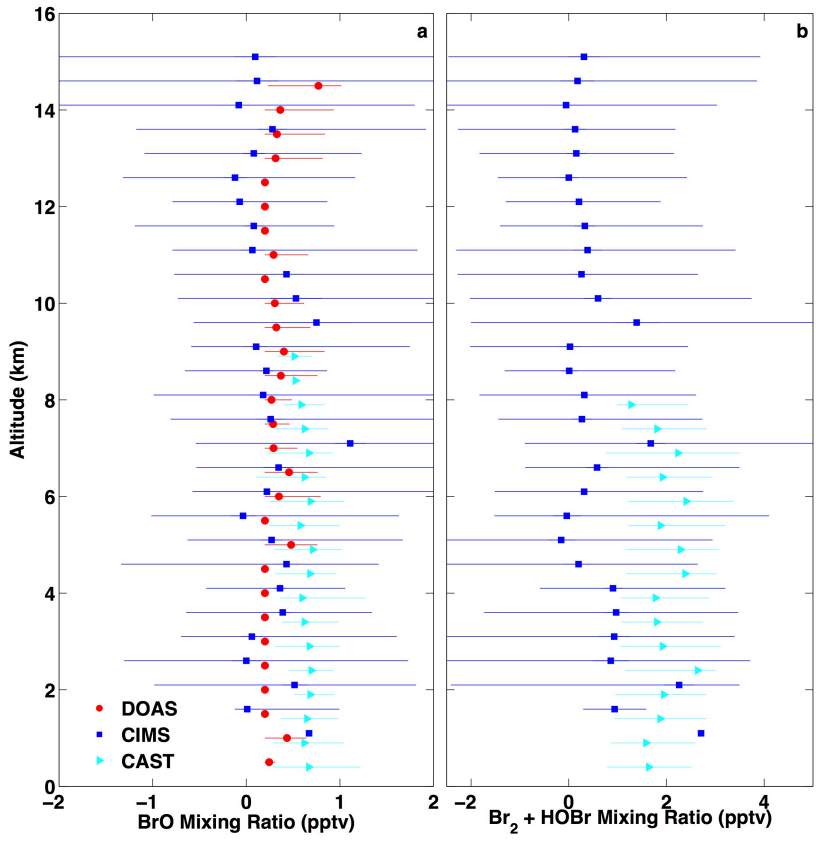

Figure 5.2: 5th, 50th, and 95th percentile of BrO observations (**a**) from the CONTRAST DOAS (red circles), CONTRAST CIMS (blue squares), and CAST CIMS (cyan triangles) instruments. Data are separated into 0.5 km altitude bins and offset for clarity. (**b**) Same as panel (**a**) except for the sum of Br_2 and HOBr observations from the CONTRAST and CAST CIMS instruments. While CAST provided observations of both Br_2 and HOBr, CONTRAST only measured the sum of the two compounds.

Inorganic bromine could potentially impact HCHO mixing ratios, particularly through the reaction of Br with HCHO. During CONTRAST, BrO and the sum of Br_2 and HOBr were the only inorganic bromine compounds measured. These measurements were sparse, frequently below the instrument LOD, and unavailable for the majority of points modeled here. Observations of BrO are also available from the CAST campaign.

In the lower troposphere, sampling in CAST was more frequent than in CONTRAST and data were more often above the LOD. To better constrain the model to BrO and Br, I use a combination of observations from both campaigns. Observations of BrO from the CAST campaign were separated into 0.5 km altitude bins. Median BrO values in CAST were, in general, higher than those observed in CONTRAST, but within the observed data range (Figure 5.2a). For a modeled data point, a mixing ratio of BrO was then assigned from the binned CAST data corresponding to the observation altitude. The model was then constrained to this value. Above the CAST flight ceiling, BrO observations from the CONTRAST AMAX-DOAS instrument were binned and assigned to the corresponding data points in the same manner. AMAX-DOAS observations were not used throughout the entire tropospheric column because lower tropospheric values are available for only one flight.

$$Br + O_3 \rightarrow BrO + O_2 \quad (5.1)$$
$$Br + CH_3CHO \rightarrow HBr + CH_3CO \quad (5.2)$$
$$BrO + h\upsilon \rightarrow Br + O \quad (5.3)$$
$$Br + HCHO \rightarrow HBr + HCO \quad (5.4)$$

To calculate Br, I assume Br is in steady state and primarily controlled by the photolysis of BrO and the reactions of Br with O_3, HCHO, and CH_3CHO, as shown in (5.1) – (5.4). Using these reactions, mixing ratios of Br were estimated using Equation (5.5), where brackets indicate concentration, k_i is the reaction constant of Br with the indicated species, and j_{BrO} is the photolysis frequency of BrO. Observations of temperature and j_{BrO} and the estimated BrO described above were used. Reaction constants for (5.4) and (5.1) were from *S P Sander et al.* [2011b] and from *Atkinson et al.* [2006] for (5.2). The box model was then constrained to this steady-state Br value.

I also constrain the model to HOBr and Br_2 from CAST. Unlike in CONTRAST, CAST made separate observations of both species. In Figure 5.2b, I compare the sum of HOBr and Br_2 from CONTRAST and CAST. As with BrO, the sum of these two species is slightly higher in CAST than during CONTRAST but within the observed range of observations. Below the CAST flight ceiling, concentrations for a given modeled point are estimated using the same method as with BrO. Above the flight ceiling, it is assumed that the mixing ratios of Br_2 and HOBr are constant and are held at the value in the highest altitude bin with observations. Modeled HCHO was rather insensitive to the constrained values for Br_2 and HOBr and varied by ~1% when the model was not constrained to both species.

$$[Br] = \frac{j_{BrO}[BrO]}{k_{O_3}[O_3] + k_{HCHO}[HCHO] + k_{CH_3CHO}[CH_3CHO]} \qquad \text{Equation (5.5)}$$

5.2.2.2 Inorganic Chlorine

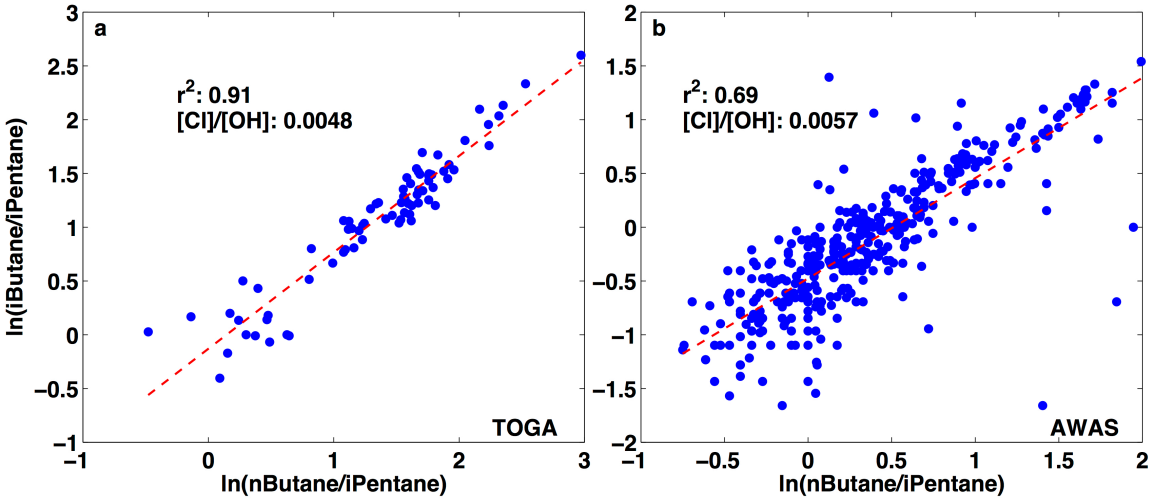

Figure 5.3: Regression of the log of the ratio of n-butane to i-pentane and i-butane to i-pentane for observations from the Total Organic Gas Analyzer (TOGA) (**a**) and Advanced Whole Air Sampler (AWAS) (**b**). The line of best fit, determined through a linear least squares regression, is shown in red. The r^2 value and the ratio of [Cl] to [OH] determined by Equation (5.7) are also shown. Data are selected using the same criteria as that for determining the points modeled with UWCM.

Since reaction with Cl is a sink for HCHO, this analysis requires an estimate of the profile of the mixing ratio of Cl. The Cl mixing ratio was estimated from ratios of various alkanes and benzene, as described in *Rudolph et al.* [1997] and *Arsene et al.* [2007]. Briefly, the ratio of different VOCs can be described by the linear relationship in Equation (5.6), where X, Y, and Z represent concentrations of alkanes or benzene. If species are exclusively removed by OH and Cl, the slope, m, can be defined with Equation (5.7), where r is the ratio of [Cl] to [OH]. Equation (5.7) can be rearranged to yield [Cl]. I have examined ratios, in all possible combinations, of propane, n-butane, i-butane, n-pentane, i-pentane, and benzene from the TOGA instrument against one another to derive the observed slope and estimate the [Cl] to [OH] ratio. Rate constants were taken from *Atkinson et al.* [2006], *Atkinson and Arey* [2003], *S P Sander et al.* [2011b], *Arsene et al.* [2007], and *Hooshiyar and Niki* [1995]. Only points meeting the UWCM modeling criteria described above were used. A similar analysis was performed with the AWAS data for the same species as well as ethane, which was not measured by TOGA. Representative regressions are shown in Figure 5.3. The average ratio, based on all regressions with an r^2 greater than 0.5 and a positive [Cl] to [OH] ratio, was 0.0073 ± 0.0045 and 0.0078 ± 0.0021 (1σ) for AWAS and TOGA, respectively. Overall, this leads to a [Cl] to [OH] ratio of 0.0074 ± 0.0038. Hydroxyl concentration was estimated for each data point by a box model run in which HCHO was constrained and chlorine chemistry was omitted. Chlorine concentration for each point was then estimated by multiplying the mean [Cl] to [OH] ratio by the modeled [OH]. When the HCHO constrained model run was repeated using estimated [Cl], [OH] varied by less than 0.1%. The profile of [Cl] found in this manner was evaluated through comparison of modeled

[HCl] with that observed in the CAST campaign (Figure 5.4). When using the mean [Cl] to [OH] ratio (0.0074) derived from observations, the model significantly overestimated HCl, particularly near the surface. At 1σ below this value (0.0036), observed and modeled HCl distributions overlap. As a result, I use this lower bound for modeling.

$$ln\left(\frac{[X]}{[Y]}\right) = m \times ln\left(\frac{[Z]}{[Y]}\right) + b \qquad \text{Equation (5.6)}$$

$$m = \left(\frac{(k_{OH})_Y + r(k_{Cl})_Y - (k_{OH})_X - r(k_{Cl})_X}{(k_{OH})_Y + r(k_{Cl})_Y - (k_{OH})_Z - r(k_{Cl})_Z}\right) \qquad \text{Equation (5.7)}$$

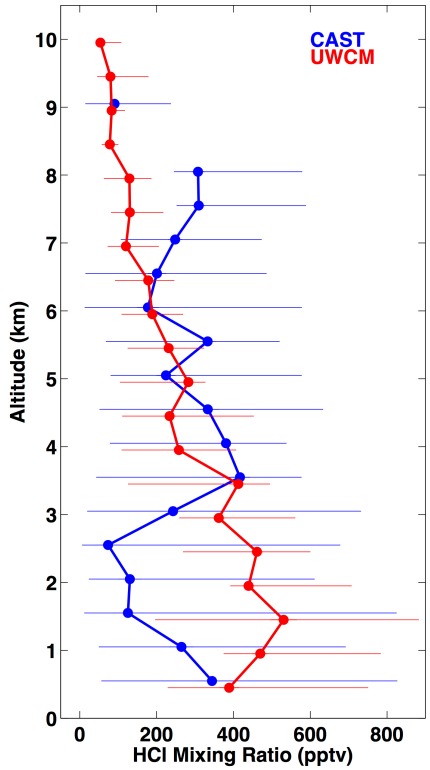

Figure 5.4: Median observed HCl from the CAST campaign (blue) and modeled HCl from UWCM (red). Data are separated into 0.5 km altitude bins and are offset for clarity. Error bars represent the 5th and 95th percentile.

5.2.3 Satellite Data

Flash data from the lightning imaging sensor (LIS) onboard the TRMM satellite [*Cecil et al.*, 2014] were used to estimate the effect of lightning on NO_x mixing ratios. Latitude and longitude for each lightning flash along the satellite track were downloaded

from https://ghrc.nsstc.nasa.gov/hydro/. Data from each flight day and preceding day were sorted into a 0.5° × 0.5° horizontal grid and summed over the entire campaign.

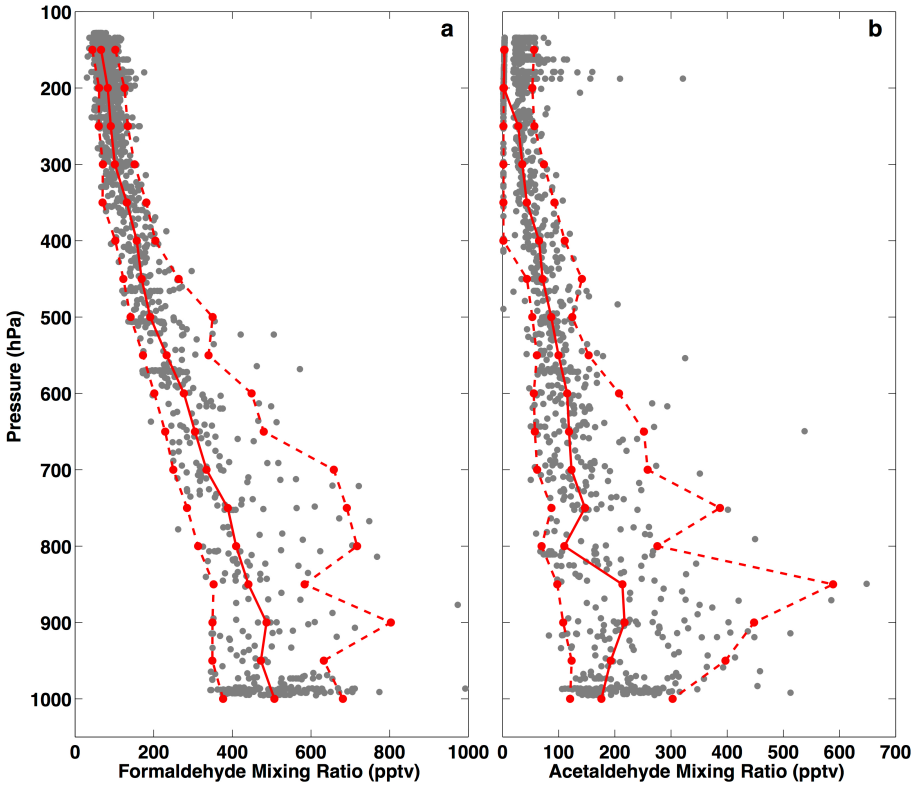

Figure 5.5: Measured (**a**) formaldehyde (HCHO) and (**b**) acetaldehyde (CH_3CHO) averaged over the TOGA observation time period (grey). 5^{th}, 50^{th}, 95^{th} percentiles for 50 hPa pressure bins are shown in red.

Total column HCHO from the Ozone Monitoring Instrument (OMI) onboard the Aura satellite was also analyzed. Aura has an overpass time of approximately 13:40 local solar time. Here, I use the Version 3, Level 2 reference sector corrected swath product [*Abad et al.*, 2015] available at mirador.gsfc.gov. Data were sorted onto a 0.25° × 0.25° horizontal grid, selected for a cloud fraction of less than 30%, and averaged over the grid cell. Only data with quality and X track quality flags of 0 were included, limiting any influence from the row anomaly. Data were then averaged to produce monthly fields. For comparison between the *in situ* derived and satellite columns, *in situ* observations were binned onto the pressure grid used for the OMI retrieval. The binned *in situ* data

were then convolved with a pressure dependent averaging kernel calculated by dividing the OMI scattering weights by the air mass factor averaged over the four nearest grid boxes to the location of the profile on the day of observation. The *in situ* derived column was then compared to the column abundance of HCHO from OMI, found by averaging OMI HCHO from the four grid boxes closes to the location of the *in* situ profile.

5.3 Results and Discussion

5.3.1 Formaldehyde Distribution

The vertical profile of all HCHO observations made in the TWP is shown in Figure 5.5. Near-surface values (observations between the surface and 975 hPa) had a median mixing ratio of 506 pptv, with maximum and minimum values of 992 and 344 pptv respectively. Formaldehyde was highest near Papua New Guinea, where isoprene and direct emission of HCHO from biomass burning likely increase HCHO as compared to the TWP background. Formaldehyde mixing ratios decay exponentially with height, reaching a median value of 74 pptv in the upper troposphere at pressures less than 300 hPa. CONTRAST HCHO measurements between 8 and 12 km were almost a factor of two higher than that observed during TRACE-P, with medians of 97 and 51 pptv, respectively. Local, upper-tropospheric HCHO maxima, with values exceeding 140 pptv, were found north of Guam and near Papua New Guinea (Figure 5.6a). The maximum north of Guam was observed during a flight designed to measure fresh, convective outflow, suggesting that convective transport of near-surface air, rich in HCHO, is a likely cause for these high upper tropospheric values. Convective effects on the HCHO distribution are explored more fully in the next section.

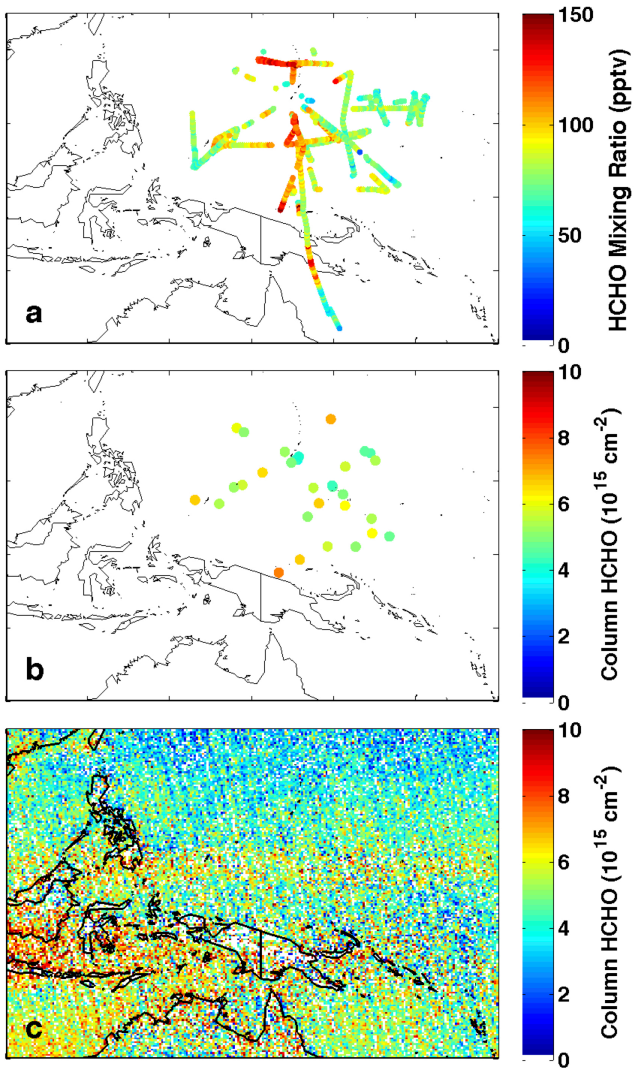

Figure 5.6: (**a**) Observed HCHO at pressures less than 300 hPa. Data are averaged over the TOGA observation time. (**b**) Tropospheric column HCHO calculated from *in situ* observations (see methods). (**c**) Total column HCHO from OMI. Data are filtered for pixels with cloud cover less than 30%, gridded to a 0.25° × 0.25° horizontal grid, and averaged over January and February 2014.

The tropospheric formaldehyde column ranged from 4.1 to 7.5 × 10^{15} molecules cm^{-2}, with a mean value of 5.6 ± 0.86 × 10^{15} molecules cm^{-2} (1σ). Corresponding with the local maxima in upper tropospheric HCHO, the highest columns were found off the coast of Papua New Guinea and north of Guam (Figure 5.6b). Three complete HCHO columns were obtained during RF06, in which the aircraft sampled air masses on either side of a frontal system to the west of Guam. Air behind the front had consistently higher

mixing ratios of anthropogenic pollutants, while air ahead of the front was more representative of pristine, marine air. Despite this difference in composition, there was only a 6% increase in column HCHO content behind the front (5.5×10^{15} molecules cm^{-2}) compared to ahead of the front (5.2×10^{15} molecules cm^{-2}). This difference is well within the variability of the observed columns, suggesting that photochemical HCHO production in aged, anthropogenic air masses is not sufficient to significantly perturb the tropical background tropospheric HCHO column significantly.

Comparisons between the *in situ* derived tropospheric columns and OMI total column HCHO show reasonable agreement. A regression of HCHO columns derived from *in situ* observations and convolved with the OMI averaging kernel and OMI HCHO is shown in Figure 5.7. Correlation between the two HCHO products is poor ($r^2 = 0.02$). Because columns in the TWP are near or below the OMI detection limit, $\sim 6 \times 10^{15}$ molecules cm^{-2}, the lack of correlation is unsurprising. On a campaign-wide basis, the OMI mean ($5.2 \pm 4.8 \times 10^{15}$ molecules cm^{-2}) is 3% smaller than the *in-situ* derived mean ($5.4 \pm 0.74 \times 10^{15}$ molecules cm^{-2}), well within the variability of the *in situ* observations. While the *in situ* observations in the tropics only span the troposphere, contribution to total column HCHO from the stratosphere is likely minimal and does not affect the comparison between the two methods. Mean HCHO mixing ratios in the mid-latitude stratosphere observed during CONTRAST, defined here as O_3 greater than 200 ppbv, were 80.6 ± 9.95 pptv. Assuming this value is constant to the top of the stratosphere as an upward bound, stratospheric HCHO could contribute an additional 0.2×10^{15} molecules cm^{-2}, or ~3% of the tropospheric column. This is well within observational variability.

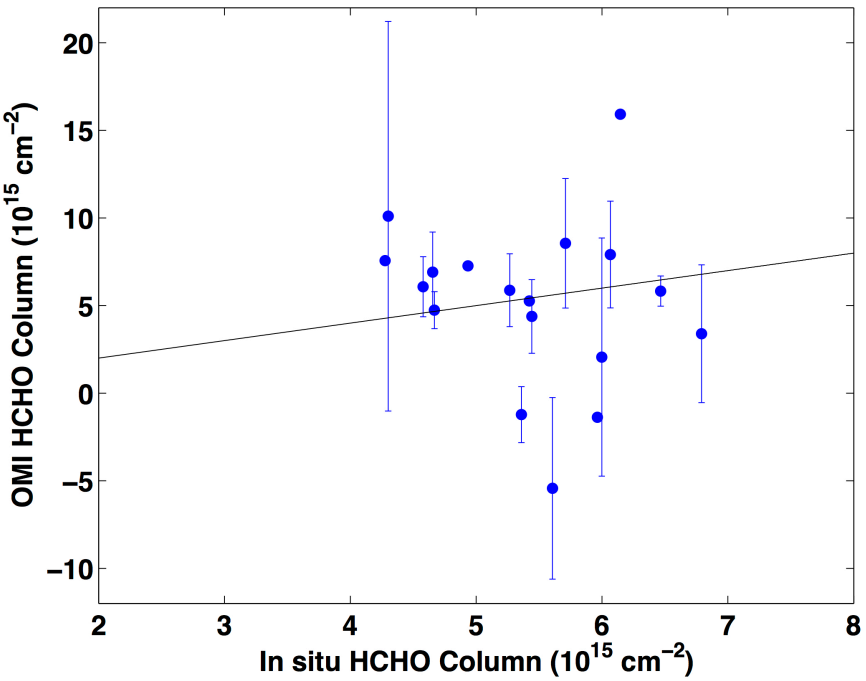

Figure 5.7: Regression of tropospheric HCHO columns derived from *in situ* observations and convolved with the OMI averaging kernel (see methods) and OMI total column HCHO. OMI data are from the same day as the observed profile and the average over the four nearest grid boxes. Grid boxes are omitted from averaging if they are missing data or have observations of column HCHO below the 5th percentile for all retrievals in the TWP. Uncertainties are the standard deviation of the averaged grid boxes. The black line is the one to one line.

OMI HCHO, averaged over January and February 2014, is shown in Figure 5.6c. The average column content for latitudes between 5 and 20°N and longitudes from 130 to 160 °E, roughly corresponding to the CONTRAST study region, for this time period was -5.33 ± 33.9 × 10^{15} molecules cm^{-2} when including all grid boxes, where the uncertainty is 1σ. I exclude those columns at latitudes less than 5° N because they are potentially influenced by direct HCHO emissions from Papua New Guinea and enhanced *in situ* production from isoprene degradation and are not representative of the TWP. The negative average is driven by a small number of grid boxes with values on the order of -1 × 10^{18}. Selecting only for values above the 5th percentile to exclude these anomalous values, the mean increases to 1.06 ± 12.7 × 10^{15} molecules cm^{-2}. The satellite observations show a far greater variability than the *in situ* derived columns. Further,

given that the *in situ* columns showed little spatial or temporal variability, it is likely that OMI is underestimating HCHO columns over the TWP.

5.3.2 Convection, Aldehydes, and Upper Tropospheric HO_x

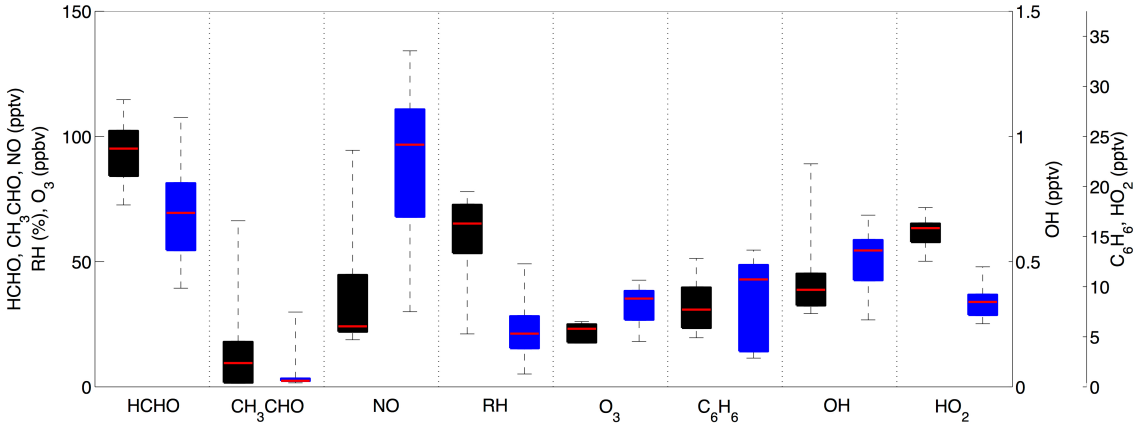

Figure 5.8: Distribution of trace gases for air parcels exposed to convection within 24 hours of observation (black) and greater than 100 hours before observation (blue). 5th, 25th, 50th, 75th, and 95th percentiles are shown for observations between 100 and 300 hPa. OH and HO_2 are output from the UWCM box model from a run in which, in addition to the parameters used in the base case, the model was also constrained to HCHO observations.

Upper tropospheric composition varies significantly between recently convected air parcels and aged parcels, defined here as air that has not been convectively lofted within 100 hours (Figure 5.8). This definition of aged air is consistent with the average time needed to advect air from Southeast Asia (5 ± 4 days) and allows for the dissipation of any convective effects. The results are insensitive to the time used to defined aged air, when the time is changed by ±20 hours. In the TWP, this convectively influenced air has characteristics of local, tropical air (*e.g.* low O_3, low NO) [*Kley et al.*, 1997; *Pan et al.*, 2015; *Rhoads et al.*, 1997], while the aged air has higher concentrations of anthropogenic pollutants and has been traced back to regions of high biomass burning, particularly in Central Africa, Southeast Asia, and Indonesia [*Anderson et al.*, 2016]. Differences in composition allow for the determination of both the effects of convection and long-range transport of anthropogenic pollutants on upper tropospheric composition.

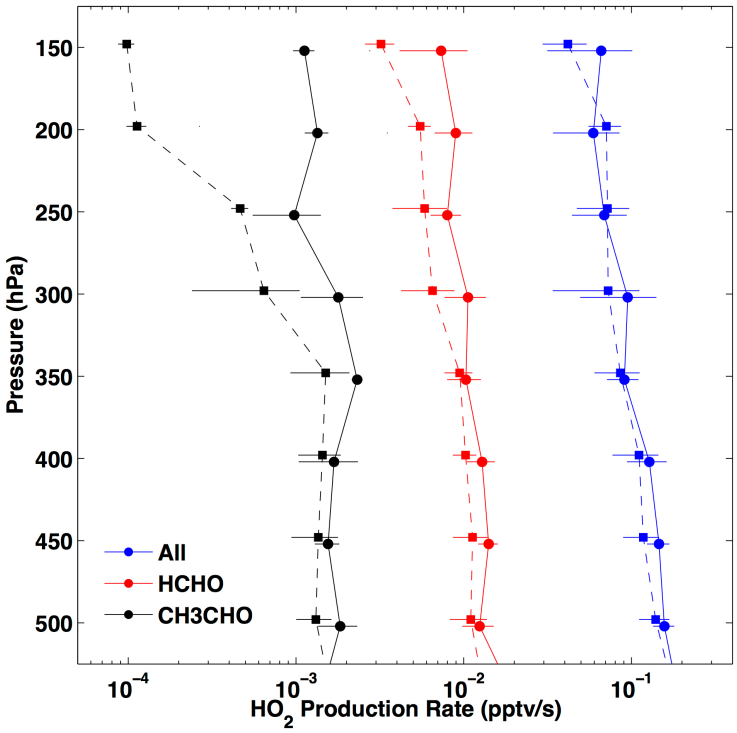

Figure 5.9: HO_2 production for background (dashed) and convectively influenced (solid) air from all species (blue) and from formaldehyde (red) and acetaldehyde (black) photolysis as output by the UWCM model.

Convective lofting of near surface aldehydes substantially alters upper tropospheric composition. Air parcels that had experienced precipitating convection within the previous 24 hours had a mean HCHO mixing ratio of 93 ± 21.6 (1σ) pptv as compared to 70 ± 21.1 pptv for the aged air parcels. Recent convection increased upper tropospheric mixing ratios by approximately 33%. There is no statistical difference between observations made 2 and 24 hours after convection, with mean HCHO mixing ratios of 94.4 and 93 pptv, respectively. Because of the short atmospheric lifetime of HCHO in the upper troposphere, on the order of hours, these observations indicate that convection promotes additional photochemical production of HCHO in the upper troposphere through the transport of precursors. Convection increases upper tropospheric acetaldehyde, a short-lived species with a vertical profile similar to that of HCHO (Figure 5.5b), by a factor of 4 (Figure 5.8). *In situ* acetaldehyde production in the TWP is

minimal; in the absence of deep convection, the upper tropospheric mixing ratio was frequently below the LOD. The acetaldehyde lifetime is on the order of 1 day, so long-range transport of direct emissions from fires or biogenic sources is highly unlikely.

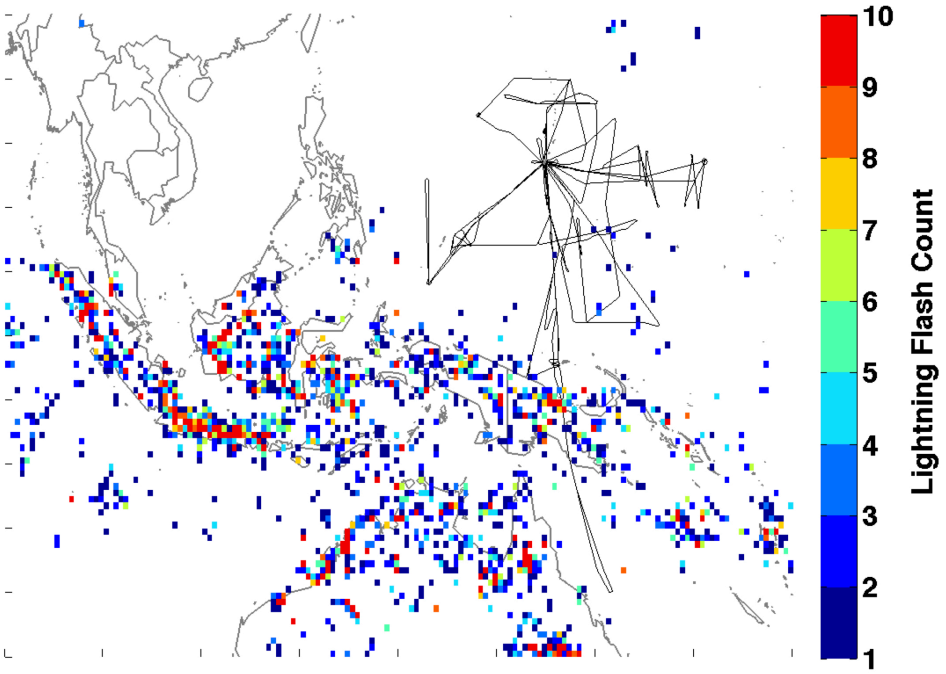

Figure 5.10: Sum of lightning flash counts for Jan. and Feb. 2014 from the Tropical Rainfall Monitoring Mission (TRMM) satellite. The CONTRAST flight tracks for all flights analyzed in this study are shown in black. Data from the satellite swaths have been gridded to a 0.5° latitude × 0.5° longitude grid.

Both formaldehyde and acetaldehyde are HO_x precursors, suggesting that increased upper tropospheric mixing ratios promoted by convection could lead to increased HO_2 production. The HO_2 production rate from photolysis of HCHO (red) and acetaldehyde (black) as calculated by a UWCM run in which the model is constrained to HCHO observations is shown in Figure 5.9. In the lower troposphere, there is no significant difference in HO_2 production between the convectively influenced and aged air parcels. At pressures less than 250 hPa, HO_2 production from formaldehyde and acetaldehyde is a factor of two and an order of magnitude larger, respectively, in the freshly convected air than in the aged air. Total HO_2 production from all sources is also shown in Figure 5.9

(blue) but does not show a significant difference between the convective and aged cases. Although convection significantly enhances the HO_2 production rate from acetaldehyde as compared to the aged case, the HO_2 production rate from acetaldehyde at 150 hPa is only 1.7% and 0.23% of the total HO_2 production rate for the convective and aged cases respectively. Production of HO_2 from acetaldehyde photolysis is unimportant in the upper troposphere for either case. For HO_2 production from HCHO, however, the contribution to total HO_2 production increases from 7.5% to 11% from the aged to the convective case. Previous research in the TWP suggests that convective transport of CH_3OOH [*Prather and Jacob*, 1997] and H_2O_2 [*Jaegle et al.*, 1997] from the MBL were the dominant factors in controlling tropical, upper tropospheric HO_x and that contributions from HCHO were insignificant. Production of HO_2 from HCHO photolysis is important during the CONTRAST campaign, although, as discussed below, a large fraction of the upper tropospheric HCHO results from CH_3OOH oxidation.

$$HO_2 + NO \rightarrow NO_2 + OH \quad (5.5)$$

The anthropogenic influence on the aged air alters the partitioning of HO_x compared to convectively influenced air parcels, driving HO_x from HO_2 to OH via reaction with NO. Mixing ratios of HO_2 and OH are calculated from a UWCM run in which the model was constrained to HCHO observations. Calculated HO_2 is a factor of 2 higher in the convectively influenced air than in the aged air (Figure 5.8). Conversely, OH and NO are 1.4 and 4.0 times higher in the aged air than the tropically controlled parcels, respectively. OH is produced through photolysis of O_3 and the subsequent reaction of the $O(^1D)$ radical with H_2O as well as through the reaction of HO_2 with NO. The low NO mixing ratios in the pristine marine air lead to slow conversion of HO_2 to

OH by (5.5). Production of lightning NO_x in the convectively influenced air is apparently negligible, as demonstrated by the low NO mixing ratios and the low lightning flash count in the CONTRAST study region (Figure 5.10). Even though relative humidity is higher in the convectively influenced case, the absolute water vapor mixing ratio is still low because of the cold, upper tropospheric temperatures, resulting in slow primary production of OH. Elevated benzene, with an atmospheric lifetime on the order of 6 days, suggests long-range transport of anthropogenic pollution in the aged air. *Anderson et al.* [2016] show that the high abundances of NO observed during CONTRAST results from transport of biomass burning emissions with the possible influence of lightning generated NO_x from outside of the TWP. NO from these large-scale fires forces the equilibrium between the two HO_x species to higher OH and lower HO_2 than in the tropically influenced air. This is in contrast to the mid-troposphere where the combination of high O_3 and low H_2O in the polluted air actually leads to lower OH as compared to the convectively controlled background [*Nicely et al.*, 2016].

5.3.3 Box Model Results

5.3.3.1 Box Model Evaluation

The box model generally captures HCHO mixing ratios in the lower troposphere accurately. The results of the box modeling analysis (Figure 5.11 and Figure 5.12) include only data points that had not experienced convection within the previous 24 hours to allow for HCHO production to reach photochemical steady state. The high r^2 (0.84) for a linear least squares regression between the box model output and the *in situ* observations (Figure 5.12a) suggests that the model is able to capture gross variations in HCHO mixing ratios. At pressures greater than 500 hPa, the average agreement between

the observations and the model is within 10% (Figure 5.11c), indicating that the chemistry controlling HCHO abundance in the lower troposphere is well-characterized. The ratio of measured to modeled near-surface HCHO (pressures > 900 hPa) is slightly less than unity (0.90). This overestimate likely results from the lack of deposition in the model and also suggests that direct oceanic emissions are not an important HCHO source in the TWP.

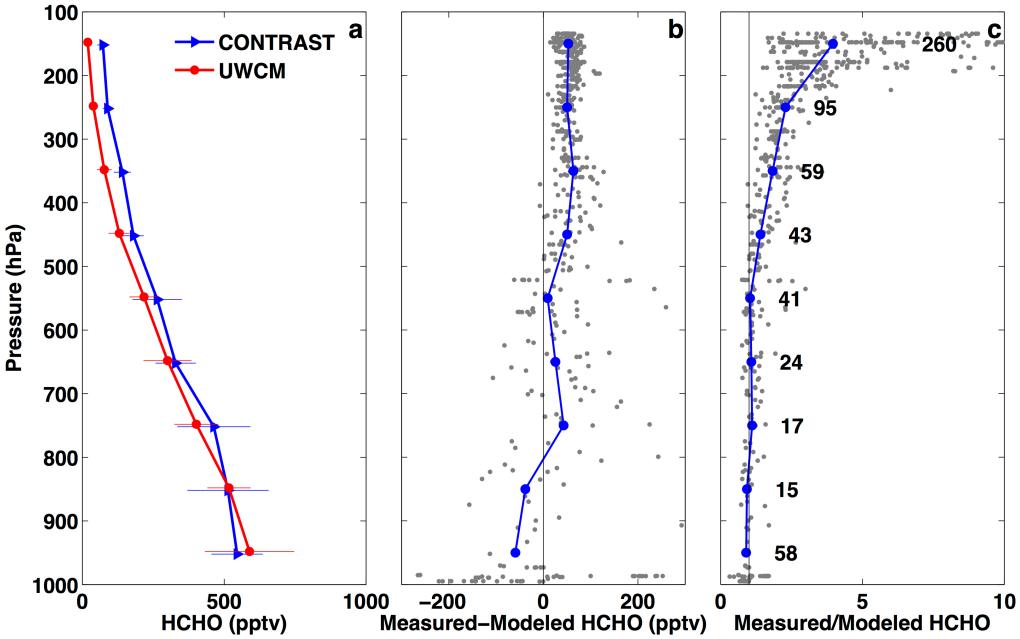

Figure 5.11: (**a**) Mean values of observed (blue) and UWCM modeled (red) formaldehyde in 50 hPa pressure bins for air parcels not experiencing convection within 24 hours of observation. Error bars are 1σ. (**b**) The difference between measured and modeled formaldehyde (grey). Mean values for 50 hPa pressure bins are shown in blue. (**c**) Same as (**b**) but the ratio of measured to modeled HCHO. Numbers indicate the number of observations in each pressure bin.

While the model and observations agree on average, the accuracy of individual data points varies widely, with the absolute difference between measured and modeled HCHO ranging between -300 and 300 pptv. Variability in the model at this pressure level is larger than the observations, with 1σ values of 156 and 89.7 pptv, respectively. For pressures between 500 and 900 hPa (Figure 5.11a), the model slightly underestimates the HCHO mixing ratio, on average, but values lie within the 1σ spread of the observations.

The number of observations in each pressure bin is shown in Figure 5.11c. The spread in the model output decreases with altitude, sometimes being lower than the spread in observations by a factor of 2, indicating that the model is unable to capture the variability in the observations.

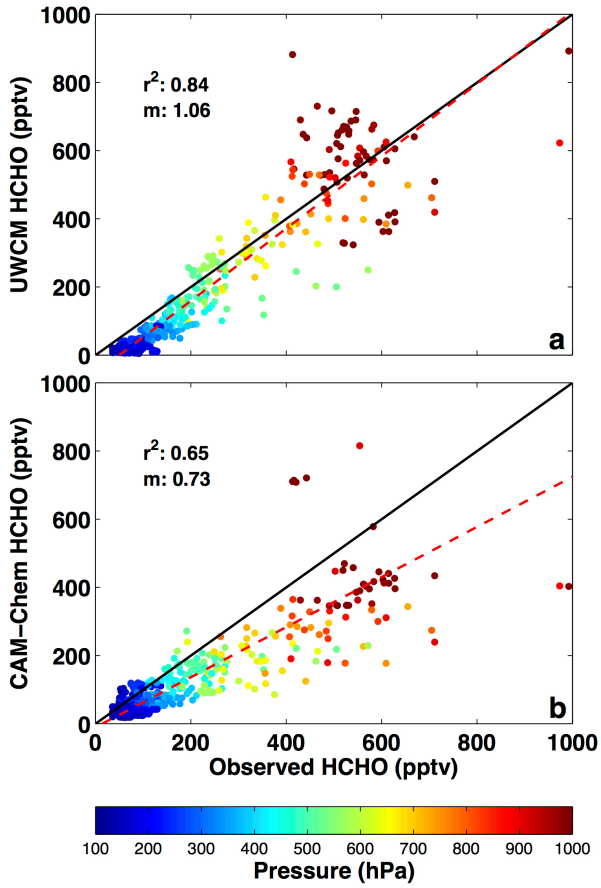

Figure 5.12: Regression of measured to UWCM (**a**) and CAM-Chem (**b**) modeled HCHO colored by pressure. The one-to-one line is shown in black, and the line of best fit, found using a linear least squares regression, in red. The slope (m) and r^2 are also shown.

At pressures less than 500 hPa, the box model significantly underestimates the observed mixing ratios, suggesting inadequacies in the chemical mechanism or missing HCHO precursors. For the upper troposphere, the measured to modeled ratio varies between 1.40 at 450 hPa to 3.96 at 150 hPa. While this ratio increases with decreasing pressure, the absolute difference between the measured and modeled HCHO stays

relatively constant, ranging between 50 and 64 pptv (Figure 5.11b). As at higher pressures, the 1σ spread of the modeled HCHO for a particular pressure bin are up to a factor of 2 lower than that in the observations. At the 150 hPa level, for example, the 1σ values for measured and modeled HCHO are 19.8 and 10.8 pptv, respectively.

Observational uncertainties could contribute to the difference between the measured and modeled values. Multiple box model runs were conducted in which observations of a given species were perturbed by its 2σ measurement uncertainty for RF11. Although it is too computationally expensive to perform this analysis for all modeled data, the results for RF11 can be considered representative of the entire campaign. Figure 5.13 shows the percentage change in HCHO from the base model run caused by these perturbations for all species analyzed as well as total uncertainty, found by adding the individual uncertainties in quadrature. In the lower troposphere, where there is relatively good agreement between observations and the model, the total uncertainty (2σ) in modeled HCHO due to the measurement uncertainty is 21% (Figure 5.13b). The dominant contributors to this uncertainty are NO (7%), Cl (8%), $j_{HCHO(HCO)}$ (8%), j_{NO2} (9%), and $j_{HCHO(H2)}$ (13%), where $j_{HCHO(HCO)}$ and $j_{HCHO(H2)}$ refer to the HCHO photolysis pathways in reactions (1.62) and (1.61), respectively. This low uncertainty shows significant improvement over earlier campaigns in remote regions, where instrument uncertainties were often a limiting factor in understanding HCHO chemistry [*Wagner et al.*, 2002]. In the upper troposphere, total uncertainty in modeled HCHO is 26%. As in the lower troposphere, Cl (8%), $j_{HCHO(HCO)}$ (9%), and $j_{HCHO(H2)}$ (17%) each contribute significantly to the overall uncertainty. In addition, uncertainty in acetaldehyde measurements leads to a 12% uncertainty in modeled HCHO. The relative

importance in the estimated Cl mixing ratio suggests the need for better inorganic chlorine observations to constrain photochemical HCHO production more accurately.

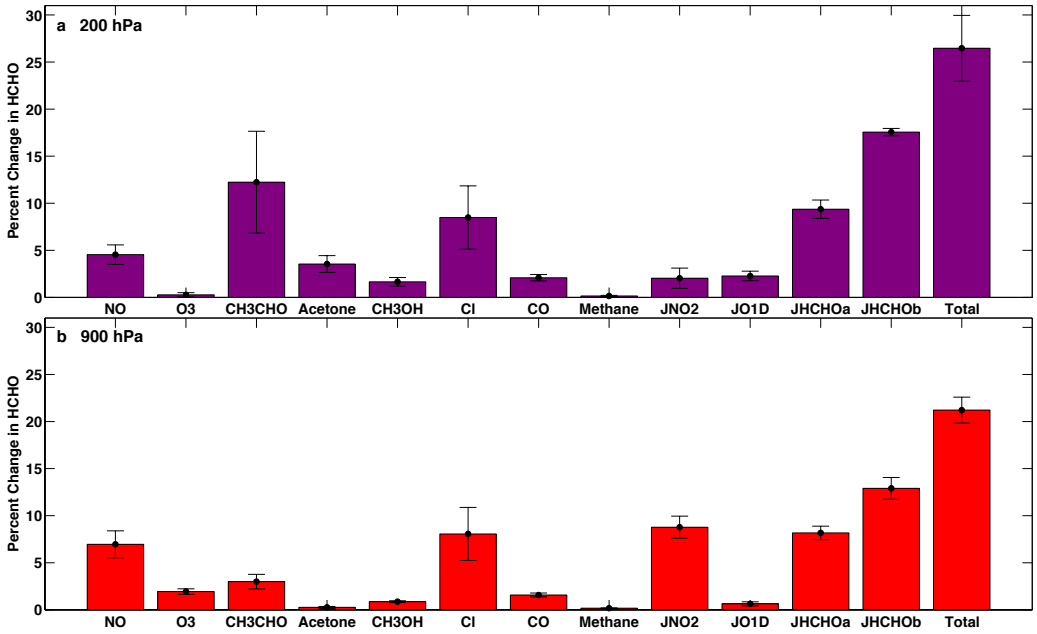

Figure 5.13: The percent uncertainty in the UWCM modeled HCHO value for RF11 (13 Feb. 2014) for pressures between 150 and 250 hPa (**a**) and 850 and 950 hPa (**b**). Each value is the mean uncertainty found by perturbing the indicated observed species by the measurement's 2σ uncertainty. Error bars show one standard deviation of the mean uncertainty. Total uncertainty is found by adding the uncertainty associated with each species in quadrature. JHCHOa is the photolysis constant for (1.62), and JHCHOb, for (1.61).

Low mixing ratios of HCHO in the upper troposphere and their associated uncertainties could also contribute to the differences between measurement and the model. Formaldehyde measurement uncertainty is on the order of 30 pptv. The large volumetric flow rate through the inlet, on the order of 25 L min^{-1}, prevents any significant adsorption and later desorption of HCHO on the inlet tubing, although it is possible that trace amounts do undergo this process. In addition, small quantities of HCHO from radical precursors could be produced *in situ* in the instrument or tubing. While this is not likely a significant contributor to measurement in the lower troposphere in the TWP, where HCHO mixing ratios are comparatively high, at the low HCHO mixing ratios present in the upper troposphere even the addition of a few pptv from either

of these processes could affect observed HCHO by several percent. Nevertheless, the ~30 pptv uncertainty in the observations combined with these potential measurement artifacts and the 26% uncertainty in modeled HCHO are insufficient to explain the 50 – 60 pptv difference between observed and modeled values.

$$CH_3O_2 + OH \rightarrow CH_2O_2 + H_2O \quad (5.6)$$
$$CH_3O_2 + OH \rightarrow CH_3O + HO_2 \quad (5.7)$$
$$CH_3O_2 + OH \rightarrow CH_3OH + O_2 \quad (5.8)$$

The reaction of CH_3O_2 with OH has been suggested as a potentially important CH_3O_2 sink in the remote atmosphere [*Fittschen et al.*, 2014], and here, I explore the potential impact of that reaction on HCHO production. *Fittschen et al.* [2014] suggest three viable reaction pathways for this reaction ((5.6)-(5.8)). I performed three additional box model runs in which I include one of the suggested reaction pathways, using a rate constant of 2.8×10^{-10} cm^3 $molecules^{-1}$ s^{-1} [*Bossolasco et al.*, 2014] for each. In addition, a fourth model run was conducted in which I assumed each reaction was equally likely. For the run including only (5.8), the model was initialized with but not constrained to observed CH_3OH, while the same constraints as in the base run were used for the other three runs. The results from these four runs, along with the observations and output from the base run are shown in Figure 5.14.

At pressures greater than 800 hPa, reaction (5.7) increases HCHO by ~10 pptv as compared to the base run, primarily by increasing the importance of reaction (1.53). All other scenarios lead to reductions in HCHO in the lower troposphere ranging from 65 to 140 pptv, as compared to the base case. Between 500 and 800 hPa, HCHO observations and the model base case have a median modeled to observation ratio of 1.10, showing good agreement. Differences between the "All" and CH_2OO scenarios at these pressure

levels, however, are on the order of 30-50 pptv. This disagreement suggests that, if the reaction between CH_3O_2 and OH does proceed at the rate suggested in the literature, there is a significant source of HCHO missing from these results. It is likely, however, based on the agreement between model results and observations here and in other field campaigns conducted in remote environments, that either (5.7) is the dominant reaction pathway or the reaction of CH_3O_2 with OH proceeds at a rate much slower than that suggested by *Bossolasco et al.* [2014]. In the upper troposphere, there is no substantive change in modeled HCHO when including any of the CH_3O_2 + OH reaction pathways. This reaction has no relevance for HCHO production at high altitudes in the TWP and cannot explain the difference between measured and modeled HCHO.

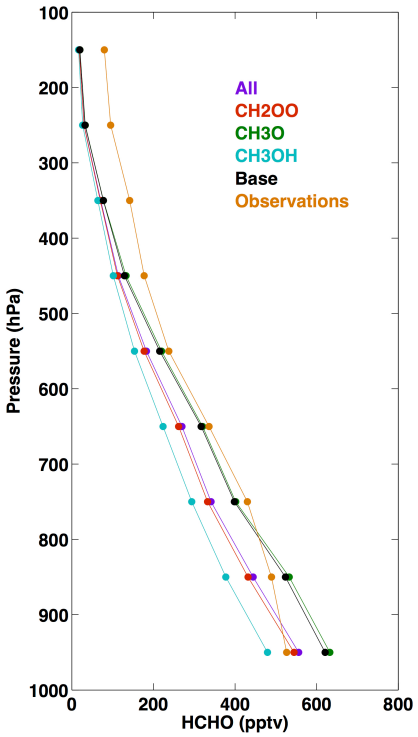

Figure 5.14: Median HCHO in 100 hPa pressure bins for observations (orange) and 5 box model runs with varied chemical mechanisms. The base scenario (black) contains only the MCM and halogen chemistry used throughout this study. Other scenarios include the base chemistry along with the CH_3O_2 reaction with OH, assuming different products: CH_3OH (cyan), CH_2OO (red), CH_3O (green), and a combination of these three products (purple).

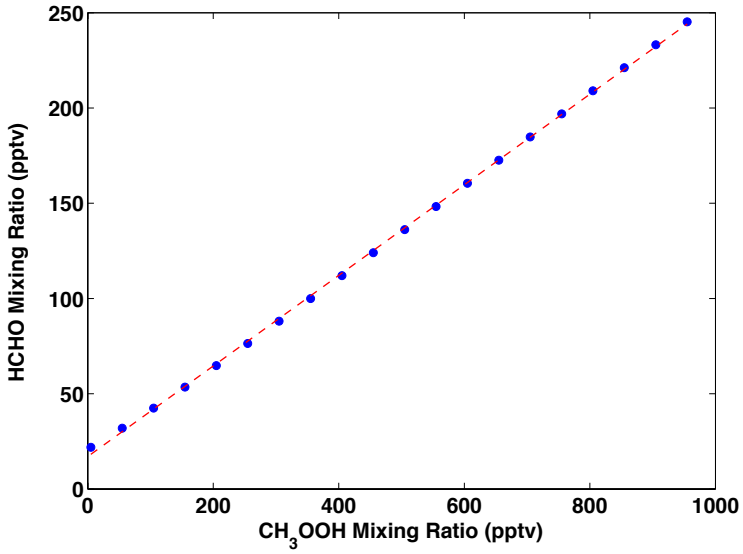

Figure 5.15: The variation in box modeled HCHO with CH_3OOH. Mean values of all box model input from all modeled flights between 200 and 300 hPa were used. The model was also constrained to CH_3OOH in 50 pptv intervals from 5 pptv to 995 pptv. The red dashed line is the line of best fit found using a linear least squares regression.

Another potential reason for disagreement between observations and the model is a HCHO source not well constrained in the box model. *Prather and Jacob* [1997] suggest that convective transport of CH_3OOH (Methyl hydroperoxide - MHP) can significantly alter upper tropospheric composition. The atmospheric lifetime of MHP allows it to persist in the upper troposphere in comparatively high concentrations for days after convection. To determine the possible impact of convective transport of MHP on HCHO production, I performed an additional box model run in which I constrained the model to average values of all the input parameters from the base run for observations between 100 and 200 hPa. In addition, the model is then constrained to mixing ratios of MHP, which was not measured during CONTRAST, ranging from near 0 to 1000 pptv. The results are shown in Figure 5.15 and reveal a linear relationship between modeled HCHO and constrained MHP. The measured mean of HCHO at these pressures (72.8 pptv) suggests an upper tropospheric MHP mixing ratio of ~235 pptv. This value is consistent with the upper tropospheric (~14 km) MHP values found in the PEM-West

campaign and used by *Prather and Jacob* [1997] but significantly higher than that seen by *Snow et al.* [2007] over the Atlantic. For the base UWCM model run, the mean MHP mixing ratio for observations between 100 and 200 hPa is only 5 pptv, with a maximum of 25 pptv. The box model's inability to produce reasonable mixing ratios of MHP suggests that the low MHP is the likely source of the disagreement between the observations and the model. Photochemical MHP production alone is insufficient to explain the quantities of MHP necessary to reproduce the HCHO observed during CONTRAST. Convective transport of this species from the lower troposphere is likely one of the driving mechanisms for HCHO production in the upper troposphere. Convection not only helps control upper tropospheric HCHO levels through direct transport of HCHO but also through transport of its precursors. This convective transport also implies that there likely exists significant spatial variability in upper tropospheric HCHO composition between the eastern and western Pacific as well as temporal variability associated with ENSO.

5.3.3.2 Chemical Sources and Sinks of HCHO

I now assess the importance of individual precursor molecules in HCHO production. To determine the relative importance of a given compound to HCHO formation, additional zero-out box model runs in which the model was not constrained to a given species were also performed. The difference, both absolute and percentage, in HCHO mixing ratio from these runs and the base runs are shown in Figure 5.16. In the case of acetaldehyde, the model was also not constrained to the higher order aldehydes, propanal and butanal, which can form small concentrations of acetaldehyde photochemically. In the halogen case, all halogen chemistry was omitted. Non-

linearities in the model chemistry prevent exact determination of the contributions for each species using this method, but the relative importance can be determined. This is particularly true at pressures greater than 500 hPa, where the box model accurately captures HCHO mixing ratios to within ~10%. In the upper troposphere, where observations can be a factor of 4 higher than the model, the percentage contributions for individual species is less certain, but nonetheless, important information can still be elucidated.

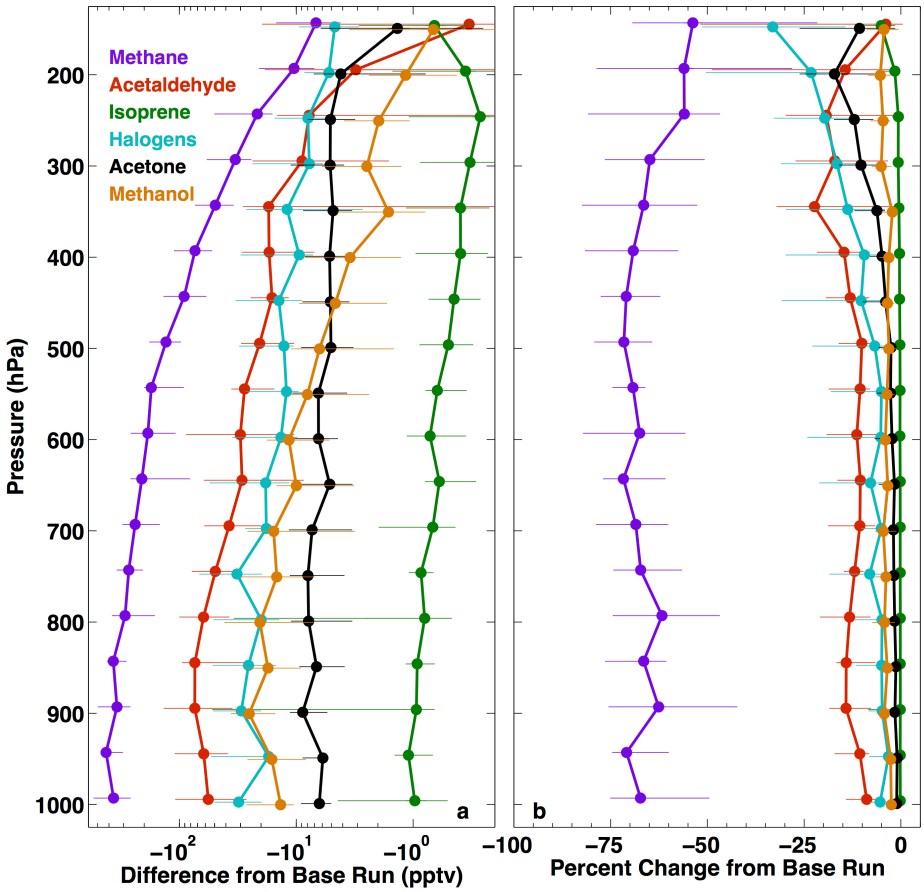

Figure 5.16: Median of the absolute (**a**) and percent (**b**) change in HCHO from the base run and runs conducted without constraining the model to observations of the indicated species. Error bars are the 5th and 95th percentile.

In agreement with previous studies, CH_4 oxidation is the primary contributor to HCHO production, accounting for between 55 and 65% of total HCHO throughout the tropospheric column. As discussed in Section 5.3.3.1, MHP convectively transported

from the surface is likely a major contributor to upper tropospheric HCHO, suggesting that the contribution from CH_4 at these pressures is even greater than indicated in Figure 5.16. Despite the remote location, HCHO production from VOCs is also significant. Acetaldehyde is responsible for 10-15% of total HCHO production in the lower troposphere. At pressures less than 200 hPa, acetaldehyde contributes less than 1 pptv of HCHO on average. In some instances, however, HCHO production from acetaldehyde can be as high as 20 pptv, a significant fraction of total HCHO. Acetaldehyde is primarily removed by photolysis and OH oxidation and has an atmospheric lifetime on the order of 1 day in the upper troposphere, implying that the observed acetaldehyde most be produced locally, likely from photochemical production in the ocean surface layer and the subsequent transport to the upper troposphere through deep convection. Contributions from methanol and acetone are generally on the order of 5%, while production from isoprene is negligible, except in air parcels observed near Papua New Guinea.

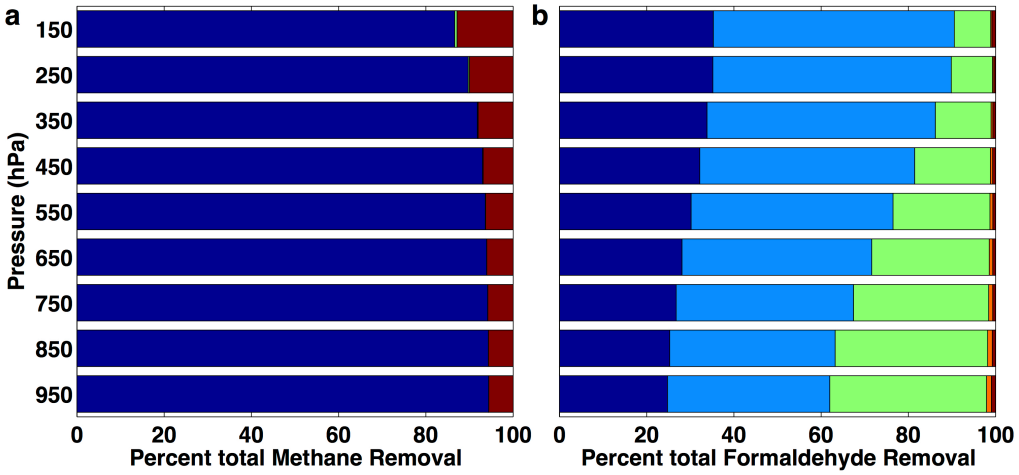

Figure 5.17: (**a**) Percent of CH_4 lost to each sink as calculated by the UWCM model. Data are sorted into 100 hPa pressure bins and averaged over all modeled data points. Oxidation by OH (dark blue); oxidation by Cl (red); and reaction with $O(^1D)$ (green). (**b**) Same as (**a**) except for HCHO. Photolysis to HO_2 (dark blue); photolysis to H_2 (light blue); reaction with OH (green), Cl (orange), and Br (red).

Halogens both produce and remove HCHO but act as a net source, generating between 10 and 50 pptv of HCHO throughout the tropospheric column, primarily from methane oxidation. This translates to less than 10% of HCHO production in the lower troposphere but is the second most important source after CH_4 at 150 hPa. This increase in the halogen impact on HCHO is dependent on the relative importance of the reaction of Cl with CH_4 as compared to OH oxidation. At pressures between the surface and 450 hPa, Cl only accounts for between 6-7% of CH_4 oxidation (Figure 5.17a). In the upper troposphere, however, this fraction doubles to 13%. The low upper tropospheric OH abundance, driven by cold temperatures and the resultant low water vapor, increases the importance of methane oxidation by Cl. Methane photolyzes primarily in the vacuum ultraviolet region, so photolysis in the upper troposphere is negligible.

In contrast, halogen chemistry is relatively unimportant for HCHO removal, accounting for only 1-2% of HCHO destruction throughout the tropospheric column (Figure 5.17b), in agreement with previous studies [*Toyota et al.*, 2004; *Wagner et al.*, 2002]. In the lower troposphere, the remaining chemical removal of HCHO is almost evenly distributed among the two photolytic pathways and reaction with OH. As with CH_4 removal, the reaction of HCHO with OH decreases in importance with decreasing pressure as OH concentrations decrease. At 150 hPa, this reaction accounts for only 8% of total HCHO removal, while reaction (1.61) accounts for 55%, and reaction (1.62) accounts for ~35%.

5.3.4 CAM-Chem Results

Global chemistry models play an important role in understanding the processes driving atmospheric chemical composition, particularly for difficult to observe species.

Nicely et al. [2016] found that eight CTMs that participated in POLMIP underestimate OH concentration in the TWP. In addition to a consistent underestimate of NO_x mixing ratios, they find that underestimates of HCHO mixing ratios in the upper troposphere contribute to this incorrect OH. Near the surface, they find that underestimates in acetaldehyde, an OH sink, by the POLMIP models lead to overestimates in OH. Here, I investigate more fully the representation of HCHO in CAM-Chem run in specified dynamics mode.

CAM-Chem uniformly underestimates HCHO throughout the troposphere. Figure 5.18a shows a comparison between observed HCHO and that output by CAM-Chem for RF11. Output from CAM-Chem at the latitude and longitude along the GV flight track are shown in the background while the observed HCHO is plotted over this "curtain". The CAM-Chem data are then interpolated to the flight altitude, and a regression of these values against the observations is shown in panel b. As with the photochemical box model, CAM-Chem consistently underestimates HCHO throughout the tropospheric column, with a mean measurement to model ratio of 0.56 ± 0.20. Upper tropospheric values are uniformly low in CAM-Chem. In the middle troposphere, the model frequently captures the placement of local maxima but again consistently underestimates their magnitude. The strong linearity between the model and observations ($r^2 = 0.86$) does show, however, that the model is able to capture the variability in HCHO observations. A thorough analysis of the HCHO sources and sinks in CAM-Chem is needed to discern the cause of this consistent underestimate.

First, I investigate the representation of the HCHO precursors methanol, methane, acetone, and acetaldehyde in CAM-Chem during RF11 (Figure 5.18c-j). Methane, the

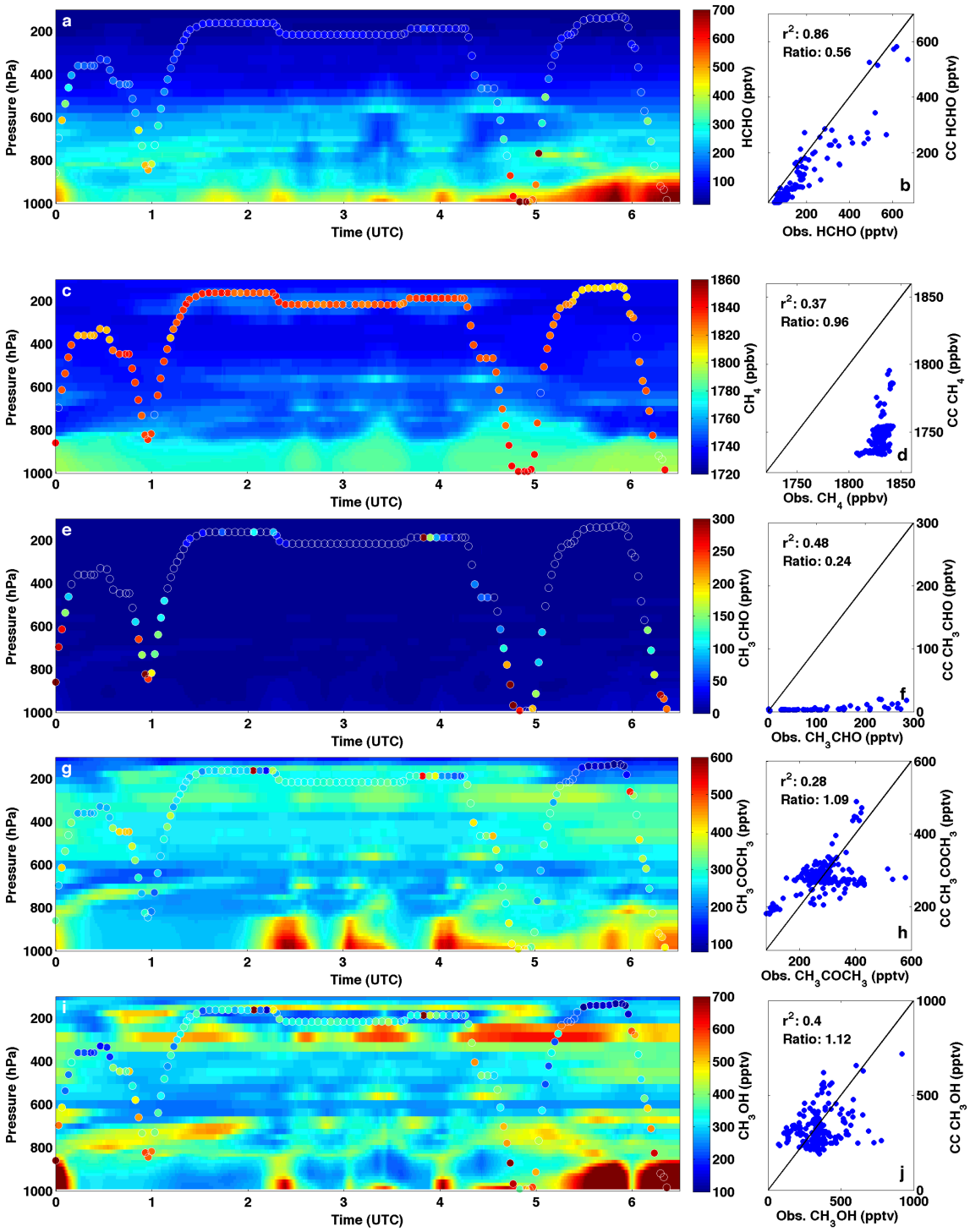

Figure 5.18: (**a**) CAM-Chem (background) run in specified dynamics mode output along the flight track and observed (circles outlined in white) HCHO for RF11 (13 Jan. 2014). (**b**) Regression of modeled and observed HCHO with modeled values interpolated to the observation pressure. The black line is the 1:1 line. The r^2 and mean ratio of modeled to observed HCHO is also shown. Analogous figures for CH_4 (**c** & **d**), CH_3CHO (**e** & **f**), CH_3COCH_3 (**g** & **h**), and CH_3OH (**i** & **j**) are also shown.

dominant HCHO precursor, is slightly underestimated during this flight with a mean ratio of 0.96 ± 0.0056 (r^2 = 0.37). This underestimate, which is larger in the upper troposphere than near the surface, could contribute to the modeled HCHO estimate, although it is unlikely it can explain the almost factor of two difference. Acetaldehyde, the second most important HCHO precursor in the TWP, is significantly underestimated with a measured to modeled ratio of 0.24 ± 0.50. The large standard deviation in the ratio results from the model capturing the low acetaldehyde mixing ratios aloft but failing to capture the higher mixing ratios near the surface. For this flight, CAM-Chem shows little variation in acetaldehyde mixing ratio throughout the tropospheric column, likely from a combination of omission of oceanic acetaldehyde emissions [*Nicely et al.*, 2016] as well as misrepresentation of secondary production [*Read et al.*, 2012]. CAM-Chem captures the mean observed mixing ratios of the other two important HCHO precursors in the TWP, acetone and methanol, for RF11. The mean ratio of observed to modeled methanol and acetone are 1.12 ± 0.54 and 1.09 ± 0.35, respectively. Despite the model being within 15% of the observed values on average for these two species, the r^2 of both correlations is relatively poor (0.28 for acetone and 0.49 for methanol); disagreement for individual data points could lead to errors in HCHO. Examination of Figure 5.18 suggests that some of this disagreement is the shifting in altitude or time of local maxima in the model as compared to the observations, implying the model performance is better than regression analysis suggests.

Comparisons between observations and model output of the two HCHO photolytic pathways are shown in Figure 5.19. For $j_{HCHO(H2)}$, lower tropospheric values show excellent agreement for observed rates between 5 and 12 × 10^{-5} s^{-1}. At photolysis

frequencies greater than this value, modeled j_{HCHO} remains relatively constant, while the observations increase to almost 20×10^{-5} s^{-1} in some cases. This leads to an average modeled to observed ratio of 0.92 ± 0.18. Local maxima in j_{HCHO} likely result from observations over clouds below the GV and the resultant increase in upwelling radiation associated with backscatter from these clouds. It is highly unlikely that the model would place convective clouds in their actual locations, resulting in differences between the model and observations. Uncertainty in the observed HCHO photolysis rates could further add to this disagreement. Similar results are found for $j_{HCHO(HCO)}$. Analysis of RF11 suggests that large differences between the observed and modeled j_{HCHO} values only manifest in differences in HCHO in the upper troposphere. This underestimate in j_{HCHO} suggests that the model is removing upper tropospheric HCHO too slowly. Because CAM-Chem already underestimates upper tropospheric HCHO, this further underestimate in the dominant HCHO sink is likely masking other errors in the model.

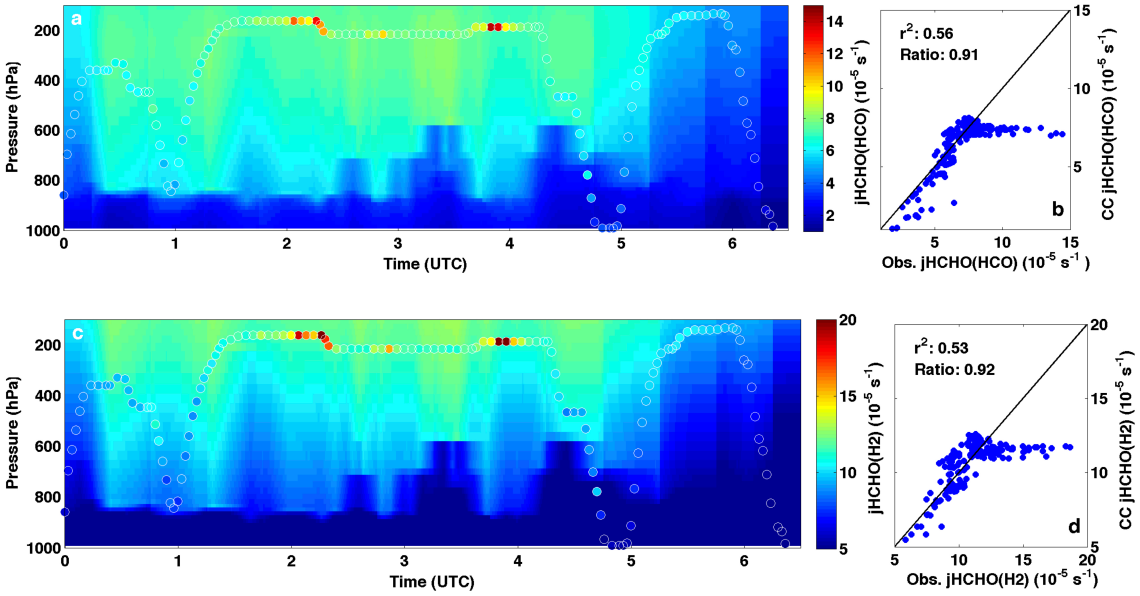

Figure 5.19: Same as Figure 5.18 except for $j_{HCHO(HCO)}$ (**a** & **b**) and $j_{HCHO(H2)}$ (**c** & **d**). $j_{HCHO(HCO)}$ is the photolysis frequency for (1.62), and $j_{HCHO(H2)}$, for (1.61).

A similar comparison for these species was conducted over the entire CONTRAST campaign. A regression of measured to CAM-Chem modeled HCHO for all flights analyzed here (Figure 5.12b) again shows consistent underestimate throughout the troposphere. In contrast with the box model results, however, several modeled values at low pressures lie above the 1:1 line. In the upper troposphere, at pressures less than 300 hPa, the model underestimates observed HCHO by ~34 pptv, or approximately a factor of 2 (Figure 5.21). This is on the order of the ISAF measurement uncertainty at these low mixing ratios. At pressures greater than 500 hPa, however, this difference increases to between 100 and 200 pptv, suggesting errors in the model. The two HCHO photolysis frequencies both have good linearity between observations and the model, with r^2 values of ~0.80, but with a larger underestimate by the model throughout the troposphere than seen only in RF11 (Figure 5.19). This likely propagates the compensating error caused by the underestimate in the HCHO photolytic sink throughout the tropospheric column. Acetaldehyde is consistently underestimated for all flights with a mean modeled to observed ratio of 0.08 ± 0.15. Methane also shows results similar to RF11 with moderate linearity between measurement and model but with a consistent model underestimate. The agreement for acetone and methanol is relatively poor when considered over the entire campaign with r^2 values of 0.13 and 0.03, respectively. The model consistently overestimates acetone (mean modeled to observed ratio = 1.52) while methanol is slightly overestimated but with significant spread around the 1:1 line (1σ of ratios = 1.15). Overestimate of acetone would increase HCHO production in CAM-Chem while underestimate of methanol would lead to a model underestimate of HCHO. Based on the box model results discussed earlier, however, both of these species contribute less than

10% to total HCHO formation at most pressure levels, so it is unlikely that the errors in these species can explain the consistent underestimate in HCHO.

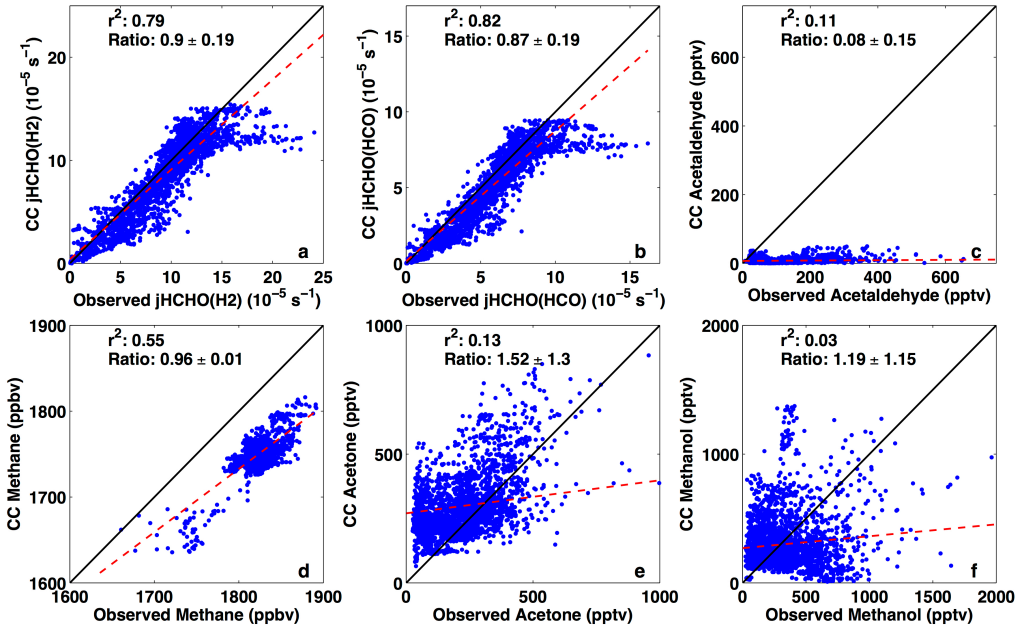

Figure 5.20: Regression of observed photolysis of HCHO to H_2 (**a**), photolysis of HCHO to HCO (**b**), acetaldehyde (**c**), methane (**d**), acetone (**e**), and methanol (**f**) to the corresponding modeled value from CAM-Chem along the flight track. Data are for flights RF04 – RF15 for observations made between 20 N and 20 S. The 1:1 line is shown in black while the line of best fit, found using a linear least squares regression, is shown in red. The r^2 for each regression as well as the mean and standard deviation of the ratio of modeled to observed species is also shown.

To determine the relative impacts of errors in methane, methanol, acetaldehyde, acetone, and the two formaldehyde photolysis pathways on modeled HCHO, additional runs of the UWCM box model were performed. Here, values of species from CAM-Chem were interpolated to the CONTRAST flight track for all flights. Individual box model runs were performed in which observed values of one of these species was replaced with the CAM-Chem values. In addition, CAM-Chem also significantly underestimates NO_x mixing ratios throughout the troposphere during the CONTRAST study period [*Nicely et al.*, 2016]. The reaction of NO with CH_3O_2 is instrumental in converting CH_4 to HCHO, while NO is also necessary to maintain OH levels needed to

oxidize VOCs. Thus, I performed an additional run constrained to CAM-Chem NO. The difference between these runs and the base UWCM run are shown in Figure 5.22.

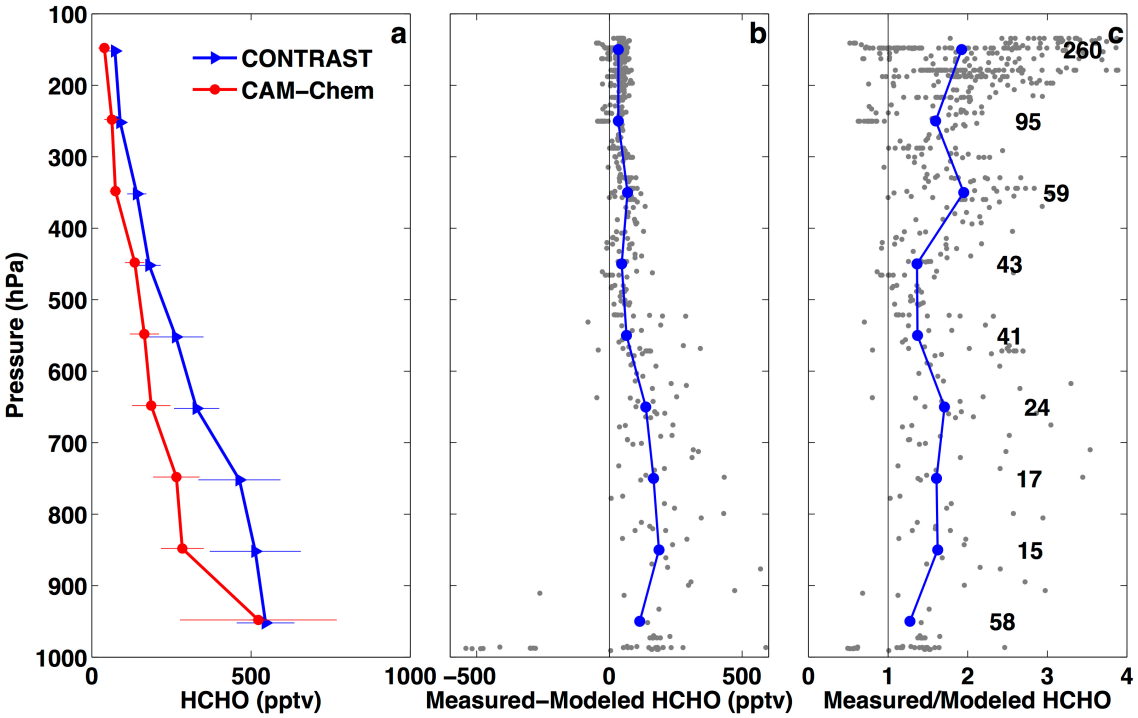

Figure 5.21: Same as Figure 5.11 except for CONTRAST observations and model output from CAM-Chem interpolated to the CONTRAST flight track.

Underestimates in NO and acetaldehyde are driving the CAM-Chem underestimate of HCHO. Replacing observed NO with that from CAM-Chem results in reductions of HCHO between 70 and 190 pptv at pressures greater than 500 hPa; replacing observed acetaldehyde results in reductions between 20 and 75 pptv. At these pressures, CAM-Chem underestimates HCHO by between 64 and 190 pptv (Figure 5.21), suggesting that the combination of errors in NO and acetaldehyde mixing ratios are more than sufficient to explain the difference between CAM-Chem and observations. In the upper troposphere, the resultant decreases in modeled HCHO, while smaller (between 6 and 45 pptv), still explain a large portion of the model underestimate. At 950 hPa, the underestimate of the two HCHO photolysis pathways results in increases in HCHO of 58

and 34 pptv for the H_2 and HCO pathways, respectively. At pressures less than this, the CAM-Chem photolysis frequencies do not result in large changes to modeled HCHO. Replacing the observed CH_4 and CH_3OH with the CAM-Chem values results in decreases in HCHO near the surface on the order of 10 pptv each, while changes to upper tropospheric values of HCHO are negligible. CAM-Chem acetone results in changes on the order of 1-2 pptv throughout the tropospheric column, suggesting that the poor agreement between measurement and model for this species does not affect overall HCHO.

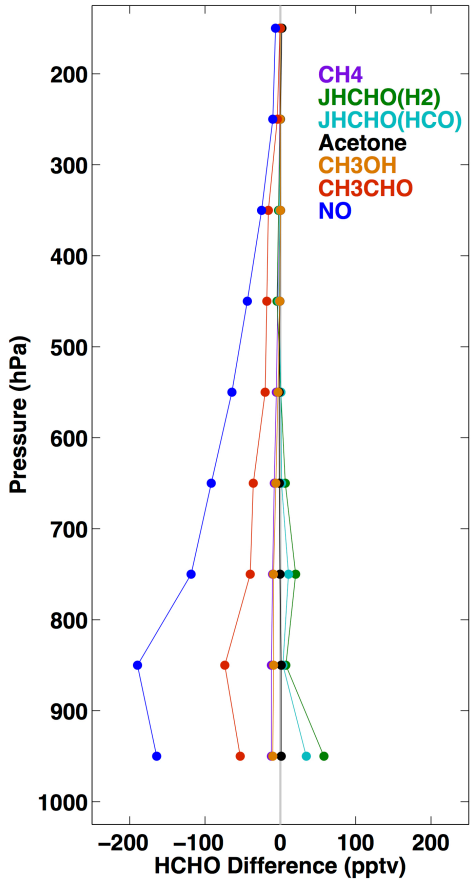

Figure 5.22: Difference between the base box model run, constrained with observations from CONTRAST, and model runs in which the indicated species or photolysis frequency was taken from CAM-Chem. CAM-Chem values were interpolated to the flight track. Positive (negative) values indicate an increase (decrease) in box-modeled HCHO when using the CAM-Chem output. Output are sorted into 100 hPa bins.

5.4 Conclusions

Formaldehyde observations made in the TWP during the CONTRAST campaign ranged from ~500 pptv near the surface to ~75 pptv in the upper troposphere, exhibiting significantly larger mixing ratios than observed in previous studies in the TWP. A combination of back trajectories and satellite observations of precipitation and cloud top height were used to determine the time since an observed air parcel had last seen precipitating convection. Air parcels that had experienced convection within 24 hours had 33% higher HCHO and a factor of 4 higher acetaldehyde than aged parcels, suggesting that convection in the west Pacific warm pool significantly increases upper tropospheric HCHO through transport of HCHO rich air. The aged air parcels, which have higher concentrations of the anthropogenic pollutants NO and benzene, shift the HO_x balance, resulting in OH abundance that is a factor of 1.4 higher than estimated for the local, convectively controlled air parcels. Remarkably low NO mixing ratios were observed in air that had seen recent convection, indicating little or no production by lightning.

A photochemical box model, constrained to observations made during CONTRAST, generally agreed with HCHO observations within 10% at pressures greater than 500 hPa, suggesting that HCHO chemistry is well understood and that convective outflow does not significantly perturb HCHO in the lower half of the troposphere. In the upper troposphere, however, observations of HCHO were a factor of 4 higher than box model output. Convective transport of the HCHO precursor MHP can explain the difference between the model and observations, assuming a MHP mixing ratio of ~235 pptv. Box model analysis also shows that CH_4 and acetaldehyde are the dominant HCHO

precursors in the TWP, with minor contributions from acetone and methanol. Halogen chemistry acts as a net HCHO source, primarily through the reaction of Cl with CH_4.

Output from the CAM-Chem model was compared to observations, and it was shown that the model underestimates HCHO throughout the troposphere. Consistent underestimations of NO and acetaldehyde are the primary drivers of the difference between observed and modeled HCHO throughout the tropospheric column, suggesting the need for improvements to both the emissions and chemistry of these species in the model. This underestimate in NO not only affects HCHO chemistry, but likely affects the partitioning of the HO_x species in the upper troposphere for aged air parcels.

Chapter 6 Conclusions

6.1 Summary and Implications

Data collected during the 2011 DISCOVER-AQ field campaign in the Baltimore/Washington Region (BWR) were used to evaluate CO and NO_x emissions in the 2011 NEI. The average emissions ratio for the region was seen to be 11.2 ± 1.2 mol CO/mol NO_x, 21% higher than that predicted by the NEI. Comparisons between *in situ* and remote observations and CMAQ model output show agreement in CO emissions of 15 ± 11% while NO_x emissions are overestimated by 51-70% in Maryland. Satellite observations of CO by MOPITT show agreement with the CMAQ model within 3% over most of the eastern United States. CMAQ NO_y mixing ratios were a factor of two higher than observations and result from a combination of errors in emissions as well as PAN and alkyl nitrate chemistry, as shown by comparison of three CMAQ model runs. Point source NO_x emissions are monitored and agree with modeled emissions within 1% on a monthly basis. Because of this accuracy and the NEI assertion that approximately 3/4 of emissions in the Baltimore Washington region are from mobile sources, the majority of this overestimate is likely from errors in mobile source emissions estimates. The MOVES model's treatment of emissions from aging vehicles should be investigated; the NEI overestimate of NO_x emissions could indicate that engines produce less NOx and catalytic converters degrade more slowly than assumed by MOVES2010. There is also evidence that catalytic converters have a dependency on ambient temperature, not captured in MOVES. The more recent 2011 NEI has an even lower CO/NO_x emissions ratio than the projection used in this study; it overestimates NO_x emissions by an even larger margin. The implications of these findings for US air quality policy are that NO_x

concentrations near areas of heavy traffic are overestimated and ozone production rates in these locations are slower than models indicate. Results also suggest that ambient ozone concentrations will respond more efficiently to NO_x emissions controls but additional sources may need to be targeted for reductions.

Subsequent studies have confirmed and expanded upon the results of *Anderson et al.* [2014]. *Travis et al.* [2016] investigated the representation of NO_y species in the GEOS-Chem CTM through comparison of observations of these species during the Studies of Emissions, Atmospheric Composition, Clouds and Climate Coupling by Regional Surveys (SEAC^{4}RS) campaign, conducted in the Southeastern US during August and September 2013. They found that a 60% reduction in non-power plant emissions of NO_x in the 2011 NEI was required for the model to match observations of NO_x, HNO_3, and isoprene nitrates. In addition, this reduction in NO_x emissions was necessary to bring observations of measured and modeled nitrate deposition fluxes in agreement. *Kim et al.* [2016] developed a fuel-based inventory of NO_x emissions and evaluated it through comparison to observations during the CALNEX campaign conducted in the South California Air Basin. They found that their emissions inventory, when used to run WRF-Chem, accurately captured observations of NO_2 in the region. The *Kim et al.* [2016] inventory has since been expanded over the United States, and in the Eastern US, preliminary results suggest that the 2011 NEI overestimates NO_x emissions by 50-60% [*McDonald et al.*, 2015], in good agreement with *Anderson et al.* [2014].

Canty et al. [2015] investigated the impacts of reducing mobile NO_x emissions by 50% on modeled NO_2 and O_3 in CMAQ. Through comparisons of model output to

various OMI NO_2 products, we found that CMAQ, when run with the default mobile emissions for 2007, significantly overestimates tropospheric NO_2 columns in most urban regions in the eastern US and underestimates these values in rural regions. Reducing the mobile NO_x emissions by half, also reduces the modeled to observed ratio of NO_2 columns in urban regions from 1.56 to 1.21, significantly improving agreement. When pairing the 50% mobile NO_x reduction with improvements to the representation of alkyl nitrate chemistry in the CB05 mechanism and comparing the results to air quality monitoring sites across the eastern United States, the number of false positives of the average daily maximum 8h surface ozone (*i.e.* modeled O_3 values higher than the former NAAQS of 75 ppbv when observed values were below this threshold) decreased by half. In *Goldberg et al.* [2016], we compared a baseline run of the Comprehensive Air-Quality Model with Extensions (CAMx) with default chemistry and emissions to one in which, among other changes, mobile NO_x emissions were reduced by 50%. We find that, in the modified model run, surface O_3 in Maryland attributable to on-road mobile emissions is reduced by 36% as compared to the baseline run, while O_3 attributable to electricity generation increases by 31%, confirming one of the suggested implications of the NO_x emissions overestimate revealed in *Anderson et al.* [2014].

Observations from the CONTRAST field campaign reveal the prevalence of structures with high O_3 and low H_2O mixing ratios in the tropical western Pacific. These structures had mean O_3 and RH of 55 ppbv and 5%, respectively, as compared to background values of 22 ppbv and 63%. Back trajectory analysis using HYSPLIT connect all the observed HOLW structures to biomass burning regions in tropical Africa and Southeast Asia. Further, the O_3 in these structures shows strong correlations with the

tracers CO ($r^2 = 0.61$) and HCN ($r^2 = 0.80$), while CO correlates with C_6H_6 ($r^2 = 0.67$), and C_2H_2 ($r^2 = 0.68$), also suggesting a biomass burning origin. Photochemical box modeling of these filaments shows an ozone production rate of ~2 ppbv/day. This *in situ* production, in combination with the ~50 ppbv O_3 background in the African and Southeast Asian biomass burning regions, can reproduce the observed O_3 anomalies. The low relative humidity in these structures most likely results from the combination of large-scale descent in the tropics, associated with the Hadley circulation, and the associated warming with this descent. Back trajectory analysis shows that these air parcels descend approximately 200 hPa, remain south of the jet core, and increase slightly in water vapor mixing ratio in transit to the TWP. Drying of air in the mid-latitudes, as has been suggested in the literature, is inconsistent with this analysis and the observed chemical composition of the HOLW structures. Because O_3 in these filaments has frequently been attributed to transport from the mid-latitudes, it is likely that biomass burning emissions have a stronger influence on the radiative forcing of climate from tropospheric O_3 than is commonly appreciated.

The distribution, sources, and sinks of HCHO in the TWP, as well as their representation in the CAM-Chem model were explored in Chapter 5. Observed HCHO ranged from ~500 pptv near the surface to 74 pptv at pressures less than 300 hPa. On average, total column HCHO from OMI agreed to within 5% of the tropospheric column content derived from *in situ* observations, although the satellite observations showed a much larger range than the *in situ* observations. Convection increased upper tropospheric HCHO by about 30%, while it increased acetaldehyde by a factor of 4. It was also found that the transport of polluted air from outside of the TWP shifted the HO_x equilibrium, so

that OH mixing ratios were higher in the polluted air than in convectively influenced marine air by a factor of 1.4 because of the higher NO abundance associated with anthropogenically influenced air. A photochemical box model, driven by *in situ* observations, was able to reproduce HCHO mixing ratios within 10% for observations at pressures greater than 500 hPa. At 200 hPa, observations were a factor of 4 greater than modeled. It was shown that the most likely cause of this disagreement was the convective transport of the HCHO precursor, CH_3OOH, which would need an upper tropospheric mixing ratio of ~230 pptv to reproduce the observed HCHO. The dominant HCHO precursors were found to be CH_4 and acetaldehyde, which contributed between 10 and 20% of total HCHO throughout the tropospheric column. While destruction by halogen radicals was responsible for less than 1% of total HCHO loss, oxidation of CH_4 by Cl in the upper troposphere, where OH concentrations are low, was found to contribute to ~15% of total CH_4 oxidation. Finally, it was found that the CAM-Chem model underestimates HCHO throughout the troposphere, likely due to the model underestimates of acetaldehyde and NO.

6.2 Recommendations for Future Work

In this work, I show that the NEI overestimates mobile NO_x emissions by 51-70% in the BWR. Increasing both the spatial and temporal scales analyzed here by performing similar regression analyses for CO and NO_y could expand the conclusions made here to other regions in the US and better address disagreement with other published studies, particularly in California, Colorado, and Texas. DISCOVER-AQ data provide an excellent opportunity to extend this analysis. Additional portions of the campaign were conducted in California (Winter 2013), Houston (Fall 2013), and Denver (Summer 2014)

with similar sampling strategies and instrumentation, allowing for direct comparison of observed emissions ratios. The Wintertime Investigation of Transport, Emission, and Reactivity (WINTER) campaign, conducted during Feb-Mar 2015 in the BWR, would allow for determination of seasonality in CO/NO_x emissions ratios, although comparisons to DISCOVER-AQ would be complicated by changes in emissions and the vehicle fleet in the 4 years between the two studies.

The EPA has substantially changed the NEI since the analysis described here was conducted. Here, I used a projection to 2011 from the 2005 NEI, which estimated on-road NO_x emissions using MOVES2010. The EPA has now released the 2011 NEI version 2 as well as MOVES2014, which aims to provide better estimates of mobile NO_x emissions than previous model versions. These new emissions inventories should be evaluated in a similar manner as the version used here, to determine whether changes to the inventory bring closer agreement between observations and the model. For the state of Maryland, the 2011 NEI version 2 has an even lower CO/NO_x emissions ratio than the projection used in this study, suggesting that changes to the model have actually led to larger errors in emissions from mobile sources, though this claim must be investigated further. As suggested in section 2.3.1, there likely exists a temperature dependence on the CO/NO_x emissions ratio not captured by the MOVES model. Further investigation of this topic is also warranted.

Another potentially interesting study suggested by the CMAQ evaluation of NO_x emissions is an investigation into the poor agreement between measured and modeled PAN. Modeled PAN is a factor of 2.3 higher than observations in both the baseline and chemistry + emissions runs and is a large contributor to the high NO_y bias in the model.

The CMAQ analysis used in this study employed the Carbon Bond mechanism version 5 (CB05), which has since been updated to version 6. A deeper investigation into the representation of organic precursors, including their kinetics, in the model is warranted. Given the comparatively long lifetime of PAN, transport processes in the model could also be responsible for this overestimate. Again, data from the subsequent DISCOVER-AQ field campaigns could aid in this analysis.

The analysis of the HOLW structures from CONTRAST suggests several research questions. The observations discussed here are limited temporally and to further investigate the prevalence of these structures observations from different seasons and years should be analyzed. Satellite observations of tropospheric O_3, from AIRS, the Technology Experiment Satellite (TES), or the soon-to-be launched Stratospheric Aerosol and Gas Experiement (SAGE) III instrument could be combined with water vapor observations from AIRS to examine the temporal and spatial variability of these structures. Difficulties in retrieving tropospheric O_3 as well as the limited vertical extent of some of the structures may complicate the analysis, however. CONTRAST lacked measurements of total NO_y, many of the individual NO_y constituents, and aerosol species. Previous and future field campaigns that measure(d) these species, such as the HIAPER Pole-to-Pole Observations (HIPPO) campaign conducted from 2009 to 2011 and the Atmospheric Tomography mission (ATom) scheduled to start in 2016, could provide additional insight into the sources of these structures.

The representation of these HOLW structures in chemical transport and climate models should also be investigated. The climate community depends on these models to analyze the interactions between chemistry and climate, and it should be ensured that the

models can accurately reproduce the processes that create the HOLW structures. If the models do not capture the high O_3, it is likely that they are underestimating biomass burning emissions, missing reactions in their chemical mechanisms, failing to loft and transport the plumes, or some combination thereof. For the CONTRAST study period, CAM-Chem underestimated both NO and CO [*Nicely et al.*, 2016], suggesting that biomass burning emissions are not accurately represented in the model. This could be a result of the FINN emissions inventory or processes within CAM-Chem itself.

One of the primary implications of this study is that tropical biomass burning likely has a more significant influence on the radiative forcing of climate than is commonly appreciated because the O_3 in these HOLW structures is often attributed to transport from the mid-latitudes. Further, *Stoller et al.* [1999] found that these structures cap convection by altering the local radiative heating profile. Modeling studies should be conducted to determine the global and local radiative impact of both the O_3 and water vapor. Global chemistry/climate models could be run with and without biomass burning emissions to determine the difference in radiative forcing, once it has been shown that models are capable of accurately reproducing the composition of the filaments with the correct mechanism.

Potential impacts of these structures on the chemical composition of the TWP should also be investigated. *Nicely et al.* [2016] show that OH is depressed in the HOLW structures, as compared to the local background, primarily due to the low water in the filaments. If the O_3 in these structures were at the background value, it is likely that OH would be even lower. Lower OH mixing ratios would extend the lifetime of some halogen compounds, including CH_2Br_2, which could allow for larger amounts of these

species to be transported to the stratosphere where they deplete O_3. Modeling studies could be performed to determine the impact of tropical biomass burning on both the transport of these halogen species to the stratosphere and the resultant effect on stratospheric O_3 concentration.

Investigation of the spatial heterogeneity and temporal variability in HCHO across the Pacific should also be investigated. Here, I show that upper tropospheric HCHO observed during CONTRAST is higher than in previous studies, attributable in part to convective lofting of near surface HCHO and CH_3OOH, a HCHO precursor, into the TTL. While OMI does provide daily coverage over much of the Pacific, the instrument only provides total column content and is hindered by the near-detection limit values in the TWP. Again, observations from the upcoming ATom field campaign will help provide insight into the question of temporal variability in upper tropospheric HCHO and its relationship to convection, as the campaign will transect the Pacific during the four seasons using the same measurement technique as in CONTRAST. Measurements of OH during this campaign could also provide insight into the difference in the oxidation capacity of convectively and anthropogenically influenced air masses in the remote Pacific. Observations of CH_3OOH could provide confirmation of the importance of convective lofting of this species for HCHO production. Likewise, observations of acetaldehyde could provide constraints on the seasonality of oceanic emissions of this species.

Further investigation of the impacts of oceanic acetaldehyde emissions on HCHO production in CTMs is currently underway. Applying the methodology of *Millet et al.* [2010] to observations of the absorption of gelbstoff and detrital material at 443 nm from

the MODIS Aqua instrument, I will calculate fluxes of acetaldehyde from the ocean and include those emissions in an additional CAM-Chem model run over the CONTRAST domain. Output from this run will then be compared to observations and the baseline CAM-Chem run for various species. In addition, *Millet et al.* [2010] report that comparisons between observed and modeled acetaldehyde, when including oceanic emissions, agree near the surface but that the model still consistently underestimates the observed acetaldehyde in the middle and upper troposphere. They attribute this disagreement to uncertainties in the observations. Measurement technologies have increased significantly over those used in the campaigns analyzed by *Millet et al.* [2010]. Comparison of an updated CAM-Chem model run to the CONTRAST observations will allow for testing of this hypothesis.

Chapter 7 Bibliography

Abad, G. G., X. Liu, K. Chance, H. Wang, T. P. Kurosu, and R. Suleiman (2015), Updated Smithsonian Astrophysical Observatory Ozone Monitoring Instrument (SAO OMI) formaldehyde retrieval, *Atmospheric Measurement Techniques*, *8*(1), 19-32, doi:10.5194/amt-8-19-2015.

Akagi, S. K., R. J. Yokelson, C. Wiedinmyer, M. J. Alvarado, J. S. Reid, T. Karl, J. D. Crounse, and P. O. Wennberg (2011), Emission factors for open and domestic biomass burning for use in atmospheric models, *Atmospheric Chemistry and Physics*, *11*(9), 4039-4072, doi:10.5194/acp-11-4039-2011.

Alexander, B., M. G. Hastings, D. J. Allman, J. Dachs, J. A. Thornton, and S. A. Kunasek (2009), Quantifying atmospheric nitrate formation pathways based on a global model of the oxygen isotopic composition (delta O-17) of atmospheric nitrate, *Atmospheric Chemistry and Physics*, *9*(14), 5043-5056.

Allen, D. J., K. E. Pickering, R. W. Pinder, B. H. Henderson, K. W. Appel, and A. Prados (2012), Impact of lightning-NO on eastern United States photochemistry during the summer of 2006 as determined using the CMAQ model, *Atmospheric Chemistry and Physics*, *12*(4), 1737-1758, doi:10.5194/acp-12-1737-2012.

Alvarado, M. J., et al. (2010), Nitrogen oxides and PAN in plumes from boreal fires during ARCTAS-B and their impact on ozone: an integrated analysis of aircraft and satellite observations, *Atmospheric Chemistry and Physics*, *10*(20), 9739-9760, doi:10.5194/acp-10-9739-2010.

Amato, P., F. Demeer, A. Melaouhi, S. Fontanella, A. S. Martin-Biesse, M. Sancelme, P. Laj, and A. M. Delort (2007), A fate for organic acids, formaldehyde and methanol in cloud water: their biotransformation by micro-organisms, *Atmospheric Chemistry and Physics*, *7*(15), 4159-4169.

Anderson, D. C., et al. (2014), Measured and modeled CO and NOy in DISCOVER-AQ: An evaluation of emissions and chemistry over the eastern US, *Atmospheric Environment*, *96*, 78-87, doi:10.1016/j.atmosenv.2014.07.004.

Anderson, D. C., et al. (2016), A pervasive role for biomass burning in tropical high ozone/low water structures, *Nature Communications*, *7*, doi:10.1038/ncomms10267.

Andreae, M. O., and P. Merlet (2001), Emission of trace gases and aerosols from biomass burning, *Global Biogeochemical Cycles*, *15*(4), 955-966, doi:10.1029/2000gb001382.

Apel, E. C. (2003), A fast-GC/MS system to measure C2 to C4 carbonyls and methanol aboard aircraft, *Journal of Geophysical Research*, *108*(D20), doi:10.1029/2002jd003199.

Arellano, A. F., P. S. Kasibhatla, L. Giglio, G. R. van der Werf, and J. T. Randerson (2004), Top-down estimates of global CO sources using MOPITT measurements, *Geophysical Research Letters*, *31*(1), doi:10.1029/2003gl018609.

Arkinson, H. L., T. F. Hanisco, G. M. Wolfe, and R. R. Dickerson (in preparation), Evaluation of a new in situ airborne formaldehyde instrument with laser induced fluorescence based on observations from the DC3 campaign.

Arsene, C., A. Bougiatioti, M. Kanakidou, B. Bonsang, and N. Mihalopoulos (2007), Tropospheric OH and Cl levels deduced from non-methane hydrocarbon measurements in a marine site, *Atmospheric Chemistry and Physics*, *7*(17), 4661-4673.

Ashfold, M. J., et al. (2015), Rapid transport of East Asian pollution to the deep tropics, *Atmospheric Chemistry and Physics*, *15*(6), 3565-3573, doi:10.5194/acp-15-3565-2015.

Atkinson, R., and J. Arey (2003), Atmospheric degradation of volatile organic compounds, *Chemical Reviews*, *103*(12), 4605-4638, doi:10.1021/cr0206420.

Atkinson, R., S. M. Aschmann, W. P. L. Carter, A. M. Winer, and J. N. Pitts (1982), Alkyl Nitrate Formation from the NOx Air Photoxidations of C2-C8 N-Alkanes, *Journal of Physical Chemistry*, *86*(23), 4563-4569, doi:10.1021/j100220a022.

Atkinson, R., D. L. Baulch, R. A. Cox, J. N. Crowley, R. F. Hampson, R. G. Hynes, M. E. Jenkin, M. J. Rossi, and J. Troe (2006), Evaluated kinetic and photochemical data for atmospheric chemistry: Volume II - gas phase reactions of organic species, *Atmospheric Chemistry and Physics*, *6*, 3625-4055.

Atlas, E. (1988), Evidence for Greater than or Equal to 3 Alkyl Nitrates in Rural Remote Atmospheres, *Nature*, *331*(6155), 426-428, doi:10.1038/331426a0.

Avnery, S., D. L. Mauzerall, J. Liu, and L. W. Horowitz (2011), Global crop yield reductions due to surface ozone exposure: 1. Year 2000 crop production losses and economic damage, *Atmospheric Environment*, *45*(13), 2284-2296, doi:10.1016/j.atmosenv.2010.11.045.

Ayers, G. P., R. W. Gillett, H. Granek, C. deServes, and R. A. Cox (1997), Formaldehyde production in clean marine air, *Geophysical Research Letters*, *24*(4), 401-404, doi:10.1029/97gl00123.

Baidar, S., H. Oetjen, S. Coburn, B. Dix, I. Ortega, R. Sinreich, and R. Volkamer (2013), The CU Airborne MAX-DOAS instrument: vertical profiling of aerosol extinction and trace gases, *Atmospheric Measurement Techniques*, *6*(3), 719-739, doi:10.5194/amt-6-719-2013.

Ban-Weiss, G. A., J. P. McLaughlin, R. A. Harley, M. M. Lunden, T. W. Kirchstetter, A. J. Kean, A. W. Strawa, E. D. Stevenson, and G. R. Kendall (2008), Long-term changes in emissions of nitrogen oxides and particulate matter from on-road gasoline and diesel vehicles, *Atmospheric Environment*, *42*(2), 220-232, doi:10.1016/j.atmosenv.2007.09.049.

Barth, M. C., et al. (2015), The Deep Convective Clouds and Chemistry (DC3) field campaign, *Bulletin of the American Meteorological Society*, *96*(8), 1281-1309, doi:10.1175/bams-d-13-00290.1.

Barth, M. C., S. Sillman, R. Hudman, M. Z. Jacobson, C. H. Kim, A. Monod, and J. Liang (2003), Summary of the cloud chemistry modeling intercomparison: Photochemical box model simulation, *Journal of Geophysical Research-Atmospheres*, *108*(D7), doi:10.1029/2002jd002673.

Beaver, M. R., et al. (2012), Importance of biogenic precursors to the budget of organic nitrates: observations of multifunctional organic nitrates by CIMS and TD-LIF during BEARPEX 2009, *Atmospheric Chemistry and Physics*, *12*(13), 5773-5785, doi:10.5194/acp-12-5773-2012.

Bell, M. L., R. D. Peng, and F. Dominici (2006), The Exposure-Response Curve for Ozone and Risk of Mortality and the Adequacy of Current Ozone Regulations, *Environmental health perspectives*, *114*(4), 532-536.

Bertram, T. H., et al. (2007), Direct measurements of the convective recycling of the upper troposphere, *Science*, *315*(5813), 816-820, doi:10.1126/science.1134548.

Bishop, G. A., B. G. Schuchmann, D. H. Stedman, and D. R. Lawson (2012), Multispecies remote sensing measurements of vehicle emissions on Sherman Way in Van Nuys, California, *Journal of the Air & Waste Management Association*, *62*(10), 1127-1133, doi:10.1080/10962247.2012.699015.

Blake, N. J., et al. (1999), Influence of southern hemispheric biomass burning on midtropospheric distributions of nonmethane hydrocarbons and selected halocarbons over the remote South Pacific, *Journal of Geophysical Research-Atmospheres*, *104*(D13), 16213-16232, doi:10.1029/1999jd900067.

Borbon, A., et al. (2012), Transport and chemistry of formaldehyde by mesoscale convective systems in West Africa during AMMA 2006, *Journal of Geophysical Research: Atmospheres*, *117*(D12), n/a-n/a, doi:10.1029/2011jd017121.

Bossolasco, A., E. P. Farago, C. Schoemaecker, and C. Fittschen (2014), Rate constant of the reaction between CH3O2 and OH radicals, *Chemical Physics Letters*, *593*, 7-13, doi:10.1016/j.cplett.2013.12.052.

Boylan, P., D. Helmig, and J. H. Park (2014), Characterization and mitigation of water vapor effects in the measurement of ozone by chemiluminescence with nitric oxide, *Atmospheric Measurement Techniques*, *7*(5), 1231-1244, doi:10.5194/amt-7-1231-2014.

Brioude, J., et al. (2013), Top-down estimate of surface flux in the Los Angeles Basin using a mesoscale inverse modeling technique: assessing anthropogenic emissions of CO, NOx and CO2 and their impacts, *Atmospheric Chemistry and Physics*, *13*(7), 3661-3677, doi:10.5194/acp-13-3661-2013.

Brown, S. S., et al. (2004), Nighttime removal of NOx in the summer marine boundary layer, *Geophysical Research Letters*, *31*(7), doi:10.1029/2004gl019412.

Bytnerowicz, A., and M. E. Fenn (1996), Nitrogen deposition in California forests: A review, *Environ. Pollut.*, *92*(2), 127-146, doi:10.1016/0269-7491(95)00106-9.

Canty, T. P., L. Hembeck, T. P. Vinciguerra, D. C. Anderson, D. L. Goldberg, S. F. Carpenter, D. J. Allen, C. P. Loughner, R. Salawitch, and R. R. Dickerson (2015), Ozone and NOx chemistry in the eastern US: Evaluation of CMAQ/CB05 with OMI data, *Atmospheric Chemistry and Physics*, *15*, 10965-10982.

Carslaw, D. C., S. D. Beevers, J. E. Tate, E. J. Westmoreland, and M. L. Williams (2011), Recent evidence concerning higher NOx emissions from passenger cars and light duty vehicles, *Atmospheric Environment*, *45*(39), 7053-7063, doi:10.1016/j.atmosenv.2011.09.063.

Carter, W. P. L., and R. Atkinson (1989), Alkyl nitrate formation from the atmospheric photooxidation of alkanes: A revised estimation method, *Journal of Atmospheric Chemistry*, *8*(2), 165-173, doi:10.1007/bf00053721.

Castellanos, P., L. T. Marufu, B. G. Doddridge, B. F. Taubman, J. J. Schwab, J. C. Hains, S. H. Ehrman, and R. R. Dickerson (2011), Ozone, oxides of nitrogen, and carbon monoxide during pollution events over the eastern United States: An evaluation of emissions and vertical mixing, *Journal of Geophysical Research*, *116*(D16), doi:10.1029/2010jd014540.

Cau, P., J. Methven, and B. Hoskins (2007), Origins of dry air in the tropics and subtropics, *Journal of Climate*, *20*(12), 2745-2759, doi:10.1175/jcli4176.1.

Cazorla, M., G. M. Wolfe, S. A. Bailey, A. K. Swanson, H. L. Arkinson, and T. F. Hanisco (2015), A new airborne laser-induced fluorescence instrument for in situ detection of formaldehyde throughout the troposphere and lower stratosphere, *Atmospheric Measurement Techniques*, *8*(2), 541-552, doi:10.5194/amt-8-541-2015.

Cecil, D. J., D. E. Buechler, and R. J. Blakeslee (2014), Gridded lightning climatology from TRMM-LIS and OTD: Dataset description, *Atmospheric Research*, *135*, 404-414, doi:10.1016/j.atmosres.2012.06.028.

Chameides, W. L., et al. (1992), Ozone Precurosr Relationships in the Ambient Atmosphere, *Journal of Geophysical Research-Atmospheres*, *97*(D5), 6037-6055.

Chandra, S., J. R. Ziemke, B. N. Duncan, T. L. Diehl, N. J. Livesey, and L. Froidevaux (2009), Effects of the 2006 El Nino on tropospheric ozone and carbon monoxide: implications for dynamics and biomass burning, *Atmospheric Chemistry and Physics*, *9*(13), 4239-4249.

Chang, W. N., B. G. Heikes, and M. H. Lee (2004), Ozone deposition to the sea surface: chemical enhancement and wind speed dependence, *Atmospheric Environment*, *38*(7), 1053-1059, doi:10.1016/j.atmosenv.2003.10.050.

Chatfield, R. B., and A. C. Delany (1990), Convection Links Biomass Burning to Increased Tropical Ozone - However Models will tend to Overpredict O3, *Journal of Geophysical Research-Atmospheres*, *95*(D11), 18473-18488, doi:10.1029/JD095iD11p18473.

Chen, D., G. Huey, D. J. Tanner, R. J. Salawitch, E. Atlas, L. L. Pan, P. Wales, D. C. Anderson, R. S. Hornbrook, and E. Apel (2016), Airborne measurements of BrO and the sum of HOBr and Br2 during the CONvective TRansport of Active Species in the Tropics campaign, *in preparation*.

Clarke, J. F., E. S. Edgerton, and B. E. Martin (1997), Dry deposition calculations for the clean air status and trends network, *Atmospheric Environment*, *31*(21), 3667-3678, doi:10.1016/s1352-2310(97)00141-6.

Clemitshaw, K. C., J. Williams, O. V. Rattigan, D. E. Shallcross, K. S. Law, and R. A. Cox (1997), Gas-phase ultraviolet absorption cross-sections and atmospheric lifetimes of several C-2-C-5 alkyl nitrates, *Journal of Photochemistry and Photobiology a-Chemistry*, *102*(2-3), 117-126, doi:10.1016/s1010-6030(96)04458-9.

Collins, W. J., R. G. Derwent, C. E. Johnson, and D. S. Stevenson (2000), The impact of human activities on the photochemical production and destruction of tropospheric ozone, *Quarterly Journal of the Royal Meteorological Society*, *126*(566), 1925-1951, doi:10.1256/smsqj.56618.

Cooper, O. R., R.-S. Gao, D. Tarasick, T. Leblanc, and C. Sweeney (2012), Long-term ozone trends at rural ozone monitoring sites across the United States, 1990-2010, *Journal of Geophysical Research: Atmospheres*, *117*(D22), n/a-n/a, doi:10.1029/2012jd018261.

Cooper, O. R., et al. (2010), Increasing springtime ozone mixing ratios in the free troposphere over western North America, *Nature*, *463*(7279), 344-348, doi:10.1038/nature08708.

Crosson, E. R. (2008), A cavity ring-down analyzer for measuring atmospheric levels of methane, carbon dioxide, and water vapor, *Applied Physics B-Lasers and Optics*, *92*(3), 403-408, doi:10.1007/s00340-008-3135-y.

Crumeyrolle, S., G. Chen, L. Ziemba, A. Beyersdorf, L. Thornhill, E. Winstead, R. Moore, M. A. Shook, and B. Anderson (2013), Factors that influence surface PM2.5 values inferred from satellite observations: perspective gained for the Baltimore-Washington Area during DISCOVER-AQ, *Atmospheric Chemistry and Physics Discussions*, *13*(9), 23421-23459, doi:10.5194/acpd-13-23421-2013.

Crutzen, P. J., L. E. Heidt, J. P. Krasnec, W. H. Pollock, and W. Seiler (1979), Biomass Burning as a Source of Atmospheric Gases: CO, H2, N2O, NO, CH3Cl, and COS, *Nature*, *282*(5736), 253-256, doi:10.1038/282253a0.

Dallmann, T. R., and R. A. Harley (2010), Evaluation of mobile source emission trends in the United States, *Journal of Geophysical Research-Atmospheres*, *115*, doi:10.1029/2010jd013862.

Danielsen, E. F. (1968), Stratospheric-Tropospheric Exchange Based on Radioactivity, Ozone and Potential Vorticity, *Journal of the Atmospheric Sciences*, *25*(3), 502-&, doi:10.1175/1520-0469(1968)025<0502:stebor>2.0.co;2.

Davidson, E. A., and W. Kingerlee (1997), A global inventory of nitric oxide emissions from soils, *Nutrient Cycling in Agroecosystems*, *48*(1-2), 37-50, doi:10.1023/a:1009738715891.

de Gouw, J. A., D. D. Parrish, G. J. Frost, and M. Trainer (2014), Reduced emissions of CO2, NOx, and SO2from U.S. power plants owing to switch from coal to natural gas with combined cycle technology, *Earth's Future*, *2*(2), 75-82, doi:10.1002/2013ef000196.

de Gouw, J. A., C. Warneke, D. D. Parrish, J. S. Holloway, M. Trainer, and F. Fehsenfeld (2003), Emission sources and ocean uptake of acetonitrile (CH3CN) in the atmosphere, *Journal of Geophysical Research*, *108*(D11), doi:10.1029/2002jd002897.

Deeter, M. N., S. Martinez-Alonso, D. P. Edwards, L. K. Emmons, J. C. Gille, H. M. Worden, J. V. Pittman, B. C. Daube, and S. C. Wofsy (2013), Validation of MOPITT Version 5 thermal-infrared, near-infrared, and multispectral carbon monoxide profile retrievals for 2000-2011, *Journal of Geophysical Research-Atmospheres*, *118*(12), 6710-6725, doi:10.1002/jgrd.50272.

Deeter, M. N., H. M. Worden, D. P. Edwards, J. C. Gille, and A. E. Andrews (2012), Evaluation of MOPITT retrievals of lower-tropospheric carbon monoxide over the United States, *Journal of Geophysical Research-Atmospheres*, *117*, doi:10.1029/2012jd017553.

Derwent, R. G., and M. E. Jenkin (1991), Hydrocarbons and the Long-Range Transport of Ozone and PAN across Europe, *Atmospheric Environment Part a-General Topics*, *25*(8), 1661-1678, doi:10.1016/0960-1686(91)90025-3.

Dessler, A. E., and K. Minschwaner (2007), An analysis of the regulation of tropical tropospheric water vapor, *Journal of Geophysical Research-Atmospheres*, *112*(D10), doi:10.1029/2006jd007683.

Dickerson, R. R., M. O. Andreae, T. Campos, O. L. Mayol-Bracero, C. Neususs, and D. G. Streets (2002), Analysis of black carbon and carbon monoxide observed over the Indian Ocean: Implications for emissions and photochemistry, *Journal of Geophysical Research-Atmospheres*, *107*(D19), doi:10.1029/2001jd000501.

Dickerson, R. R., B. G. Doddridge, P. Kelley, and K. P. Rhoads (1995), Large-scale pollution of the atmosphere over the remote Atlantic Ocean: Evidence from Bermuda, *Journal of Geophysical Research*, *100*(D5), 8945-8952.

Dickerson, R. R., K. P. Rhoads, T. P. Carsey, S. J. Oltmans, J. P. Burrows, and P. J. Crutzen (1999), Ozone in the remote marine boundary layer: A possible role for halogens, *Journal of Geophysical Research*, *104*, 21,385-321,395, doi:0148-0227/99/1999JD900023$09.00.

DiGangi, J. P., et al. (2011), First direct measurements of formaldehyde flux via eddy covariance: implications for missing in-canopy formaldehyde sources, *Atmospheric Chemistry and Physics*, *11*(20), 10565-10578, doi:10.5194/acp-11-10565-2011.

Doraiswamy, P., C. Hogrefe, W. Hao, R. F. Henry, K. Civerolo, J.-Y. Ku, G. Sistla, J. J. Schwab, and K. L. Demerjian (2009), A diagnostic comparison of measured and model-predicted speciated VOC concentrations, *Atmospheric Environment*, *43*(36), 5759-5770, doi:10.1016/j.atmosenv.2009.07.056.

Draxler, R. R., and G. D. Hess (1997), Description of the HYSPLIT_4 modeling system*Rep. ERL ARL-224*, 24 pp, NOAA Air Resources Laboratory, Silver Spring, MD.

Duncan, B. N., J. A. Logan, I. Bey, I. A. Megretskaia, R. M. Yantosca, P. C. Novelli, N. B. Jones, and C. P. Rinsland (2007), Global budget of CO, 1988-1997: Source estimates and validation with a global model, *Journal of Geophysical Research-Atmospheres*, *112*(D22), doi:10.1029/2007jd008459.

Duncan, B. N., et al. (2010), Application of OMI observations to a space-based indicator of NOx and VOC controls on surface ozone formation, *Atmospheric Environment*, *44*(18), 2213-2223, doi:10.1016/j.atmosenv.2010.03.010.

Economou, C., and N. Mihalopoulos (2002), Formaldehyde in the rainwater in the eastern Mediterranean: occurrence, deposition and contribution to organic carbon budget, *Atmospheric Environment*, *36*(8), 1337-1347, doi:10.1016/s1352-2310(01)00555-6.

Emmerson, K. M., and M. J. Evans (2009), Comparison of tropospheric gas-phase chemistry schemes for use within global models, *Atmospheric Chemistry and Physics*, *9*(5), 1831-1845, doi:10.5194/acp-9-1831-2009.

Emmons, L. K., et al. (2015), The POLARCAT Model Intercomparison Project (POLMIP): overview and evaluation with observations, *Atmospheric Chemistry and Physics*, *15*(12), 6721-6744, doi:10.5194/acp-15-6721-2015.

Farmer, D. K., P. J. Wooldridge, and R. C. Cohen (2006), Application of thermal-dissociation laser induced fluorescence (TD-LIF) to measurement of HNO3, Sigma alkyl nitrates, Sigma peroxy nitrates, and NO2 fluxes using eddy covariance, *Atmospheric Chemistry and Physics*, *6*, 3471-3486.

Fernandez, R. P., R. J. Salawitch, D. E. Kinnison, J. F. Lamarque, and A. Saiz-Lopez (2014), Bromine partitioning in the tropical tropopause layer: implications for stratospheric injection, *Atmospheric Chemistry and Physics*, *14*(24), 13391-13410, doi:10.5194/acp-14-13391-2014.

Finlayson-Pitts, B. J., and J. N. Pitts (1999), *Chemistry of the Upper and Lower Atmosphere*, 1st ed., Academic Press, UK.

Fiore, A. M., D. J. Jacob, J. A. Logan, and J. H. Yin (1998), Long-term trends in ground level ozone over the contiguous United States, 1980-1995, *Journal of Geophysical Research-Atmospheres*, *103*(D1), 1471-1480, doi:10.1029/97jd03036.

Fiore, A. M., D. J. Jacob, R. Mathur, and R. V. Martin (2003), Application of empirical orthogonal functions to evaluate ozone simulations with regional and global models, *Journal of Geophysical Research-Atmospheres*, *108*(D19), doi:10.1029/2002jd003151.

Fiscus, E. L., F. L. Booker, and K. O. Burkey (2005), Crop responses to ozone: uptake, modes of action, carbon assimilation and partitioning, *Plant Cell and Environment*, *28*(8), 997-1011, doi:10.1111/j.1365-3040.2005.01349.x.

Fishman, J., K. Fakhruzzaman, B. Cros, and D. Nganga (1991), Identification of Widespread Pollution in the Southern-Hemisphere Deduced from Satellite Analyses, *Science*, *252*(5013), 1693-1696, doi:10.1126/science.252.5013.1693.

Fishman, J., V. Ramanathan, P. J. Crutzen, and S. C. Liu (1979), Tropospheric ozone and climate, *Nature*, *282*(5741), 818-820, doi:10.1038/282818a0.

Fittschen, C., L. K. Whalley, and D. E. Heard (2014), The Reaction of CH3O2 Radicals with OH Radicals: A Neglected Sink for CH3O2 in the Remote Atmosphere, *Environmental Science & Technology*, *48*(14), 7700-7701, doi:10.1021/es502481q.

Folkins, I., R. Chatfield, D. Baumgardner, and M. Proffitt (1997), Biomass burning and deep convection in southeastern Asia: Results from ASHOE/MAESA, *Journal of Geophysical Research-Atmospheres*, *102*(11D), 13291-13299, doi:10.1029/96jd03711.

Forster, P. M. D., and K. P. Shine (1997), Radiative forcing and temperature trends from stratospheric ozone changes, *Journal of Geophysical Research-Atmospheres*, *102*(D9), 10841-10855, doi:10.1029/96jd03510.

Fortems-Cheiney, A., F. Chevallier, I. Pison, P. Bousquet, M. Saunois, S. Szopa, C. Cressot, T. P. Kurosu, K. Chance, and A. Fried (2012), The formaldehyde budget as seen by a global-scale multi-constraint and multi-species inversion system, *Atmospheric Chemistry and Physics*, *12*(15), 6699-6721, doi:10.5194/acp-12-6699-2012.

Fried, A., et al. (2011), Detailed comparisons of airborne formaldehyde measurements with box models during the 2006 INTEX-B and MILAGRO campaigns: potential evidence for significant impacts of unmeasured and multi-generation volatile organic

carbon compounds, *Atmospheric Chemistry and Physics*, *11*(22), 11867-11894, doi:10.5194/acp-11-11867-2011.

Fried, A., et al. (2003), Airborne tunable diode laser measurements of formaldehyde during TRACE-P: Distributions and box model comparisons, *Journal of Geophysical Research*, *108*(D20), doi:10.1029/2003jd003451.

Fried, A., et al. (2008), Role of convection in redistributing formaldehyde to the upper troposphere over North America and the North Atlantic during the summer 2004 INTEX campaign, *Journal of Geophysical Research*, *113*(D17), doi:10.1029/2007jd009760.

Friedfeld, S., M. Fraser, K. Ensor, S. Tribble, D. Rehle, D. Leleux, and F. Tittel (2002), Statistical analysis of primary and secondary atmospheric formaldehyde, *Atmospheric Environment*, *36*(30), 4767-4775, doi:10.1016/s1352-2310(02)00558-7.

Frost, G. J., et al. (2002), Comparisons of box model calculations and measurements of formaldehyde from the 1997 North Atlantic Regional Experiment, *Journal of Geophysical Research-Atmospheres*, *107*(D7-8), doi:10.1029/2001jd000896.

Fueglistaler, S., A. E. Dessler, T. J. Dunkerton, I. Folkins, Q. Fu, and P. W. Mote (2009), Tropical Tropopause Layer, *Reviews of Geophysics*, *47*, 31, doi:10.1029/2008rg000267.

Fuhrer, J., L. Skarby, and M. R. Ashmore (1997), Critical levels for ozone effects on vegetation in Europe, *Environ. Pollut.*, *97*(1-2), 91-106, doi:10.1016/s0269-7491(97)00067-5.

Fujita, E. M., D. E. Campbell, B. Zielinska, J. C. Chow, C. E. Lindhjem, A. DenBleyker, G. A. Bishop, B. G. Schuchmann, D. H. Stedman, and D. R. Lawson (2012), Comparison of the MOVES2010a, MOBILE6.2, and EMFAC2007 mobile source emission models with on-road traffic tunnel and remote sensing measurements, *Journal of the Air & Waste Management Association*, *62*(10), 1134-1149, doi:10.1080/10962247.2012.699016.

Fusco, A. C., and J. A. Logan (2003), Analysis of 1970-1995 trends in tropospheric ozone at Northern Hemisphere midlatitudes with the GEOS-CHEM model, *Journal of Geophysical Research-Atmospheres*, *108*(D15), doi:10.1029/2002jd002742.

Galewsky, J., A. Sobel, and I. Held (2005), Diagnosis of subtropical humidity dynamics using tracers of last saturation, *Journal of the Atmospheric Sciences*, *62*(9), 3353-3367, doi:10.1175/jas3533.1.

Gao, R. S., K. H. Rosenlof, D. W. Fahey, P. O. Wennberg, E. J. Hintsa, and T. F. Hanisco (2014), OH in the tropical upper troposphere and its relationships to solar radiation and reactive nitrogen, *Journal of Atmospheric Chemistry*, doi:10.1007/s10874-014-9280-2.

Garcia, A. R., R. Volkamer, L. T. Molina, M. J. Molina, J. Samuelson, J. Mellqvist, B. Galle, S. C. Herndon, and C. E. Kolb (2006), Separation of emitted and photochemical formaldehyde in Mexico City using a statistical analysis and a new pair of gas-phase tracers, *Atmospheric Chemistry and Physics*, *6*, 4545-4557.

Gerbig, C., S. Schmitgen, D. Kley, A. Volz-Thomas, K. Dewey, and D. Haaks (1999), An improved fast-response vacuum-UV resonance fluorescence CO instrument, *Journal of Geophysical Research-Atmospheres*, *104*(D1), 1699-1704, doi:10.1029/1998jd100031.

Gettelman, A., et al. (2004), Validation of Aqua satellite data in the upper troposphere and lower stratosphere with in situ aircraft instruments, *Geophysical Research Letters*, *31*(22), doi:10.1029/2004gl020730.

Giglio, L., I. Csiszar, and C. O. Justice (2006), Global distribution and seasonality of active fires as observed with the Terra and Aqua Moderate Resolution Imaging Spectroradiometer (MODIS) sensors, *Journal of Geophysical Research-Biogeosciences*, *111*(G2), doi:10.1029/2005jg000142.

Goldberg, D. L., C. P. Loughner, M. Tzortziou, J. W. Stehr, K. E. Pickering, L. T. Marufu, and R. R. Dickerson (2014), Higher surface ozone concentrations over the Chesapeake Bay than over the adjacent land: Observations and models from the DISCOVER-AQ and CBODAQ campaigns, *Atmospheric Environment*, *84*, 9-19, doi:10.1016/j.atmosenv.2013.11.008.

Goldberg, D. L., et al. (2016), CAMx ozone source attribution in the eastern United States using guidance from observations during DISCOVER-AQ Maryland, *Geophysical Research Letters*, doi:10.1002/2015GL067332.

Goode, J. G., R. J. Yokelson, R. A. Susott, and D. E. Ward (1999), Trace gas emissions from laboratory biomass fires measured by open-path Fourier transform infrared spectroscopy: Fires in grass and surface fuels, *Journal of Geophysical Research-Atmospheres*, *104*(D17), 21237-21245, doi:10.1029/1999jd900360.

Granier, C., et al. (2011), Evolution of anthropogenic and biomass burning emissions of air pollutants at global and regional scales during the 1980-2010 period, *Climatic Change*, *109*(1-2), 163-190, doi:10.1007/s10584-011-0154-1.

Grosjean, D., E. Grosjean, and A. W. Gertler (2001), On-road emissions of carbonyls from light-duty and heavy-duty vehicles, *Environmental Science & Technology*, *35*(1), 45-53, doi:10.1021/es001326a.

Hallock-Waters, K. A., B. G. Doddridge, R. R. Dickerson, S. Spitzer, and J. D. Ray (1999), Carbon monoxide in the US Mid-Atlantic troposphere: Evidence for a decreasing trend, *Geophysical Research Letters*, *26*(18), 2861-2864, doi:10.1029/1999gl900609.

Hansen, J., M. Sato, and R. Ruedy (1997), Radiative forcing and climate response, *Journal of Geophysical Research-Atmospheres*, *102*(D6), 6831-6864, doi:10.1029/96jd03436.

Hanson, P. J., and S. E. Lindberg (1991), Dry deposition of reactive nitrogen compounds: A review of leaf, canopy, and non-foliar measurements, *Atmospheric Environment Part a-General Topics*, *25*(8), 1615-1634, doi:10.1016/0960-1686(91)90020-8.

Harris, N. R. P., et al. (2016), Co-ordinated Airborne Studies in the Tropics (CAST), *Bulletin of the American Meteorological Society*, doi:10.1175/BAMS-D-14-00290.1.

Hayashi, H., K. Kita, and S. Taguchi (2008), Ozone-enhanced layers in the troposphere over the equatorial Pacific Ocean and the influence of transport of midlatitude UT/LS air, *Atmospheric Chemistry and Physics*, *8*(10), 2609-2621.

He, H., et al. (2014), An elevated reservoir of air pollutants over the Mid-Atlantic States during the 2011 DISCOVER-AQ campaign: Airborne measurements and numerical simulations, *Atmospheric Environment*, *85*, 18-30, doi:10.1016/j.atmosenv.2013.11.039.

He, H., et al. (2013), Trends in emissions and concentrations of air pollutants in the lower troposphere in the Baltimore/Washington airshed from 1997 to 2011, *Atmospheric Chemistry and Physics Discussions*, *13*(2), 3135-3178, doi:10.5194/acpd-13-3135-2013.

Heagle, A. S. (1989), Ozone and Crop Yield, *Annual Review of Phytopathology*, *27*, 397-423, doi:10.1146/annurev.py.27.090189.002145.

Heikes, B., M. H. Lee, D. Jacob, R. Talbot, J. Bradshaw, H. Singh, D. Blake, B. Anderson, H. Fuelberg, and A. M. Thompson (1996), Ozone, hydroperoxides, oxides of nitrogen, and hydrocarbon budgets in the marine boundary layer over the South Atlantic, *Journal of Geophysical Research-Atmospheres*, *101*(D19), 24221-24234, doi:10.1029/95jd03631.

Heikes, B., J. Snow, P. Egli, D. O'Sullivan, J. Crawford, J. Olson, G. Chen, D. Davis, N. Blake, and D. Blake (2001), Formaldehyde over the central Pacific during PEM-Tropics B, *Journal of Geophysical Research-Atmospheres*, *106*(D23), 32717-32731, doi:10.1029/2001jd900012.

Hernández, M. D. A., J. Burkert, L. Reichert, D. Stöbener, J. Meyer-Arnek, J. P. Burrows, R. R. Dickerson, and B. G. Doddridge (2001), Marine boundary layer peroxy radical chemistry during the AEROSOLS99 campaign: Measurements and analysis, *Journal of Geophysical Research*, *106*(D18), 20833, doi:10.1029/2001jd900113.

Holland, E. A., B. H. Braswell, J. Sulzman, and J. F. Lamarque (2005), Nitrogen deposition onto the United States and western Europe: Synthesis of observations and models, *Ecol. Appl.*, *15*(1), 38-57, doi:10.1890/03-5162.

Holland, E. A., F. J. Dentener, B. H. Braswell, and J. M. Sulzman (1999), Contemporary and pre-industrial global reactive nitrogen budgets, *Biogeochemistry*, *46*(1-3), 7-43, doi:10.1023/a:1006148011944.

Holloway, T., H. Levy, and P. Kasibhatla (2000), Global distribution of carbon monoxide, *Journal of Geophysical Research-Atmospheres*, *105*(D10), 12123-12147, doi:10.1029/1999jd901173.

Holton, J. R., P. H. Haynes, M. E. McIntyre, A. R. Douglass, R. B. Rood, and L. Pfister (1995), Stratosphere-Troposphere Exchange, *Reviews of Geophysics*, *33*(4), 403-439, doi:10.1029/95rg02097.

Holzinger, R., C. Warneke, A. Hansel, A. Jordan, W. Lindinger, D. H. Scharffe, G. Schade, and P. J. Crutzen (1999), Biomass burning as a source of formaldehyde, acetaldehyde, methanol, acetone, acetonitrile, and hydrogen cyanide, *Geophysical Research Letters*, *26*(8), 1161-1164, doi:10.1029/1999gl900156.

Hooghiemstra, P. B., M. C. Krol, P. Bergamaschi, A. T. J. de Laat, G. R. van der Werf, P. C. Novelli, M. N. Deeter, I. Aben, and T. Röckmann (2012), Comparing optimized CO emission estimates using MOPITT or NOAA surface network observations, *Journal of Geophysical Research*, *117*(D6), doi:10.1029/2011jd017043.

Hooshiyar, P. A., and H. Niki (1995), Rate constantes for the gas-phase reactions of Cl-Atoms with C2-C-8 alkanes at T=296+/-2K, *International Journal of Chemical Kinetics*, *27*(12), 1197-1206, doi:10.1002/kin.550271206.

Horowitz, L. W., A. M. Fiore, G. P. Milly, R. C. Cohen, A. Perring, P. J. Wooldridge, P. G. Hess, L. K. Emmons, and J. F. Lamarque (2007), Observational constraints on the chemistry of isoprene nitrates over the eastern United States, *Journal of Geophysical Research-Atmospheres*, *112*(D12), doi:10.1029/2006jd007747.

Houyoux, M. R., and J. M. Vukovich (1999), Updates to the Sparse Matrix Operator Kernel Emissions (SMOKE) Modeling System and Integration with Models-3, in *The Emission Inventory: Regional Strategies for the Future*, edited, Air and Waste Management Association, Raleigh, NC.

Hudman, R. C., L. T. Murray, D. J. Jacob, D. B. Millet, S. Turquety, S. Wu, D. R. Blake, A. H. Goldstein, J. Holloway, and G. W. Sachse (2008), Biogenic versus anthropogenic sources of CO in the United States, *Geophysical Research Letters*, *35*(4), 5, doi:10.1029/2007gl032393.

Hurst, D. F., D. W. T. Griffith, and G. D. Cook (1994), Trace Gas Emissions from Biomass Burning in Tropical Australian Savannas, *Journal of Geophysical Research-Atmospheres*, *99*(D8), 16441-16456, doi:10.1029/94jd00670.

Ide, T., T. Nakayama, K. Takahashi, and Y. Matsumi (2008), Thermal decomposition rate of N2O5 measured by cavity ring-down spectroscopy, *International Journal of Chemical Kinetics*, *40*(10), 679-684, doi:10.1002/kin.20351.

IPCC (2013), *Climate Change 2013: The Physical Science Basis. Contribution of Working Group I to the Fifth Assessment Report of the Intergovernmental Panel on Climate Change* 1535 pp., Cambridge University Press, Cambridge, United Kingdom and New York, NY.

Jacob, D. J., et al. (1996), Origin of ozone and NOx in the tropical troposphere: A photochemical analysis of aircraft observations over the South Atlantic basin, *Journal of Geophysical Research-Atmospheres*, *101*(D19), 24235-24250, doi:10.1029/96jd00336.

Jaegle, L., et al. (2000), Photochemistry of HOx in the upper troposphere at northern midlatitudes, *Journal of Geophysical Research-Atmospheres*, *105*(D3), 3877-3892, doi:10.1029/1999jd901016.

Jaegle, L., D. J. Jacob, W. H. Brune, D. Tan, I. C. Faloona, A. J. Weinheimer, B. A. Ridley, T. L. Campos, and G. W. Sachse (1998a), Sources of HOx and production of ozone in the upper troposphere over the United States, *Geophysical Research Letters*, *25*(10), 1709-1712, doi:10.1029/98gl00041.

Jaegle, L., D. J. Jacob, Y. Wang, A. J. Weinheimer, B. A. Ridley, T. L. Campos, G. W. Sachse, and D. E. Hagen (1998b), Sources and chemistry of NOx in the upper troposphere over the United States, *Geophysical Research Letters*, *25*(10), 1705-1708, doi:10.1029/97gl03591.

Jaegle, L., et al. (1997), Observed OH and HO2 in the upper troposphere suggest a major source from convective injection of peroxides, *Geophysical Research Letters*, *24*(24), 3181-3184, doi:10.1029/97gl03004.

Jaegle, L., L. Steinberger, R. V. Martin, and K. Chance (2005), Global partitioning of NOx sources using satellite observations: Relative roles of fossil fuel combustion, biomass burning and soil emissions, *Faraday Discussions*, *130*, 407-423, doi:10.1039/b502128f.

Jaffe, D. A., and N. L. Wigder (2012), Ozone production from wildfires: A critical review, *Atmospheric Environment*, *51*, 1-10, doi:10.1016/j.atmosenv.2011.11.063.

Jenkin, M. E., S. M. Saunders, and M. J. Pilling (1997), The tropospheric degradation of volatile organic compounds: A protocol for mechanism development, *Atmospheric Environment*, *31*(1), 81-104, doi:10.1016/s1352-2310(96)00105-7.

Jenkin, M. E., S. M. Saunders, V. Wagner, and M. J. Pilling (2003), Protocol for the development of the Master Chemical Mechanism, MCM v3 (Part B): tropospheric degradation of aromatic volatile organic compounds, *Atmospheric Chemistry and Physics*, *3*, 181-193.

Jenkin, M. E., J. C. Young, and A. R. Rickard (2015), The MCM v3.3.1 degradation scheme for isoprene, *Atmospheric Chemistry and Physics*, *15*(20), 11433-11459, doi:10.5194/acp-15-11433-2015.

Jerrett, M., R. T. Burnett, C. A. Pope, K. Ito, G. Thurston, D. Krewski, Y. L. Shi, E. Calle, and M. Thun (2009), Long-Term Ozone Exposure and Mortality, *New England Journal of Medicine*, *360*(11), 1085-1095, doi:10.1056/NEJMoa0803894.

Johanson, C. M., and Q. Fu (2009), Hadley Cell Widening: Model Simulations versus Observations, *Journal of Climate*, *22*(10), 2713-2725, doi:10.1175/2008jcli2620.1.

Jones, N. B., K. Riedel, W. Allan, S. Wood, P. I. Palmer, K. Chance, and J. Notholt (2009), Long-term tropospheric formaldehyde concentrations deduced from ground-based fourier transform solar infrared measurements, *Atmospheric Chemistry and Physics*, *9*(18), 7131-7142.

Kaiser, J., et al. (2015), Evidence for an unidentified non-photochemical ground-level source of formaldehyde in the Po Valley with potential implications for ozone production, *Atmospheric Chemistry and Physics*, *15*(3), 1289-1298, doi:10.5194/acp-15-1289-2015.

Kaiser, J. W., et al. (2012), Biomass burning emissions estimated with a global fire assimilation system based on observed fire radiative power, *Biogeosciences*, *9*(1), 527-554, doi:10.5194/bg-9-527-2012.

Kim, S. W., A. Heckel, S. A. McKeen, G. J. Frost, E. Y. Hsie, M. K. Trainer, A. Richter, J. P. Burrows, S. E. Peckham, and G. A. Grell (2006), Satellite-observed US power plant NOx emission reductions and their impact on air quality, *Geophysical Research Letters*, *33*(22), doi:10.1029/2006gl027749.

Kim, S. W., et al. (2016), Modeling the weekly cycle of NOx and CO emissions and their impacts on O3 in the Los Angeles-South Coast Air Basin during the CalNex 2010 field campaign, *Journal of Geophysical Research: Atmospheres*, *121*, 1340-1360, doi:10.1002/2015JD024292.

Kita, K., et al. (2002), Photochemical production of ozone in the upper troposphere in association with cumulus convection over Indonesia, *Journal of Geophysical Research-Atmospheres*, *108*(D3), doi:10.1029/2001jd000844.

Kleinman, L. I. (2002), Ozone production rate and hydrocarbon reactivity in 5 urban areas: A cause of high ozone concentration in Houston, *Geophysical Research Letters*, *29*(10), doi:10.1029/2001gl014569.

Kley, D., H. G. J. Smit, H. Voemel, H. Grassl, V. Ramanathan, P. J. Crutzen, S. Williams, J. Meywerk, and S. J. Oltmans (1997), Tropospheric water-vapour and ozone cross-sections in a zonal plane over the central equatorial Pacific Ocean, *Quarterly Journal of the Royal Meteorological Society*, *123*, 2009-2040.

Kondo, Y., et al. (2004), Impacts of biomass burning in Southeast Asia on ozone and reactive nitrogen over the western Pacific in spring, *Journal of Geophysical Research*, *109*(D15), doi:10.1029/2003jd004203.

Kopacz, M., et al. (2010), Global estimates of CO sources with high resolution by adjoint inversion of multiple satellite datasets (MOPITT, AIRS, SCIAMACHY, TES), *Atmospheric Chemistry and Physics*, *10*(3), 855-876.

Kuhlbusch, T. A., J. M. Lobert, P. J. Crutzen, and P. Warneck (1991), Molecular Nitrogren Emissions from Denitrification during Biomass Burning, *Nature*, *351*(6322), 135-137, doi:10.1038/351135a0.

Labonne, M., F. M. Breon, and F. Chevallier (2007), Injection height of biomass burning aerosols as seen from a spaceborne lidar, *Geophysical Research Letters*, *34*(11), doi:10.1029/2007gl029311.

Lacaux, J. P., R. Delmas, C. Jambert, and T. A. J. Kuhlbusch (1996), NOx emissions from African savanna fires, *Journal of Geophysical Research-Atmospheres*, *101*(D19), 23585-23595, doi:10.1029/96jd01624.

Lamarque, J. F., et al. (2012), CAM-chem: description and evaluation of interactive atmospheric chemistry in the Community Earth System Model, *Geoscientific Model Development*, *5*(2), 369-411, doi:10.5194/gmd-5-369-2012.

Lamarque, J. F., P. Hess, L. Emmons, L. Buja, W. Washington, and C. Granier (2005), Tropospheric ozone evolution between 1890 and 1990, *Journal of Geophysical Research-Atmospheres*, *110*(D8), doi:10.1029/2004jd005537.

Lancaster, D. G., A. Fried, B. Wert, B. Henry, and F. K. Tittel (2000), Difference-frequency-based tunable absorption spectrometer for detection of atmospheric formaldehyde, *Applied Optics*, *39*(24), 4436-4443, doi:10.1364/ao.39.004436.

Lary, D. J. (2005), Halogens and the chemistry of the free troposphere, *Atmospheric Chemistry and Physics*, *5*, 227-237.

Le Breton, M., et al. (2013), Airborne hydrogen cyanide measurements using a chemical ionisation mass spectrometer for the plume identification of biomass burning forest fires, *Atmospheric Chemistry and Physics*, *13*(18), 9217-9232, doi:10.5194/acp-13-9217-2013.

Lelieveld, J., and F. J. Dentener (2000), What controls tropospheric ozone?, *Journal of Geophysical Research-Atmospheres*, *105*(D3), 3531-3551, doi:10.1029/1999jd901011.

Li, C., J. Joiner, N. A. Krotkov, and L. Dunlap (2015), A new method for global retrievals of HCHO total columns from the Suomi National Polar-orbiting Partnership Ozone Mapping and Profiler Suite, *Geophysical Research Letters*, *42*(7), 2515-2522, doi:10.1002/2015gl063204.

Liang, J. Y., L. W. Horowitz, D. J. Jacob, Y. H. Wang, A. M. Fiore, J. A. Logan, G. M. Gardner, and J. W. Munger (1998), Seasonal budgets of reactive nitrogen species and ozone over the United States, and export fluxes to the global atmosphere, *Journal of Geophysical Research-Atmospheres*, *103*(D11), 13435-13450, doi:10.1029/97jd03126.

Liao, J., et al. (2012), Observations of inorganic bromine (HOBr, BrO, and Br2) speciation at Barrow, Alaska, in spring 2009, *Journal of Geophysical Research*, *117*, doi:10.1029/2011jd016641.

Lin, M. Y., L. W. Horowitz, S. J. Oltmans, A. M. Fiore, and S. M. Fan (2014), Tropospheric ozone trends at Mauna Loa Observatory tied to decadal climate variability, *Nature Geoscience*, *7*(2), 136-143, doi:10.1038/ngeo2066.

Lindhjem, C. E., A. K. Pollack, A. DenBleyker, and S. L. Shaw (2012), Effects of improved spatial and temporal modeling of on-road vehicle emissions, *Journal of the Air & Waste Management Association*, *62*(4), 471-484, doi:10.1080/10962247.2012.658955.

Lindinger, W., A. Hansel, and A. Jordan (1998), Proton-transfer-reaction mass spectrometry (PTR-MS): on-line monitoring of volatile organic compounds at pptv levels, *Chemical Society reviews*, *27*(5), 347-354, doi:10.1039/a827347z.

Lipari, F., and S. J. Swarin (1982), Determination of formaldehyde and other aldehydes in autmobile exhaust with an improved 2,4-dinitrophenylhydrazine method, *Journal of Chromatography*, *247*(2), 297-306, doi:10.1016/s0021-9673(00)85953-1.

Lobert, J. M., D. H. Scharffe, W. M. Hao, and P. J. Crutzen (1990), Importance of Biomass Burning in the Atmospheric Budgets of Nitrogen-Containing Gases, *Nature*, *346*(6284), 552-554, doi:10.1038/346552a0.

Logan, J. A. (1989), Ozone in Rural Areas of the United States, *Journal of Geophysical Research-Atmospheres*, *94*(D6), 8511-8532, doi:10.1029/JD094iD06p08511.

Logan, J. A., M. J. Prather, S. C. Wofsy, and M. B. McElroy (1981), Tropospheric chemistry - A global perspective, *Journal of Geophysical Research-Oceans and Atmospheres*, *86*(NC8), 7210-7254, doi:10.1029/JC086iC08p07210.

Loughner, C. P., et al. (2014), Impact of bay breeze circulations on surface air quality and boundary layer export, *Journal of Applied Meteorology and Climatology*, doi:http://dx.doi.org/10.1175/JAMC-D-13-0323.1.

Lu, Z., D. G. Streets, B. de Foy, L. N. Lamsal, B. N. Duncan, and J. Xing (2015), Emissions of nitrogen oxides from US urban areas: estimation from Ozone Monitoring Instrument retrievals for 2005–2014, *Atmospheric Chemistry and Physics Discussions*, *15*(10), 14961-15003, doi:10.5194/acpd-15-14961-2015.

Madronich, S. (1992), Implications of recent total atmospheric ozone measurements for biologically-active ultraviolet-radiation reaching the earth's surface, *Geophysical Research Letters*, *19*(1), 37-40, doi:10.1029/91gl02954.

Mahajan, A. S., L. K. Whalley, E. Kozlova, H. Oetjen, L. Mendez, K. L. Furneaux, A. Goddard, D. E. Heard, J. M. C. Plane, and A. Saiz-Lopez (2010), DOAS observations of formaldehyde and its impact on the HOx balance in the tropical Atlantic marine boundary layer, *Journal of Atmospheric Chemistry*, *66*(3), 167-178, doi:10.1007/s10874-011-9200-7.

Mapes, B. E., and P. Zuidema (1995), Radiative-Dynamical Consequences of Dry Tongues in the Tropical Troposphere, *Journal of the Atmospheric Sciences*, *53*(4), 620-638.

Marbach, T., S. Beirle, U. Platt, P. Hoor, F. Wittrock, A. Richter, M. Vrekoussis, M. Grzegorski, J. P. Burrows, and T. Wagner (2009), Satellite measurements of formaldehyde linked to shipping emissions, *Atmospheric Chemistry and Physics*, *9*(21), 8223-8234, doi:10.5194/acp-9-8223-2009.

Martin, R. V., D. J. Jacob, K. Chance, T. P. Kurosu, P. I. Palmer, and M. J. Evans (2003), Global inventory of nitrogen oxide emissions constrained by space-based observations of NO2 columns, *Journal of Geophysical Research-Atmospheres*, *108*(D17), doi:10.1029/2003jd003453.

Maryland Department of the Environment, edited.

Mauzerall, D. L., J. A. Logan, D. J. Jacob, B. E. Anderson, D. R. Blake, J. D. Bradshaw, B. Heikes, G. W. Sachse, H. Singh, and B. Talbot (1998), Photochemistry in biomass burning plumes and implications for tropospheric ozone over the tropical South Atlantic, *Journal of Geophysical Research-Atmospheres*, *103*(D7), 8401-8423, doi:10.1029/97jd02612.

McDonald, B. C., R. Ahmadov, S. A. McKeen, S.-W. Kim, G. Frost, and M. Trainer (2015), Modeling Ozone in the Eastern United States Using a Fuel-Based Mobile Source Emissions Inventory, in *American Geophysical Union*, edited, San Francisco.

McDonald, B. C., T. R. Dallmann, E. W. Martin, and R. A. Harley (2012), Long-term trends in nitrogen oxide emissions from motor vehicles at national, state, and air basin scales, *Journal of Geophysical Research: Atmospheres*, *117*(D21), n/a-n/a, doi:10.1029/2012jd018304.

McFarland, M., D. Kley, J. W. Drummond, A. L. Schmeltekopf, and R. H. Winkler (1979), Nitric-Oxide measurements in the equatorial Pacifc region, *Geophysical Research Letters*, *6*(7), 605-608, doi:10.1029/GL006i007p00605.

McGrath, J. M., A. M. Betzelberger, S. Wang, E. Shook, X.-G. Zhu, S. P. Long, and E. A. Ainsworth (2015), An analysis of ozone damage to historical maize and soybean yields in the United States, *Proceedings of the National Academy of Sciences*, 201509777, doi:10.1073/pnas.1509777112.

Meinshausen, M., et al. (2011), The RCP greenhouse gas concentrations and their extensions from 1765 to 2300, *Climatic Change*, *109*(1-2), 213-241, doi:10.1007/s10584-011-0156-z.

Meyers, T. P., B. B. Hicks, R. P. Hosker, J. D. Womack, and L. C. Satterfield (1991), Dry deposition inferential measurement techniques 2: Seasonal and annual deposition rates of sulfur and nitrate, *Atmospheric Environment Part a-General Topics*, *25*(10), 2361-2370, doi:10.1016/0960-1686(91)90110-s.

Millet, D. B., et al. (2010), Global atmospheric budget of acetaldehyde: 3-D model analysis and constraints from in-situ and satellite observations, *Atmospheric Chemistry and Physics*, *10*(7), 3405-3425, doi:10.5194/acp-10-3405-2010.

Millet, D. B., et al. (2006), Formaldehyde distribution over North America: Implications for satellite retrievals of formaldehyde columns and isoprene emission, *Journal of Geophysical Research-Atmospheres*, *111*(D24), doi:10.1029/2005jd006853.

Morales, R. (1998), Carbon Monoxide, Ozone, and Hydrocarbons in the Baltimore Metropolitan Area, University of Maryland, College Park.

Moxim, W. J., H. Levy, and P. S. Kasibhatla (1996), Simulated global tropospheric PAN: Its transport and impact on NOx, *Journal of Geophysical Research-Atmospheres*, *101*(D7), 12621-12638, doi:10.1029/96jd00338.

Mulik, J., R. Puckett, D. Williams, and E. Sawicki (1976), Ion Chromotographic Analysis of Sulfate and Nitrate in Ambient Aerosols, *Analytical Letters*, *9*(7), 653-663.

Nault, B. A., C. Garland, S. E. Pusede, P. J. Wooldridge, K. Ullmann, S. R. Hall, and R. C. Cohen (2015), Measurements of CH3O2NO2 in the upper troposphere, *Atmospheric Measurement Techniques*, *8*(2), 987-997, doi:10.5194/amt-8-987-2015.

Newell, R. E., V. Thouret, J. Y. N. Cho, P. Stoller, A. Marenco, and H. G. Smit (1999), Ubiquity of quasi-horizontal layers in the troposphere, *Nature*, *398*(6725), 316-319, doi:10.1038/18642.

Nicely, J. M., et al. (2016), An Observationally Constrained Evaluation of the Oxidative Capacity in the Tropical Western Pacific, *Journal of Geophysical Research - Atmospheres*, *in review*.

Oltmans, S. J., et al. (2001), Ozone in the Pacific tropical troposphere from ozonesonde observations, *Journal of Geophysical Research-Atmospheres*, *106*(D23), 32503-32525, doi:10.1029/2000jd900834.

Oltmans, S. J., et al. (2006), Long-term changes in tropospheric ozone, *Atmospheric Environment*, *40*(17), 3156-3173, doi:10.1016/j.atmosenv.2006.01.029.

Orlando, J. J., G. S. Tyndall, and J. G. Calvert (1992), Thermal-decomposition pathways for peroxyacetyl nitrate (PAN) - Implications for atmospheric methyl nitrate levels, *Atmospheric Environment Part a-General Topics*, *26*(17), 3111-3118, doi:10.1016/0960-1686(92)90468-z.

Palmer, P. I., D. J. Jacob, A. M. Fiore, R. V. Martin, K. Chance, and T. P. Kurosu (2003), Mapping isoprene emissions over North America using formaldehyde column observations from space, *Journal of Geophysical Research-Atmospheres*, *108*(D6), doi:10.1029/2002jd002153.

Pan, L. L., et al. (2016), The Convective Transport of Active Species in the Tropics (CONTRAST) Experiment, *Bulletin of the American Meteorological Sciences*, doi:10.1175/BAMS-D-14-00272.1.

Pan, L. L., et al. (2014), Thunderstorms enhance tropospheric ozone by wrapping and shedding stratospheric air, *Geophysical Research Letters*, *41*(22), 7785-7790, doi:10.1002/2014gl061921.

Pan, L. L., et al. (2015), Bimodal Distribution of Tropical Free Tropospheric Ozone over the Western Pacific Revealed by Airborne Observations, *Geophysical Research Letters*, *42*, doi:10.1002/2015GL065562.

Pan, L. L., J. C. Wei, D. E. Kinnison, R. R. Garcia, D. J. Wuebbles, and G. P. Brasseur (2007), A set of diagnostics for evaluating chemistry-climate models in the extratropical tropopause region, *Journal of Geophysical Research*, *112*(D9), doi:10.1029/2006jd007792.

Paris, J. D., A. Stohl, P. Nedelec, M. Y. Arshinov, M. V. Panchenko, V. P. Shmargunov, K. S. Law, B. D. Belan, and P. Ciais (2009), Wildfire smoke in the Siberian Arctic in summer: source characterization and plume evolution from airborne measurements, *Atmospheric Chemistry and Physics*, *9*(23), 9315-9327.

Park, S. K., M. S. O'Neill, P. S. Vokonas, D. Sparrow, and J. Schwartz (2005), Effects of air pollution on heart rate variability: The VA Normative Aging Study, *Environmental health perspectives*, *113*(3), 304-309, doi:10.1289/ehp.7447.

Parrington, M., et al. (2013), Ozone photochemistry in boreal biomass burning plumes, *Atmospheric Chemistry and Physics*, *13*(15), 7321-7341, doi:10.5194/acp-13-7321-2013.

Parrish, D. D. (2006), Critical evaluation of US on-road vehicle emission inventories, *Atmospheric Environment*, *40*(13), 2288-2300, doi:10.1016/j.atmosenv.2005.11.033.

Parrish, D. D., et al. (2012), Primary and secondary sources of formaldehyde in urban atmospheres: Houston Texas region, *Atmospheric Chemistry and Physics*, *12*(7), 3273-3288, doi:10.5194/acp-12-3273-2012.

Parrish, D. D., A. Stohl, C. Forster, E. L. Atlas, D. R. Blake, P. D. Goldan, W. C. Kuster, and J. A. de Gouw (2007), Effects of mixing on evolution of hydrocarbon ratios in the troposphere, *Journal of Geophysical Research-Atmospheres*, *112*(D10), doi:10.1029/2006jd007583.

Parsons, D. B., K. Yoneyama, and J. L. Redelsperger (2000), The evolution of the tropical western Pacific atmosphere-ocean system following the arrival of a dry intrusion, *Quarterly Journal of the Royal Meteorological Society*, *126*(563), 517-548, doi:10.1256/smsqj.56306.

Parton, W. J., E. A. Holland, S. J. Del Grosso, M. D. Hartman, R. E. Martin, A. R. Mosier, D. S. Ojima, and D. S. Schimel (2001), Generalized model for NOx and N2O

emissions from soils, *Journal of Geophysical Research-Atmospheres*, *106*(D15), 17403-17419, doi:10.1029/2001jd900101.

Paulot, F., J. D. Crounse, H. G. Kjaergaard, J. H. Kroll, J. H. Seinfeld, and P. O. Wennberg (2009), Isoprene photooxidation: new insights into the production of acids and organic nitrates, *Atmospheric Chemistry and Physics*, *9*(4), 1479-1501.

Paulot, F., D. K. Henze, and P. O. Wennberg (2012), Impact of the isoprene photochemical cascade on tropical ozone, *Atmospheric Chemistry and Physics*, *12*(3), 1307-1325, doi:10.5194/acp-12-1307-2012.

Perring, A. E., et al. (2009), Airborne observations of total RONO2: new constraints on the yield and lifetime of isoprene nitrates, *Atmospheric Chemistry and Physics*, *9*(4), 1451-1463.

Peters, E., F. Wittrock, K. Grossmann, U. Friess, A. Richter, and J. P. Burrows (2012), Formaldehyde and nitrogen dioxide over the remote western Pacific Ocean: SCIAMACHY and GOME-2 validation using ship-based MAX-DOAS observations, *Atmospheric Chemistry and Physics*, *12*(22), 11179-11197, doi:10.5194/acp-12-11179-2012.

Pickering, K. E., A. M. Thompson, J. R. Scala, W. K. Tao, and J. Simpson (1992), Ozone production potential following convective redistribution of biomass burning emissions, *Journal of Atmospheric Chemistry*, *14*(1-4), 297-313, doi:10.1007/bf00115241.

Pickering, K. E., et al. (1996), Convective transport of biomass burning emissions over Brazil during TRACE A, *Journal of Geophysical Research-Atmospheres*, *101*(D19), 23993-24012, doi:10.1029/96jd00346.

Pollack, I. B., T. B. Ryerson, M. Trainer, J. A. Neuman, J. M. Roberts, and D. D. Parrish (2013), Trends in ozone, its precursors, and related secondary oxidation products in Los Angeles, California: A synthesis of measurements from 1960 to 2010, *Journal of Geophysical Research-Atmospheres*, *118*(11), 5893-5911, doi:10.1002/jgrd.50472.

Poppe, D., R. Koppmann, and J. Rudolph (1998), Ozone formation in biomass burning plumes: Influence of atmospheric dilution, *Geophysical Research Letters*, *25*(20), 3823-3826, doi:10.1029/1998gl900046.

Prados, A. I., R. R. Dickerson, B. G. Doddridge, P. A. Milne, J. L. Moody, and J. T. Merrill (1999), Transport of ozone and pollutants from North America to the North Atlantic Ocean during the 1996 Atmosphere/Ocean Chemistry Experiment (AEROCE) intensive, *Journal of Geophysical Research*, *104*(D21), 26219, doi:10.1029/1999jd900444.

Prather, M. J., and D. J. Jacob (1997), A persistent imbalance in HOx and NOx photochemistry of the upper troposphere driven by deep tropical convection, *Geophysical Research Letters*, *24*(24), 3189-3192, doi:10.1029/97gl03027.

Rappenglueck, B., G. Lubertino, S. Alvarez, J. Golovko, B. Czader, and L. Ackermann (2013), Radical precursors and related species from traffic as observed and modeled at an urban highway junction, *Journal of the Air & Waste Management Association*, *63*(11), 1270-1286, doi:10.1080/10962247.2013.822438.

Read, K. A., L. J. Carpenter, S. R. Arnold, R. Beale, P. D. Nightingale, J. R. Hopkins, A. C. Lewis, J. D. Lee, L. Mendes, and S. J. Pickering (2012), Multiannual Observations of Acetone, Methanol, and Acetaldehyde in Remote Tropical Atlantic Air: Implications for Atmospheric OVOC Budgets and Oxidative Capacity, *Environmental Science & Technology*, *46*(20), 11028-11039, doi:10.1021/es302082p.

Read, K. A., et al. (2008), Extensive halogen-mediated ozone destruction over the tropical Atlantic Ocean, *Nature*, *453*(7199), 1232-1235, doi:10.1038/nature07035.

Rex, M., et al. (2014), A tropical West Pacific OH minimum and implications for stratospheric composition, *Atmospheric Chemistry and Physics*, *14*(9), 4827-4841, doi:10.5194/acp-14-4827-2014.

Rhoads, K. P., P. Kelley, R. R. Dickerson, T. P. Carsey, M. Farmer, D. L. Savoie, and J. M. Prospero (1997), Composition of the troposphere over the Indian Ocean during the monsoonal transition, *Journal of Geophysical Research-Atmospheres*, *102*(D15), 18981-18995, doi:10.1029/97jd01078.

Ridder, T., C. Gerbig, J. Notholt, M. Rex, O. Schrems, T. Warneke, and L. Zhang (2012), Ship-borne FTIR measurements of CO and O3 in the Western Pacific from 43° N to 35° S: an evaluation of the sources, *Atmospheric Chemistry and Physics*, *12*(2), 815-828, doi:10.5194/acp-12-815-2012.

Ridley, B. A., and F. E. Grahek (1990), A Small, Low-Flow, High-Sensitivity Reaction Vessel for NO Chemiluminescence Detectors, *Journal of Atmospheric and Oceanic Technology*, *7*(2), 307-311, doi:10.1175/1520-0426(1990)007<0307:aslfhs>2.0.co;2.

Roy, A. A., P. J. Adams, and A. L. Robinson (2014), Air pollutant emissions from the development, production, and processing of Marcellus Shale natural gas, *Journal of the Air & Waste Management Association*, *64*(1), 19-37, doi:10.1080/10962247.2013.826151.

Rudolph, J., B. Ramacher, C. PlassDulmer, K. P. Muller, and R. Koppmann (1997), The indirect determination of chlorine atom concentration in the troposphere from changes in the patterns of non-methane hydrocarbons, *Tellus Series B-Chemical and Physical Meteorology*, *49*(5), 592-601, doi:10.1034/j.1600-0889.49.issue5.13.x.

Sachse, G. W., G. F. Hill, L. O. Wade, and M. G. Perry (1987), Fast-Response, High-Precision Carbon Monoxide Sensor using a Tunable Diode Laser Absorption Technique, *Journal of Geophysical Research-Atmospheres*, *92*(D2), 2071-2081, doi:10.1029/JD092iD02p02071.

Salawitch, R. J., et al. (2002), Chemical loss of ozone during the Arctic winter of 1999/2000: An analysis based on balloon-borne observations, *Journal of Geophysical Research-Atmospheres*, *107*(D20), doi:10.1029/2001jd000620.

Sander, R., et al. (2011a), The atmospheric chemistry box model CAABA/MECCA-3.0, *Geoscientific Model Development*, *4*(2), 373-380, doi:10.5194/gmd-4-373-2011.

Sander, S. P., et al. (2011b), Chemical Kinetics and Photochemical Data for Use in Atmospheric Studies, Evaluation No. 17, *JPL Publication 10-6 Rep.*, Jet Propulsion Laboratory, Pasadena, CA.

Saunders, S. M., M. E. Jenkin, R. G. Derwent, and M. J. Pilling (2003), Protocol for the development of the Master Chemical Mechanism, MCM v3 (Part A): tropospheric degradation of non-aromatic volatile organic compounds, *Atmospheric Chemistry and Physics*, *3*, 161-180.

Sauvage, B., V. Thouret, A. M. Thompson, J. C. Witte, J. P. Cammas, P. Nedelec, and G. Athier (2006), Enhanced view of the "tropical Atlantic ozone paradox" and "zonal wave one" from the in situ MOZAIC and SHADOZ data, *Journal of Geophysical Research-Atmospheres*, *111*(D1), doi:10.1029/2005jd006241.

Schumann, U., and H. Huntrieser (2007), The global lightning-induced nitrogen oxides source, *Atmospheric Chemistry and Physics*, *7*(14), 3823-3907.

Seinfeld, J. H., and S. N. Pandis (2006), *Atmospheric Chemistry and Physics: From Air Pollution to Climate Change*, 2 ed., 1203 pp., John Wiley & Sons, Hoboken, NJ.

Selin, N. E., S. Wu, K. M. Nam, J. M. Reilly, S. Paltsev, R. G. Prinn, and M. D. Webster (2009), Global health and economic impacts of future ozone pollution, *Environmental Research Letters*, *4*(4), doi:10.1088/1748-9326/4/4/044014.

Shen, L., L. J. Mickley, and A. P. K. Tai (2015), Influence of synoptic patterns on surface ozone variability over the eastern United States from 1980 to 2012, *Atmospheric Chemistry and Physics*, *15*, 10925-10938, doi:10.5194/acp-15-10925-2015.

Shetter, R. E., and M. Muller (1999), Photolysis frequency measurements using actinic flux spectroradiometry during the PEM-Tropics mission: Instrumentation description and some results, *Journal of Geophysical Research-Atmospheres*, *104*(D5), 5647-5661, doi:10.1029/98jd01381.

Shindell, D., and G. Faluvegi (2009), Climate response to regional radiative forcing during the twentieth century, *Nature Geoscience*, *2*(4), 294-300, doi:10.1038/ngeo473.

Silva, R. A., et al. (2013), Global premature mortality due to anthropogenic outdoor air pollution and the contribution of past climate change, *Environmental Research Letters*, *8*(3), doi:10.1088/1748-9326/8/3/034005.

Singh, H. B., et al. (2004), Analysis of the atmospheric distribution, sources, and sinks of oxygenated volatile organic chemicals based on measurements over the Pacific during TRACE-P, *Journal of Geophysical Research-Atmospheres*, *109*(D15), doi:10.1029/2003jd003883.

Singh, H. B., et al. (2000), Biomass burning influences on the composition of the remote South Pacific troposphere: analysis based on observations from PEM-Tropics-A, *Atmospheric Environment*, *34*(4), 635-644, doi:10.1016/s1352-2310(99)00380-5.

Skalska, K., J. S. Miller, and S. Ledakowicz (2010), Trends in NOx abatement: A review, *Science of the Total Environment*, *408*(19), 3976-3989, doi:10.1016/j.scitotenv.2010.06.001.

Snow, J. A., B. G. Heikes, H. Shen, D. W. O'Sullivan, A. Fried, and J. Walega (2007), Hydrogen peroxide, methyl hydroperoxide, and formaldehyde over North America and the North Atlantic, *Journal of Geophysical Research-Atmospheres*, *112*(D12), doi:10.1029/2006jd007746.

Sprenger, M. (2003), A northern hemispheric climatology of cross-tropopause exchange for the ERA15 time period (1979–1993), *Journal of Geophysical Research*, *108*(D12), doi:10.1029/2002jd002636.

Staehelin, J., J. Thudium, R. Buehler, A. Volzthomas, and W. Graber (1994), Trends in Surface Ozone Concentrations at Arosa (Switzerland), *Atmospheric Environment*, *28*(1), 75-87, doi:10.1016/1352-2310(94)90024-8.

Staudt, A. C., D. J. Jacob, J. A. Logan, D. Bachiochi, T. N. Krishnamurti, and N. Poisson (2002), Global chemical model analysis of biomass burning and lightning influences over the South Pacific in austral spring, *Journal of Geophysical Research-Atmospheres*, *107*(D14), doi:10.1029/2000jd000296.

Stein, A. F., R. R. Draxler, G. D. Rolph, B. J. B. Stunder, M. D. Cohen, and F. Ngan (2015), NOAA's HYSPLIT Atmospheric Transport and Dispersion Modeling System, *Bulletin of the American Meteorological Society*, *96*(12), 2059-2077, doi:10.1175/bams-d-14-00110.1.

Stevenson, D. S., et al. (2006), Multimodel ensemble simulations of present-day and near-future tropospheric ozone, *Journal of Geophysical Research-Atmospheres*, *111*(D8), doi:10.1029/2005jd006338.

Stevenson, D. S., et al. (2013), Tropospheric ozone changes, radiative forcing and attribution to emissions in the Atmospheric Chemistry and Climate Model Intercomparison Project (ACCMIP), *Atmospheric Chemistry and Physics*, *13*(6), 3063-3085, doi:10.5194/acp-13-3063-2013.

Stickler, A., et al. (2007), Chemistry, transport and dry deposition of trace gases in the boundary layer over the tropical Atlantic Ocean and the Guyanas during the GABRIEL field campaign, *Atmospheric Chemistry and Physics*, *7*(14), 3933-3956.

Stickler, A., H. Fischer, J. Williams, M. de Reus, R. Sander, M. G. Lawrence, J. N. Crowley, and J. Lelieveld (2006), Influence of summertime deep convection on formaldehyde in the middle and upper troposphere over Europe, *Journal of Geophysical Research*, *111*(D14), doi:10.1029/2005jd007001.

Still, T. J., S. Al-Haider, P. W. Seakins, R. Sommariva, J. C. Stanton, G. Mills, and S. A. Penkett (2006), Ambient formaldehyde measurements made at a remote marine boundary layer site during the NAMBLEX campaign - a comparison of data from chromatographic and modified Hantzsch techniques, *Atmospheric Chemistry and Physics*, *6*, 2711-2726.

Stohl, A., et al. (2003), Stratosphere-troposphere exchange: A review, and what we have learned from STACCATO, *Journal of Geophysical Research-Atmospheres*, *108*(D12), doi:10.1029/2002jd002490.

Stoller, P., et al. (1999), Measurements of atmospheric layers from the NASA DC-8 and P-3B aircraft during PEM-Tropics A, *Journal of Geophysical Research-Atmospheres*, *104*(D5), 5745-5764, doi:10.1029/98jd02717.

Susskind, J., G. Molnar, L. Iredell, and N. G. Loeb (2012), Interannual variability of outgoing longwave radiation as observed by AIRS and CERES, *Journal of Geophysical Research-Atmospheres*, *117*, doi:10.1029/2012jd017997.

Thompson, A. M. (1980), Wet and dry removal of tropospheric formaldehyde at a coastal site, *Tellus*, *32*(4), 376-383.

Thompson, A. M., et al. (2012), Southern Hemisphere Additional Ozonesondes (SHADOZ) ozone climatology (2005-2009): Tropospheric and tropical tropopause layer (TTL) profiles with comparisons to OMI-based ozone products, *Journal of Geophysical Research-Atmospheres*, *117*, doi:10.1029/2011jd016911.

Thompson, A. M., K. E. Pickering, D. P. McNamara, M. R. Schoeberl, R. D. Hudson, J. H. Kim, E. V. Browell, V. Kirchhoff, and D. Nganga (1996), Where did tropospheric ozone over southern Africa and the tropical Atlantic come from in October 1992? Insights from TOMS, GTE TRACE A, and SAFARI 1992, *Journal of Geophysical Research-Atmospheres*, *101*(D19), 24251-24278, doi:10.1029/96jd01463.

Thornton, J. A., et al. (2002), Ozone production rates as a function of NOx abundances and HOx production rates in the Nashville urban plume, *Journal of Geophysical Research-Atmospheres*, *107*(D12), doi:10.1029/2001jd000932.

Tian, B., E. J. Fetzer, B. H. Kahn, J. Teixeira, E. Manning, and T. Hearty (2013), Evaluating CMIP5 models using AIRS tropospheric air temperature and specific humidity climatology, *Journal of Geophysical Research-Atmospheres*, *118*(1), 114-134, doi:10.1029/2012jd018607.

Tost, H., P. Joeckel, A. Kerkweg, A. Pozzer, R. Sander, and J. Lelieveld (2007), Global cloud and precipitation chemistry and wet deposition: tropospheric model simulations with ECHAM5/MESSy1, *Atmospheric Chemistry and Physics*, *7*(10), 2733-2757.

Toyota, K., Y. Kanaya, M. Takahashi, and H. Akimoto (2004), A box model study on photochemical interactions between VOCs and reactive halogen species in the marine boundary layer, *Atmospheric Chemistry and Physics*, *4*, 1961-1987.

Travis, K. R., et al. (2016), NOx emissions, isoprene oxidation pathways, vertical mixing, and implications for surface ozone in the Southeast United States, *Atmospheric Chemistry and Physics Discussions*, doi:10.5194/acp-2016-110.

Turpin, B. J., and H.-J. Lim (2001), Species Contributions to PM2.5 Mass Concentrations: Revisiting Common Assumptions for Estimating Organic Mass, *Aerosol Science and Technology*, *35*(1), 602-610, doi:10.1080/02786820119445.

US EPA (2005), Acid rain program, 2004 progress report, *EPA Rep. EPA 430-R-05-012 Rep.*, Washington, D.C.

US EPA (2008), Integrated Science Assessment for Oxides of Nitrogen - Health Criteria, *EPA/600/R-08/071 Rep.*, US EPA, Washington, DC.

US EPA (2010), Integrated Science Assessment for Carbon Monoxide, *EPA/600/R-09/019F Rep.*, United States Environmental Protection Agency, Washington, DC.

US EPA (2011), Emissions Inventory Final Rule TSD, *EPA-HQ-OAR-2009-0491 Rep.*, U.S. Environmental Protection Agency Office of Air and Radiation, Office of Air Quality Planning and Standards, Air Quality Assessment Division, Washington, DC.

US EPA (2012), User Guide for MOVES2010b *EPA-420-B-12-001b Rep.*, 202 pp, Office of Transportation and Air Quality, US Environmental Protection Agency, Washington, DC.

Van Dingenen, R., F. J. Dentener, F. Raes, M. C. Krol, L. Emberson, and J. Cofala (2009), The global impact of ozone on agricultural crop yields under current and future air quality legislation, *Atmospheric Environment*, *43*(3), 604-618, doi:10.1016/j.atmosenv.2008.10.033.

van Vuuren, D. P., et al. (2011), The representative concentration pathways: an overview, *Climatic Change*, *109*(1-2), 5-31, doi:10.1007/s10584-011-0148-z.

Verstraeten, W. W., J. L. Neu, J. E. Williams, K. W. Bowman, J. R. Worden, and K. F. Boersma (2015), Rapid increases in tropospheric ozone production and export from China, *Nature Geoscience*, *8*(9), 690-695, doi:10.1038/ngeo2493.

Vestreng, V., L. Ntziachristos, A. Semb, S. Reis, I. S. A. Isaksen, and L. Tarrason (2009), Evolution of NOx emissions in Europe with focus on road transport control measures, *Atmospheric Chemistry and Physics*, *9*(4), 1503-1520, doi:10.5194/acp-9-1503-2009.

Vigouroux, C., et al. (2009), Ground-based FTIR and MAX-DOAS observations of formaldehyde at Reunion Island and comparisons with satellite and model data, *Atmospheric Chemistry and Physics*, *9*(24), 9523-9544.

Volkamer, R., P. Sheehy, L. T. Molina, and M. J. Molina (2010), Oxidative capacity of the Mexico City atmosphere - Part 1: A radical source perspective, *Atmospheric Chemistry and Physics*, *10*(14), 6969-6991, doi:10.5194/acp-10-6969-2010.

Voulgarakis, A., M. E. Marlier, G. Faluvegi, D. T. Shindell, K. Tsigaridis, and S. Mangeon (2015), Interannual variability of tropospheric trace gases and aerosols: The role of biomass burning emissions, *Journal of Geophysical Research: Atmospheres*, *120*(14), 7157-7173, doi:10.1002/2014jd022926.

Wagner, V., R. von Glasow, H. Fischer, and P. J. Crutzen (2002), Are CH2O measurements in the marine boundary layer suitable for testing the current understanding of CH4 photooxidation?: A model study, *Journal of Geophysical Research*, *107*(D3), doi:10.1029/2001JD000722.

Wang, T., V. T. F. Cheung, M. Anson, and Y. S. Li (2001), Ozone and related gaseous pollutants in the boundary layer of eastern China: Overview of the recent measurements at a rural site, *Geophysical Research Letters*, *28*(12), 2373-2376, doi:10.1029/2000gl012378.

Wang, T., X. L. Wei, A. J. Ding, C. N. Poon, K. S. Lam, Y. S. Li, L. Y. Chan, and M. Anson (2009), Increasing surface ozone concentrations in the background atmosphere of Southern China, 1994-2007, *Atmospheric Chemistry and Physics*, *9*(16), 6217-6227.

Waugh, D. W. (2005), Impact of potential vorticity intrusions on subtropical upper tropospheric humidity, *Journal of Geophysical Research-Atmospheres*, *110*(D11), doi:10.1029/2004jd005664.

Waugh, D. W., and L. M. Polvani (2000), Climatology of intrusions into the tropical upper troposphere, *Geophysical Research Letters*, *27*(23), 3857-3860, doi:10.1029/2000gl012250.

Waugh, D. W., L. M. Polvani, and R. A. Plumb (1994), Nonlinear, Barotropic Response to a Localized Topographic Forcing - Formation of a Tropical Surf Zone and its Effect on Interhemispheric Propagation, *Journal of the Atmospheric Sciences*, *51*(11), 1401-1416, doi:10.1175/1520-0469(1994)051<1401:nbrtal>2.0.co;2.

Wayne, R. P., et al. (1991), The Nitrate Radical - Physics, Chemistry and the Atmosphere, *Atmospheric Environment Part a-General Topics*, *25*(1), 1-203, doi:10.1016/0960-1686(91)90192-a.

Whalley, L. K., et al. (2010), The chemistry of OH and HO2 radicals in the boundary layer over the tropical Atlantic Ocean, *Atmospheric Chemistry and Physics*, *10*(4), 1555-1576, doi:10.5194/acp-10-1555-2010.

Wiedinmyer, C., S. K. Akagi, R. J. Yokelson, L. K. Emmons, J. A. Al-Saadi, J. J. Orlando, and A. J. Soja (2011), The Fire INventory from NCAR (FINN): a high resolution global model to estimate the emissions from open burning, *Geoscientific Model Development*, *4*(3), 625-641, doi:10.5194/gmd-4-625-2011.

Williams, E. J., B. M. Lerner, P. C. Murphy, S. C. Herndon, and M. S. Zahniser (2009), Emissions of NOx, SO2, CO, and HCHO from commercial marine shipping during Texas Air Quality Study (TexAQS) 2006, *Journal of Geophysical Research-Atmospheres*, *114*, doi:10.1029/2009jd012094.

Wolfe, G. M., and J. A. Thornton (2011), The Chemistry of Atmosphere-Forest Exchange (CAFE) Model – Part 1: Model description and characterization, *Atmospheric Chemistry and Physics*, *11*(1), 77-101, doi:10.5194/acp-11-77-2011.

Worden, H. M., M. N. Deeter, D. P. Edwards, J. C. Gille, J. R. Drummond, and P. Nedelec (2010), Observations of near-surface carbon monoxide from space using MOPITT multispectral retrievals, *Journal of Geophysical Research-Atmospheres*, *115*, doi:10.1029/2010jd014242.

Yokelson, R. J., R. Susott, D. E. Ward, J. Reardon, and D. W. T. Griffith (1997), Emissions from smoldering combustion of biomass measured by open-path Fourier transform infrared spectroscopy, *Journal of Geophysical Research-Atmospheres*, *102*(D15), 18865-18877, doi:10.1029/97jd00852.

Yoneyama, K., and D. B. Parsons (1999), A proposed mechanism for the intrusion of dry air into the Tropical Western Pacific region, *Journal of the Atmospheric Sciences*, *56*(11), 1524-1546, doi:10.1175/1520-0469(1999)056<1524:apmfti>2.0.co;2.

Yu, S., R. Mathur, J. Pleim, G. Pouliot, D. Wong, B. Eder, K. Schere, R. Gilliam, and S. T. Rao (2012), Comparative evaluation of the impact of WRF-NMM and WRF-ARW meteorology on CMAQ simulations for O3 and related species during the 2006 TexAQS/GoMACCS campaign, *Atmospheric Pollution Research*, doi:10.5094/apr.2012.015.

Zeng, G., J. E. Williams, J. A. Fisher, L. K. Emmons, N. B. Jones, O. Morgenstern, J. Robinson, D. Smale, C. Paton-Walsh, and D. W. T. Griffith (2015), Multi-model simulation of CO and HCHO in the Southern Hemisphere: comparison with observations and impact of biogenic emissions, *Atmospheric Chemistry and Physics*, *15*(13), 7217-7245, doi:10.5194/acp-15-7217-2015.

Zhou, X. L., and K. Mopper (1997), Photochemical production of low-molecular-weight carbonyl compounds in seawater and surface microlayer and their air-sea exchange, *Marine Chemistry*, *56*(3-4), 201-213, doi:10.1016/s0304-4203(96)00076-x.

Zhu, J., and X.-Z. Liang (2013), Impacts of the Bermuda High on Regional Climate and Ozone over the United States, *Journal of Climate*, *26*(3), 1018-1032, doi:10.1175/jcli-d-12-00168.1.

Ziemke, J. R., S. Chandra, B. N. Duncan, M. R. Schoeberl, O. Torres, M. R. Damon, and P. K. Bhartia (2009), Recent biomass burning in the tropics and related changes in tropospheric ozone, *Geophysical Research Letters*, *36*(15), n/a-n/a, doi:10.1029/2009gl039303.

Zondlo, M. A., M. E. Paige, S. M. Massick, and J. A. Silver (2010), Vertical cavity laser hygrometer for the National Science Foundation Gulfstream-V aircraft, *Journal of Geophysical Research-Atmospheres*, *115*, doi:10.1029/2010jd014445.